

ABSTRACT

Velu, Yogeshwar Karunakaran. 3D Structures formed by a Robotic and Meltblowing Integrated System (under the directions of Professors. Abdelfattah M. Seyam and Tushar K. Ghosh).

Meltblown nonwovens have been produced as 2D web structures for a variety of end uses. Investigation into the development of 3D structures, has led to the integration of meltblown and robotic technology to form the Robotic Fiber Assembly and Control System. The effects of various process parameters including the fiber stream approach angle and the curvature of the collecting surface on the structural properties of the webs such as the diameter and orientation distribution of the fibers and the pore size distribution on the webs has been investigated. The interrelationships between these structural parameters have been explored and a statistical model developed.

Orientation distribution, and the fiber diameter distribution of the webs were measured on image analysis software, while the pore size distribution was measured using equipment developed on the basis of capillary flow technique. SAS was used to develop the correlations between the structural parameters of the web. In general, all the webs show a larger percentage of fibers orienting in the machine direction (MD). The webs with finer fiber diameter produced webs with smaller pore diameter.

The take-up speed of the collector had a significant influence on the orientation and diameters of the fibers in the web. Finer fibers were formed which are more oriented in the machine direction as the take-up speed of the collecting surface increased resulting in the formation of a web which has pores with finer diameter. A decrease in the polymer throughput demonstrated a decrease in the fiber diameter, the pore diameter and the basis weights of the webs. The resulting webs also produced pores that are of finer diameter. Lower attenuating air pressures produced larger diameter fibers. The average pore diameter of the analyzed meltblown fabrics decreased significantly when the attenuating air pressure was increased. Increasing the die to collector distance (DCD) shows a decrease in the percentage of fibers that are oriented in the machine direction. An increase in the DCD also exhibits an initial decrease followed by an increase in the

average pore size confirming the existence of different “zones” in the space between the die and collector.

The increase in fiber stream approach angle shows an initial decrease followed by significant increase in the pore size of the web. Compared to the webs formed at low approach angles, analyses of the webs formed at higher approach angles shows that the fibers are more randomly arranged at higher approach angles. The relative frequency of fiber oriented in the machine direction increased significantly when the curvature of the collecting surface increases while the average pore size of the web decreases, due to the increased orientation of fibers in the direction of collection.

The pore diameter is found to be directly proportional to the fiber diameter and inversely related to the web anisotropy parameter. The relationship that was established for the 2D webs correlates to the relationship developed for the 3D web structures.

3D Structures Formed by a Robotic and Meltblowing Integrated System

by

YOGESHWAR KARUNAKARAN VELU

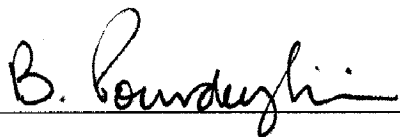
*A DISSERTATION SUBMITTED TO THE GRADUATE FACULTY OF
NORTH CAROLINA STATE UNIVERSITY
IN PARTIAL FULFILLMENT OF THE
REQUIREMENTS FOR THE DEGREE OF
DOCTOR OF PHILOSOPHY*

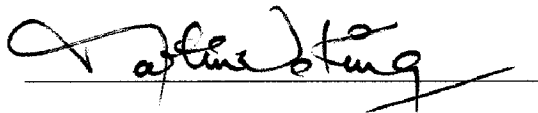
FIBER AND POLYMER SCIENCE

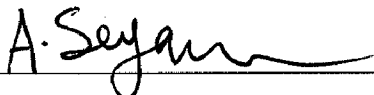
RALEIGH

2003

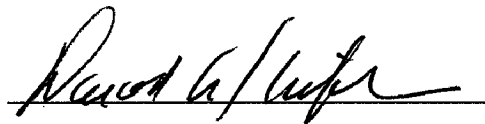
APPROVED BY:

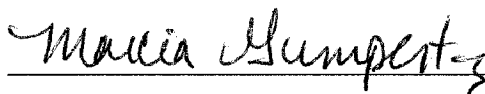






(Co-Chair of Advisory Committee)







(Co-Chair of Advisory Committee)

DEDICATION

Dedicated
To
HIS Lotus Feet
For
HIS Infinite Grace;

My Parents,
Pankaja Selvi and Karunakaran Arcot Mohanavelu;
and;
in the **memory** of the unborn
Baby Velu

BIOGRAPHY

Yogeshwar was born in Bangalore, India, on the 9th day of December 1969. On completing his schooling he joined Bangalore University leading to a degree in Textile Technology. He worked in various textile industries as an intern during the summers of his undergraduate studies, while tutoring high school students during the semester sessions. He worked as an assistant quality control manager in Birla Synthetics, India. He then joined Clemson University to pursue a Masters degree in Textile Science. During his Masters program at Georgia Tech, he worked as a Research engineer in the Image analysis lab.

He joined NCSU for Ph.D. in Fiber and Polymer Science in 1999 and worked part time with Nonwovens Co-operative Research Center (NCRC) during the last year.

He is married to the former Ms. Vijayalakshmi (Viju) Nithayanandam and they have a son Dhananjay Narayan Velu.

ACKNOWLEDGEMENTS

I thank Professors Abdelfattah Seyam, and Tushar Ghosh co-chairmen of my advisory committee for their guidance throughout the current research. I also thank the other members of my advisory committee, Drs. Marcia Gumpertz, Behnam Pourdeyhimi, Donald Shiffler and Martin King for the guidance. I would like to place on record my special appreciation to Dr. Behnam Pourdeyhimi for his constant support, guidance and for being there during the rough bumps in this stretch of the journey.

I would like to thank the College of Textiles, NCSU for giving me the opportunity to continue my education here. I appreciate the financial support from the Army Research Office towards this project. I sincerely thank the Directors and staff of Nonwoven Co-operative Research Center for making me a part of the NCRC family and also for the support during my years as a student at NCSU.

I would like to thank all of my friends, teachers and extended family, whose support and sincere contribution to my education and growth is just too large to list.

I would like to thank my in-laws for their prayers. Anitha, well, you know the reason why we could not make it for your wedding.

I appreciate the sacrifice of my brother, Saravanan, in foregoing the opportunity to continue his education in the US, in my favor. I thank my sister, Indira Priyadharshini, who has been a constant source of encouragement during the rough spots in this long road and for having the confidence that I would succeed in achieving what I set out to obtain. Chirag now you know why we could not meet you in your initial years. Anand, thanks for being there to support her so that Mom and Dad could be here. Mom and Dad, thanks for the confidence, encouragement, love and all the other sacrifices.

Viju, thanks for all the support, encouragement, love, and patience through these years. Dhananjay, seeing you at the end of a day makes all the stress vanish and hence the struggle to reach a goal worth its effort.

TABLE OF CONTENTS

LIST OF TABLES	vii
LIST OF FIGURES	viii
1. INTRODUCTION	1
2. LITERATURE REVIEW	5
2.1 INTRODUCTION	5
2.2 MELTBLOWING PROCESS	5
2.3 APPLICATIONS OF MELTBLOWN NONWOVENS	12
2.4 STRUCTURE OF MELTBLOWN WEBS	14
2.4.1 Variables Influencing Meltblown Web Characteristics	15
2.4.2 Process Variables	15
2.4.3 Material Variables.....	16
2.4.4 Simulation of Nonwoven Structures	22
2.5 CHARACTERIZATION OF MELTBLOWN WEBS	27
2.5.1 Fabric Uniformity or Basis Weight.....	27
2.5.2 Fiber Orientation Distribution.....	29
2.5.3 Fiber Diameter and its Distribution	39
2.5.4 Pore Size Distribution	44
3. EQUIPMETS, MATERIALS AND METHODS	54
3.1 ROBOTIC FIBER ASSEMBLY AND CONTROL SYSTEM	54
3.1.1 Modifications to RFACS	57
3.1.2 Curvature of the Collecting Surface.....	60
3.2 MATERIALS	64
3.3 EXPERIMENTAL DESIGN	71
3.3.1 Polymer Throughput	71
3.3.2 Attenuating Air Pressure.....	71
3.3.3 Web Take-up Speed.....	72
3.3.4 Die to Collector Distance.....	72
3.3.5 Fiber Stream Approach Angle	72
3.3.6 Curvature of the Collecting Surface.....	75
3.4 RANDOMIZATION PROCEDURE AND SAMPLE COLLECTION	75
3.5 WEB CHARACTERIZATION TECHNIQUES	77
3.5.1 ODF Measurement	77
3.5.2 Fiber Diameter Distribution.....	78
3.5.3 Pore Size Distribution	79
3.5.4 Basis Weight	85
3.6 STATISTICAL ANALYSIS	86

4. PROCESS VARIATION AND STRUCTURAL PARAMETERS.....	88
4.1 INFLUENCE OF POLYMER THROUGHPUT	88
4.2 INFLUENCE OF ATTENUATING AIR PRESSURE	97
4.3 INFLUENCE OF WEB TAKEUP SPEED.....	103
4.4 INFLUENCE OF DIE TO COLLECTOR DISTANCE	112
4.5 INFLUENCE OF FIBER STREAM APPROACH ANGLE	120
4.6 INFLUENCE OF CURVATURE OF COLLECTING SURFACE.....	129
5. INTERACTION BETWEEN STRUCTURAL PARAMETERS	138
5.1 GEOMETRICAL PARAMETERS OF A SIMULTAED PORE	139
5.2 STATISTICAL MODELING OF FIBER DIAMETER, PORE DIAMETER AND	
ANISOTROPY PARAMETER INTERACTIONS	149
6. CONCLUSIONS	156
7. RECOMMENDATIONS.....	159
8. BIBLIOGRAPHY	160
APPENDIX.....	166

LIST OF TABLES

Table 2.1: Advantages and Disadvantages of Increasing the Melt Flow in Polypropylene Resin	18
Table 2.2: Polyesters for Meltblowing.....	19
Table 2.3: Comparison of Methods for the Measurement of Basis Weight of Nonwovens	29
Table 2.4: Fiber Diameter from Different Methods.....	40
Table 2.5: List of Comparative Values to Show Equivalence of Reciprocal Hydraulic Radius and Twice the Reciprocal Mean Radius of Capillary	46
Table 3.1: Control Algorithm in 3D Space for Constant DCD.....	59
Table 3.2: Control Algorithm in 3D Space for Constant DCD and Surface Speed of Collector	59
Table 3.3: Meltblowing Unit Specifications for Polypropylene.....	65
Table 3.4: Meltblowing Unit Specifications for COPE	66
Table 3.5: Process Conditions for the COPE webs and the Corresponding Random Order for 2D webs	76
Table 3.6: Random order for the PP to Investigate the Effects of Approach Angle.....	76
Table 3.7: Sample Data from Pore Size Measurement of a Meltblown PP Fabric	
a) Data from the Sensors of the Equipment.....	84
b) Data Calculated Using the Equations	85
Table 4.1: Average Diameter of Fibers and Anisotropy Parameter of Fibers at Various Throughputs of MB PP Webs	93
Table 4.2: Average Fiber Diameter at Various Attenuating Air Pressure for MB PP Webs.....	102
Table 4.3: Average Diameter of Fibers and Anisotropy Parameter of PP MB Webs at Various Take-up Speeds	109
Table 4.4: Diameter of Fibers and Anisotropy Parameter of MB PP Webs at Various DCD	117
Table 4.5: Chi-Square Statistic for Fiber Diameter and Pore Diameter of 3D Webs Formed at Different Approach Angle.....	126
Table 4.6: Chi-Square and its Probability for the Fiber and Pore Diameter of Webs Formed at Different Curvatures	132
Table 5.1: Simulation Conditions for the Webs.....	143
Table 5.2: ANOVA and Regression of Structural Parameter Estimate for the Planar Web.....	150
Table 5.3: ANOVA and Regression of Structural Parameter Estimate for the 3D Web	153

LIST OF FIGURES

Figure 2.1: Schematic of a meltblowing system.....	7
Figure 2.2: Schematic of a screw extruder.....	8
Figure 2.3: Schematic of the metering pump.....	9
Figure 2.4: Schematic Representation of the Die Assembly and Web Collection	10
Figure 2.5: Cross sectional view of positive feed back of the die	11
Figure 2.6: Cross sectional view of negative feed back of the die	11
Figure 2.7: Effects of extruder screw speed and attenuating air pressure on fiber diameter	16
Figure 2.8: Effect of Increasing MFR's on the Tenacity and Bursting strength of the Web.....	18
Figure 2.9: Degradation time for Polypropylene Resin	21
Figure 2.10: Example of Poisson Line Network.....	23
Figure 2.11: Monte Carlo Simulation of a Physical System.....	26
Figure 2.12: Representation of the ODF.....	31
Figure 2.13: Tangent Representation of a Single Fiber	31
Figure 2.14: Variation of Rupture Strength and Fiber Orientation with direction in Random Laid Web.....	35
Figure 2.15: Variation of Rupture Strength and Fiber Orientation with direction in Cross Laid Web	36
Figure 2.16: An Example of a Binary Image of the Web.	38
Figure 2.17: A typical SEM picture of the Melt Blown Web at very High Magnification	41
Figure 2.18: A typical Fiber diameter distribution in a melt blown web.....	42
Figure 2.19: Micrograph of Shot Defects in Melt blown Polypropylene Web.....	43
Figure 2.20: Filaments that form "shots" exhibiting the touching phenomena close to the die	43
Figure 2.21: Illustration of longitudinal section of interconnected voids forming pores	45
Figure 2.22: Definition of Surface Tension at a Point P.....	47
Figure 2.23: Equilibrium of surface tensions at a line of Contact	48
Figure 2.24: (a) Capillary Rise and (b) Capillary Depression	49
Figure 2.25: Pore size distribution curves for Staple fiber Needle Punched Nonwoven Geotextile.....	51
Figure 2.26: Pore size distribution curves for continuous filament Needle Punched Nonwoven Geotextile.....	52
Figure 2.27: Pore size distribution curves for continuous filament Thermal bonded Nonwoven Geotextile	52

Figure 3.1: Robotic Fiber Assembly and Control System	55
Figure 3.2: Seventh-Axis Support Structure showing Lathe and Serial Measurement Board Box	55
Figure 3.3: Front and top view of the die in the cage	57
Figure 3.4: A conical mold with an elliptical path along which the fibers were laid	57
Figure 3.5: Positioning of the Die relative to the Mold for Variation in the Curvature of the Collecting Surface	58
Figure 3.6: Left handed Cartesian co-ordinate system superimposed on the schematic of RFACS	60
Figure 3.7: Curvature of an Arc in a Plane	61
Figure 3.8: Various curvatures on the collecting surface	61
Figure 3.9: Cross-section, parallel to the XY plane of the torso.....	62
Figure 3.10: DSC thermal analysis of the COPE resin.....	65
Figure 3.11: DSC Thermal Scan for PP resin.....	66
Figure 3.12: Nordson Desk Top Meltblown Extruder.....	67
Figure 3.13: CONAIR Dryer with hopper and Controls.....	68
Figure 3.14: SEM Image containing SHOT on COPE webs (a Composed Image of Various Samples Produced during Preliminary Trails)	70
Figure 3.15: The Die with SHOT formed at the nosepiece tip	70
Figure 3.16: Schematic of Fiber Stream Approach Angle on a Collecting Drum.....	73
Figure 3.17: Fiber Stream Approach Angle on a Conical Mold.....	74
Figure 3.18: Sampling Procedure for Structural Analyses	77
Figure 3.19: SEM image of a Polyurethane Co-polyester webs at 500 magnification	79
Figure 3.20: Schematic of the Capillary Flow Equipment	80
Figure 3.21: Typical Pressure versus Airflow curve for Pore Size Distribution Measurement on the PMI	82
Figure 3.22: Flow Chart for calculating the pore size and its distribution	84
Figure 4.1: ODF for MB COPE webs at different polymer throughputs.....	89
Figure 4.2: Anisotropy Parameter for MB COPE webs at different polymer throughputs.....	90
Figure 4.3: Cumulative frequency distribution of fiber diameters at different polymer throughput rates for MB COPE webs.....	91
Figure 4.4: Average Pore Size and Basis Weight for MB PP Fabrics for variation in the Polymer Throughput	92
Figure 4.5: SEM Picture of the COPE web at 9.6×10^{-2} g/min/hole throughput	94

Figure 4.6: SEM Picture of the MB COPE web at 1.8×10^{-2} g/min/hole Polymer Throughput.....	95
Figure 4.7: Cumulative Frequency for MB PP fabrics for variation in the Polymer Throughput.....	96
Figure 4.8: Effect of Attenuating Air Pressure on the Fiber Diameter Distribution of the COPE MB Webs	98
Figure 4.9: Scanning Electron Micrograph of the COPE webs produced at 0.7 bar attenuating air pressure.....	99
Figure 4.10: Scanning Electron Micrograph of the MB COPE webs produced at 2.8 bar attenuating air pressure.....	100
Figure 4.11: Cumulative Frequency (%) for MB PP webs for variation in attenuating air pressure.....	101
Figure 4.12: Average pore size for MB PP Webs for variation in the attenuating air pressure.....	102
Figure 4.13: ODF for MB COPE webs at different Collector Take-up Speeds	103
Figure 4.14: Anisotropy parameter for MB COPE webs at different Collector Take-up Speeds	104
Figure 4.15: Cumulative distribution of Fiber diameter distribution for MB COPE webs as a function of the Take-up speed.....	106
Figure 4.16: Scanning Electron micrograph of the MB COPE web at 6.09 m/min take-up speed.....	107
Figure 4.17: Scanning Electron micrograph of the MB COPE web at 14.33 m/min take-up speed.....	108
Figure 4.18: Average Pore Size and Basis Weight for MB PP webs for variation in the collecting drum Take-up Speed.....	110
Figure 4.19: Cumulative Flow Frequency for MB PP Webs for variation in the Web Take up Speed.....	111
Figure 4.20: Influence of DCD on ODF of COPE MB Webs	112
Figure 4.21: Anisotropy Parameter for COPE MB Webs at a various DCD.....	113
Figure 4.22: Fiber Diameter Distribution for COPE MB Webs at a various DCD ...	114
Figure 4.23: Pore Size Distribution for MB PP Fabrics at different Die to Collector Distances.....	115
Figure 4.24: Average Pore Diameter Distribution for MB PP Webs with Varying Collecting Distances.....	116
Figure 4.25: Scanning Electron Micrograph of the COPE MB web at 15.24 cm DCD.....	118
Figure 4.26: Scanning Electron Micrograph of the COPE MB web at 35.46 cm DCD	119

Figure 4.27: ODF for PP MB 3D webs formed at different Approach Angles	121
Figure 4.28: Comparative Anisotropy parameter for PP MB webs.....	122
Figure 4.29: Fiber Diameter Distribution of the MB PP web 3D webs formed at varying approach angles.....	123
Figure 4.30: Average pore diameter and fiber diameter of PP 3D MB webs formed at varying approach angles	124
Figure 4.31: Cumulative Frequency of PP 3D MB webs formed at varying approach angles	125
Figure 4.32: Range of pore size distribution of PP 3D MB webs formed at different approach angles	126
Figure 4.33: SEM Image of the MB PP web at 90 degree Approach Angle	127
Figure 4.34: SEM Image of the MB PP web at 37 degree Approach Angle	128
Figure 4.35: ODF for webs at PP MB webs collected at different curvatures.....	129
Figure 4.36: Anisotropy parameter for PP MB webs collected at different curvatures along the mold.....	130
Figure 4.37: Basis weight for PP MB webs collected at different curvatures of the collecting surface	131
Figure 4.38: Curvature effects on the die to collecting distance of the fibers at different points on the die (Plan of the Die and Curved Surface)	132
Figure 4.39: Average pore diameter and fiber diameter of PP 3D MB webs obtained at different curvatures	133
Figure 4.40: Cumulative Frequency of PP 3D MB webs formed at different curvatures.....	134
Figure 4.41: Cumulative Frequency of PP 3D MB webs formed at different curvatures.....	135
Figure 4.42: SEM Image of MB PP web at 1.95 m^{-1} Curvature.....	136
Figure 4.43: SEM Image of MB PP web at 10 m^{-1} Curvature.....	137
Figure 5.1: An irregular pore with a bounding rectangle and best-fit ellipse	139
Figure 5.2: Fibrous Structure with a Pore.	140
Figure 5.3: Simulated Structures with varying ODF	142
Figure 5.4: Variation in the Pore Roundness as a function of Standard Deviation of Orientation and Area Density.....	144
Figure 5.5: Pore radius variation as a function of Standard Deviation of Orientation and Roundness of the pore.....	145
Figure 5.6: Pore Area as a variation of the density of the web and the Standard Deviation of Orientation.....	146

Figure 5.7: Variation of Minor axis of the Best-fit Ellipse with the Standard Deviation of Orientation and Area of the Pore.	147
Figure 5.8: Variation of the Width of the Best-fit Rectangle with Standard Deviation of Orientation and Area of Pore	148
Figure 5.9: Scatter plot of the Pore Diameter, Anisotropy Parameter and Fiber Diameter for the planar webs.	151
Figure 5.10: Plot showing the relationship between the predicted Pore diameter and observed pore diameter for the planar webs.....	152
Figure 5.11: Plot showing the relationship between the predicted Pore diameter and observed pore diameter for the 3D webs.....	154
Figure 5.12: Scatter Plot of the observed and predicted pore diameters for the 3D webs	155

1 INTRODUCTION

Traditionally, nonwoven fiber webs are produced as two-dimensional (2D) flat sheet structures. Many of the applications of nonwoven webs are three-dimensional (3D) structures that have to be constructed from the flat sheets of the webs. The 2D webs are packaged and transported by their producers to a converter. The converter then has to form appropriate patterns from the web and produce the final 3D structure either by fusing and/or sewing the patterns together. Research in the area of nonwovens has concentrated in areas of specialized equipment for faster and larger machines, adaptation of the machines and processes to newer polymers / fibers. It has also focused on improvements in technologies, for measuring and monitoring techniques, for basis weight uniformity and developing the knowledge base in the area of understanding the structure property relationships. A majority of the research is in the area of manufacture and use of 2D nonwoven sheet structures.

The 3D webs that would be produced can be engineered to have particular fluid handling properties, softness, strength properties, abrasive properties and aesthetic properties. Articles such as personal care products, garments, medical products, lightweight components for protective fabrics and cleaning products can be produced. Seams and joining in a protective clothing usually constitute the “weak-links”. The larger the number of seams and joints, the greater the potential for splitting of the garment pieces; this can be disastrous for users (fire fighters, healthcare personnel, etc.) who rely on protective clothing that covers the entire or part of body surface area. It is assumed that protective clothing or suits may need to be multi-layered, multi-component systems to be fully effective in their purpose. Nonwoven webs when introduced into the protective clothing will form one or more of the multi-layered system.

The initial experiments to produce 3D nonwoven structures have been reported by Miura and Hosokawa [1]. They produced nonwoven structures, which were rich in resin with a high resin to fiber ratio (4:1). They used staple fibers to form the nonwoven web and convert them into 3D structures that were held together with a resin. Griesbach *et al* [2, 3] patented a technology to form a shaped nonwoven fabric comprising of the continuous spun bond filaments made by directly forming the spun bond filaments into a web in a single process. The spun bond filaments are bonded together with an adhesive polymeric

component so that the shape of the fabric is retained. More recently Innovent Engineered Solutions [4] have developed a meltblowing machine with a collection system that is capable of forming 3D pockets on the collection belts.

In order that the nonwoven web produced have uniformity / desired properties all along the 3D structure, precise control of the fiber placement on the collecting system is very essential. This can be achieved by the use of the meltblown technology to produce fine fibers. For the purposes of spraying the meltblown fibers on to a collecting surface (that can be 3D in nature), it is essential that the die on the extruder of meltblown system be mounted on a flexible robotic arm. Also, a similar flexibility for the collecting surface throws open a whole range of complex 3D structures that can be precisely produced with predictable structural and physical properties.

In the formation of meltblown webs currently in practice, the position and orientation of the die are fixed. Molten polymer is extruded through a series of orifices in a die. The orifices are surrounded by hot air that is traveling at high velocity. The laminar sheet of hot air attenuates the polymer stream, breaks it into fibers of varying length and carries it to a suitable forming surface. The forming surface is either a rotating drum or a moving belt. The fibers in the web are characterized by their extreme entanglement, which produces coherence and strength to the web. The entanglement of these long fibers makes it impossible to remove one complete fiber from the web [5]. The fibers in the web structures usually have a broad range of diameters ranging from less than one micron to about 25 microns [6]. The fine fibers that are produced yield a very high surface area per unit weight of the web. This will lead to the formation of lightweight webs that can have excellent filtration properties [7, 8].

The arrangement of the fibers is due to the spiral flow of air, as it moves away from the die and the preferential movement of the collecting surface. The randomness of fiber arrangement in the web is lost due to the preferential movement of the collecting surface. This causes the fibers to orient in the direction of the movement of the collecting surface (machine direction or MD). Since the meltblowing system uses an attenuating air system to draw and orient the fibers, the distance between the polymer delivering orifice and the collecting surface influences the fiber characteristics and the resultant web properties.

The time interval spent by the fibers in flight before being collected on the surface influences the fiber orientation, strength and surface properties [5].

The usefulness of molded fabrics so obtained depends on the performance characteristics of the web structures. The desired performance characteristics are strength, abrasion resistance, tear resistance, burst strength, elastic recovery, air/moisture permeability, moisture/fluid absorption (rate and capacity), filtration characteristics, etc. Each of these characteristics is influenced by the structure of the fibers in the web, fiber diameter and its distribution, pore size and its distribution, basis-weight of the web, fiber/polymer properties, etc. For a given polymeric resin, the ability to alter the parameters of the meltblowing machine leads to the formation of webs of varying characteristics that can find applications in the fields of filtration, medical and surgical products and liquid absorption products.

The Robotic Fiber Assembly and Control System (RFACS) developed at North Carolina State University [9] is a unique combination of the melt blown technology and robotic technology to produce 3D structures of nonwoven meltblown webs. The polymer is processed in the extruder and the molten polymer exits from the die placed on the end-effector of the robot. The fibers are collected on a suitable collecting device, placed on an additional external axis of the robotic assembly. The integration of the robot with the desktop meltblowing equipment has been completed. An understanding of the structural properties of 2D webs and a control over the basis weight distribution of webs produced on a mold using this system had already been developed [9]. The effect of the fiber stream approach angle (discussed in detail in Chapter 3) on the orientation distribution of the fibers had been completed.

With the background of the process thus developed, the objective of my research is to produce 3D meltblown web structures using the novel robotic and meltblown technology integrated system. Further, it is the objective to gain a basic understanding of the relationship between the additional process parameters, (viz. the fiber stream approach angle and curvature of the collecting surface) on the structural properties of the web thus formed. Further, the interrelationship between the structural parameters of the webs so formed has to be investigated. Although there is available literature on the studies of the interrelationships between the fiber diameter and the pore size of the web formed, the

other important parameter of the structure, the fiber orientation distribution has not been included simultaneously in any of the studies of the “real” webs. Hence an attempt will be made to develop a relationship between the structural parameters of the web, namely the diameter of the pore sizes, fiber diameter and fiber orientation. The formation of 3D webs raises two critical issues with respect to the process. They are the collecting surface for the continuous application of the fibers and the control of movement of the die.

Attempts would also be made to use different polymeric resins for the production of the web structures and the use of elastomeric polymer in the process would be investigated. The process parameters of the meltblowing system that would be varied include the traditional parameters viz., polymer throughput, attenuating air pressure, die to collector distance and the web collector take-up speed (surface speed of the collector). Additionally, the parameters that is possible due to the flexible movement of the die, the fiber stream approach angle and more importantly the curvature of the collecting surface. The effect of varying the process parameters on the structural parameters of the web would also be undertaken.

Before discussing the modifications that had to be made to the RFAC System, a review of the meltblown technology with the effects of the process parameters on the structure of the web produced is discussed in Chapter 2. Chapter 2 also contains a discussion on the simulation techniques that have been developed to predict the web characteristics and a review of the characterization techniques.

Chapter 3 discusses the RFACS and its modifications, materials and methods used to produce the webs. The experimental techniques actually used to characterize the webs are also discussed in Chapter 3. The results obtained from these characterizations as a function of the process variables is discussed in Chapter 4, while the inter-relationship between the structural parameters is discussed in Chapter 5. This followed by a few conclusions, based on the current work in Chapter 6 and the recommendations for future work in Chapter 7.

2 LITERATURE REVIEW

2.1 INTRODUCTION

In the early 1950's, Naval Research Laboratory started the investigation into the development of microfiber that was less than 5 micron in diameter [10]. The motivation for this work was the need for microdenier fibers for filters on drone aircraft used to monitor radiation and to collect radioactive particles from the upper atmosphere using organic fibers [11]. Melt blown technology, as it is known today, was developed from the initial work conducted at the Naval Research Laboratory. Meltblown fibers are characterized by their extremely small diameters. The unique microdenier character of the meltblown fibers produces high cover per unit weight, high surface area per unit weight and fine porosity. The resulting web structures are lightweight and have extremely high filtration efficiency, good barrier properties, and high insulating value [12, 13].

2.2 MELTBLOWING PROCESS

The meltblowing process has been defined as a single step production of thermoplastic nonwoven fabric of micro denier fibers, which are produced by a combination of filament extrusion and hot gas attenuation into discontinuous fibers propelled on to a collection belt, or drum, for web formation. Fibers are formed during melt blowing because of the attenuating action of the hot air under pressure on the molten polymer that has passed through the die orifices. The converging sheets of air perform the functions of attenuation of the filaments, breaking down of the filaments into fibers of varying length and transporting the fibers to a collecting surface. The fibers in the web are characterized by their extreme entanglement, which produces coherence and strength to the web. The entanglement of these long fibers makes it impossible to remove one complete fiber from the web [5]. The fibers in the web structures usually have a broad range of diameters ranging from less than one micron to about 25 microns [6]. The fine fibers that are produced yield a very high surface area per unit weight of the web. This will lead to the formation of lightweight fabrics that can have excellent filtration properties [7, 8].

In the formation of meltblown webs, currently in practice, the position and orientation of the die are fixed. The arrangement of the fibers is due to the spiral flow of air, as it

moves away from the die and the preferential movement of the collecting surface. The randomness of fiber arrangement in the web is lost due to the preferential movement of the collecting surface. This causes the fibers to orient in the direction of the movement of the collecting surface (machine direction or MD). Since the meltblowing system uses an attenuating air system to draw and orient the fibers, the distance between the polymer delivering orifice and the collecting surface influences the fiber characteristics and the resultant web properties. This distance is usually called as the Die-to-Collector Distance (DCD). The time interval spent by the fibers in flight before being collected on the surface influences the fiber orientation, strength and surface properties [5]. The process of attenuation takes place within approximately 200 microseconds and at short distances from the die [8, 13]. In the melt blowing process the gas performs the task of attenuating the polymer as it is extruded from the die [8, 13]. The force of the gas attenuates the fiber from approximately 500-micron diameter at the die orifice down to as small as 0.1 micron. This is a 5000 times reduction in the diameter of the fiber with 25 million times reduction in the cross-sectional area of the fiber. To aid the process of melt blowing, the viscosity and the degree of polymerization of the polymers used in melt blowing processes is, usually, lower than that used in the conventional melt spinning processes [13].

The schematic of a melt blowing process is shown in Figure 2.1. The polymer in a Meltblowing process is extruded through a die containing multiple orifices. Convergent streams of hot air, carried by insulated lines, exiting the die assembly from the top and bottom of the die nosepiece, attenuate the polymer to form fine diameter fibers that are collected on the collector. If the polymer exiting from the die is not attenuated, due to various reasons, defects such as “shots” or “ropes” are formed. “Shots” has been defined as the polymer beads in the nonwoven web that has not formed fibers [5]. “Ropes” have been defined as joining of polymer material or fibers that are formed due to the entanglement of fibers and bonding [5]. These defects in the nonwoven web are attributed to the polymeric resin and also the process related conditions. The filaments that exit from the die orifices are broken down into fibers and scattered as individual fibers by the air stream that is formed due to the converging air sheets. These individual fibers are

then deposited on a collecting surface [15]. Typical Meltblowing equipment consists of an extruder, metering pump, die assembly, web formation, and winding [16].

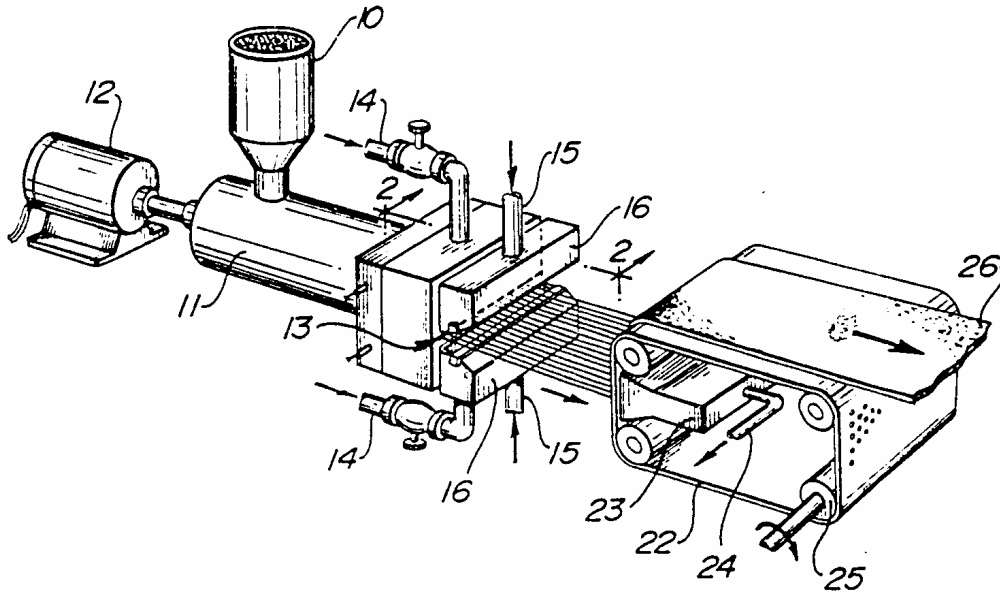


Figure 2.1: Schematic of a meltblowing system [14]

2.2.1.1 Extruder

The extruder (Figure 2.2) is essentially a screw conveyor, carrying pellets of the polymer forward and compacting the polymer with the aid of the external heat and the friction from the viscous flow [17]. Polymer pellets are fed into the extruder hopper that supplies the pellets to the screw by gravity feed. The screw rotates within a heated barrel, which is divided into different zones to control the temperature of the barrel. The screw, and the barrel, is divided into feed, transition, and metering zones. The polymer is exposed to incrementally higher temperatures in the successive heating zones of the barrel, which causes the polymer to melt and reach the desired temperature. In the feed zone the polymer is preheated in a deep channel screw and is conveyed to the transition zone. The screw in the transition zone has a decreasing depth channel that aids in the compression and homogenization of the melting polymer. The molten polymer that is delivered to the metering section serves to generate maximum pressure for pumping the polymer. The

pressure on the polymer is highest at this point and is controlled by a breaker plate and screen pack (see Figure 2.2). The screen pack and the breaker plate also serve to filter out the dust and dirt particles [15, 17]. In the extruder the polymer is exposed to incrementally increasing temperatures in consecutive heating zones. It can be easily observed that the incremental increases in temperatures from the first heating zone in the extruder and beyond are in sequence with the final and desired extrusion or Meltblowing temperature.

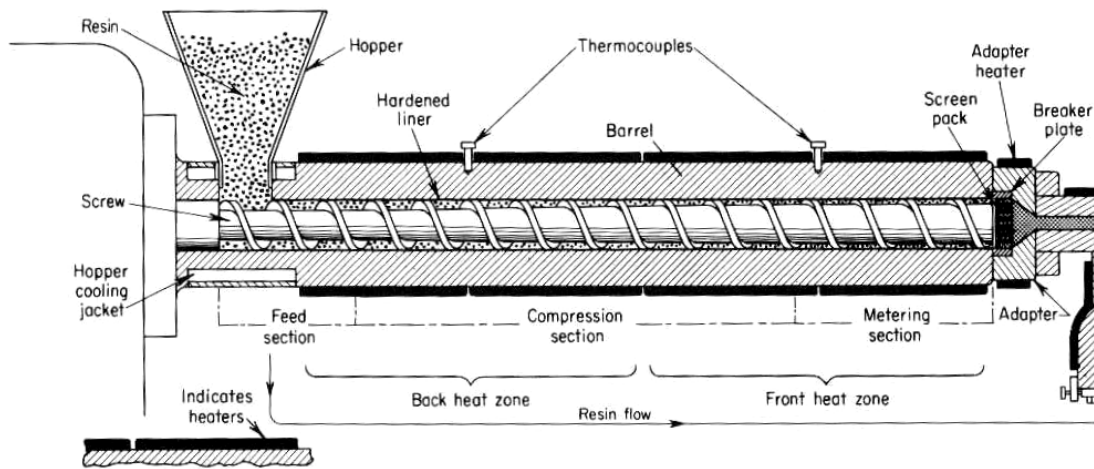


Figure 2.2: Schematic of a screw extruder [17]

2.2.1.2 Metering Pump

A metering pump (see Figure 2.3) is a positive displacement constant volume device for uniform melt delivery to the die assembly [15]. The metering pump typically has two inter meshing gears that are counter rotating which helps to control the flow of the polymer. Each gear tooth is filled with the polymer on the suction side and the polymer is released on the discharge side there by having a positive displacement of the polymer. The polymer subsequently enters the “die”, which is heated to the desired Meltblowing temperature.

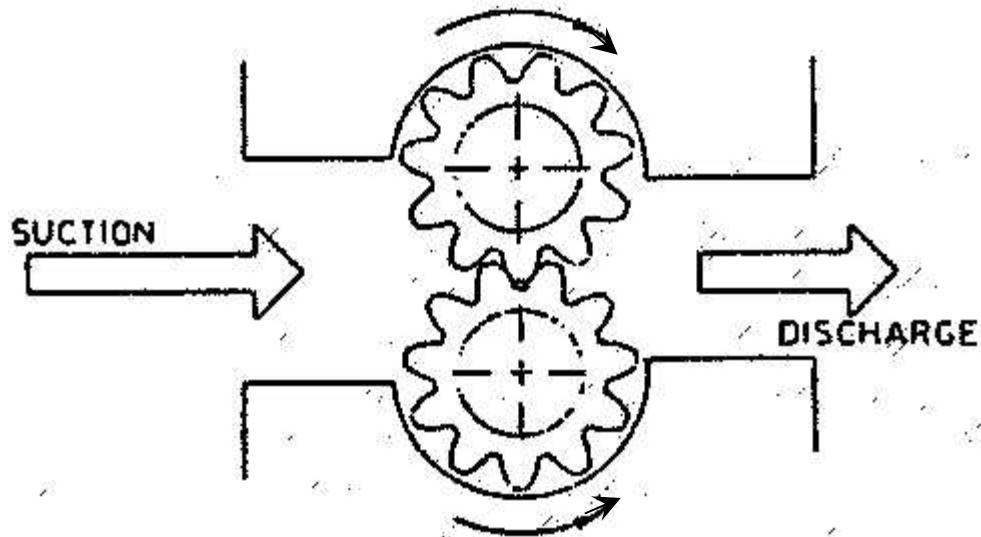


Figure 2.3: Schematic of the Metering Pump [15]

2.2.1.3 Die Assembly

The critical component of the melt blowing process is the die assembly [17]. Figure 2.4 is a schematic representation of the die assembly and collection system. The die assembly has three distinct components and is heated to the desired Meltblowing temperature [18]. The three components of the die are the die nosepiece, the air manifolds and the polymer feed distribution. The die assembly can be set up in three configurations, as discussed in the following section. The polymer feed distribution is critical since the die has no mechanical control over the variations in the polymer flow across the die width. The feed distribution needs to be such that the flow and the residence of the polymer in the die remain the same across the width of the die. The die nosepiece is a wide and hollow, tapered piece of metal having several orifices across its width. The polymer is extruded from these orifices to form filament strands. An inert hot compressed gas (usually air), is forced through the air manifolds of the die. The heated gas, known as primary air, then flows through the gas slots and attenuates the filament strands to form fine fibers [18]. The orifices are usually 0.4 mm in diameter spaced at 1 to 4 per millimeter. The gas manifolds supply the high velocity hot air through the slots to the top and bottom sides of the nosepiece.

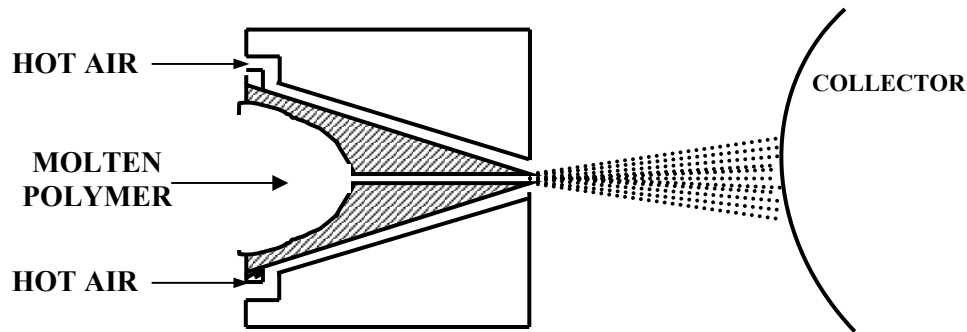


Figure 2.4: Schematic representation of the die assembly and web collection

Melt blown dies are set up in three different configurations, no setback, positive setback (die nose piece is sticking out arrangement) and negative setback (die nose piece is sunk in). When the die nose is not sticking out of the assembly then it is called as no set-back and will cause the attenuating air stream to converge directly at the die tip [19]. The positive setback is illustrated in Figure 2.5, while the negative setback is illustrated in Figure 2.6. The convergence of the attenuating air stream is dependent on the distance of the set back and the configuration of the die. A negative set back will lead to the convergence of the air stream within the die, while a positive set back will lead to the convergence outside of the die. The positive setback is usually used for the production of continuous filaments, while the negative setback yields the discontinuous fibers. The size of the orifice has little importance as long as it is large enough to pass the melt without plugging. In the system studied by Wente *et al* [10] the row of openings of the preferred design are 0.036 cm wide and 0.05 cm apart. As a result of this spacing, flat surfaces between the grooves are 0.015 cm wide and form dead spaces that separate the fibers in the blast. Of greater importance is the height of the slits through which the air is passed before attenuating the molten polymer as it is exiting the die orifices. Use of relatively large gas exit slots (i.e. 1- 3 mm) has a disadvantage that high quantities of gas are required as high rates of flow are necessary to produce fine fibers, especially of diameters smaller than 3 μm . Flow rates at the slot exits are typically 171 to 240 m/s [20]. The length of the individual orifice and their diameter influence the “back pressure” required to yield a given polymer feed rate [17]. This back pressure (also called ram pressure) is influenced by the speed of the screw, which advances the polymer material through the extruder. The polymer throughput rates determine the production speeds and

characteristics of the fibers formed by the system. Typical polymer throughput rates are in the range of 0.05 – 0.5 g/min/hole [21].

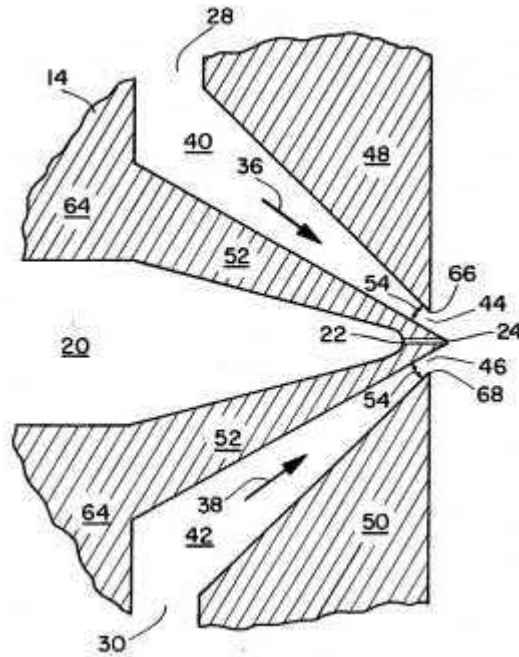


Figure 2.5: Cross sectional view of Positive Set Back of the Die [19]

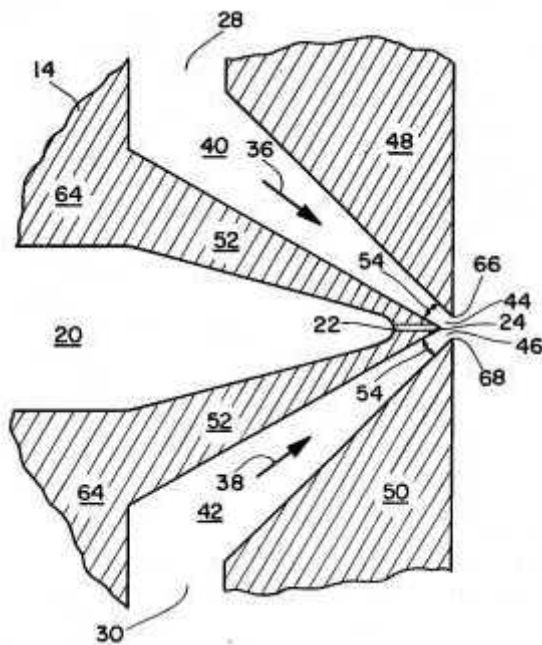


Figure 2.6: Cross sectional view of negative set back of the die [19]

2.2.1.4 Web Collection

The filament strand that is produced at the orifice is subjected to the high velocity gas that attenuates the filament and breaks it down into fibers. As the fibers move towards the collecting screen (usually a perforated belt or drum), the ambient air (also known as the secondary air) cools and solidifies the fibers. These are randomly deposited on the screen of the collector forming a self-bonded nonwoven web. The fibers are usually randomly placed on the screen, but are slightly biased in the direction of the machine due to the directionality imparted by the moving collector screen. A vacuum applied on the inner surface of the collector screen enhances the application of the fibers to the collector surface. Because meltblowing uses an attenuating air stream to draw and orient the fibers, the distance between the die orifice and the collecting distance is crucial and influences the fiber and the resultant web characteristics. This distance is called the die-to-collector distance (DCD). Varying the DCD can produce structures with varying properties from soft and bulky webs to stiff and rigid webs [5, 15, 22].

2.3 APPLICATIONS OF MELTBLOWN NONWOVENS

Melt blowing process produces fibers that are orders of magnitude smaller than those produced using conventional melt spinning. Hence these webs of fine fibers, with high surface area per unit weight and high cover per unit weight, are ideal materials for filtration, insulation and liquid absorption [22]. Modified melt blown webs with additives present on the fibers can be used for the adsorption of gases.

2.3.1.1 Filtration Media

Melt-blown process was developed for the purposes of producing webs to filter radioactive particles from the upper atmosphere [10]. Therefore the filtration segment still remains as the major single market for the meltblown nonwoven webs and is composed of both, liquid and gaseous filtration markets. Usually the meltblown filtration media is used for critical applications, where the microfiber structure is utilized to give a superior filtration capability [26]. A broad range of specific filtration applications is served by melt blown webs. The best-known segment is the surgical facemask filter media. Gaseous filtration applications include individual room filters and re-circulators, coalescence filters to remove water from a gas stream, cartridge filters and others.

Solid accumulation in front of the filter media and retention of particles in the filter media are the two major mechanisms of filtration [23]. In the first case a cake of the filtered particles are collected in the up stream of the filter media. The meltblown webs are used as filtration media in the later case, where they are used to retain particles that flow through the filter [23]. In the methods of filtration using meltblown webs, the structure of the web influences the efficiency of the process. As the number of fibers increases the filtration efficiency¹ increases. The greater the number of fibers, the higher will be the probability of interception of the particles. The other factors that affect the filtration efficiency are the void volume in the web, and the distance between the filter fibers [23]. The fineness of the fiber diameter, leading to a corresponding increase in the collector surface area of the fibers, and the orientation distribution of the fibers in the web make the meltblown nonwoven webs ideal for filter material.

2.3.1.2 Thermal Insulators

Meltblown nonwoven webs are excellent insulators as the microfibers in the web hold motionless air effectively against their surface. The thermal resistance of the fibers is directly related to the fiber fineness and finer fibers have a higher insulation compared to the larger diameter fibers [24]. Meltblown webs have been used as thermal insulators in electrical applications, and as lining material in the sports wear and protective garments. Fine fibers in the web hold the air effectively and offer very high resistance to conduction of air. Because of the nature of the structure, the void fraction of the web is very high and hence the overall conductivity of the material decreases from about by an order of magnitude.

2.3.1.3 Medical Products

The medical and surgical applications of the meltblown products cover a variety of specific applications. Because of its critical nature, the products must meet specific properties to ensure that they perform properly for the intended end use. The major medical/surgical applications of the melt blown webs have been in the disposable gowns and drape, sterilization wraps, gloves and table covers.

¹ $\text{FiltrationEfficiency}(\%) = \frac{\text{RetainedParticles}}{\text{TotalParticles}} \times 100$

The principal function in these applications is the creation of an artificial barrier between the patient and surgical team. With the increase in the potential contamination and spread of disease through the fluids of the body it has become increasingly necessary that the surgical team be well protected from the bodily fluids originating in the patients body. Hence the gowns, caps and drapes have to act as barrier material and also be coupled with “comfort”. This can be achieved if there is good moisture vapor transmission through the barrier and be impervious to liquids.

The meltblown web provides the barrier properties to many liquids such as blood, alcohol, water and other bodily fluids, while the microfiber nature of the web allows the water vapor to transmit and impart the necessary comfort in all of the spunbond /meltblown/ spunbond (SMS) webs. Meltblown webs have replaced paper and wet form webs, for sterilization wraps. The wraps are SMS structures that offer barrier against liquids and are gas permeable to allow the penetration of the gaseous sterilant. Apart from the vapor transmission and barrier properties the medical fabrics should have good strength, resistance to tearing, anti-static properties, and fire retardant. All of these properties can be obtained in a meltblown web while maintaining a lower cost.

2.3.1.4 Liquid Absorption

The meltblown fibers in a variety of physical forms are designed and used as an absorbent of liquid particles. These materials either have absorbent particles present in the structure of the web or the structure of the web is designed to absorb the liquid particles. Melt blown webs are used as diaper linings, sanitary napkins and as disposable vacuum cleaner bags.

2.4 STRUCTURE OF MELT BLOWN WEBS

The fibers in meltblown webs are usually randomly arranged, with a slight bias in the machine direction. This preferential orientation is due to the movement of the collecting surface [13]. A review of the published literature indicates that the variation in the length of the fibers in the web has not been quantified, but a highly magnified image of the web, shows that the fibers do exhibit a variation in their length. Warner *et al* [25] have shown that the diameters of the fibers in the melt blown webs exhibit a log – normal distribution. Depending on the process and material variables the diameters of the micro-fibers in the

web range from sub-micron to about 20 microns while the macro-fibers have diameters to about 50 microns [5, 15, 25].

2.4.1 Variables Influencing Meltblown Web Characteristics

During the Meltblowing process the polymer from the hopper is subjected to different temperatures and pressures before it is extruded through the die orifice as filaments. The high velocity hot air attenuates the filaments and eventually breaks them into fibers. The attenuated fibers are then blown at high velocity on to a collecting surface. During these processes the physical and mechanical properties of the resultant web are developed. It has been determined by Shambaugh *et al* [8] that most of the fiber diameter reduction occurs when the polymer is in semi-molten state and that little drawing of the quenched fibers occurs before deposition on to the collector drum [26]. The distribution and alignment of fibers in the web affect the tensile strength of the nonwoven web [27, 28]. The distribution of the fibers in the web is dependent on the velocity of the attenuating air and the polymer throughput in the system. The input air pressure and temperature determine the attenuating air velocity. The rate of polymer feed, along with the temperatures that the polymer experiences as it passes through the extruder determine the viscosity of the polymer and the fiber formation [17, 21]. These variables that affect the structure and the properties of the web are called the control variables and can be categorized as process variables and material variables.

2.4.2 Process Variables

The processing variables used to produce the melt blown web affect the structure and properties of the web. The processing variables are classified into on-line variables and off-line variables [29]. The on-line variables have been defined as those that can be altered during the production of the meltblown web. For a given polymer and die configuration the control variables that affect the web are the on-line variables. These are the polymer throughput, polymer melt temperature, die temperature, gas flow rate and gas temperature, screw speed, and die-to-collector distance [29, 30]. Studies conducted by Malkan *et al* [15] and Farer *et al* [9] have shown that the average fiber diameter increases with increase in the screw speed (increasing the polymer through put in the

system). Also as the attenuating air pressure increases the fiber diameter decreases, as shown in Figure 2.7.

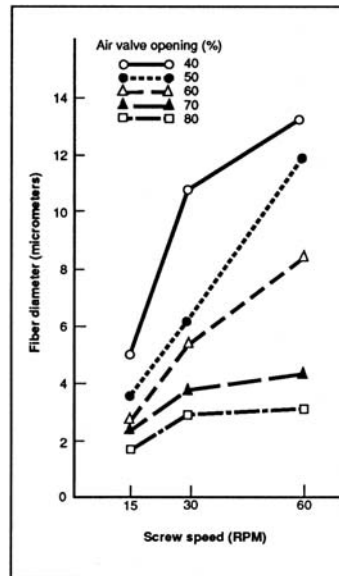


Figure 2.7: Effects of extruder screw speed and attenuating air pressure on fiber diameter [29].

The off-line variables cannot be altered during the operation of the Meltblowing machine and requires the machine to be in non-operational mode. These variables are the die hole size, die set back, air gap and design parameters. The type of set back on the die determines the location of the convergence of the air streams. A positive set back is used for the production of the continuous filaments, while a negative set back will yield discontinuous fibers. The air gap affects the air pressure of the exiting gas and hence the structure of the fibers produced [29].

2.4.3 Material Variables

The material variables include the polymer type, molecular weight distribution, polymer degradation, and additives to the polymer. The melt blowing process needs polymer with low melt viscosity. Usually the polymer in the melt blown process is extruded with its melt viscosity roughly one order of magnitude lower than that employed in the conventional melt spinning process. Okada *et. al* [13] have shown that the melt viscosity of the polymers, in melt blowing, at the orifice is in the range of 200 to 500 poise. In general polymers, which can give an acceptable low melt viscosity at suitable processing temperatures, can be melt blown into webs. In order to produce webs that are uniform,

the melt blown process requires that the polymer have a low molecular weight and a narrow molecular weight distribution [15]. The molecular weight is directly related to the melt viscosity and inversely proportional to the melt-flow rate (MFR)². Polymers with higher MFR allow higher throughputs and lower operating temperatures. The molecular weight distribution and melt viscosity determine the level of polymer degradation. Initially polymers with very low MFR (about 12) were used in Meltblowing applications. Within the first decade of the development of the process the resins with MFR of 35 were processed and later to resins with 300 to 500 MFR. Recently resins with MFR in the range of 800 to 1200 have become available through further advances and efforts undertaken by polymer manufacturers. A wide variety of polymers can be processed by Meltblowing equipment, but polypropylene appears to be the main resin that is used by the manufacturers. Homopolymers of polypropylene (PP) resins in the range of 600 to 1500 MFRs and copolymers of PP in the range of 600 to 1100 has been reported by Haides [31]. The data as reported by Haides that products with very high melt flow rates have fibers with finer diameter, with some loss in tenacity and bursting strength is concurred by Malkan *et. al* (Figure 2.8). However increasing the MFRs decreases the energy required to process the polymer and hence produces products, which are cheaper. The advantages and disadvantages of increasing the MFR of polypropylene resins is given in Table 2.1

² The melt flow rate (MFR), or the melt flow index (MFI) is a function of the polymer molecular weight. It provides an estimate for the molecular weight of the polymer. The longer the chain length of the polymer, higher is their molecular weight and lower melt flow. The melt flow rate of polymers, commonly called the MFR is also correlated to the intrinsic viscosity of the material (IV).

Table 2.1: Advantages and Disadvantages of increasing the melt flow in Polypropylene resin (35 MFR to 1500 MFR) [31].

- Reduced Energy Consumption
- Increased Softness of hand
- Reduced processing temperature
- Increased web porosity
- Reduced shot size
- Increased strength to weight ratio
- Lower tenacity
- Lower bursting strength

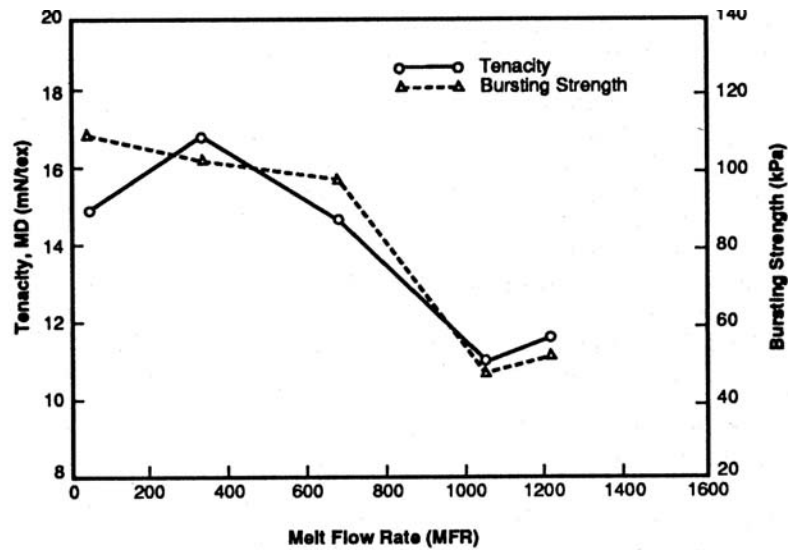


Figure 2.8: Effect of Increasing MFR's on the Tenacity and Bursting strength of the Web [29].

A variety of polyesters suitable for melt blowing have also been developed. These polyesters have viscosity in the range of 1400 to 13000 poise [32]. Copolyesters containing polyesters and polyurethane have also been produced [33]. A detailed list of polymeric resins used in the production of melt blown nonwoven webs as been enumerated by Farer [9].

Table 2.2: Polyesters for Melt Blowing [9]

- Amorphous Adhesive Polymer
- Copolyester (Kodabond 5116)
- High Melting Nonadhesive or matrix polyester
- Crystallized Pellets (Kodapak PET 7352, PET 9899U, PET 5214)
- Uncrystallized Pellets (Kodar A 150 Copolyester, Ektar PCT 3879)

2.4.3.1 Influence of Die to Collector Distance (DCD)

Typically, meltblown nonwoven fabrics are formed at DCDs ranging from 18 to 70 cm, and more commonly ranging from 10 to 46 cm [34]. Nonwoven fabrics produced when fibers are collected at relatively short distances will be more compact than those collected at greater distances. It has been noted that the DCD as a variable may be used to vary the nonwoven properties such as drape, elasticity, resilience, appearance, and the like [35]. The webs formed using about 55° C lower attenuating air temperatures at close collecting distances has not only been energy efficient on the system, but also produced webs that have improved web formation and uniformity [36, 37]. DCD and amount of attenuating gas volume/velocity manufacturing parameters counter act each other on their effects on the web properties. Shorter DCD produce smaller pore sizes in resultant webs while lower attenuating air velocity increases resultant pore size [5]. Studies conducted by Bresee *et al* [38, 39, 40], indicate that the fiber diameter varies depending upon the die orifice and DCD. The rate of the change of the diameter decreases significantly when the DCD increases, but there is the attenuation of the fiber up until 30 cm, indicating that the fibers although crystallized beyond 5 cm, are attenuated by the elongational force on the fibers. The formation of the meltblown web, being a complex process involving various parameters, the attenuation of the fiber and its crystallization is further influenced by the attenuating fluid. As the DCD increases the web density and tensile strength decreases, while the tear strength, softness and pore size (measured by permeability) increases [5, 41].

2.4.3.2 Influence of Attenuating Fluid

The flow rates and the temperatures of the attenuating fluids impact the fiber diameter. At low attenuating air pressures (0.18 to 1.4 bar), large diameter fibers (above 20 microns) are produced. Micro-fibers in the web are produced when the attenuating air

pressure is in the range of 1.4 to 7 bar. The fiber diameter is also influenced by other process parameters such as the polymer flow rate and throughputs, the intrinsic viscosity³ (IV) of the polymer etc. When a high IV polymer is used for the processing, higher attenuating air pressures will still produce macro fibers [35]. Changing the temperature of the fluid appears to have no influence on the fiber crystallinity while increasing the flow rates show a reduction in the crystallinity in the fibers with reduced diameters [8, 38]. At moderate airflow rates the polymer melt produces larger average diameters with an increasing tendency for the fibers to form ropes. This is also further dependent on polymer flow rates [21]. Air resistance and filtration performance are shown to increase as processing air pressure is increased, but proceed through a maximum when plotted against temperature [5].

2.4.3.3 Influence of Polymer Melt Flow Rate (MFR)

The MFR of the polymer is related to the molecular weight of the polymeric resin. As the melt flow rate increases, the viscosity of the polymeric resin and its molecular weight decrease. The meltblown nonwoven webs produced using higher MFR resins show a decrease in their tensile strength due to the decrease in the molecular weights [5, 42]. Finer diameters in the web are obtained when the melt viscosity of the resin is low. Hence the low MFR resins require higher processing temperatures in the extruder and die [43]. While high MFR resins on the other hand need high shear extruders for effective melt pumping [43]. As the MFR of the resin increases the web density, fiber diameter, pore size (permeability), tensile and tear strength increase while the softness of the web decreases [5]. Although an increase in the MFR should intuitively imply that the fiber diameter in the web should decrease, it is not the case. The fiber diameter is dependent on the polymer throughput rate, the attenuating air temperature and the temperature at the

³ Intrinsic viscosity (IV) $[\eta]$: Viscosity is the resistance to flow and is defined as “the measure of energy dissipated by a fluid in motion as it resists an applied shearing force”. Intrinsic viscosity is the limit of the reduced and inherent viscosities as the concentration of the polymeric solute reaches zero. It represents the capacity of the polymer to increase viscosity. It is a practical measure of the molecular weight of high polymers. Higher intrinsic viscosity implies the polymer has a higher molecular weight.

$$[\eta] = KM^a$$

where a and K are Mark – Houwink constants and is the M = Viscosity average molecular weight of the polymer

die orifice [42, 44]. Higher MFR (lower molecular weight) resins allow higher throughput rates and lower operating temperatures which in turn reduce the energy consumption for the production of the web [42].

2.4.3.4 Influence of Processing Temperature and Polymer Degradation

In meltblowing the polymeric resin is processed at higher temperatures than the melt temperatures. Typically, when the resin (polyolefin and polyesters) is exposed to high temperatures, the resin undergoes thermal degradation. The duration of exposure to high temperatures is very small, in the meltblowing process, and hence only small amounts of degradation occurs. The reduction in the residence time of the resin in the high temperature sections of the meltblowing system also reduces the degradation of the polymer. A study conducted by Schwarz [45], on polypropylene, indicates that the duration for degradation is related to the exposure temperature (see Figure 2.9).

Altering the processing temperatures in the extruder can control the occurrence of shots in the web [43]. While lower temperatures in the initial zones aids in the mixing of the polymer, higher temperatures in the final zones of the extruder decreases the occurrence of shots in the web. Any increase in the polymer degradation results in the increased number of shots in the web, along with increased apparent density, decreased softness, tensile and tear strength [5].

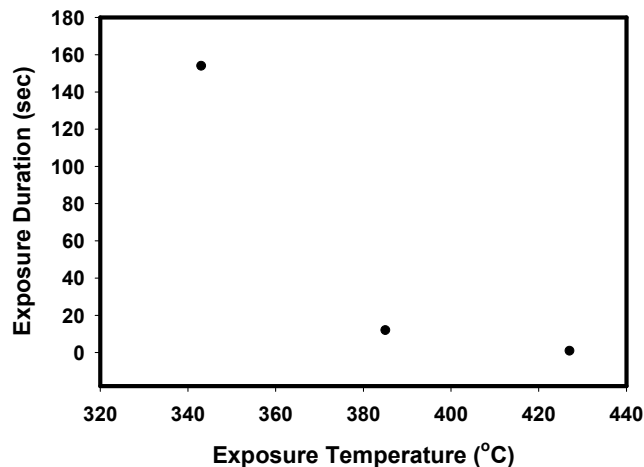


Figure 2.9: Degradation time for Polypropylene Resin [45]

2.4.3.5 Influence of the Collector Take-up speed

The rate at which the collecting surface moves, influence the basis weight of the nonwoven web. The structural arrangement of the fibers in the web are also affected by the take – up speed of the collecting surface [39]. The structure of the web is dynamic near the die and is fixed when it forms a web on the collecting surface. The speeds of the collecting surface, along with its distance from the die, determine the drag and elongational force that will be applied on the fiber. Studies by Bresee *et al* [46, 47, 48] show that the elongational force that is present at the surface on the collector attenuates the fibers even after they have been partially crystallized.

2.4.4 Simulation of Nonwoven Structures

The properties of the nonwoven web are affected by the nature of the fibers and the way in which these are fibers arranged in the web. Hence there have been studies to relate the structural properties of the webs by the simulation of web structures [46]. Various authors have attempted to simulate the structure of nonwoven webs for the purposes of predicting the performance of the webs. All of the simulations have the fundamental assumptions that the fibers in the web lie in the same plane as that of the web. The structure of the fiber is also assumed to be of cylindrical cross section. In studies conducted by Piekaar and Clarenburg [47], the webs are assumed to be of multiple layers of fibers. Each layer is considered to have a random arrangement of fibers in them. It is well known that the nonwoven webs from spunbond and meltblown process have little or no order in the thickness of the webs and hence the webs have been considered to be 2D planar structures [48].

The interaction between the fiber diameter and the pore size that is formed has been investigated on these simulated webs [49]. The probabilistic models, for porous media, that have been investigated by the various researchers include the filtration behavior of granular materials, flow through fibrous filters by Piekaar *et al* [47], nonwoven coalscers by Abdel-Ghani *et al* [46] and geotextiles by Lombard *et al* [49]. Pourdeyhimi *et al* [62] have improved on the techniques developed for specific applications in characterizing the nonwoven webs. All of the simulations have used Monte Carlo simulation techniques (described in section 2.4.4.1) to develop the structure of the web. On the simulated web

structures, Abdel-Ghani *et al* [46], have proposed an expression for an average area (a_m) of the pore as

$$a_m = \frac{\pi n D_f^2}{(1-n)^2} \quad (1)$$

where n is the porosity of the filter and D_f is the diameter of the fiber. According to this equation the area of the pore is directly related to the fiber diameter, but this method still needs numerical calculations to simulate the structure and obtain the pore size. The pores are not circular, rather polygonal in nature. Matheron [50] has developed a theory based on geometrical probabilities to characterize the geometry of Poisson networks induced in a space of m dimensions. An example of Poisson line network is shown in (Figure 2.10) and according to this theory the pore size distribution in the web is

$$F_f(d) = 1 - \left[\left(\frac{4\mu d}{\pi T_g D_f \rho_f} + 1 \right)^{\frac{T_g}{D_f}} \exp\left(\frac{-4\mu d}{\pi T_g D_f^2 \rho_f} \right) \right] \quad (2)$$

where

- d - pore diameter (μm)
- μ - mass per unit area of web (gsm)
- T_g - Thickness of the web
- D_f - fiber diameter
- ρ_f - density of the polymer used

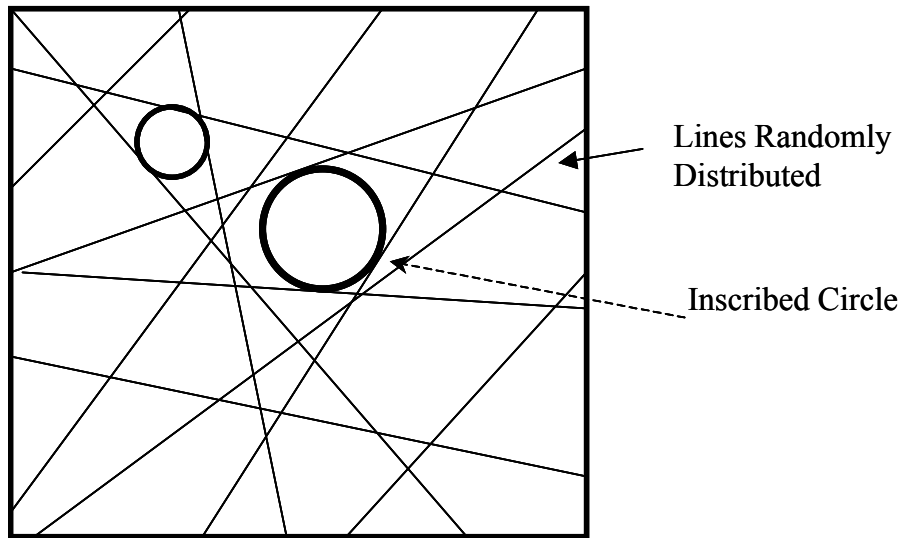


Figure 2.10 : Example of Poisson Line Network

A comparison of theoretical and experimental values for a thermally nonwoven geotextile by Lombard *et al* [49] indicate that the calculated value of the pore size is smaller than the apparent opening size of the pore. This is due to the distortion of the web structure during the hydrodynamic method of determination of the actual pore size. This leads to the formation of webs, which are not made of circular filaments as expected in the equation. The equation mentioned has its limitation and in that it assumes that the web is a uniform random filament network. The structure of the web i.e. orientation and diameter distribution of the fibers, play a crucial role in the determination of the pore size and its distribution.

The methods used to develop the random lines (representing the fibers) in the simulated web has been discussed in detail by Abdel-Ghani *et al*[46] and further, its application to determine the orientation distribution of the web having continuous and discontinuous lines, by Pourdeyhimi *et al* [62]. These methods developed to determine the orientation distribution function for simulated web structures is discussed in the section on characterizing orientation distribution functions.

2.4.4.1 Monte Carlo Simulation Technique

Monte Carlo methods make up that field of experimental mathematics which involves experiments on random numbers, and are thus well suited to probabilistic problems concerning the behavior and outcome of random processes. These techniques were initially developed during the 1940's as a research tool for the working of the atomic bomb and have since been used in various fields including medicine, operations research, chemistry, and applied mechanics [51]. The methods can be loosely described as statistical simulation models, where statistical simulation is defined in quite general terms to be any method that utilizes sequences of random numbers to perform the simulation. The concept of random sampling is essential to the modeling technique. The analogy of Monte Carlo methods to games of chance is a good one, but the "game" is a physical system, and the outcome of the game is not a pot of money or stack of chips (unless simulated) but rather a solution to some problem. The "winner" is the scientist, who judges the value of his results on their intrinsic worth, rather than the extrinsic worth of his holdings. Statistical simulation methods may be contrasted to conventional numerical discretization methods, which typically are applied to ordinary or partial differential

equations that describe some underlying physical or mathematical system. In many applications of Monte Carlo, the physical process is simulated directly, and there is no need to even write down the differential equations that describe the behavior of the system. The only requirement is that the physical (or mathematical) system be described by probability density functions (pdf's) [52].

In order to describe a problem with infinite outcomes, such as, the case of a single fiber orientation, during the formation of a meltblown web, we have to understand statistical concepts such as cumulative distributive functions and probability density functions. If we consider a set of exhaustive and exclusive events each characterized by a number η , then the following definitions can be made. The number η is a random variable, and its associated cumulative distributive function $F(y)$ is defined as the probability that the event which occurs has a value η less than or equal to y [51, 52].

$$F(y) = P(\eta \leq y) \tag{3}$$

Now, if $F(y)$ has a derivative $f(y)$, then this derivative is called the probability density function (pdf) [53]. The probability density function can be used to describe the probability that the η , lies between the interval $[a, b]$ as

$$P(a \leq \eta \leq b) = \int_a^b f(y)dy \tag{4}$$

If the range of possible values for η is $[y_{\max}, y_{\min}]$ then the probability density function $f(y)$, is normalized such that

$$\int_{y_{\min}}^{y_{\max}} f(y)dy = 1 \tag{5}$$

Furthermore, the cumulative distribution function $F(y)$, should be monotonically increasing on the interval $[y_{\max}, y_{\min}]$, with $F(y_{\min}) = 0$ and $F(y_{\max}) = 1$.

An example of an arbitrary physical system illustrating the idea of Monte Carlo simulation is shown in (Figure 2.11). Assuming that the evolution of the physical system can be described by probability density functions (pdf's), then the Monte Carlo simulation can proceed by sampling from these pdf's, which necessitates a fast and effective way to generate random numbers uniformly distributed on the interval 0 to 1. The outcome of

these random samplings, or trials, must be accumulated or tallied in an appropriate manner to produce the desired result, but the essential characteristic of Monte Carlo is the use of random sampling techniques to arrive at a solution of the physical problem.

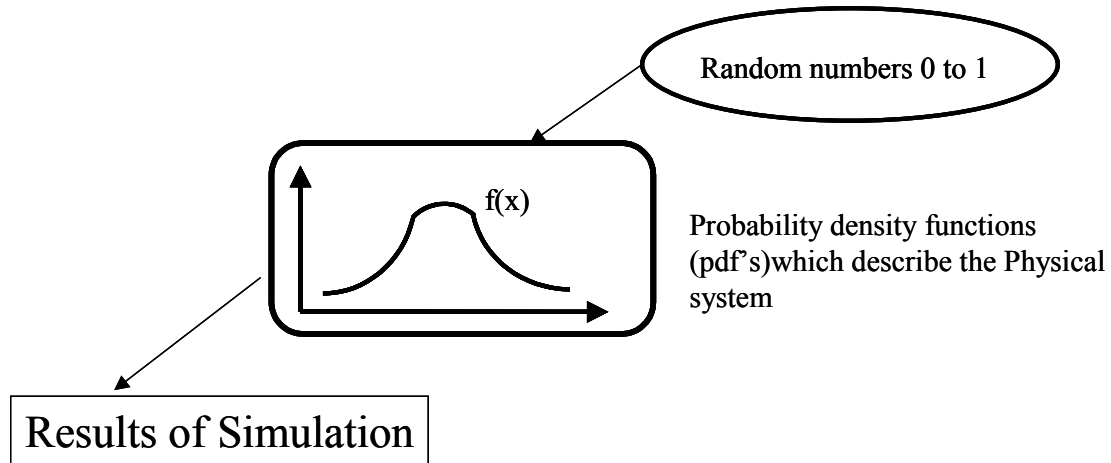


Figure 2.11: Monte Carlo Simulation of a Physical System

The primary components of a Monte Carlo simulation method include the following [51]:

- Probability distribution functions (pdf's)* - the physical (or mathematical) system must be described by a set of pdf's.
- Random number generator* - a source of random numbers uniformly distributed on the unit interval must be available.
- Sampling rule* - a prescription for sampling from the specified pdf's, assuming the availability of random numbers on the unit interval, must be given.
- Scoring (or tallying)* - the outcomes must be accumulated into overall tallies or scores for the quantities of interest.
- Error estimation* - an estimate of the statistical error (variance) as a function of the number of trials and other quantities must be determined.
- Variance reduction techniques* - methods for reducing the variance in the estimated solution to reduce the computational time for Monte Carlo simulation
- Parallelization and vectorization* - algorithms to allow Monte Carlo methods to be implemented efficiently on advanced computer architectures.

2.5 CHARACTERIZATION OF THE MELTBLOWN WEBS

The increasing success and demand for meltblown nonwovens in a wide variety of applications have influenced the need to develop the characterization and testing techniques for the webs produced. The results obtained from the testing techniques provide information, which will help the producers of the nonwovens in improving their quality, developing products and in predicting the overall performance of the web.

The characterization of nonwoven products encompasses the determination and evaluation of various properties that can be broadly classified into physical properties and mechanical properties. As the current research involves the investigation of the structural properties only those properties will be discussed. The physical properties can be defined as the properties that characterize the physical and structural nature of the nonwoven product. These include the basis weight uniformity of the product, the dimensional properties such as the length, width and thickness, and the structural properties such as the fiber orientation distribution, the distribution of fiber diameter, and pore size.

2.5.1 Fabric Uniformity or Basis weight

Nonwoven webs have a high productivity rate. These webs need to be measured using a mass uniformity measurement technique. Most properties of webs as well as the variations in the web properties are known to be influenced by the uniformity of the web, which is the optical or the basis weight uniformity. There are contact and non-contact form of on-line measuring the basis weight of the webs.

The non-contact type methods are all based on the principle that the amount of energy absorbed, reflected, refracted and/or diffracted from the web is dependent on the mass of the web. The methods that are used are,

- **Light Radiation Method:** An incandescent or fluorescent light source is placed on one side of the web, while a detector is placed on the other side of the web. The fraction of the light that passes through the web is monitored to determine the basis weight of the web that is formed. Haigh-Chadwick's Microweb [54] is a photoelectric measuring system that uses a series of photocells at uniform intervals of the web. These cells monitor the obscuration by the fibers of light from a uniformed light source. Autocount [55] is another photoelectric system that measures the basis weight of the webs. The light from the source is split and one beam is made to pass through the web, while the other is directly measured by the photocell. The advantage of this method is to take into account the aging of the light source or changes in the external voltage of

the system. The problems due to vibrations in the tungsten filament can be overcome by using Laser light source. Johnson and Henderson [56], have recommended a method to measure the basis weight of fibrous batt. The fibrous batt (carded) obscures about 75% of the incident light. The web is illuminated from one side with infrared radiation and the transmitted radiation is received by a multiplicity of detectors placed over the entire width of the web. The output signal is representative of the basis weight of the web. In a similar system a camera is used to determine the basis weight. The detector of the camera is placed in the center of the web and it scans the entire width of the web [57]. The area inspected by this system is dependent on the take-up speed of the web, the number of pixels per scan, and the number of scans per unit time. Independent of the type of sensors used the optical methods are restricted to light weight webs, since light must be transmitted through the web. The major disadvantage of the optical method is that the amount of the energy transmitted through the web is significantly affected by material properties other than the mass of the web.

- Contacting or Electro mechanical systems: The contacting type of uniformity measuring systems determine the mass of the web based on the force applied or the thickness measurement of the web, which is then converted to the mass of the web. This objective can be achieved by a number of means each with its own advantages and disadvantages. However the major disadvantage of the contacting type of online measurement of the web uniformity is that the sensor is in contact with the web and can induce defects on the web. In some systems the web passes between two surfaces, and if the distance between the surfaces is kept constant, the force required to keep the surfaces at the fixed distances will be proportional to the mass of the web. In the WIRA web monitor [58], the web passes through a nip created by a full width driven bottom roller and a small top-measuring roller. A pressure transducer in contact with its top surface monitors the vertical movement of the top-measuring roller. This pressure transducer generates the voltage proportional to the force required to hold the rolls in position and thus is an indirect measure of the mass of the web.

When the basis weight of the web is measured offline, Association of the Nonwovens Fabrics Industry (INDA) and European Disposables and Nonwovens Association (EDANA) refer to the American Society for Testing Materials (ASTM) technique D3776 for the measurement of the basis weight of the sample. The Deustches Institut for Normung (DIN), the British Standards (BS) and the International Organisation for Standardization (ISO) are also very similar to the ASTM standard. The various standards are compared in the Table 2.3.

Table 2.3: Comparison of Methods for the Measurement of Basis Weight of Nonwoven [59]

Method	ASTM D377 (and D5261)	ISO 9073-1	INDA (IST 30-1)	EDANA-40.0
Applications	Roll Goods, Full width samples, Ribbons and Small Samples	Roll Goods, Full width samples, Ribbons and Small Samples	Roll Goods, Full width samples, Ribbons and Small Samples	Roll Goods, Full width samples, Ribbons and Small Samples
Conditioning	20 ± 1 °C, 65 ± 2% RH, 24 hrs ⁴	20 ± 2 °C, 65 ± 2% RH, 24 hrs ⁵	20 ± 1 °C, 65 ± 2% RH, 24 hrs ⁴	20 ± 2 °C, 65 ± 2% RH, 24 hrs ⁵
Sample Size	10000 mm ²	50000 mm ²	10000 mm ²	10000 mm ²
Replications	Minimum of 5	Minimum of 5	Minimum of 5	Minimum of 3
Report	Method used, conditioning, mean and standard deviation significant to 3 digits.	Average, standard deviation, number of samples.	Mean and Standard deviation significant to 3 digits and number of samples	Size of samples, Weight in kg rounded to by not more than 0.1 %
Precision	0.01 % ⁶	0.5%	0.01%	0.1%

The major differences between the European and America Standards are in the method of conditioning. It is required in the European standards to have 24 hours of conditioning at standard laboratory conditions with a narrower range, while in the American Standards the temperature range is wider and 24 hours of conditioning is not always required.

2.5.2 Fiber Orientation Distribution

Nonwoven webs, basically due to the method of collection of the web, are not random structures. The webs have a preferential direction for the arrangement of fibers due to the movement of the collector in a particular direction. One of the objectives of the industry has been to produce webs that have the same properties in all directions. The spatial distribution of the fibers in the webs is an important structural feature that significantly influences many physical and mechanical properties of the web [60]. This distribution of

⁴ Conditioning for most samples

⁵ Conditioning for all samples

⁶ The Precision Developed is for Woven Fabrics.

the individual fibers (orientation distribution) in the web causes variation of the properties in different directions of the web and influences the other physical properties and the mechanical properties of the webs [27, 60, 61, 62]. From the quality standpoint, it is important that the orientation distribution of the fibers remain within a narrow range, from one point on the web to the other.

2.5.2.1 Orientation Distribution Function (ODF)

Various authors have attempted to define the distribution of fibers in a nonwoven web using different techniques. Backer and Petterson [28] have given a definition of the ODF as the distribution function of fibers with respect to angle between the fiber and a reference direction in a 15° interval. Similar definitions have also been given by Hearle *et. al* [27].

The orientation distribution function (ODF), $f(\theta)$, for a planar, thin, 2D fabric is a density function [27, 63, 64], such that $f(\theta)d\theta$ is the probability of finding fibers oriented in the range $(\theta - d\theta/2 < \theta \leq \theta + d\theta/2)$. The integral of the function $f(\theta)d\theta$ from θ_1 to θ_2 is the probability that a fiber will have an orientation between angles θ_1 and θ_2 [27, 63]. This distribution is referred to as two-dimensional ODF [19]. By definition,

$$\int_0^{\pi} f(\theta)d\theta = 1. \quad (6)$$

is a property of $f(\theta)$. Operationally, in a fiberweb sample area containing fiber segments of equal length (Δl),

$$f(\theta)d\theta = \frac{N(\theta)d\theta}{\int_0^{\pi} N(\theta)d\theta}. \quad (7)$$

Where $N(\theta)$ is the number of fibers oriented in the interval $(\theta - d\theta/2 < \theta \leq \theta + d\theta/2)$. Note that a long fiber can be considered as a collection of fiber segments of equal length Δl .

As shown in Figure 2.12, the number of fibers in a given interval of angle with a particular reference represents the frequency of the fibers in that direction. The

normalized form of these values for the entire range from 0 to 180 degrees represents the orientation distribution of the fibers in the sample.

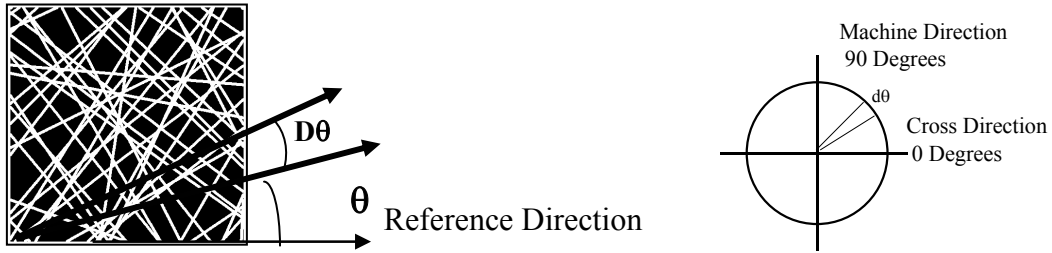


Figure 2.12: Representation of the ODF

A functional form of the ODF has been developed based on the number of fibers in a particular direction. As the fibers do not lay in a straight line, Komori and Makishima [65] defined a 2 dimensional structure of fiber webs in which fibers have arbitrarily bent configurations as shown in Figure 2.13. They suggested that the directions of the tangent at the point of consideration could approximate the directions of the bent fibers. This is achieved by dividing the fibers into small imaginary segments. The size of the segments affects the ODF and hence, it can be defined only for infinitesimally small lengths of the fibers.

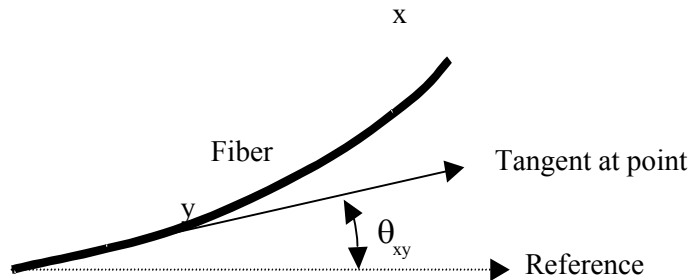


Figure 2.13: Tangent Representation of a Single Fiber [27]

Equation below is the functional form of the ODF, where $N(\theta)$ is the number of fibers oriented in the direction $d\theta$.

$$\psi(\theta) = \frac{N(\theta)}{\sum_{\theta=0}^{\theta=180} N(\theta)} \quad (8)$$

The orientation distribution function (ODF) $\psi(\theta)$, for planar, thin, fabric is function of the angle θ . It is a density function such that the integral of the function $\psi(\theta)$ from an angle θ_1 to θ_2 is equal to the probability that a fiber will have an orientation between the angles θ_1 and θ_2 . The function ψ additionally must satisfy the following conditions [66]:

$$\psi(\theta + \pi) = \psi(\theta) \quad (9)$$

$$\int_0^{\pi} \psi(\theta) d\theta = 1 \quad (10)$$

2.5.2.2 Anisotropy

Nonwoven webs are highly anisotropic material and their properties are greatly dependent on the way in which the fibers are laid in the web. Anisotropy of the web allows the user to isolate the structural properties of the web in different directions. This property of the web can be used to engineer structures, which will serve a specific end use. Hearle and Stevenson [27] investigated the effect of anisotropy on the tensile properties of three webs with different number percentage of fibers in the various directions. The cross-laid webs were found to have maximum breaking strength in the cross direction while the parallel laid webs had the maximum strength in the machine direction. Although, random laid structures should have uniform breaking strength in all directions, it was found that their strength was largest in machine direction and decreased, as it got closer to cross direction. This could be due to the preferential realignment of the fibers during processing. Kim and Pourdeyhimi [67], have investigated the effect of anisotropy on the bending rigidity of the webs as a function of the bonding temperature of the staple carded webs. Although the temperature influenced the bending rigidity, it was still directly correlated to the anisotropy of the webs.

Anisotropy ratio is the ratio of a fabric property measured in the machine direction (over a range) to the same property measured in the cross direction (over a range). The fiber

properties that are measured modulus, polarizability, dielectric constant, as well as the number of fibers in oriented within arbitrary angles in the machine and cross directions.

$$\text{AnisotropyRatio} = \frac{\Psi(\theta)_{\max}}{\Psi(\theta)_{\min}} \quad (11)$$

This measure of anisotropy has a value of one for a perfectly random (isotropic) structures. The anisotropy ratio thus measured is not accurate, as it considers only certain arbitrarily fixed range(s) in the two principle directions. If the web that is produced is bimodal, as in cross lapped carded webs, the anisotropy ratio would be close to one indicating that the web is isotropic. For this reason, \cos^2 anisotropy parameter f_p has been developed, using the ODF $\psi(\theta)$ [48, 68], which will be used in the current study. f_p can be defined as

$$f_p = 2\langle \cos^2\theta \rangle - 1 \quad (12)$$

Where

$$\langle \cos^2\theta \rangle = \frac{\int_0^\pi \psi(\theta) \cos^2(\theta_{\text{ref}} - \theta_i) d\theta}{\int_0^\pi \psi(\theta) d\theta} \quad (13)$$

The value of \cos^2 anisotropy parameter lies between -1 and 1 . The values of the anisotropy parameter for a perfectly random assembly of fibers are zero. If the value of the orientation parameter is 1 , all the fibers are aligned in a particular direction, while a value of -1 indicates that all the fibers are aligned in the perpendicular direction.

2.5.2.3 ODF Monitoring Systems

An online measurement of ODF of fibers in a lightweight nonwoven requires that the system is non-destructive, reliable, precise, accurate and applicable to diverse processes. The system needs to evaluate the ODF and also give the anisotropy parameter. The measurement of ODF by using Equation 12 is not valid for structures that have a 3 dimensional nature (i.e having a large thickness); it is used in the measurement of ODF for lightweight nonwovens as they can be considered to be 2 dimensional. Hence, in principle any property of the web that gives the anisotropic nature of the web because of

the number of fibers oriented in that direction can be used to predict the ODF and vice versa.

2.5.2.4 Visual Methods

The visual method of measuring the number of fibers is the most rigorous method of determining the ODF of the web. Visual methods can be used to measure the ODF in thin nonwoven webs under magnifying conditions. The fibers can then be counted either by using selectively dyed fibers or by observations of all fibers. The disadvantage of this technique is that it is a time consuming process.

The earliest attempts of measuring the ODF of the fibers in a web were by visual techniques in the paper industry using 1% by volume of dyed fibers in the slurry during manufacturing process and the orientation of the dyed fibers were measured using a protractor. Crosby et.al [69] improved on this method by using a digital analysis technique to magnify the fibers and determine the ODF from the co-ordinates of the fiber tips.

Backer and Petterson [28] used photomicrographs of nonwoven fabrics to determine the ODF of the web. A circle of 5.7 cm diameter was drawn on the photograph and a horizontal line was drawn across the photograph indicating the cross direction (CD). The angle θ was determined by measuring the angle between the fiber axis and the reference line. The number of fibers in a 10° incremental interval was measured and the relative frequency determined.

Hearle and Stevenson [27], used a projection microscope to study the ODF of carded webs, in similar principle to that used by Backer and Petterson. The image of the web was projected on to a screen with the superimposed image of a marked circle. The circle was divided into several segments, each of 10° intervals on the projected image at a magnification of 320 X. The number of fibers in each segment of the circle was used for the determination of the ODF. Similar procedures have been reported by various authors for determining the ODF of light weight webs (less than 20 g/m^2). For heavier webs the magnification needed to see the fibers imposes a constraint on the individual counting the number of fibers. All visual techniques are time consuming and can be used for comparison and calibration purposes.

2.5.2.5 Mechanical Methods

The tensile properties of the web are affected by the fiber orientation distribution in the web. Hence using the tensile data, at either zero span gage length or a short gage length, the ODF of the web can be estimated at regular angular increments. Zero span length methods are widely used in the paper industry based on the assumption that the fibers in the paper are straight and that when they are clamped at zero span length the tensile strength is from the individual fiber contribution oriented in the various directions. Cowan, *et al* [70] evaluated mechanical properties of the fabric at various gage lengths and extrapolated to zero gage length. The ratio of the strengths in the machine to the cross direction was determined as a measure of the anisotropy parameter for the fabric. Results obtained by Hearle *et al* [61] on carded webs are shown as polar plots in Figure 2.14 and Figure 2.15. They indicate that there is a strong correlation between the ODF of the web and the mechanical properties of the web [27].

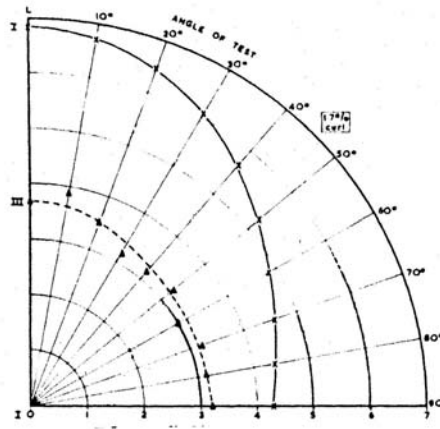


Figure 2.14: Variation of Rupture Strength and Fiber Orientation with direction in Random Laid Web [27].

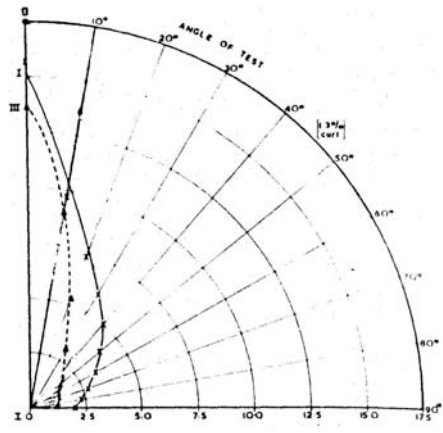


Figure 2.15: Variation of Rupture Strength and Fiber Orientation with direction in Cross Laid Web [27]

2.5.2.6 Electrical Conductivity Methods

Tsai and Bresee [71] used the electrical conductivity principal to measure the ODF of the fibers in the nonwoven webs. The underlying assumption in this measurement is that all fibers in the web will conduct electricity. Hence the conduction will be the most along the direction in which there are more fibers. The electrical resistance R of a cylindrical sample of material is given by

$$R = \rho \frac{L}{A} \quad (14)$$

where ρ is the resistivity of the material, L is the length and A is the area of cross-section of the sample. Ohm's law states that the resistance offered by the sample is the ratio of the voltage difference (V) applied across the sample to the current (I) flowing through the sample.

With the assumption that all the fibers are straight and the points where the probes are located do not contribute to the conductivity, the current I_j , flowing in the direction j is proportional to n_j number of fibers bridging the distance between the two probe ends. Thus,

$$I_j = \frac{VA_f}{\rho L} n_j \quad (15)$$

where A_f is the effective cross-sectional area of the average fiber in the direction j .

The ODF in terms of probability P_j in each of the directions is given by the Equation below

$$P_j = \frac{I_j}{\sum_{j=1}^{j=k} I_j} \quad (16)$$

where k is the total number of measurements at different angles covering the entire range of angles of the web.

2.5.2.7 Image Analysis Techniques

Image analyses techniques are used both on-line to measure the orientation at rapid rates and impart quality control over the web and also, off-line to research the structure-property relationships of the web. The results obtained from these tests are independent of the mechanical characteristics of the fiber. Any radiation from x-rays to infrared rays

can be used in principal to obtain the image of the web [72, 73]. A low intensity source of the rays like far infrared or sub-millimeter laser beam traversing the fibrous structure can be used to produce the image.

Image analysis techniques use the intensity of the gray levels of the different pixels to determine the presence of the fibers and the orientation of the fibers. The image that is obtained of the web is analyzed using different algorithms to determine the ODF of the fibers in the web. The different algorithms used for the analysis of the webs are:

- Direct tracking [62]: This technique is similar to tracking the path of the fiber by visual methods. The image of the web is initially converted to a binary image. This is done by dividing the gray levels in the image into two groups. If an image is only of the fibers and the back ground, then there will be a clear demarcation between the gray levels of the fiber and the background. In this process the fibers are assumed to be black with a white background (Figure 2.16). The fibers are then thinned to obtain a pixel thick fiber, since only the direction and number of fibers in a direction is relevant to determine the ODF. Using the tracking algorithm that detects the presence or absence of a fiber in each pixel surrounding a pixel, the direction and end-point of the fiber is determined. The assumption that fibers do not severely kink or bend within one pixel is utilized, in the case of bent fibers. Hence a span of $+45^\circ$ to -45° of the current pixel is used to identify the next pixel of the same fiber. On determining the number of fibers in each direction, a frequency table is developed to obtain the ODF of the web. Although this technique gives excellent correlation between the data obtained with a simulated image, this technique assumes that all webs are a 2 dimensional structure. Hence if the web has more than one layer in it, the fibers, which cross each other in different layers of the web, will affect the results obtained.



Figure 2.16: An Example of a binary image of the web [62].

- Fourier Transform [74]: The intensity spectra of the pixels in the image are decomposed into the frequency domain with appropriate magnitude and phase values. The intensity of the gray scale in the frequency image represents the

magnitude of the various components of the image. The discrete Fourier transform is used to determine the rate at which intensity transition occurs in a particular direction. If the fibers are oriented in one direction, the respective frequencies will be high in the perpendicular direction in the spatial domain.

- Image processing and character recognition techniques have been used by Bresee and Yan [75], to determine the mean fiber orientation, fiber orientation distribution and the anisotropy ratio. The information given in the article does not explain the techniques used to obtain the data, but show a good correlation between the orientation and the mechanical properties of the web.

The entire image analyses techniques described in determining the ODF of the fibers are for thin webs. Even though the techniques described herein have been used for carded webs, Farer [37] has used the Fourier Transform technique to determine the ODF of the meltblown webs. In principle, all of these techniques can be used to determine the ODF of meltblown webs, as there are no standard methods that have been developed by any of the standards organizations.

2.5.3 Fiber Diameter and its Distribution

Compared to the conventional melt spinning process, meltblowing produces webs with very fine fiber diameters and a broader distribution of the diameters [90]. The diameter of the fiber affects the structure, “hand” and the mechanical properties of the web. The fact that meltblown processes produce soft webs is widely recognized. This is essentially because the fibers are typically very small in diameter.

Shambaugh *et al* [8, 76] have conducted on-line measurements of the fiber diameter along the thread line during melt blowing. They have used high-speed flash photographic techniques to obtain the image of the fiber. The diameter of the fiber was measured by viewing the negative under a microscope with a micrometer eyepiece. The entire process was calibrated using an image of fine wire of known diameter.

The data obtained by measuring the fiber diameter for studies conducted by Shambaugh *et al* [76] is given in Table 2.4. The first column indicates the different process conditions in the production of the fibers. As can be seen from the last column of Table 2.4, the variation between the data obtained from on-line measurements and off-line measurements is not constant. Although it is claimed that the procedure used to measure the diameter gives the average diameter with a narrow distribution, the entire process is conducted on a single fiber using a single orifice and hence the technique cannot be

applied to a melt blown system with multiple orifices. A further potential source of error when the diameter is measured using an on-line photographic technique is the transverse vibration of the fiber during melt blowing.

Table 2.4: Fiber Diameter from Different Methods [90]

Case	Diameter (μm)		% Difference
	On-line Image	Off-line Image	
1	82.0	77.3	6.1
2	64.2	61.7	4.1
3	54.5	52.6	3.6
4	45.5	44.1	3.2
5	34.5	32.9	4.9
6	30.0	27.0	11.1
7	71.7	69.6	3.0

The measurement of the fiber diameter in the nonwoven webs that have been reported in literature is based on the capture of the image using various techniques [29, 75]. Yan and Bresee have developed a system where in the diameter is measured using an automated system. The equipment consists of two illumination sources (one is a microscope condenser assembly and the other is a light source for low magnification images), a mount to place the sample web, and a monochrome camera. The system has an automated focus control. The image from the sample of the web placed on the holder (36 x 6 inches or 24 X 24 inches) is obtained and processed to determine the diameter and its distribution. The system requires the user to input the number of fibers to be measured (0 to 4).

Farer utilized an automated image analysis technique developed by Pourdeyhimi [9, 77]. The procedure followed by Farer is to obtain a scanning electron micrograph of the web and use the automated software to determine the diameter distribution. The image analysis software “measures the distribution of fiber diameters by finding the central medial axis along each fiber axis. At every pixel along the central medial axis intensity relative to the distance from the edges of the fiber image is assigned. The observed

intensities are representative of the fiber diameter and are subsequently used to calculate the overall distribution [9]”.

The primary requirement in any of the image processing techniques is to identify the edges of the fiber. Although these techniques can be used to process the image and determine the diameter of the fibers at extremely fast rate, the techniques are not error free. The various problems usually encountered are listed below.

- When the web is thick, and the fibers are in different layers with a variation in the focus of the image capturing system, it is quite difficult for any system to identify the edges of the fibers.
- As is seen in Figure 2.17, the intersection of two or more fibers at one node causes the fibers to be measured as a thick fiber or the entire node will appear as a “shot”.
- When two or more fibers are formed such that they are side by side or placed staggered next to each other, the fiber diameter will be over estimated.

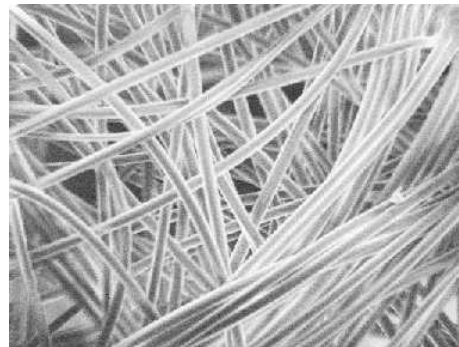


Figure 2.17: A typical SEM picture of the Melt Blown Web at very high magnification [29]

As in the case of the ODF measurements, the various standards organization doesn't have any standard testing technique to measure the fiber diameter distribution. Further to eliminate all the possible errors, the ideal case of measuring the fiber diameter would be, to produce a very good image of the web at a suitable magnification using the electron microscopy techniques and then analyze the image manually using suitable calibration scale. The manual analyses consists of the following steps:

- determine the length of a pixel of the image
- identify the edges of the fibers in the image
- count the number of pixels between two edges of the fiber

The analyses of the fiber diameter using this technique produce a log normal distribution (Figure 2.18) of the fibers similar to what has been suggested in the literature [78].

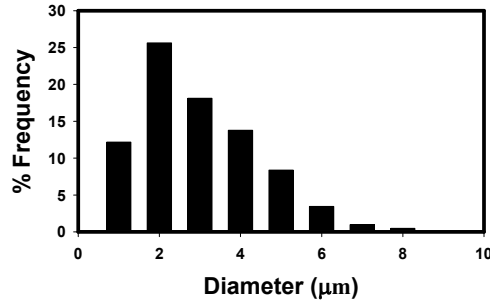


Figure 2.18: A typical Fiber diameter distribution in a melt blown web [92]

2.5.3.1 Analysis of SHOT in the nonwoven webs

The term “shot” refers to the particles that are sometimes present in meltblown webs and have been defined as “groupings of molten polymer material or fibers such as occur in melt-blowing through entanglement and thermal bonding [14]”. They are not usually observed in other types of nonwoven webs. Buntin and Lohkamp [78] reported in the 1970’s that the formation of shots is due to the breakage of fibers. Shots are non-fiber forms of the polymer and the defect formation has been attributed to the raw materials used or the variations in the process conditions. Shot formation has been described to be due to the development of the meltblown technology with higher through put rates, finer die holes in the melt die, and the production of finer diameter fibers. Shot formation has not been reported in the literature where single meltblown filaments were investigated. Typical shots are shown in Figure 2.19. Shots are very undesirable in the web and the discussion that follows is about the various currently available techniques to reduce the shots and also attempts to quantify the shots in the webs.

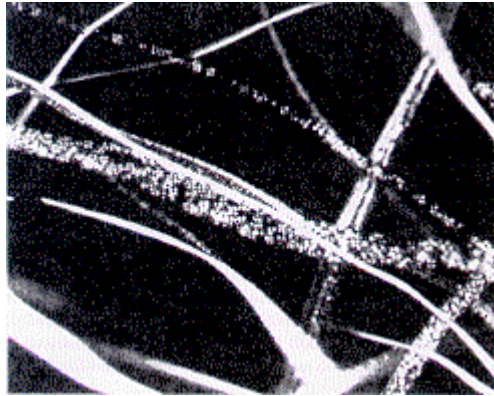


Figure 2.19: Micrograph of Shot Defects in Melt blown Polypropylene Web [25]

The absence of the shots when single filaments were produced suggests that the shots are not formed due to the broken fibers that snap back. Milligan *et al.* [79] conducted high-speed photography studies of the formation of shots in meltblown web formation and concluded that, as seen in Figure 2.20, the shots are formed only if the filaments touch each other near the die. They further classified the types of shots into two, viz. the shots which appear randomly in the web as polymer film spots after melting, and those that are formed with evidence of melting, but are large diameter filaments.

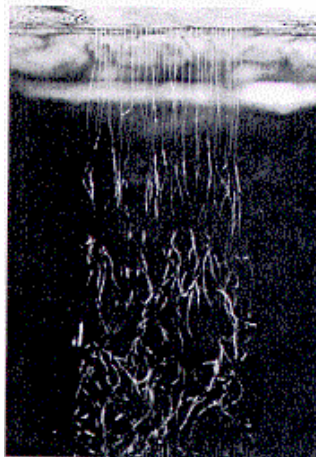


Figure 2.20: Filaments that form “shots” exhibiting the touching phenomena close to the die [79]

As is observed during the current research, shots are formed if the orifices in the die are plugged during the processing of the polymer. Molten polymer, which consists of fused fibers, arrives at the collector and forms a spot. The basic technique used to quantify the number of shots in a unit area of the web begins with the visual inspection of the web. A

one-inch square of the sample has been examined under a 40X magnification and the number of shots normalized by the basis weight of the sample has been defined as the shot intensity [80]. The data reported by the authors indicate that the shot intensity increases with the increase in the through put rate, and decreases with the increase in the air velocity. Yan and Bresee [75], have utilized the fact that the shots have different physical structures and hence will produce optical effects. The images of a shot will have gray levels in that they are less bright than the background and hence the gradient in the gray level is used to identify the shots. As in any image analysis technique, the identification of the object of interest is dependent on the object itself and the surrounding region of the object. If the object of interest, in this case the shot, is having the same brightness and gray levels as the surrounding then it would be harder task to identify the shot. The brightness of the shot is dependent on the shape, relative size, texture, and edge structure of the shot.

2.5.4 Pore Size Distribution

2.5.4.1 Definition of Pore Size

“Pore size” is usually defined in conjunction with a pore size distribution obtained by an experimental technique. The pore size so determined is in terms of a model used to measure the quantity. If the pore size is determined similar to particle size, using a sieving technique then the size of the pore will be the diameter of the sieve that will be used. Usually the pore size distribution is determined by measuring the dependence of a physical quantity on a control parameter decided by the experimenter. In a capillary flow experiment, the volume of fluid penetrating the system is measured as a function of the pressure applied on the system. The pore size is calculated from the pressure using Young and Laplace’s equation of capillarity and under the assumption that the pores are a bundle of tubes. The diameter of the tube is the size of the pore. A detailed discussion of this method is done in the succeeding sections.

Pore size and size distribution have a significant effect over a wide range of phenomena from the absorbency of fine powders in chemical catalysis to the frost resistance in bricks. The macroscopic properties of any porous media are influenced by the pore structure. Dullein [23] has defined pore structure parameters as those properties

completely determined by the structure of the pore in the medium and are not affected by any other parameter. These properties represent the average behavior of the media [23]. The porous media contain numerous voids having different shapes and sizes [81]. Bear has defined a porous medium as “a portion of space occupied by heterogeneous or multiphase matter. At least one of the phases comprising this matter is not solid [82]”. The solid phase is the solid matrix and the non-solid phase, which is a fluid, is called the void space (or pore space). There are two kinds of void spaces, the interconnected and the isolated voids. The interconnected voids are continuous and form pores. These are classified as blind pores and through pores as shown in Figure 2.21. The blind pores are interconnected only from one side and usually contribute negligibly to the transport of fluids through the media. The closed pores are isolated and cannot contribute to the transport of matter across the porous medium. The interconnected through pores are also known as the “effective pore space” and is primarily responsible for the transport of fluids through the porous medium [81, 82].

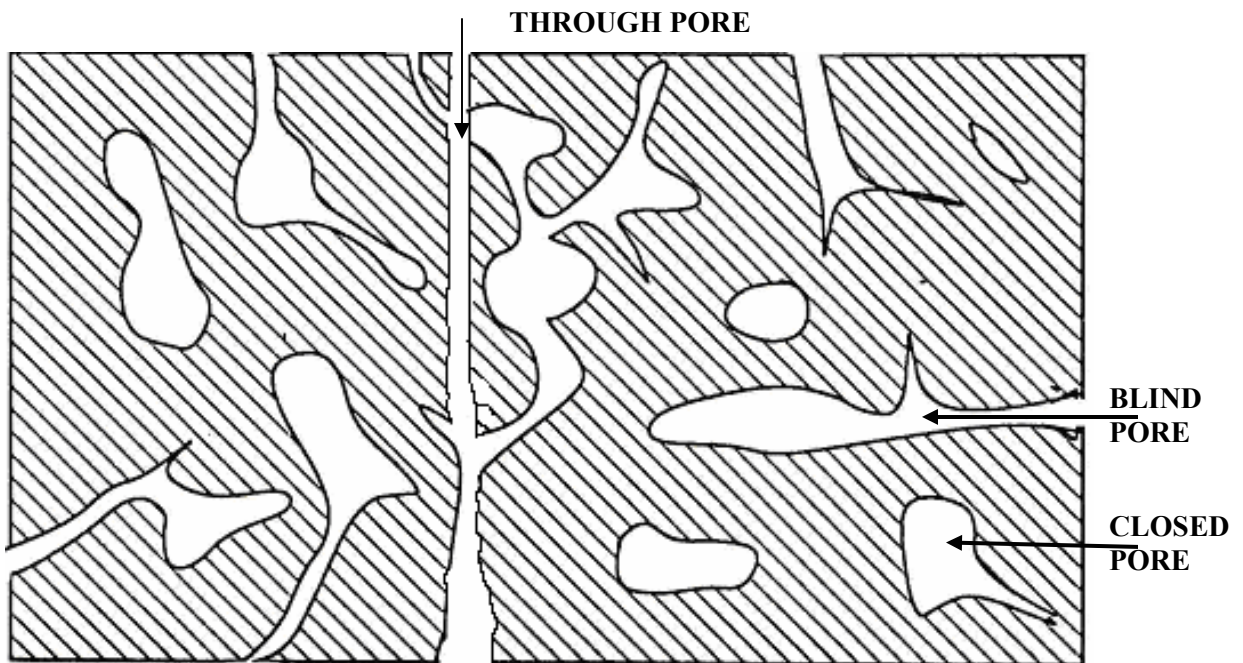


Figure 2.21: Illustration of longitudinal section of interconnected voids forming pores [81]

As is seen in Figure 2.21, the walls of the pores diverge and converge in an irregular manner and hence the cross-section of the pore changes drastically along the length of the pore [83]. Hence, it is necessary to define a pore before discussing the pore size. A pore

can be defined “as a portion of space bounded by solid surfaces and by planes erected where the hydraulic radius, r_H , of the space exhibits a minima [23]”. The local minima, when identified, define an arbitrary pore size. The hydraulic radius of a capillary of uniform cross-section is the ratio of volume of the capillary to the surface area of a capillary. In the case of a variable cross-section, the hydraulic radius can be defined as the ratio of area of cross section to the length of the perimeter of cross section [98]. r_H , is used as a useful measure of pore size in irregularly shaped cross-sections and the relationship between r_H and mean radius of curvature, r_m for various cross sections are given in Table 2.5.

Table 2.5: List of Comparative values to Show Equivalence of Reciprocal Hydraulic Radius and Twice the reciprocal mean radius of capillary [23]

Cross Section		$(1/r_1) + (1/r_2)$	$1/r_H$
Circle		$2/r$	$2/r$
Parallel Plates		$1/b$	$1/b$
	$a : b = 2:1$	$1.50/b$	$1.54/b$
Ellipse	$a : b = 5:1$	$1.20/b$	$1.34/b$
	$a : b = 10:1$	$1.10/b$	$1.30/b$
Rectangle		$1/a + 1/b$	$1/a + 1/b$
Equilateral Triangle		$2/r_i$ ⁷	$2/r_i$
Square		$2/r_i$	$2/r_i$

⁷ r_i is the radius of the inscribed circle

2.5.4.2 Surface Tension and Contact Angle

When two fluids are in contact with each other they are separated by a thin layer, called the surface interface that could be imagined to be a stretched thin layer of infinitesimal thickness separating two homogenous fluids [85]. The tendency of this layer to stay in place rather than spontaneously decrease its size is due to the existence of a stress on the interfacial surface. The surface tension can be defined with the aid of Figure 2.22. AB is an arbitrary surface dividing the region into 1 and 2 with the region 2 exerting a tangential force $\sigma \delta l$ along the element δl on the arbitrary surface. If the surface has a uniform tension σ , which is perpendicular to the dividing section and has the same value along the dividing line AB, then σ is the surface tension at the point P [85].

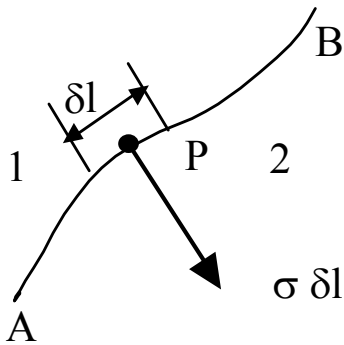


Figure 2.22: Definition of Surface Tension at a Point P.

The existence of capillary systems in the porous media implies the presence of a solid phase and at least two fluid phases. The vectorial sum of the surface tensions at the point where the phases meet is equal to zero. If we consider a drop of liquid on the smooth, plain surface as shown in Figure 2.23 the drop of liquid will maintain a finite contact angle θ between the boundaries of liquid/gas and liquid/solid long as the solid surface is non-wetting. The contact angle is defined as the angle subtended by the tangent to the liquid/gas interface at a point on the three-phase line contact and the tangent to the solid/liquid interface constructed at the same point. The contact angle is related to the surface tension of the interfaces by the equation given below.

$$\sigma_{l/g} \cos \theta = \sigma_{s/g} - \sigma_{s/l} \quad (17)$$

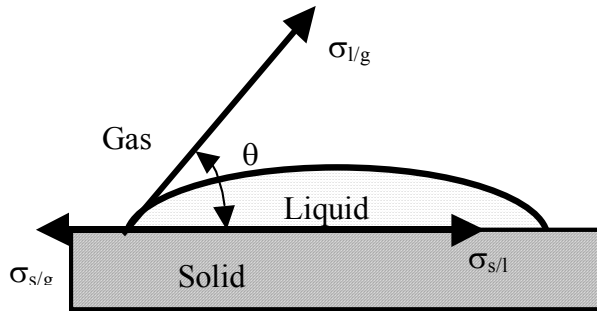


Figure 2.23: Equilibrium of surface tensions at a line of Contact

The contact angle varies from 0 degree to 180 degree and when the angle is 0 degree, the liquid spreads on the solid [86]. In the absence of a smooth surface the theoretical contact angle cannot be measured, but the apparent angle is measured [23].

Wetting Liquid and Contact Angle

The relative magnitude of the liquid-liquid interaction versus the liquid-solid interaction determines the degree to which a liquid can “wet” the solid. If the magnitude of the liquid-liquid interaction force is greater than the liquid-solid interaction then the liquid will not completely “wet” the surface of the solid. If the surface tension of the liquid is sufficiently low (i.e the liquid -liquid attractive force is small) then the solid is readily “wetted”. The contact angle θ , is equal to zero and the liquid meniscus is hemispherical. When a gas pressure is applied to the saturated surface, the liquid will be forced out when the applied pressure is greater than the liquid-solid interaction.

Techniques of measurement of Pore size and its distribution

The two main capillary techniques used for determining the pore size and its distribution are (a) intrusion type and (b) extrusion type. Mercury porosimetry is an example of the former type while the bubble point method is that for the later type [87]. Both the techniques are based on the principle of capillary flow which states that a porous material will allow a fluid to pass when the pressure applied on the system exceeds the capillary force of attraction of the fluid in the largest pore.

Theory of Capillary Flow

The capillary flow in the porous structure is based on the capillary rise phenomenon, where an excess pressure is required to cause a non-wetting liquid to climb up a narrow

capillary (Figure 2.24). The pressure difference across the interface is given by the following equation, and its sign is such that the pressure is less in the liquid than in the gas phase if the contact angle θ , is greater than 90° and more if is less than 90° .

$$\Delta P = \sigma \left[\frac{1}{r_1} + \frac{1}{r_2} \right] \cos \theta \quad (18)$$

where

- σ is the surface tension
- r_1 and r_2 are mutually perpendicular radii
- θ is the contact angle between the capillary walls and the liquid.

If the capillary is of circular cross section then the meniscus will be approximately hemispherical and the two radii will be to a mean radius of r_m , as shown in Table 2.5, and the above equation reduces to the Washburn Equation.

$$\Delta P = \sigma \left[\frac{2}{r_m} \right] \cos \theta \quad (19)$$

For a perfectly hemispherical meniscus (solution with low surface tension), the contact angle will be equal to zero and hence the pressure difference can be utilized to determine the pore radius [95].

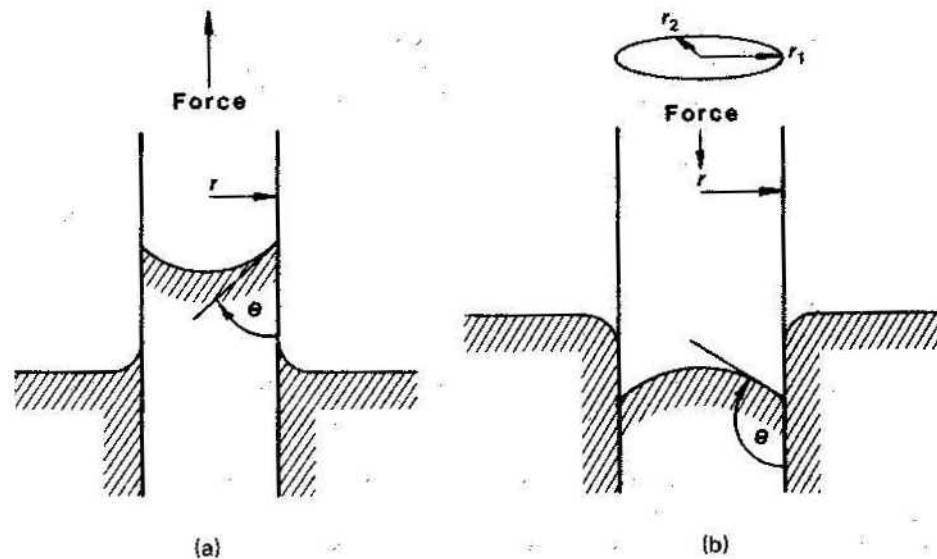


Figure 2.24: (a) Capillary Rise ($\theta < 90^\circ$) (b) Capillary Depression ($\theta > 90^\circ$) [81]

In the bubble point test the porous material is saturated with a “wetting” liquid and a gas pressure is applied to the material on one side. As the pressure increases the largest pore that is called the bubble point is opened. Further increase in the pressure causes the pores of decreasing diameters to open. The pore distribution is determined by the flow rate of the gas and the pressure difference between the saturated specimen and a “dry” specimen [87, 88]. In a mercury intrusion porosimetry the porous material is immersed in mercury and the pressure applied to force the mercury into the porous media is used to determine the pore size.

Disadvantages of using capillary flow techniques

Capillary flow techniques assume the cross section of the pore, to apply a particular model. Pores, as is seen in Figure 2.21, are not of regular cross section. Hence the values obtained from the methods are only comparative in nature. Further the presence of pores with constricted “necks” opening into large void volumes will be a true indicator of the pore size. The presence of blind pores will affect the flow of the fluid through the porous material. The assumption that the surface tension and the contact angle with the material do not change as the fluid flows through the pores needs to be verified.

Image Analysis Techniques

The image analysis techniques developed to measure the pore size of the nonwoven webs measure the pore using sieving methods. A two dimensional image of the web is analyzed by superimposing increasing sizes of the particles and maintaining a frequency count of the number particles of each size. The major disadvantage, as in any image analysis technique, is that a “good” image of the web is essential. Also the technique will not be quantitative for webs that are “3 Dimensional”. Pore size measurement on simulated nonwoven webs, by Kim *et al* [48], show that the pore size decreases with a decrease in the fiber diameter and they also decrease with a decrease in the web anisotropy. As is expected finer the fibers, at given basis weights, the webs will have larger number of fibers in an unit area of the web leading to the formation of pores with smaller diameters. On the other hand the formation of finer pore sizes at lower anisotropy needs to be investigated. The pore size, as defined by the authors, is a representation of the area of the pore and the perimeter of the pore. As the anisotropy

increases the pores that are formed become more polygonal rather than a circle, leading to an increased perimeter for the same area.

As there is no literature available on studies conducted using melt blown nonwoven webs only, pore size distribution studies on other types of nonwovens were reviewed. Xu investigated the pore size using image analysis techniques [89]. Similar to the hydraulic radius described earlier in this review, hydrodynamic diameter, has been measured on aramid and rayon nonwovens. The data indicates that the pore size decreases with increase in the web weight. The changes in the pore area are larger than in the pore diameter, implying that the particle retention ability does not change as drastically as the fluid permeability when the weight of the web changes. The data also shows that the nonwoven webs have inherently large variations in the pore size and exhibit a Poisson distribution.

Bhatia *et al.* [87] have conducted comparative studies on pore size distribution studies using various techniques on needle punched and thermally bonded nonwoven geotextile webs. The data plotted in Figure 2.25 to Figure 2.27 show that there are variations in the results obtained using the different techniques, and do not exhibit the same trends when the results from the various samples are examined.

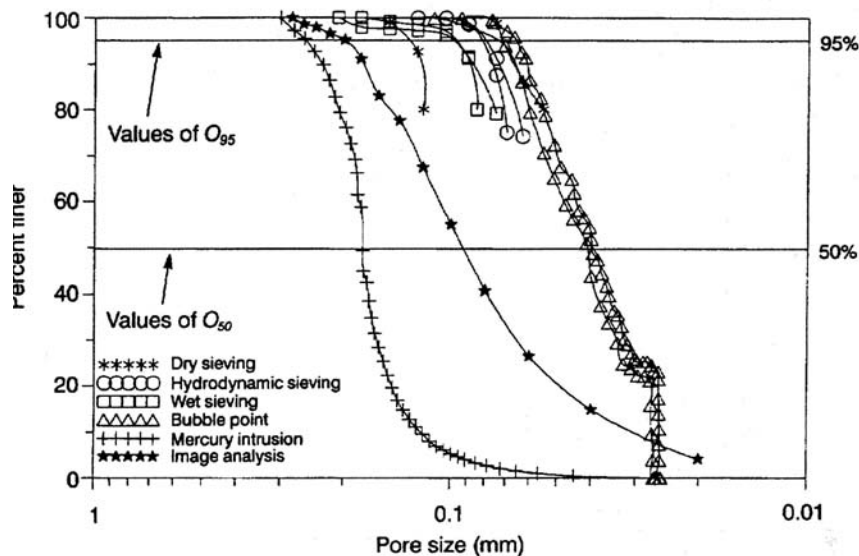


Figure 2.25: Pore size distribution curves for Staple fiber Needle Punched Nonwoven Geotextile [87].

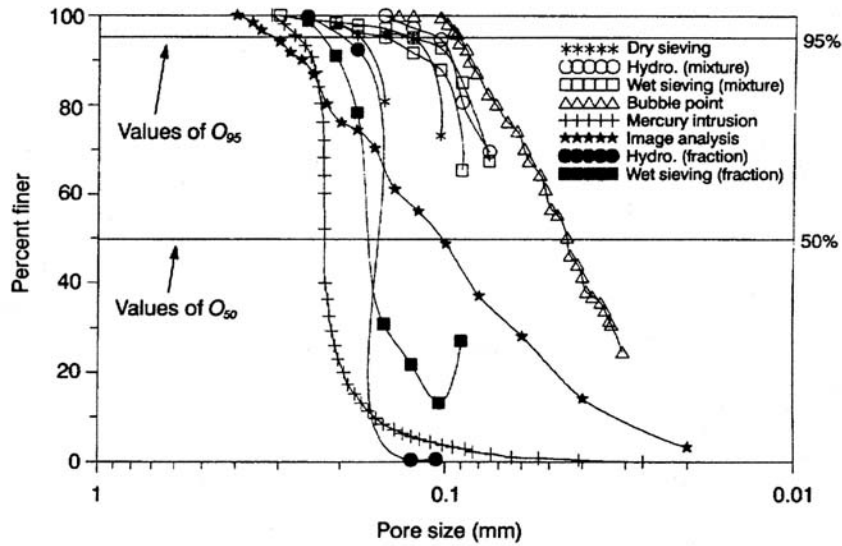


Figure 2.26: Pore size distribution curves for continuous filament Needle Punched Nonwoven Geotextile [87].

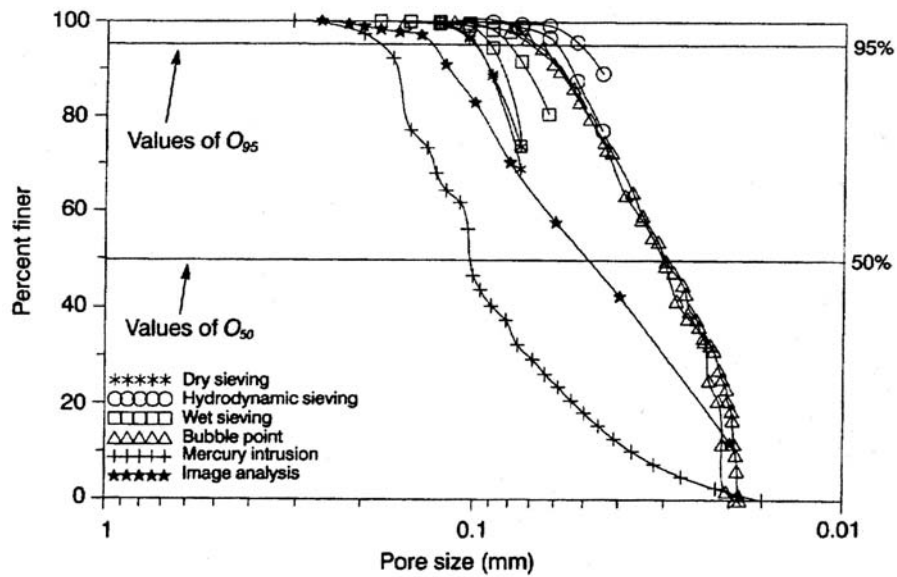


Figure 2.27: Pore size distribution curves for continuous filament Thermal bonded Nonwoven Geotextile [87]

EDANA and ISO have not developed a standard test method for the determination of the pore size and its distribution of nonwoven webs. The test method recommended by INDA is the same as that recommended by ASTM [59]. The method is primarily used

for geotextiles to determine the apparent opening size and not the pore size of the nonwoven web.

ASTM F316 1986 is the standard that was being used to measure the pore size characteristics of membrane filters by mean flow pore test and bubble point methods, which has since been discontinued [90]. Currently, there are no standardized test methods that are available from the various standardization organizations for the testing procedure to be used in the determination of pore size and its distribution of nonwoven webs.

2.6 Summary

In this review, the formation of meltblown webs and the properties that effect the formation of the meltblown webs have been discussed. Simulation studies on the structure of the nonwoven webs have been discussed. Characterization of various structural parameters has been discussed. The theory involved in the evaluation of the webs and the parameters that affect the structural properties have been reviewed.

The current techniques available for measuring the fiber diameter distribution and the fiber orientation distribution of the nonwoven webs primarily focus on image analysis techniques. Exclusive structural evaluation techniques for meltblown webs have not been developed. Investigations into the various process parameters, such as the polymer throughput, DCD, web take-up speed, fiber stream approach angle and curvature of the collecting surface on the pore size distribution of the webs have not been conducted.

3 EQUIPMENTS, MATERIALS AND METHODS

This section deals with the explanation of the equipment that was used in the formation of the meltblown structures, and the modifications that were formed to produce the 3D structures, the materials that were used, and the experiments performed to produce the samples. Also included in this section is the description of the various instruments used and the statistical procedures adopted to analyze the data.

3.1 ROBOTIC FIBER ASSEMBLY AND CONTROL SYSTEM

In order to produce 3D meltblown webs, a Robotic Fiber Assembly and Control System (RFACS, Figure 3.1) has been setup by Farer *et. al.* [9]. This has been achieved by integrating a desktop model of meltblown machine (details in section 3.1.1.1) and a commercial six-axis robot that is capable of manipulating the meltblown die in the range of positions and orientations required for use with the complex 3D shape molds. In addition, to achieve the required level of mold control needed for this process, an external seventh axis has been added (Figure 3.2). The shaped nonwoven structures are produced by meltblowing the polymer on a collapsible mold that is placed on the seventh axis. The mold is covered with cotton knit fabric to maintain the integrity of the meltblown structures and facilitate taking the fabric off the mold. The molten polymer and attenuating air are supplied to the die through two supply hoses. Two flexible hoses, one for molten polymer and the other for hot air, connect the die to the extruder. The die is placed in a cage, to aid the mounting of the die on the end-effector of the robot. Programming the movement using triangulation controls the movement of the robotic arm (end-effector).

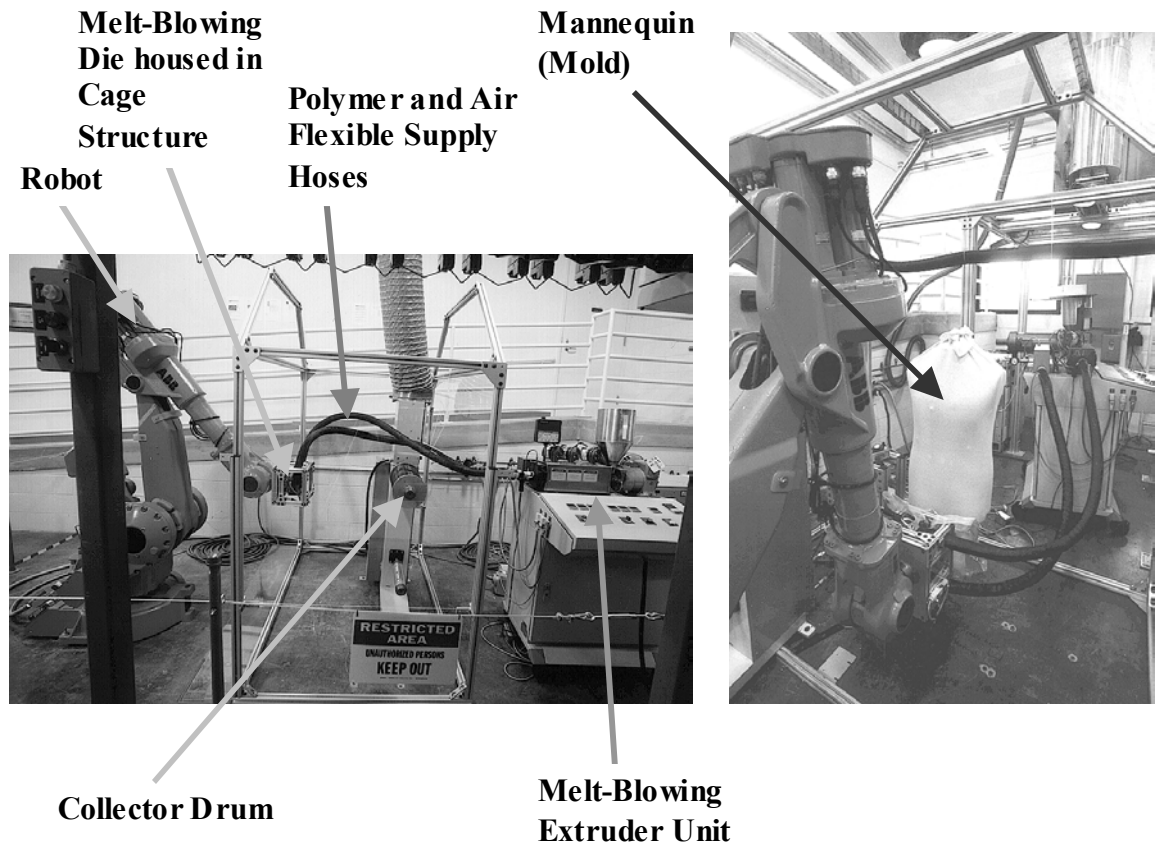


Figure 3.1: Robotic Fiber Assembly and Control System [9]

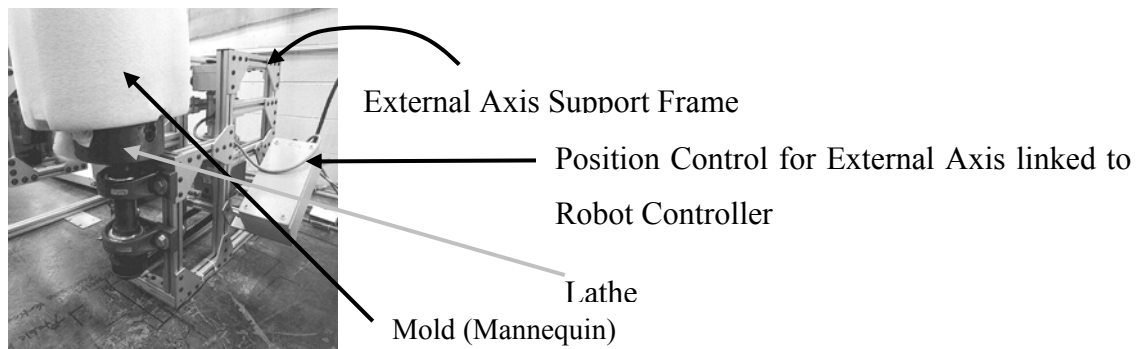


Figure 3.2: Seventh-Axis Support Structure showing Lathe and Serial Measurement Board Box [9]

Farer [37] has investigated two models of fiber deposition,

- 2D model which adjusts for DCD position, and the height of the die with respect to the mold (DCD Correction and nonlinear rotation speed correction); and
- 3D model that additionally adjusts the orientation such that the row of orifices of the die is aligned parallel to the collection surface on the mold (each orifice

is normal to the collection surface). Point coordinates on the mold shape were determined at regular intervals to develop a contour following algorithm. In the case of the 2D model, these points in 3D space were determined with the use of a pointer tip that assumes the position of the right most tip of the die. For the 3D model, a pointer mirroring the position of the die has been constructed. The coordinate on the surface of the mold is determined relative to a world coordinate system, using these pointers.

The contour-following algorithms for mold shapes using either the 2D or the 3D model, point coordinates on the mold shape were determined at regular rotational increments. These points in 3D-space for the 2D model have been determined with the aid of a pointer constructed such that the pointer tip assumes the virtual position of the right most orifice in the meltblowing die body. For the 3D model, a pointer mirroring the position of the polymer orifices has been used. The pointer is used to mark points on the mold relative to the world coordinate system. This procedure has been adopted as the means of developing the position and speed of the meltblowing die to the rotation of the mold body.

3.1.1.1 Desktop Meltblown Equipment

The desktop model of the meltblown machine, from Nordson Fibers system (formerly J&M Laboratories) consists of a single screw extruder with a $\frac{3}{4}$ inch screw (Figure 3.1). The screw barrel is equipped with 3 independently controlled heating zones capable of reaching to a temperature of 290° C. The flange attached at the end of the extruder barrel has an independent heater attached to it. The air heater has the capability of heating the air to a maximum temperature of 360° C. The removable die with an active spray width of 7.62 cm consists of 90 holes (0.04064 cm diameter) placed in a single row on a 90-degree sharp tip nosepiece. The die is capable of being heated to a maximum of 250° C. The air gap on the die is maintained with the aid of shims of 0.254 mm thick. The die is connected to the air heater and the extruder with the aid of two flexible hoses each 1.8 m long. The die is mounted in a cage (Figure 3.3) and the cage is placed on the end – effector of the robot for the free movement of the die.

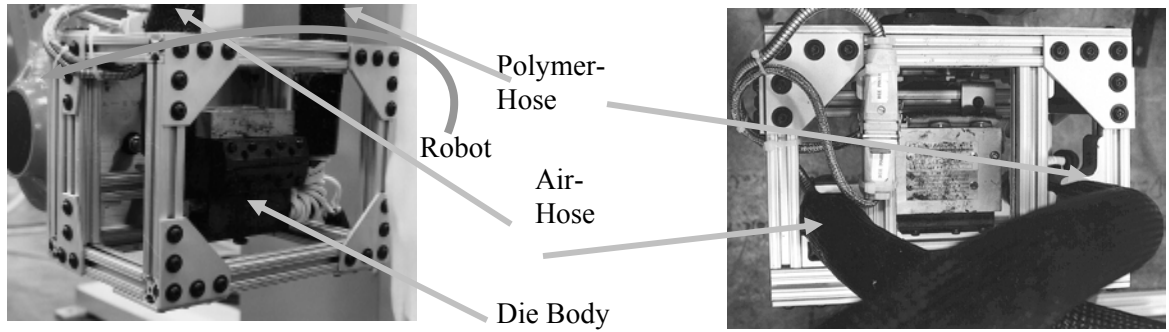


Figure 3.3: Front and top view of the die in the cage [9].

3.1.2 Modifications to RFACS

In addition to the use of the collapsible mold, a conical mold was also designed to precisely control the curvature of the collecting surface on which the web was formed (Figure 3.4). The mold was placed on the lathe previously mentioned as the seventh axis. The robotic program was modified to meet the requirements of the structure of the web.

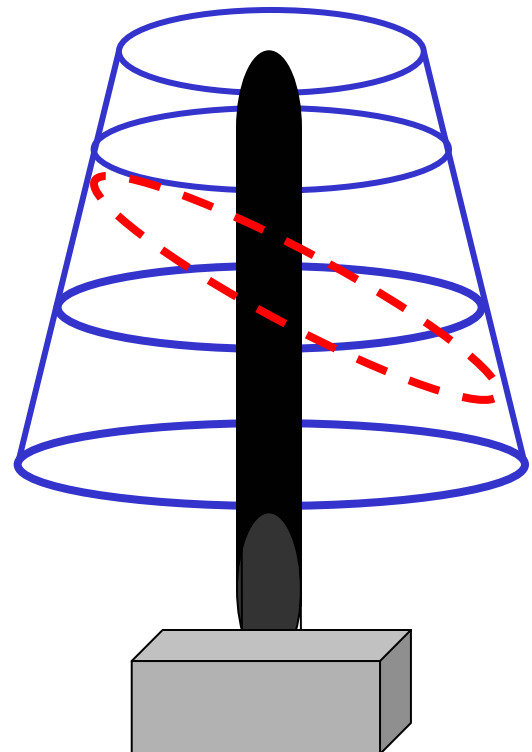


Figure 3.4: A conical mold with an elliptical path along which the fibers were laid

The conical mold was constructed such that the central axis of the mold would be mounted on the seventh axis of the RFACS. The curvature of the conical mold would remain constant throughout any single plane parallel to the floor of the laboratory. This would give samples prepared at the same curvature for analyses of their various structural properties. Also for investigation of the effects of variation in the curvature of the collecting surface, the end-effector of RFACS can be made to move continuously such that the variation in the curvature is a continuous function of the position of the web on the collecting surface. Two models were investigated to obtain a uniform basis weight of the web on the collecting surface of the web.

- the DCD is maintained constant at all heights on the mold.,
- in addition to the previous model the speed of seventh axis was altered such that the surface speed of the collector at the point of impact of the fibers on the collecting mold was maintained constant. The orientation of the die was also modified to investigate the effects of the approach angle (described in section 3.3.5)

3.1.2.1 Control Algorithm

The algorithms and programs for the two models that were investigated in the current research were developed based on triangulation theory [9]. There was precise control over the position of the die and the collecting surface. The control algorithm for the movement of the die and the seventh axis are given in Table 3.1 and Table 3.2. Figure 3.5 describes the movement of the die relative to the position of the mold with a constant DCD.

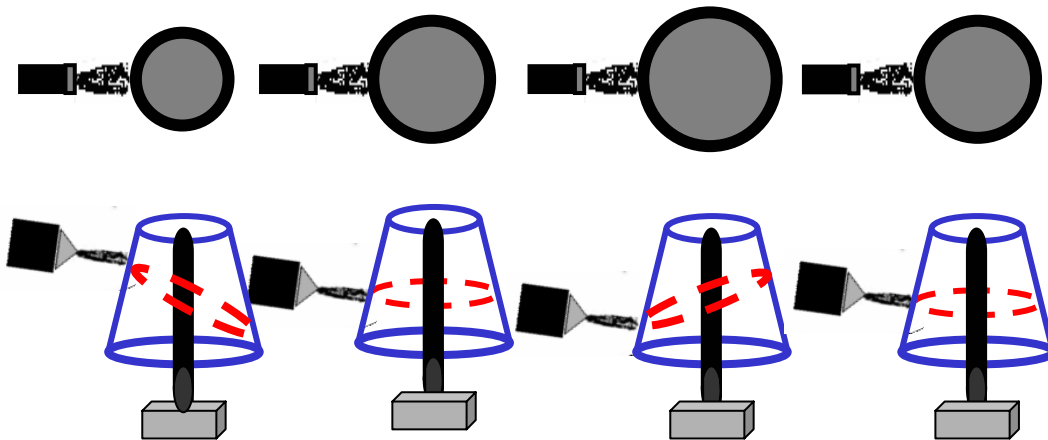


Figure 3.5: Positioning of the Die relative to the Mold for Variation in the Curvature of the Collecting Surface.

Table 3.1: Control Algorithm In 3D space For Constant DCD:

For rotation 1 (Upward movement) (Position $i = 1$ to n)

move tool to position P_1 at speed X
move mold x degrees at angular speed A
offset vertical position of tool by z
move tool to position P_2 at speed X
move mold x degrees at angular speed A
offset vertical position of tool by z
 ...
 ...
move tool to position P_i at angular speed X
move mold x degree at speed A
offset vertical position of tool by z

For rotation 2 (downward movement)

move mold $-x$ degrees at a angular speed of A
move tool to position P_{n-1} at speed X
offset vertical position of tool $-z$
move mold $-x$ degrees at a angular speed of A
move tool to position P_{n-2} at speed X
offset vertical position of tool $-z$

 ...
move tool to position P_1 at speed of X

Table 3.2: Control Algorithm In 3D space For Constant DCD and Surface Speed of Collector

For rotation 1 (Upward Movement)

move tool to position P_1 at speed X
move mold x degrees at angular speed A_1
offset vertical tool position by z
move tool to position P_2 at speed X
move mold x degrees at angular speed A_2
offset vertical tool position by z
 ...
 ...
move tool to position P_n at speed X
move mold x degrees at angular speed A_n
offset position n

For rotation 2 (downward movement)

...reverse order and also the negative angular movement

3.1.2.2 Determination of Co-ordinates on a Mold

In order to establish the co-ordinates on the mold, it is essential to establish the co-ordinate system of the 3D space in which the mold and the robot are placed. The RFACS uses a world coordinate system with the base of the robot as the origin of a left handed Cartesian co-ordinate system (Figure 3.6).

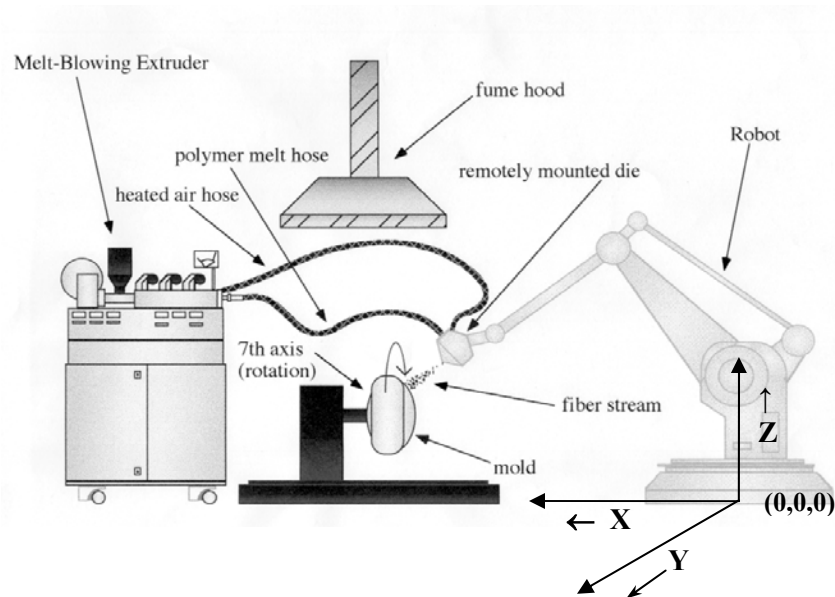


Figure 3.6: Left handed Cartesian co-ordinate system superimposed on the schematic of RFACS

3.1.3 Curvature of the Collecting Surface

The fibers from the RFACS are deposited on the collecting surface by the action of air on the fibers. When all other parameters of the process are the same, the shape of the collecting surface influences the physical structure of the web that is formed on the collecting surface. The curvature is defined as the rate of change of direction of the tangent line at the point of consideration. The curvature of an arc, which is part of a circle, is measured to be the reciprocal of the radius of the circle.

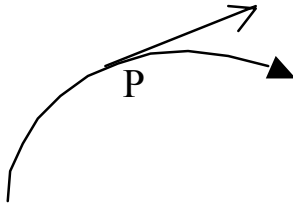


Figure 3.7: Curvature of an Arc in a Plane

Assuming that the mold is symmetrical vertically, the cross-section of the mannequin is elliptical at any point below the arms of the torso. The section shows that the mold has different curvatures at different points along its path. The effect of the curvatures on the structure of the web formed on it can be more clearly understood with the aid of the schematics shown in the Figure 3.8

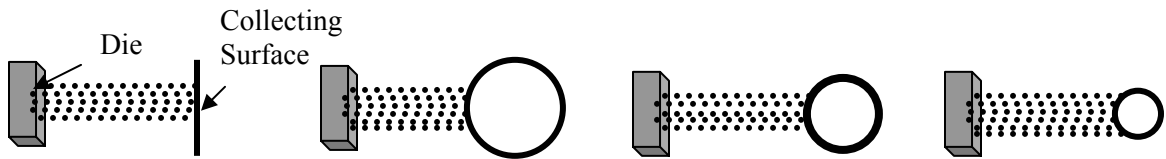


Figure 3.8: Various curvatures on the collecting surface

In the case of a plane-collecting surface the curvature of the collecting surface is shown to vary from zero, to higher values when the collecting surface is not a plane. The impact of the fibers on the collecting surface will influence the structural orientation of the fibers. The orientation of the fibers will in turn affect the pore size of the web. The basis weight uniformity of the fibers will vary for different curvatures of the collecting surface. Assume that in the figure above, the four curvatures of the collecting surface are increasing from left to right. The basis weight uniformity will decrease for the webs formed on the collecting surfaces left to right. The fiber orientation will also change from completely random structures to directionally oriented structures as we move from left to right. These hypotheses do not include the effect of the die to collector distance and the attenuating air pressure.

3.1.3.1 Measurement of Curvature of an Ellipse

In order to understand the effects of curvature and change in curvature on the structural properties of the webs formed on them, it is essential to determine the curvature of a section of a 3D space. Consider a mold whose cross – section is parallel to the XY plane, as shown in Figure 3.9, or a section of a cone as shown in Figure 3.4.

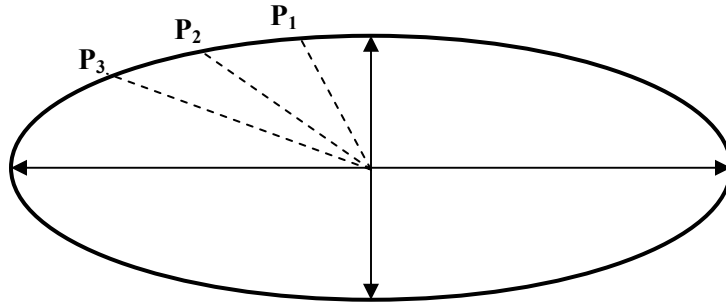


Figure 3.9: Cross-section, parallel to the XY plane of the torso

The curvature of different sections on a conical mold or cross section of a torso parallel to the XY plane can be determined by considering the section along the path of travel of the die as that of an ellipse. Assuming that the cone or the mold are symmetrical along the central z axis, if a and b are the semi-major and semi-minor axes of the ellipse in a plane, the equation of the ellipse is given by

$$\frac{x^2}{a^2} + \frac{y^2}{b^2} = 1$$

In the case of the cross section of the mold the lengths a and b can be determined by measuring the depth and width of the mold at that particular point. In the case of a plane in the cone at an angle θ , to the base of the cone length a

$$a = \frac{r_2}{\cos \theta} \text{ where } r_2 \text{ is the radius of the base of the cone. } b \text{ is equal to the radius of the}$$

circle at the point where the elliptic center intersects with the axis of the cone. The distance between the center of the ellipse and the point under consideration is the radius of the curve at that point and its reciprocal is the curvature at that point. If the dimensions of the cone or the mold cannot be determined by regular measurement, the coordinates of the center and the point under at which the curvature has to be considered can be determined by triangulation, explained in detail in the succeeding sections.

3.1.3.2 Analytical Measurement of Curvature

The curvature of an arc is defined as the rate of change of direction of the tangent line at the point of consideration. The curvature of the arc, which is part of a circle, is measured to be the reciprocal of the radius of the circle.

Assuming that there is axial symmetry on the mold, along the z – axis in the xz plane, a curve in 3D space can be analyzed as a curve in a 2D plane. Analytically, the curvature can be determined if the co-ordinates of three points on the curve, in 2D space, are known. In the case of a curve in 3D space the co-ordinates of four points are required. The distance between two points in 3D space is known to abide by the following relationship:

$$d = \sqrt{(x_2 - x_1)^2 + (y_2 - y_1)^2 + (z_2 - z_1)^2}$$

The distance between the center of the circle and a point on the curve is the radius of the curve and is a constant for arc that is a part of the circle.

For a given set of four co-ordinates, which lie on the arc of a curve, in 3D space, the equation and hence its curvature of the curve passing through those four co-ordinates can be determined. If $p_1 = (x_1, y_1, z_1)$, $p_2 = (x_2, y_2, z_2)$, $p_3 = (x_3, y_3, z_3)$, $p_4 = (x_4, y_4, z_4)$ are the four coordinates on the same curve, the center $p_c = (x_c, y_c, z_c)$, of this curve can be determined by solving the distance equations of the four coordinates with the center of the curve.

The simultaneous equations that are formed are:

$$\begin{aligned}(x_1 - x_c)^2 + (y_1 - y_c)^2 + (z_1 - z_c)^2 &= (x_2 - x_c)^2 + (y_2 - y_c)^2 + (z_2 - z_c)^2 \\(x_3 - x_c)^2 + (y_3 - y_c)^2 + (z_3 - z_c)^2 &= (x_2 - x_c)^2 + (y_2 - y_c)^2 + (z_2 - z_c)^2 \\(x_1 - x_c)^2 + (y_1 - y_c)^2 + (z_1 - z_c)^2 &= (x_4 - x_c)^2 + (y_4 - y_c)^2 + (z_4 - z_c)^2\end{aligned}$$

Solution of these simultaneous equations yields the unique co-ordinates of the center of the arc and hence the radius and curvature of this arc can be determined.

3.2 MATERIALS

Polypropylene (PP) meltblown samples were produced using PP resin with a nominal melt-flow-rate (MFR²) of 1200 (IV = 0.8), on the RFACS. The resin was obtained courtesy of Basel Inc (Formerly Montell Inc.). Polyurethane-Co-Polyester (COPE) was also used in the experiments conducted. COPE was obtained courtesy of Eastman Chemical Inc. COPE is a elastomeric copolyester ether. It is a clear, tough copolymer with elastomeric-like properties (*Ecdel 9965*[®]). It has an inherent viscosity of 1.05 and MFR of 20 g/min (at 230°C and 2.16 kg) [91]. The melting temperature of the resins was determined by a thermal analysis using a differential scanning calorimeter (DSC). The temperature of the melting peak that was observed in the DSC curve, as shown in Figure 3.10 and Figure 3.11, was taken as the temperature for 3rd zone of the extruder. The processing conditions for the two polymers are given in Table 3.3 and Table 3.4. The conditions are based on preliminary work to obtain a sample and also on the conditions developed by Farer [9] for PP. The processing conditions for COPE were based on recommended conditions for processing the polymer [91], and also through the experience gained from preliminary work done on the resin. Additionally drying and

processing of the polymer and information on purging of the extruder are given in the next section.

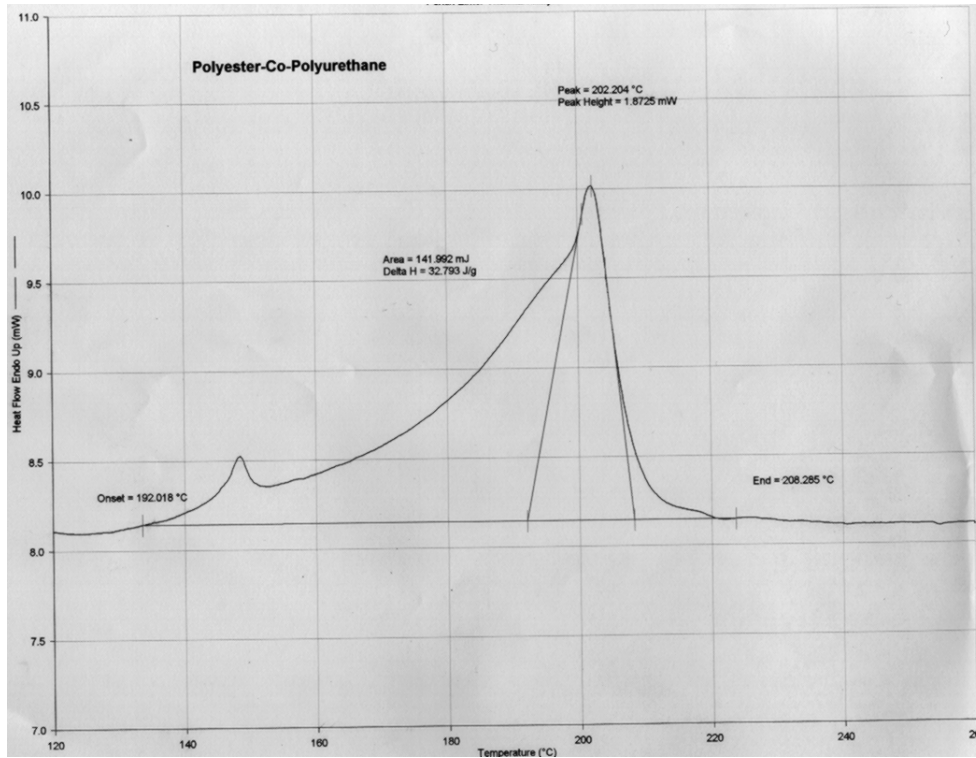


Figure 3.10: DSC thermal analysis of the COPE resin

Table 3.3: Meltblowing Unit Specifications for Polypropylene

Max. Machine Temperature: 280 °C
 1.9 cm (3/4") Single Screw, 24:1 L/D Extruder
 3 Barrel (Zones 1-3: 135 °C, 149 °C, 160 °C), 1 Flange (163 °C), and 1 Die Zone (175 °C)
 Air Heating Assembly
 1.8 m (6') Melt Transfer Hose (170 °C)
 1.8 m (6') Air Transfer Hose (= air temp.)
 Meltblowing Die
 Max. Die Temperature: 280 °C, Temperature Used: 175 °C
 7.6 cm (3") Active Spray Width
 90° Sharp-Tip Nosepiece
 12 Holes/cm (30 Holes/in.), 0.4 mm (0.016") Hole-Diameter
 Air Gap via Shims, 0.254 mm (0.010") Shim Thickness
 Positive Setback: 0.8 mm (1/32")

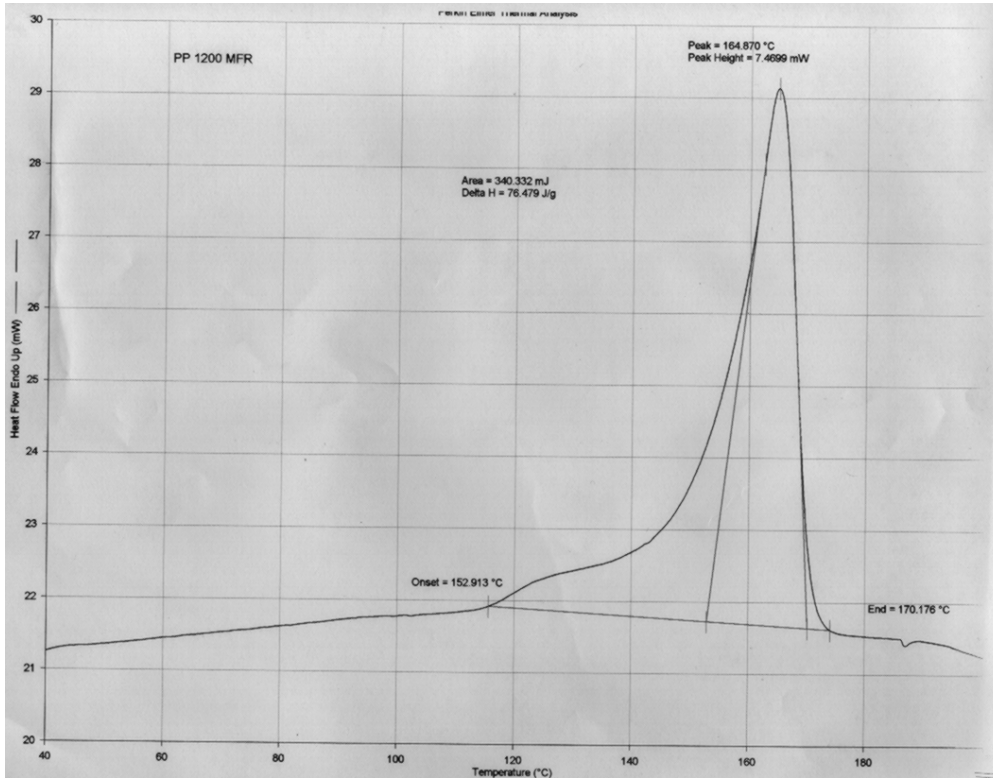


Figure 3.11: DSC Thermal Scan for PP resin.

Table 3.4: Meltblowing Unit Specifications for COPE:

1.9 cm (3/4") single screw. 24:1 L/D Extruder
 3 barrel (zones 1-3, 177, 210, 230 °C), Flange (240 °C), and Die (260 °C).
 Temperature of the air in the air heater (340 °C)
 7.6 cm (3") Active Spray Width
 90° Sharp-Tip Nosepiece
 12 Holes/cm (30 Holes/in.), 0.4 mm (0.016") Hole-Diameter
 Air Gap via Shims, 0.254 mm (0.010") Shim Thickness
 Positive Setback: 0.8 mm (1/32")

3.2.1.1 Safety Measures and Polymer Processing

While processing PP or COPE through RFACS extruder the following steps have to be taken, not only the ease of procedure but also as a safety precaution. Apart from the regular laboratory safety precautions, a long heat resistant coat, at least a 14" gloves, safety glasses and face shield should be worn at any time the equipments are operated, during the start up and shut down of the equipment and also during the adjustments made dealing with the melt hose. All references on the equipment are made with respect to Figure 3.12. At beginning of the test run, water supply that is used for cooling is turned

on and the attenuating air pressure is turned on such that the pressure gage reads to about 20 PSI. Then the equipment is switched on and the zone temperatures are set for PP resin as shown in Table 3.3. When the machine has been heated for about 45 minutes and the zone temperatures have reached the set temperatures, the equipment is purged with PP resin for about 45 minutes to an hour (usually using a low MFR resin such as a 35 to 50 MFR). Later the temperature settings are altered depending on the specifications found for the polymeric resin to be processed. If 3D structures are being formed then the die is mounted on the end effector of RFACS and the die is connected to the extruder using the flexible hoses (Figure 3.1). When the melt temperature of the hose reaches the set temperature, 25 to 30 minutes is allowed for the temperatures to stabilize in the system. When the set temperatures have been reached the extruder is cranked up with and the speed of the extruder is set to 7.5% of its maximum value, making sure that the backpressure gage does not exceed 300 PSI. If it does exceed 300 PSI, the screw speed is decrease and the pressure on the system is relieved. The temperature settings is modified to easy the flow of the polymer through the system. Later the screw speed is increased to meet the specific polymer throughput requirements.

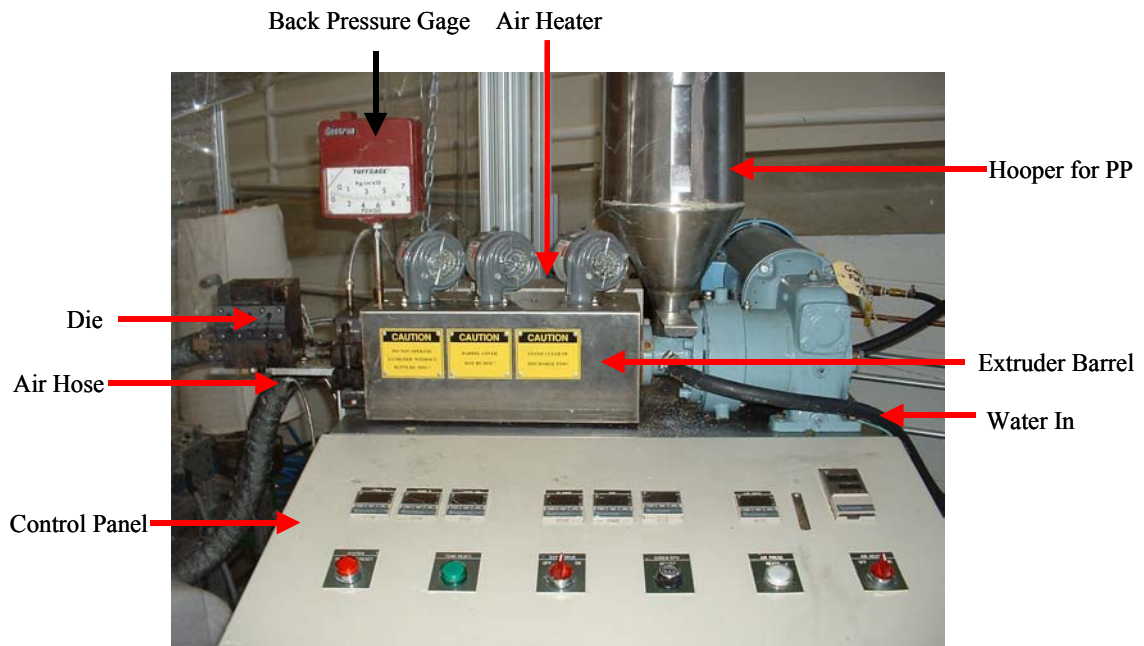


Figure 3.12: Nordson Desk Top Meltblown Extruder.

3.2.1.2 Pre-processing Drying, Purging for COPE and Elimination of SHOT

The COPE must be dried to a moisture level of approximately 0.02% before processing, or like other polyesters, it will undergo excessive hydrolytic degradation while in the melt [91]. A dehumidifying desiccant dryer capable of supplying air at 88°C (190°F) with a dew point not exceeding –30°C (–22°F) and an air volume of 0.062 m³/min/kg per hour of output is the recommended dryer to use. It is recommended that the hopper should have a capacity of 4 to 6 times the hourly output capacity of the equipment. A Conair dryer (Figure 3.13) was used for this purpose and the COPE was dried for 6 hours at the recommended temperatures.



Figure 3.13: CONAIR Dryer with hopper and Controls.

Polypropylene, high-density polyethylene, and many other materials will do a satisfactory job of purging COPE [91]. Because of the good melt stability of COPE, purging may not be necessary when the machine is shut down. However, material that is present in the extruder will crystallize requiring elevated temperatures during the next start up of the equipment. Hence, purging the extruder for 30 minutes using a PP resin of 35 to 50 MFR is recommended and the same procedure was followed during the preparation of COPE webs.

As discussed earlier, the term “shot” refers to the particles that are sometimes present in meltblown webs and have been defined as “groupings of molten polymer material or fibers that occur in melt-blowing through entanglement and thermal bonding and which has not been drawn to a diameter, similar to the diameter of surrounding fibers [20]”. The formation of shot has been attributed to the presence of multi-filaments with very low DCD. Shot that were formed on the webs formed using COPE resin are shown in Figure 3.14. Changing the DCD between the collector and the die controlled these shots. The temperature on the die was increased by 5 degrees and most importantly the throughput of the polymer was decreased. Shots were more prominently observed on the webs that were collected when the die nosepiece had not been “burnt” (cleaned). Cleaning the nosepiece and aligning spacer shims in the die decreased the SHOT in the web. Further 25° C increase in the attenuating air temperature that was initially set, and a slight increase in the air pressure through the system decreased the formation of SHOT.

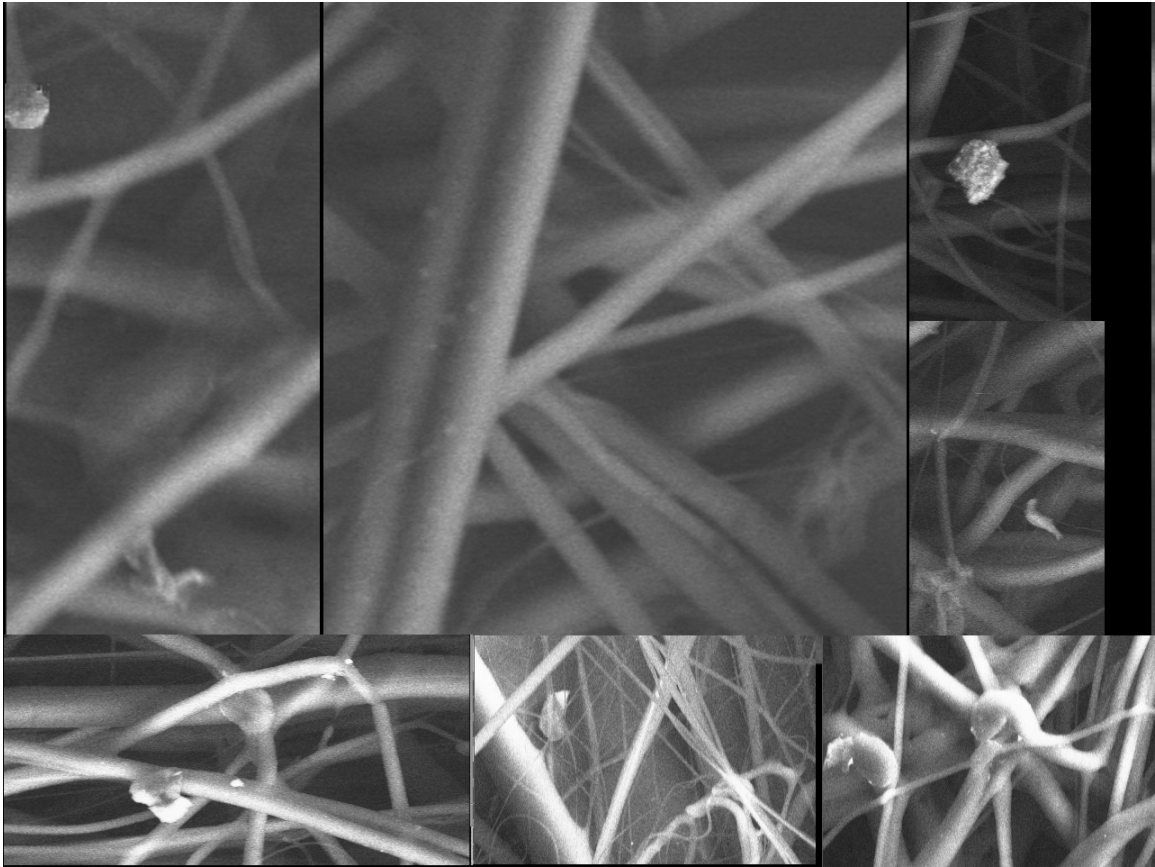


Figure 3.14: SEM Image containing SHOT on COPE webs (a Composed Image of Various Samples Produced during Preliminary Trails)



SHOT

Figure 3.15: The Die with SHOT formed at the nosepiece tip

3.3 EXPERIMENTAL DESIGN

The process parameters that would be varied include the polymer throughput, fiber stream approach angle, attenuating air pressure, die to collector distance, web take-up speed, and curvature of the collecting surface. The limits of these parameters, and the methods for calculating and measuring the curvature and approach angle, are discussed in the succeeding sections. The structural characteristics of the web that were investigated include the fiber diameter distribution, fiber orientation distribution, pore size distribution and the specific instruments used to evaluate these characteristics of the webs are also discussed.

3.3.1 Polymer Throughput

Polymer throughput affects the fiber and web characteristics that are formed. Higher the polymer throughput in the extruder the fibers that are formed would have a larger diameter. The polymer throughput also affects the basis weight of the web. As the overall goal of this research is to form lightweight, “seamless” garments the effects of polymer throughput investigated were at the lower limits of the equipment used. The polymer throughputs that were used in this investigation were 1.8, 3.7, 5.4, 8.1, and 9.6 x 10⁻² g /hole/min. The extruder does not push the polymer through the system when the polymer throughput is reduced below 1.8 x 10⁻² g /hole/min.

3.3.2 Attenuating Air Pressure

Attenuating air breaks the polymer stream into fibers, attenuates them and carries the fibers to the collecting surface. The velocity of this air affects the fiber diameter and its arrangement on the collecting surface. As already discussed, the arrangement of the fibers on the collecting surface not only affects its mechanical properties but also the filtration properties of the web. The higher the attenuating air, the finer will be the fibers formed. Depending upon the distance of the collecting surface, the effect of the velocity of attenuating air will also affect the basis weight of the web formed. The limits on the equipment for this research were 0.7 to 4.2 bar. The very high limit was determined to be unsafe operating conditions and hence the high limit was set at 2.8 bar.

3.3.3 Web Take-up Speed

The velocity of the collecting surface influences the fiber orientation in the web formed. Higher the speed, larger number of fibers will be oriented in the direction of the movement of the collecting surface. This again affects the filtration and mechanical properties of the web formed during the process. As the intention of this study is to form 3D structures, the speed of the collecting surface cannot be as high as the commercial equipments. The investigated range was 6.09 m/min to 15.24 m/min.

3.3.4 Die to Collector Distance

The die to collector distance (DCD) determines the morphological development of the polymer. If the distance is very close, studies by Shambaugh *et al.* [8], have indicated that the fibers are not fully formed and “shot” could be formed. Also the basis weight will be affected at close ranges as the high temperature attenuating air stream will “rebound” and width of the web formed will be affected. With the practical limitation of not being able to get the collecting surface any closer than 2 inches, the lower limit was set at 2 inches. Experimental study included samples collected at 2 inch increments, up to 12 inches.

3.3.5 Fiber Stream Approach Angle

The fiber stream approach angle is defined as the angle between the principal axis of polymer flow from the die and the tangential plane to the collecting surface. The approach angle (Figures 3.16 and 3.17), affects the structural and mechanical properties of the webs formed. A fiber stream approach angle of 90 degrees, when the fiber stream is normal to the collecting surface, is the commercial standard for formation of meltblown webs. The lower limit on the approach angle is set by the curvature of the collecting surface.

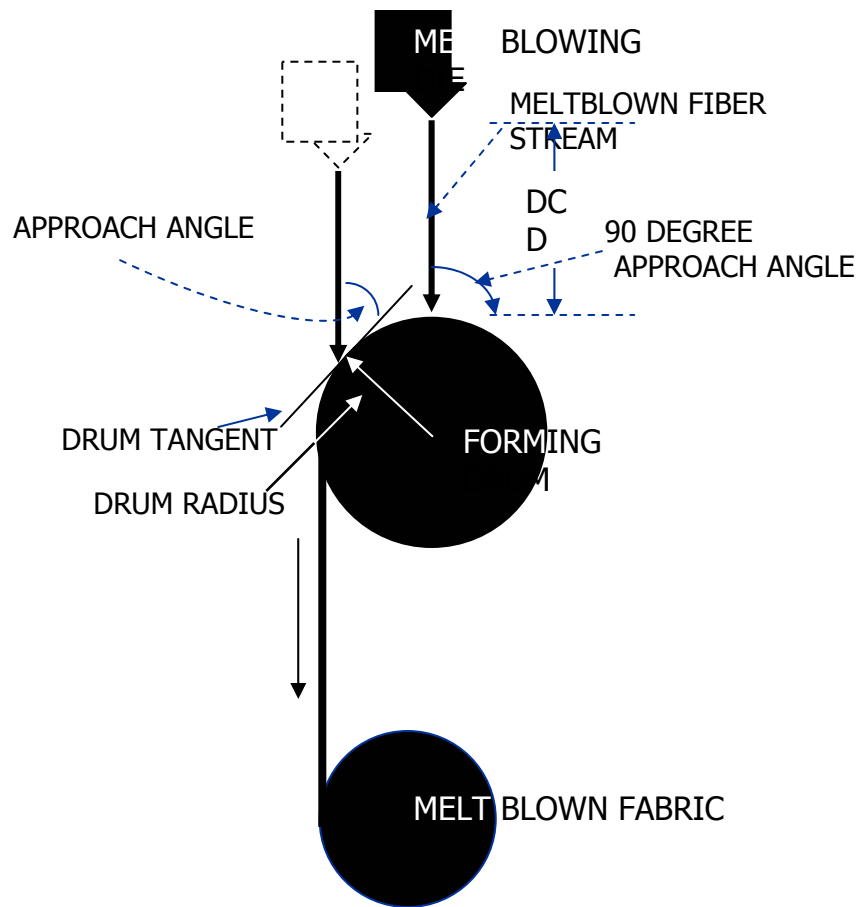


Figure 3.16: Schematic of Fiber Stream Approach Angle on a Collecting Drum [9]

When attempts are made to form the webs beyond certain angle, determined by the curvature of the collecting surface, the fibers will flare and not be placed on the collecting surface. The approach angle limit for the conical mold (Figure 3.17) used was 37 degrees at a curvature of 4.71 m^{-1} . Whereas when the webs are collected on a cylindrical drum of 9.52 m^{-1} , the limit was 26 degrees. The limit is also dependent upon the width and number of orifice rows in the die. The lower limits of the current research are the set values for an extruder die of 3 inch width with single row of orifices.

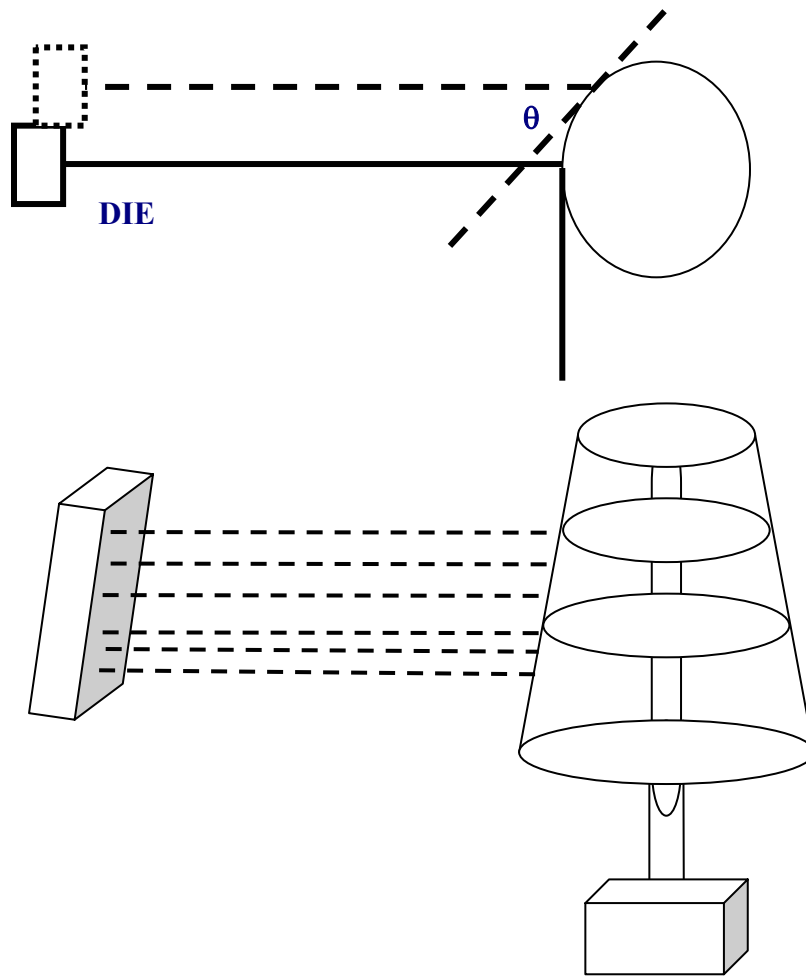


Figure 3.17: Fiber Stream Approach Angle on a Conical Mold

The co-ordinates of the space within the working range of the RFACS can be determined by moving the tip of the pointer on the end effector to that particular point in the space. The position of the seventh axis of RFACS (on which the mold is mounted) is fixed relative to the world co-ordinate system of robot. The mold is mounted on the seventh axis and a pointer is mounted on the end effector of the robot. The coordinates along a curve on the complex geometry of the mold are then determined with the aid of the position of the pointer when the pointer is moved to the said coordinate. The curvature for a curve in the mold is then determined using the analytical procedure previously described.

3.3.6 Curvature of the Collecting Surface

The rotational speed of the various coordinates of the mold mounted on the seventh axis was determined using the triangulation theory, fully described by Farer [9]. The rotational speeds of the mold were varied to change the surface speeds of the curvature.

The various curvatures that were investigated in this study were obtained from the mold of the torso and also along the elliptical path on the mold. The range curvatures investigated was from 1.94m^{-1} to 10m^{-1} .

As there is a wide range in the parameters investigated, a fully random design was not feasible to be conducted. Investigation of any given parameter was conducted by holding the other parameters at a constant value. These constant were determined by initial trials, limitations of the equipments and also from the data obtained in the literature.

3.4 RANDOMIZATION PROCEDURE AND SAMPLE COLLECTION

The web structures that were produced were collected in a random order. The random order in which the test conditions were set to produce the COPE webs are as detailed in Table 3.5. The order for the formation of the web samples were called in random, by a colleague, so as to have an unbiased order of preference for the purposes of production of the web. In the case of the samples produced for studies on the effects of approach angle using PP resin, the order is as in shown in Table 3.6. The samples for the investigation of curvature effects were obtained at the different locations of the 3D web produced on the same mold simultaneously, and hence there was no randomization involved in the

process. Multiple samples of the webs produced at the same process condition were obtained when the equipment was stabilized at each condition.

Table 3.5: Process Conditions for the COPE webs and the Corresponding Random Order for 2D Webs.

Throughput (x10 ² gmh)	Attenuating Air Pressure (bar)	Take-Up Speed(m/min)	DCD (cm)	Random Order
3.7	1.05	6.09	5.08	1
3.7	1.05	6.09	10.16	5
3.7	1.05	6.09	15.24	9
3.7	1.05	6.09	20.32	15
3.7	1.05	6.09	25.40	13
3.7	1.05	6.09	30.48	8
3.7	1.05	6.09	35.56	2
3.7	1.05	9.13	5.08	17
3.7	1.05	12.19	5.08	14
3.7	1.05	15.24	5.08	3
3.7	1.40	6.09	5.08	12
3.7	1.75	6.09	5.08	7
3.7	2.10	6.09	5.08	11
3.7	2.45	6.09	5.08	19
3.7	2.80	6.09	5.08	10
1.8	1.05	6.09	5.08	18
5.4	1.05	6.09	5.08	4
8.1	1.05	6.09	5.08	6
9.6	1.05	6.09	5.08	16

Table 3.6: Random order for the PP to investigate the effects of Approach Angle

Approach Angle (Degree)	Random Order
90	3
86	6
68	2
58	4
48	1
37	5

3.4.1.1 Sampling of the Web for Analyses

The samples from the web that were collected for the purposes of analyses were obtained with the knowledge that no two samples were from the same horizontal and vertical section of the web. A schematic example is shown in Figure 3.18. As there were multiple web samples that were available at one process condition, one sample was taken

from each web. Five tests were conducted for each structural parameter for the sample produced at each process condition. In the case of the studies on curvature effects the samples were taken from different replicates, but the location on the mold was maintained as the curvature of the collecting surface changes continuously on the mold.

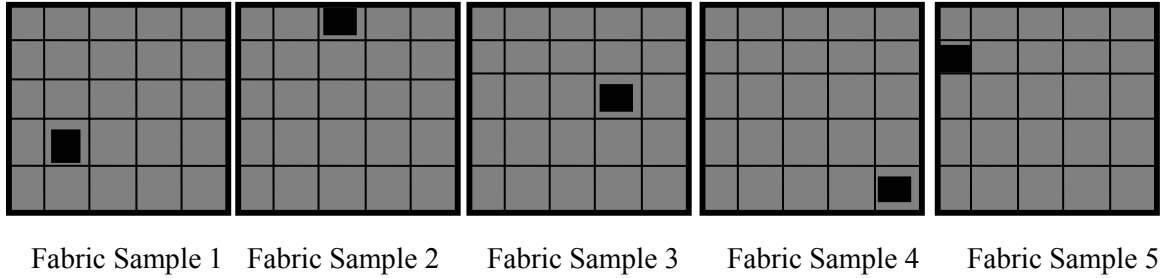


Figure 3.18: Sampling Procedure for Structural Analyses

3.5 WEB CHARACTERIZATION TECHNIQUES

3.5.1 ODF Measurement

An image analysis technique developed at Nonwovens Co-operative Research Center was used to determine the orientation of the fibers in the web. The results obtained from these tests are independent of the mechanical characteristics of the fiber. Any radiation from X-rays to infrared rays can be used in principal to obtain the image of the web [72, 73]. A low intensity source of rays like far infrared or sub-millimeter laser beam traversing the fibrous structure can be used to produce the image. Image analysis techniques use the intensity of the gray levels of the different pixels to determine the presence of the fibers and the orientation of the fibers.

Diffraction techniques are also used to measure the ODF of the fabrics directly from the diffraction pattern. A fabric when placed orthogonal to the path of a beam of laser produces a scattering pattern. The pattern thus produced is a Fourier Transform (FT) of the local structure of the fabric [62, 92, 93]. The diffraction pattern is a distribution of the intensity [94].

FT principles were used on the equipment used to measure the ODF of the webs. Diffraction patterns for the webs for 2D analysis were obtained using a low power helium-neon laser coupled with an image capture setup to measure the ODF. The

equipment is fully described by Veerabhadran [95, 96]. The image that is captured is composed of pixels of varying intensity. The intensity spectra of the pixels in the image are decomposed into the frequency domain with appropriate magnitude and phase values. The intensity of the gray scale in the frequency image represents the magnitude of the various components of the image. The discrete Fourier transform is used to determine the rate at which intensity transition occurs in a particular direction. If the fibers are oriented in one direction, the respective frequencies will be high in the perpendicular direction in the spatial domain.

In the case of webs formed to investigate the effects of fiber stream approach angle and the curvature, the images were obtained using a magnification of one on a system developed by Nonwovens Co-operative Research Center. A normal incident plane light illuminates the web. The image that is thus captured is then analyzed using Fast Fourier Transform to determine the distribution of fibers in various orientation angles [62].

3.5.2 Fiber Diameter Distribution

The materials used in the analysis of the fiber diameter are the same as that used in the analysis of the webs for fiber orientation distribution fully described in the section on materials in the previous topic. The diameter of the fibers was measured on SEM images (Figure 3.19) of the webs obtained at 500X. The SEM images were obtained on a Hitachi ESEM S3200 in the environmental mode. Multiple samples of the images were obtained and each image of the web contained more than 20 fibers. The diameters were measured using the manual measurement option using the software developed at Nonwovens Co-operative Research Center. The manual scale in the software was calibrated using the scale given at the bottom of the SEM image. A straight line across the image was drawn randomly and the diameters of all fibers, which intersected the straight line, were measured. Values obtained from multiple images of the same web were combined and grouped in 2 micron ranges.

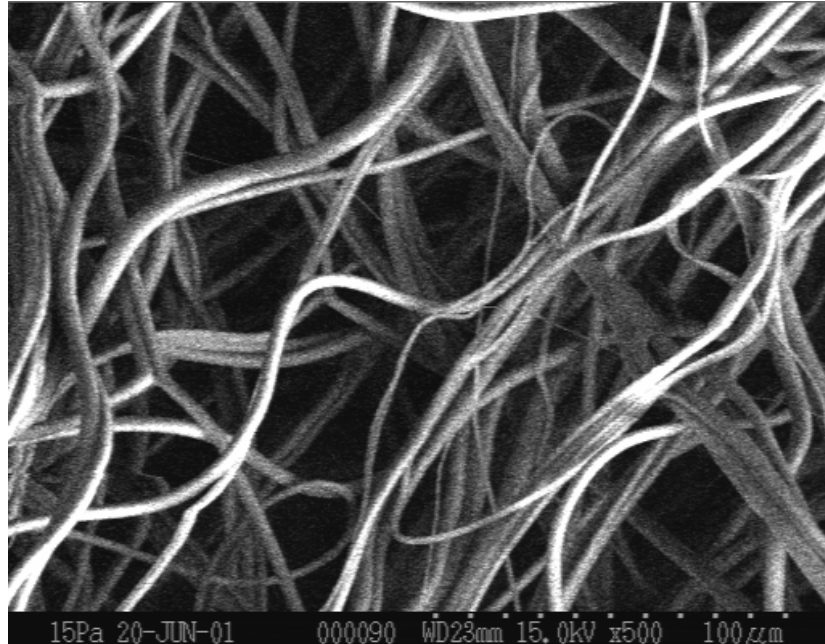


Figure 3.19: SEM image of a Polyurethane Co-polyester webs at 500 magnification

As can be seen in the image, the diameters of the fibers in the web do not change over the length of the fibers. In the case of using the software protocol to determine the diameters, the following sources of error in the measurement can occur.

- when the web is multilayered and the fibers are in different layers with a variation in the focus of the image capturing system, it is quite difficult for any system to identify the edges of the fibers.
- intersection of two or more fibers at one node causes the fibers to be measured as a thick fiber or the entire node will appear as a “shot”.
- When two or more fibers are formed such that they are side by side or placed staggered next to each other, the fiber diameter will be higher than the diameter of the individual fibers.
- the accuracy in the measurement of the diameters is dependent upon the threshold of the image, as the images need to be a binary image.

3.5.3 Pore Size Distribution

In the present study, capillary flow principles are utilized to determine the pore size and its distribution using a porometer. A computer controlled automated PMI capillary flow porometer was employed for all the tests conducted in this research. The equipment is capable of generating and measuring pressures in small intervals and gives reproducible values. Figure 3.20 shows the arrangement for capillary flow testing. A circular sample of the web is mounted between two O-rings of the adapter plates. One adapter plate is in

flush with the bottom of the chamber while the other is at the bottom of the insert that is placed on the top the sample. The insert and the sample are held in place by the cap that is screwed on the top with just sufficient pressure to prevent leakage of air and fluids, both sideways and between the O-rings. When compressed air is introduced under the sample, into the chamber, the gas flows upwards through the sample and escapes into the atmosphere through the top of the chamber. The pressurized air tries to escape through the sample by displacing the liquid in the pores of the sample.

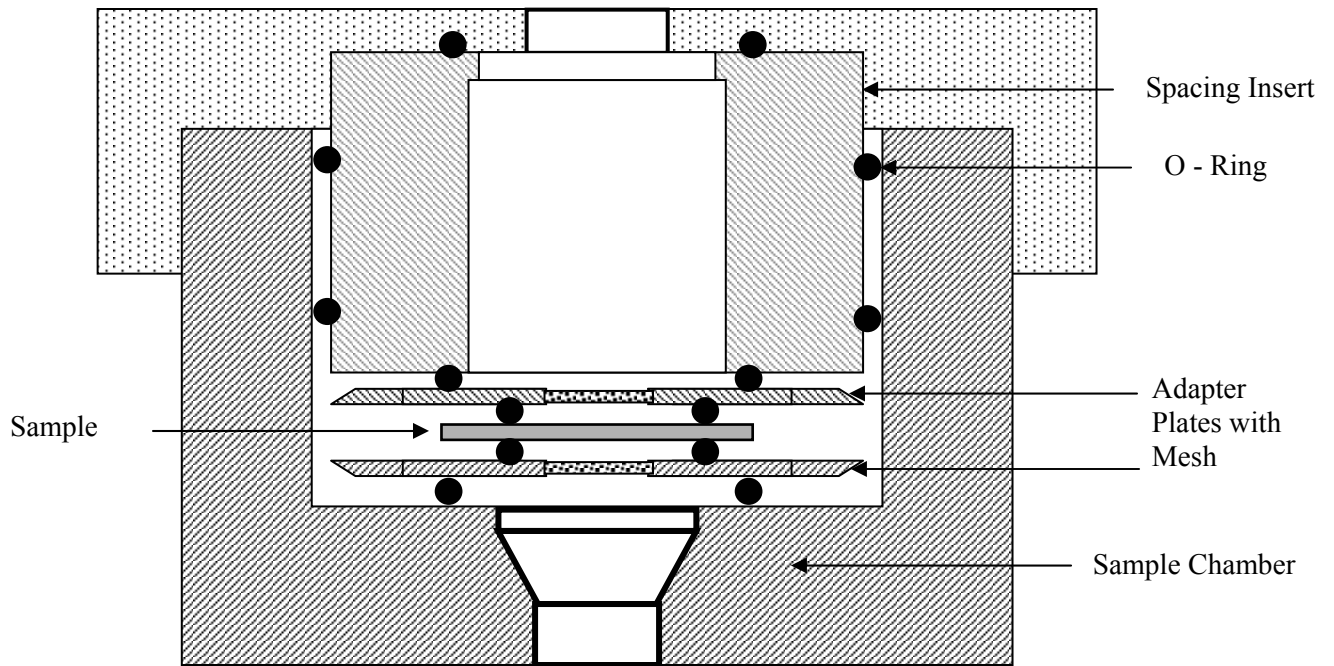


Figure 3.20: Schematic of the Capillary Flow Equipment

As the airflow is increased, the solution is removed from the pores with the largest pore (bubble point) being the first. With further increase in pressure, the solutions from smaller pores are expelled. When all the pores are free of the solution, the sample is in dry state and the airflow is continuously decreased until there is no further flow of air through the system. The pressure applied and the flow rate for the saturated sample and the dry sample are used to determine the pore size of different pores in the web. A typical pressure versus airflow curve for the wet and dry conditions is shown in Figure 3.21.

For a material of n right cylindrical pores of diameter d , Poiseuille's law gives the flow rate Q as,

$$Q = \frac{\pi n d^4 p}{128 \eta l} \quad (10)$$

where l is sample thickness, η is the viscosity of the fluid and p is the pressure drop across.

As the fluid pressure on the sample increases the fluid flows through pores of smaller diameter. On continuously increasing the flow, to open all the pores, the final flow rate Q_f is given by

$$Q_f = \frac{\pi \sum_{i=1}^f n_i d_i^4 p_f}{128 \eta l} \quad (11)$$

On expansion of this Equation and re-arrangement of flow conditions at succeeding intervals of applied pressure, the flow rate distribution at a particular diameter d_i is given by

$$\frac{n_i d_i^4}{N d^4} = \frac{\frac{Q_i}{P_i} - \frac{Q_{i-1}}{P_{i-1}}}{\frac{Q_f}{P_f}} \quad (12)$$

where $N = \sum n_i$ and $\bar{d}^4 = \frac{1}{N} \sum_{i=1}^f n_i d_i^4$

The diameter of the pore at a given pressure difference is obtained from Equation below and hence the corresponding pore size distribution.

$$d = \frac{K}{\Delta P} \tag{13}$$

where K is the constant that takes into account the surface tension of the interface and the contact angle. The value of K is 9.10, when the contact angle is zero with a wetting liquid whose surface tension is 16 dynes/cm.

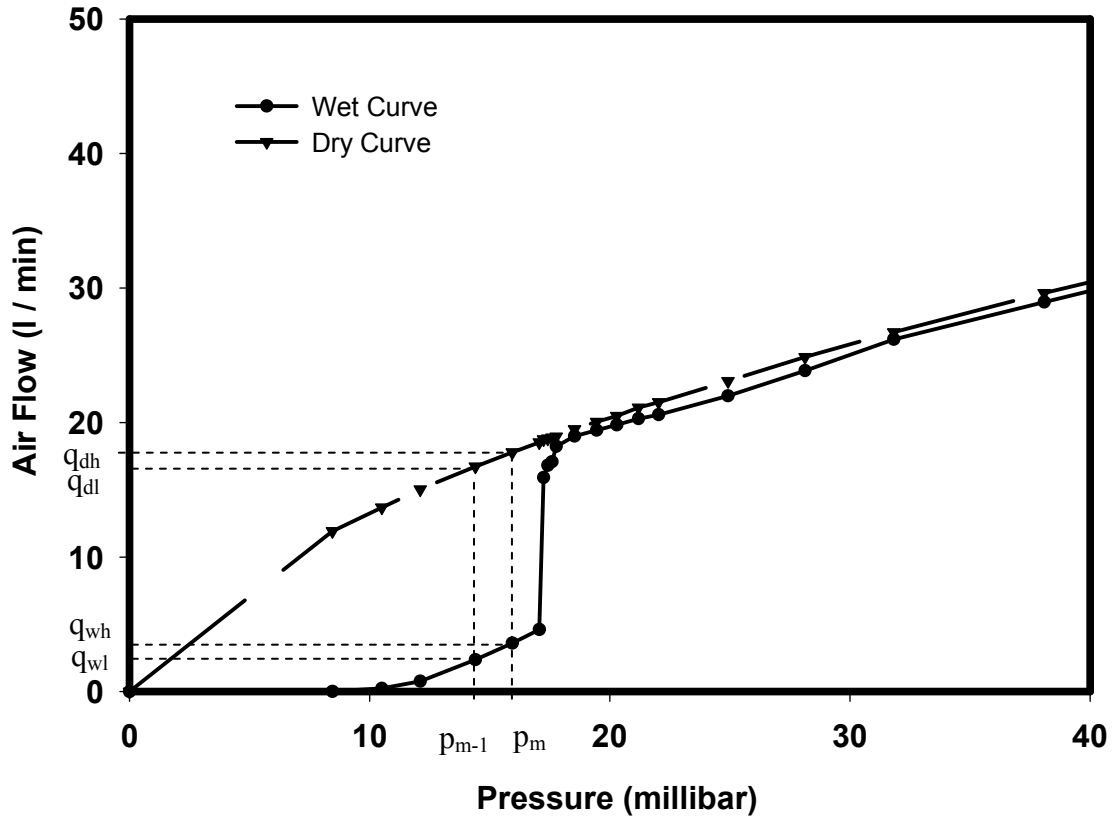


Figure 3.21: Typical Pressure versus Airflow curve for Pore Size Distribution Measurement on the PMI

We obtain the diameter distribution (D) using the equations given in ASTM F-316, for a given flow rate, as

$$D = \frac{q - q_L}{d_L - d} \quad (14)$$

Where q is the filter flow percentage in discrete intervals taking account of the difference in flow at dry and wet conditions, d is the pore diameter, and d_L is the previous pore diameter at flow percentage of q_L . The flow percentage q is given by:

$$q = \frac{Wet\ Flow_h}{Dry\ Flow_h} - \frac{Wet\ Flow_l}{Dry\ Flow_l} \quad (15)$$

Where h stands for higher pressure limit and l stands for lower pressure limit. The determination of the flow percentage can be explained, with the aid of Figure . The data recorded at the same pressures of wet and dry flow is stored in the system. In the m^{th} pressure interval, $p_m - p_{m-1}$, the corresponding wet flow values (q_{wh} and q_{wl}) and the dry flow values (q_{dh} and q_{dl}) can be determined. The q_m for this interval will be determined by the value in Equation 16.

$$q_m = \frac{q_{wh}}{q_{dh}} - \frac{q_{wl}}{q_{dl}} \quad (16)$$

3.5.3.1 Sample Calculation of Pore Size

For the purpose of clarity, a sample data generated during the measurement of pore size is used to show the calculations. The instrument generates the pressure difference, wet flow and dry flow of the fluid in liters/min. The distribution of the pore size is then calculated using the equation given in the previous section. The algorithm used by the instrument to calculate the data is given in Figure 3.22

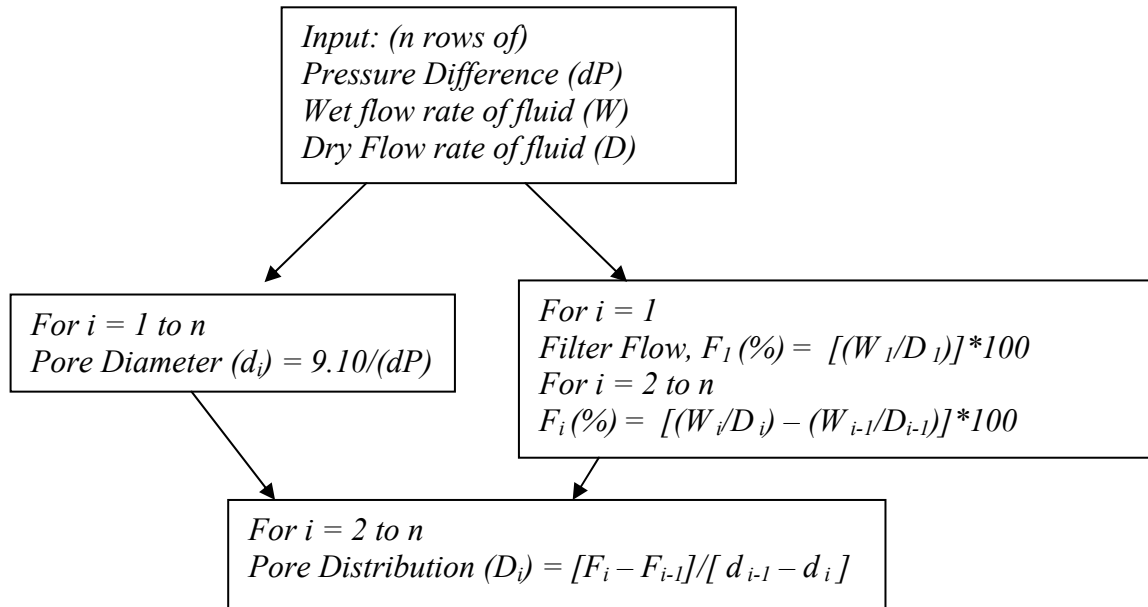


Figure 3.22: Flow Chart for calculating the pore size and its distribution

Table 3.7: Sample Data from Pore Size Measurement of for a Meltblown PP fabric (Throughput 3.7×10^{-2} g/min/hole, Attenuating Air Pressure: 1.05 bar, Take Up Speed: 8.23 m/min, DCD: 25.4 cm)

a) Data from Sensors of the Equipment

Differential Pressure (PSI)	Wet Flow (l/min)	Dry Flow (l/min)
0.0763	0.00265	11.77
0.0877	0.092	13.056
0.115	0.464	14.932
0.1279	0.928	15.514
0.1435	2.336	16.499
0.1436	2.384	16.514
0.1611	4.056	17.424
0.1615	13.892	17.46
0.1619	14.724	17.495
0.1623	15.724	17.531
0.1626	16.564	17.561
0.1808	17.704	18.462
0.2018	18.82	19.552
s0.2168	19.504	20.103
0.2414	20.56	21.353
0.2679	21.712	22.58
0.355	24.98	25.638
0.4619	28.564	28.564

b) Data Calculated Using Equations

Pore Size	Filter Flow (%)	Pore Distribution
119.30	0.02	1.0
103.79	0.68	0.04
79.15	2.40	0.10
71.17	2.87	0.36
63.43	8.18	1.06
63.39	0.28	6.29
56.50	8.84	1.28
56.36	56.29	402.22
56.22	4.60	33.00
56.08	5.53	39.94
55.98	4.63	44.70
50.35	1.57	0.28
45.11	0.36	0.07
41.99	0.76	0.24
37.71	0.00	0.00
33.98	0.00	0.00
25.64	1.28	0.05
19.71	2.57	0.43

3.5.3.2 Error in ASTM F316 1986

ASTM F316 1980 and ASTM F316 1986 have a variation in the constant that is used in the constant of proportionality C, in Equation 9. For a liquid whose surface tension is in dynes per cm² and the pressure difference is in pounds per square inch, C has to be derived in the case of the standard of 1980, while it is given to be 0.415 in the standard of 1986. The correct constant value has to be 0.56 when a pound is converted to grams and an inch is converted to centimeters. The PMI equipment uses a constant of 0.415. This has been recognized and corrected in all the calculations that have been done on the flow of fluid through the system and the respective diameters and distribution of the pore.

3.5.4 Basis Weight

In the case of 2D webs formed on the collector drum, 25 inch samples where formed. The die attached to the end-effector of the robot made a single to and fro traverse such that two layers of the fabrics were formed as a sample. The pitch between successive helices of the fabric, formed on the drum, was maintained at 7.62cm. It was achieved by maintaining the ratio of the traverse speed of the die to that of the rotating drum. The weights of a cut 2 X 2 inch samples of the webs was measured and the basis weights of the samples were than calculated from these measurements. In the case of webs formed

on the mold, (conical and torso), two layers of the fabrics were formed by rotating the seventh axis of the RFACS system in opposing directions. The webs thus formed were then at the precise locations to measure the weights of the webs.

3.6 STATISTICAL ANALYSIS

3.6.1.1 Analysis of Variance (ANOVA)

Orientation distribution function (ODF) for the various webs was analyzed using ANOVA using the statistical analysis package SAS. The frequency distribution was modeled to predict the effects of the various process conditions. To stabilize the variance in the data log of the frequency distribution was used as the predictor variable. As the sum of the frequencies in each treatment equal to 100 there can be no differences among treatment means. However there can be differences in the distribution of the frequency. The effect of the orientation angle on the process condition was investigated along with the interaction between the two parameters.

$$Y = \mu + T_i + S_{j(i)} + O_k + (TxO)_{ik} + \varepsilon_{ijk} \quad (17)$$

Where Y = log(freq)

i = 1 to n

n = 4 for polymer throughput and Take Up Speed, 6 approach angle, 10 for Curvature and 6 for DCD

j = 1 to 5 Fabric Sample

k = 1 to 18 Orientations

μ = Average log (freq)

T = Treatment Effect (process variable),

$S_{j(i)}$ ~ random sample within the treatment effect;

O = Orientation Angle Effect;

ε_{ijk} = error

3.6.1.2 Chi-Square Test

The frequency distributions of the fiber diameter and pore diameter were analyzed using the Chi-square test. Chi-square is defined as the sum of squares of independent, normally distributed variables with zero means and unit variances. The distribution of chi-square depends on the number of independent deviations, that is the degrees of freedom (df). In the current work Chi-square was used to compare the distributions obtained at different levels when varying a process condition. The values obtained are then compared to a given probability in a Chi-square table, which lists the chi-square values, and their

corresponding probabilities at a known degree of freedom and significance level. The probabilities range from a value of one when the data sets are the same to zero, which implies the data sets are different.

$$\chi_v^2 = \sum_{i=1}^n \sum_{j=1}^k \frac{(E_{ij} - O_{ij})^2}{E_{ij}} \quad (18)$$

where

O_{ij} = the observed value for the data in the i^{th} row and j^{th} column

E_{ij} = the expected value for the data in the i^{th} row and j^{th} column

$$E_{ij} = \frac{\sum O_{i.} * \sum O_{.j}}{\sum O_{ij}} \quad (19)$$

4 PROCESS VARIATION AND STRUCTURAL PARAMETERS

The various process parameters that were investigated viz; polymer throughput, DCD, attenuating air pressure, web take-up speed, curvature and fiber stream approach angle, for their influence on the structural properties of the webs formed are discussed. The properties of the webs that were examined were the basis weight, ODF, fiber diameter and pore size distribution. The process parameters of fiber stream approach angle and the curvatures of the collecting surfaces were investigated on webs formed as 3D structures while the other parameters were investigated on webs formed on a collecting drum of 21cm diameter.

4.1 INFLUENCE OF POLYMER THROUGHPUT

As discussed in section 2.5.2.2, anisotropy parameter of the web gives the overall variation of a measured property. In case of alignment of fibers, a completely random alignment of fibers will yield an anisotropy parameter of zero, while if all the fibers are aligned in one direction, the anisotropy parameter would be 1. If the fibers are aligned in a perpendicular direction the value of the anisotropy parameter would be -1.

Figure 4.1 and Figure 4.2 gives the ODF and anisotropy parameter for the melt blown fabrics formed at various throughputs, while the other process parameters are held constant. The basis weight of the fabric increases with an increase in the polymer throughput. Contrary to what has been explained earlier [9], visually there doesn't appear to be a change in the distribution frequency in the various orientation angles due to variation in polymer throughput (Figure 4.1). Although the anisotropy parameter shows an increase with more fibers being aligned in the machine direction, the increase is not significant (p-value=0.90). It appears that the variance in the anisotropy increases with increase in the polymer throughput.

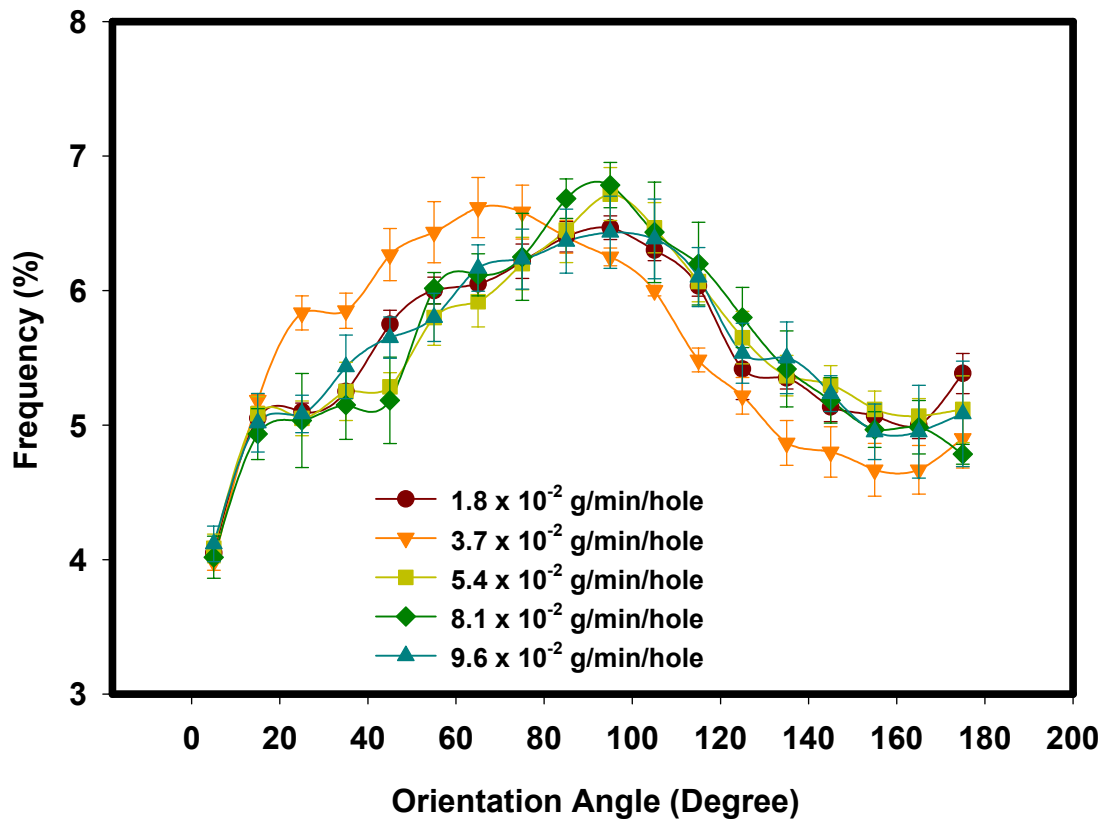


Figure 4.1: ODF for MB COPE webs at different polymer throughputs (Attenuating Air Pressure: 1.05 bar, Take Up Speed: 8.23 m/min, DCD: 25.4 cm, with Standard errors of 5 samples)

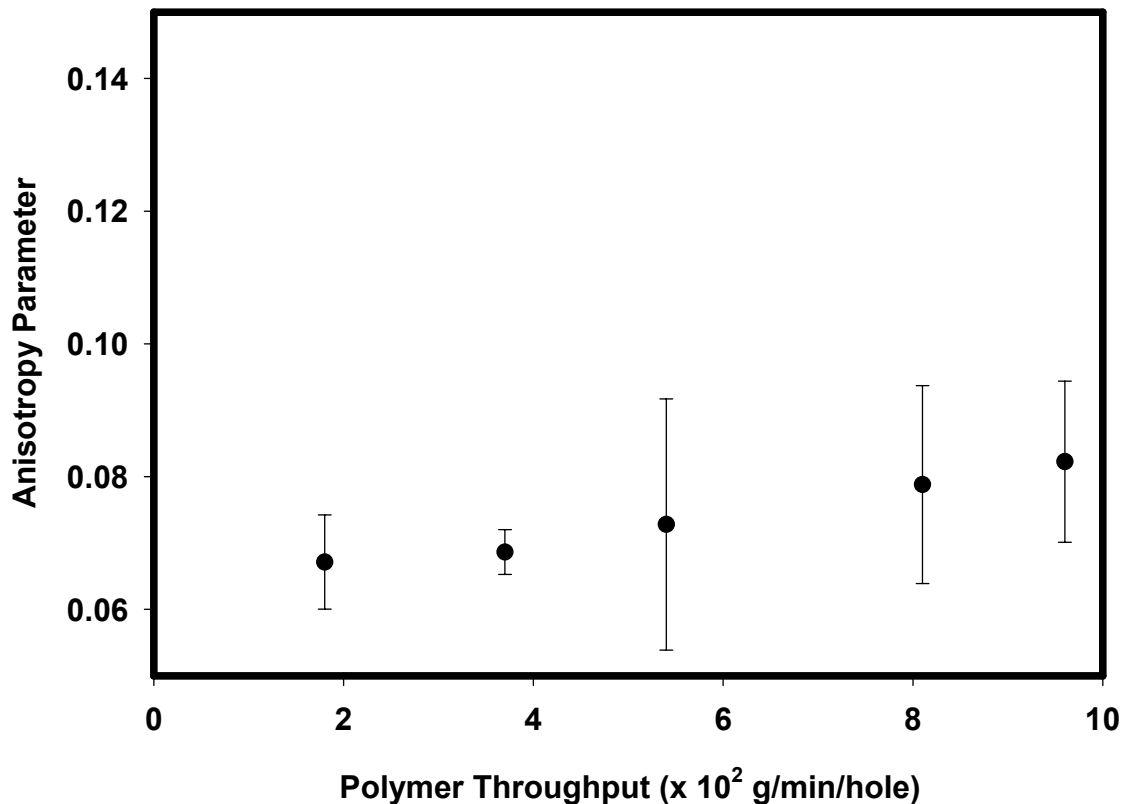


Figure 4.2: Anisotropy Parameter for MB COPE webs at different polymer throughputs (Attenuating Air Pressure: 1.05 bar, Take Up Speed: 8.23 m/min, DCD: 25.4 cm, with Standard error of the average of the 5 samples)

Statistical analysis of the data was performed to further examine the results of the effects of the polymer throughput on the ODF of the webs formed. Analysis of Variance was performed on the data obtained from ODF, rather than Chi-Square tests. Chi-Square tests, for comparing two or more frequency distributions are performed if the data is available as a frequency rather than % frequency [97]. Since the data for ODF is %Frequency ANOVA was performed on the frequency distribution data, as well as the anisotropy parameter as described in section 3.6.1.1. Both of these results are reported in the APPENDIX as Tables A-1 and A-2. The sum total of the frequencies over the range of 180 degrees always equals 100 for each sample. The frequency distribution in each sample varies. We have analyzed the data using $\log(\text{frequency})$, rather than frequency, to stabilize the variance in the data. The frequency distribution in the different angles is significantly affected by the throughput ($p\text{-value} = 0.045$). The mean anisotropy

parameter is not significantly different for different throughput, however the variance in the anisotropy parameter increases as polymer throughput increases (Figure 4.2 and Table A-2).

Figure 4.3 shows the cumulative frequency distribution of fiber diameters for varying polymer throughputs and at the set rate of attenuating air pressure. The DCD was maintained at 15.24 cm and the web was collected at the rate of 6.09 m/min. The distributions show that the fiber diameters decrease with a decrease in the polymer throughput. The cumulative curve can be explained with an example. Consider the curve for 3.7×10^{-2} g/min/hole throughput. The curve indicates that the probability of finding fibers greater than 5 microns is 0.28 (28%). At a particular cumulative frequency the range of the fiber diameters also decrease with a decrease in throughput of the polymer. Several authors have reported similar observations on the effect of the polymer throughput on the fiber diameter [9, 76].

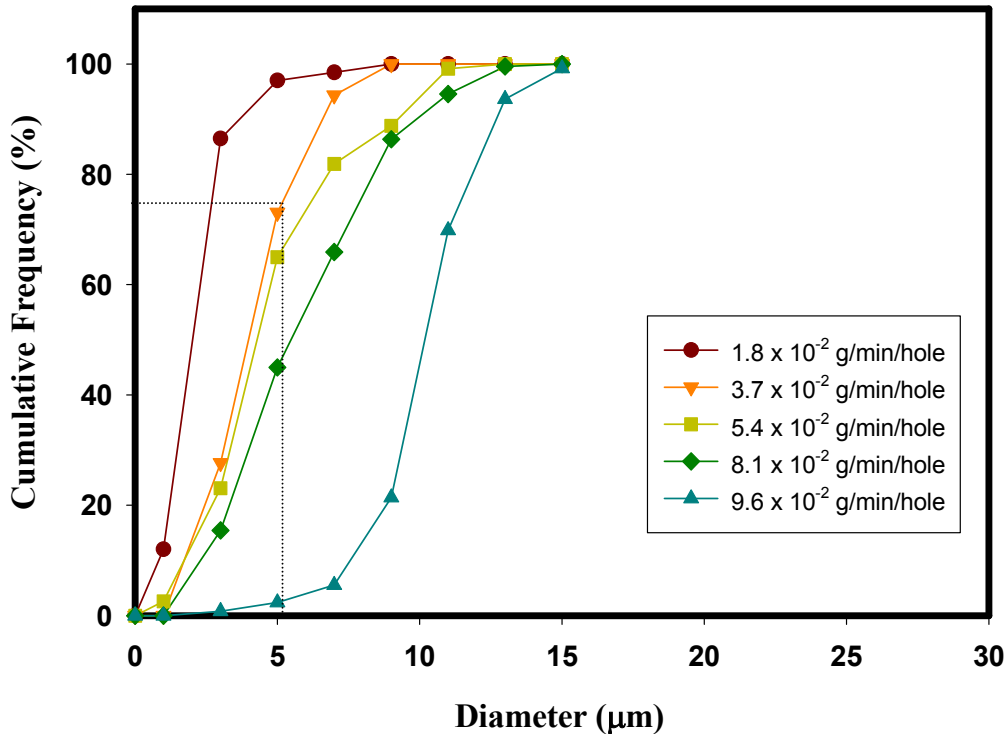


Figure 4.3: Cumulative frequency distribution of fiber diameters at different polymer throughput rates for MB COPE webs (Attenuating Air Pressure: 1.05 bar, Take Up Speed: 8.23 m/min, DCD: 15.24 cm)

A Chi-Square analysis on the diameter frequency distribution of the fibers was performed. The Chi-square value of 474.39 is higher than the critical value of 26.59 (df = $8 \times 4 = 32$, 9 diameters categories and 5 throughputs) with the corresponding Chi-square probability of <0.0001 . Hence, as expected, the polymer throughput has a significant effect on the diameter distribution of the fibers in the web.

Figure 4.4 shows average pore diameter and basis weight of the fabric at various polymer throughput levels. Similar to the influence of throughput on the fiber diameter distribution of the fibers in the web, the average diameter of the pore size of the web decreases with the decrease in the throughput of the polymer in the meltblowing system. The decrease in the fiber diameter due to decrease in the throughput decreases the pore size of the fabric. Although a decrease in the basis weight should increase the pore diameter, the results suggest that the reduction in fiber diameter has much more effect on pore size than the reduction in basis weight. As will be evident from the results obtained, the structural effect of the web on the pore size distribution is more predominant than the extruder processing parameters.

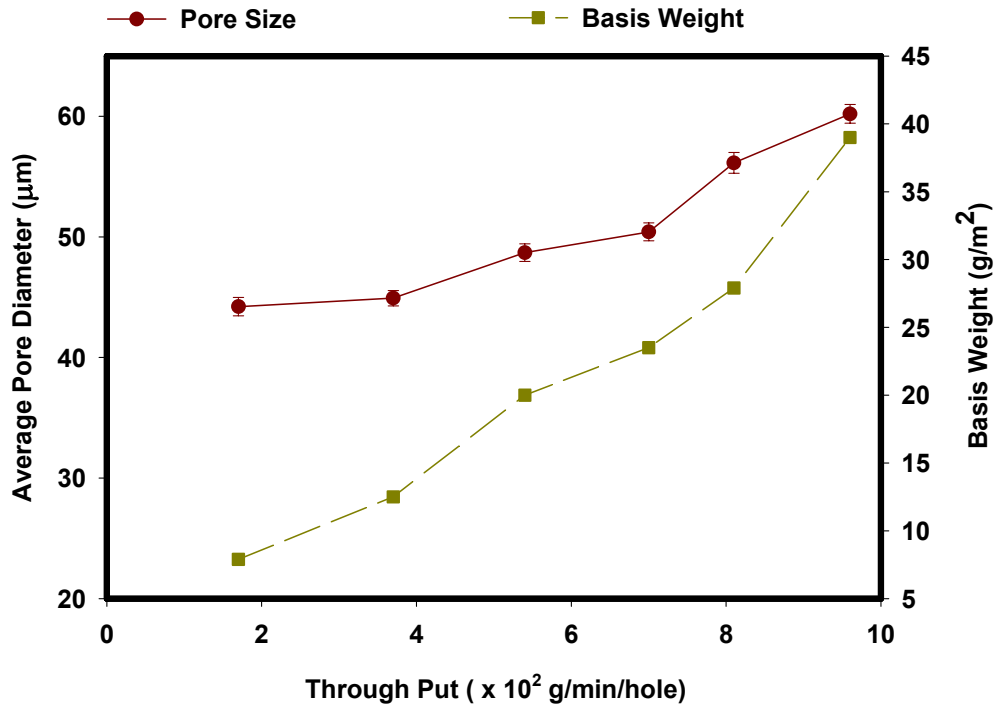


Figure 4.4: Average Pore Size and Basis Weight for MB PP Fabrics for variation in the Polymer Throughput (Take-up Speed: 6.09 m/min, Die to Collector Distance: 15.24 cm, Attenuating Air Pressure: 1.4 bar, with Standard Error of 5 Samples)

Simulation studies by Kim *et. al* [48] conducted on the variation of fiber diameter on the pore size of the webs indicate that the pore size increases with increase in the fiber diameter. In case of simulated studies, the fibers are in the same plane and the density of the fibers in a unit area is constant. An increase in the fiber diameter decreases the number of cross over points and hence the pore size increases. In the current study, the fiber diameter increases with the increase in the throughput (Figure 4.5 and Figure 4.6). This effect is also seen on the sample produced using PP resin (Table 4.1). An increase in polymer throughput increases the average diameter of the fiber and hence the number of cross over points in the web decreases. This leads to the formation of pores with larger size. As additional evidence the structure of the web, obtained by SEM techniques is shown. The web at higher throughputs has a larger pore size than the webs at lower throughputs.

Table 4.1: Average Diameter of Fibers and Anisotropy Parameter of Fibers at Various Throughputs of MB PP Webs

Through Put (X 10 ² g/min/hole)	Diameter (μm)		Anisotropy Parameter	
	Mean	Standard Error	Mean	Standard Error
1.8	3.43	0.365	0.141	0.007
3.7	6.14	0.440	0.142	0.003
5.4	6.37	0.463	0.143	0.019
8.1	7.55	0.477	0.149	0.015
9.6	12.26	0.421	0.165	0.012
Mean and Standard Error of the mean of the 5 Samples				

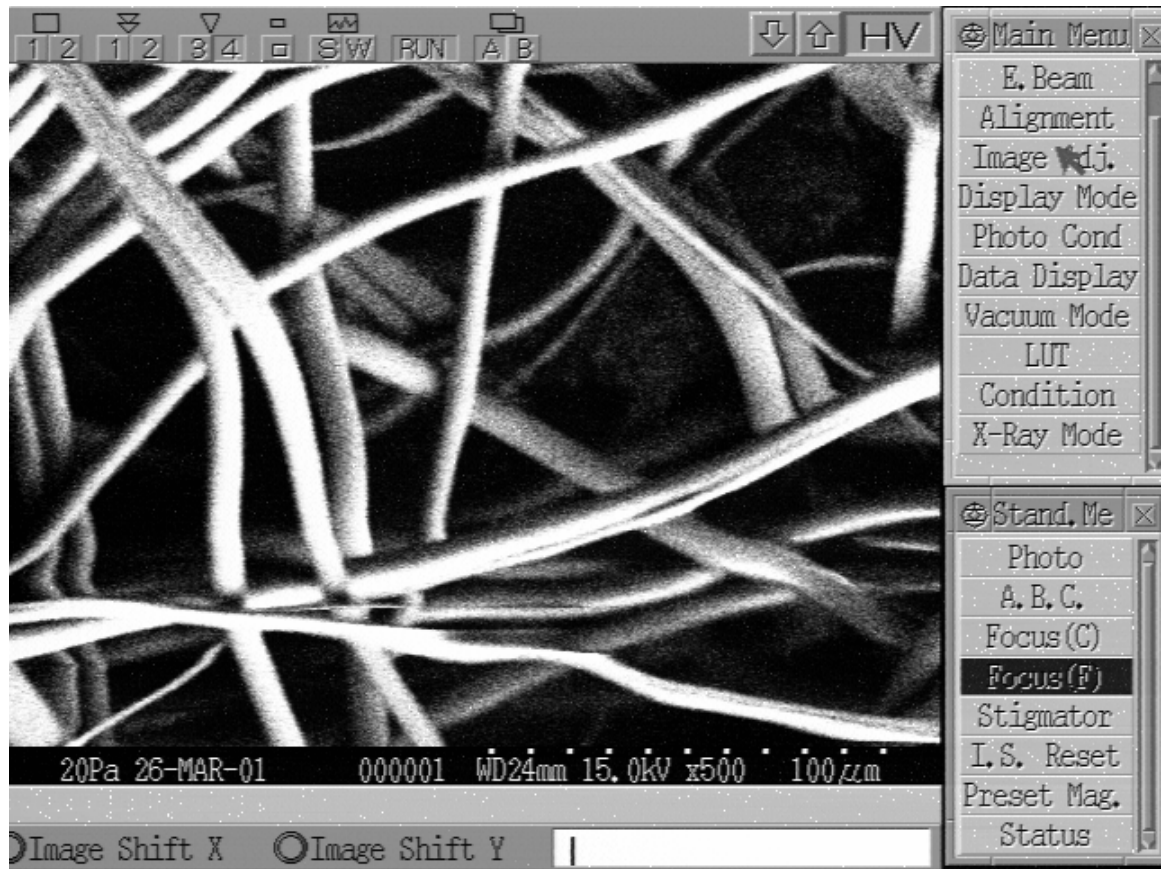


Figure 4.5: SEM Picture of the COPE web at 9.6×10^{-2} g/min/hole throughput (Take Up Speed: 8.23 m/min, Die to Collector Distance: 15.24 cm, Attenuating Air Pressure: 1.05 bar)

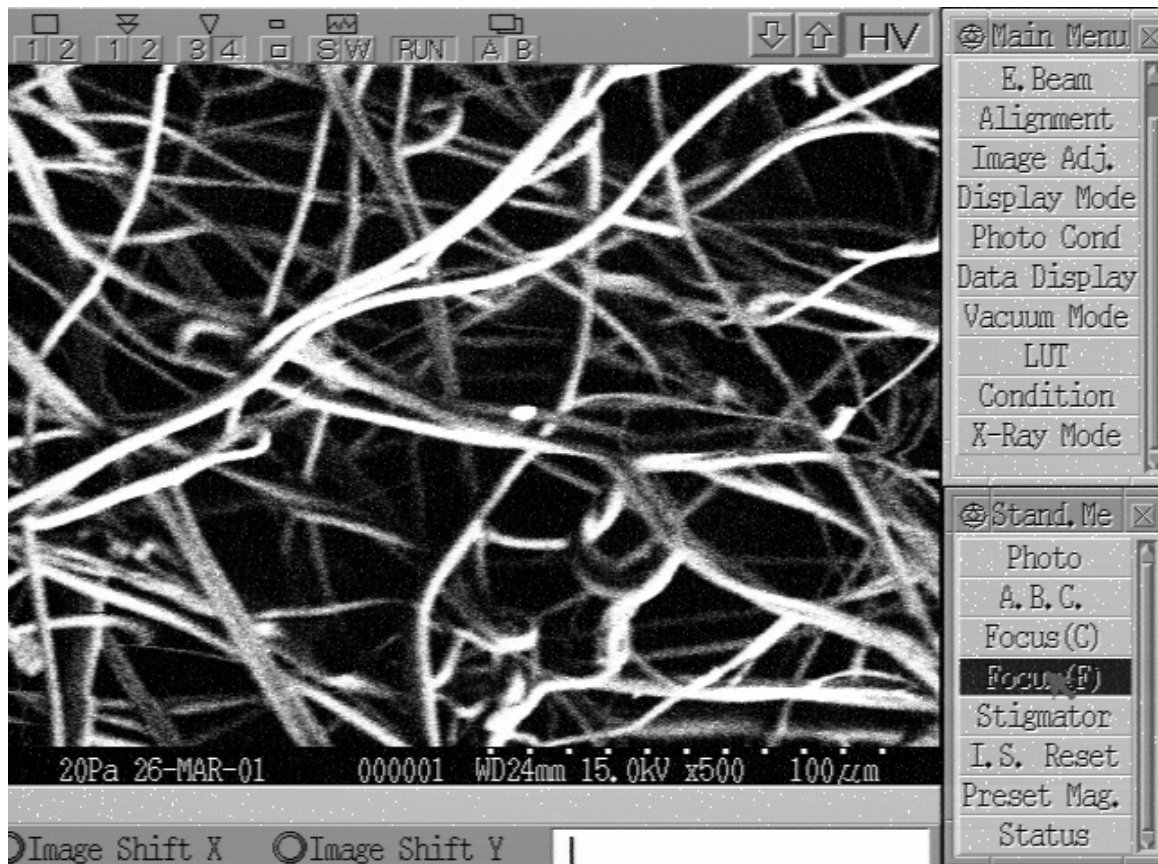


Figure 4.6: SEM Picture of the MB COPE web at 1.8×10^{-2} g/min/hole throughput (Take-Up Speed: 8.23 m/min, Die to Collector Distance: 15.24 cm, Attenuating Air Pressure: 1.05 bar)

Figure 4.7 shows the cumulative frequency for the pore size distribution at various polymer throughput levels. The cumulative frequency distribution indicates the probability of finding pores of a particular size in the web. This distribution information find applications in the design of filtration fabrics. For example, the probability that the web produced at 7.0×10^{-2} g/min/hole will be able to filter particles that are about 35 microns in diameter is 0.3 (30%). A chi-square analysis of the pore diameter frequency distribution indicates that the chi-square probability is <0.001 with a chi-square value of 1128 (df = $32 \times 5=160$, 33 pore diameters, 6 polymer throughputs). This indicates that the values in the distributions are different from each other.

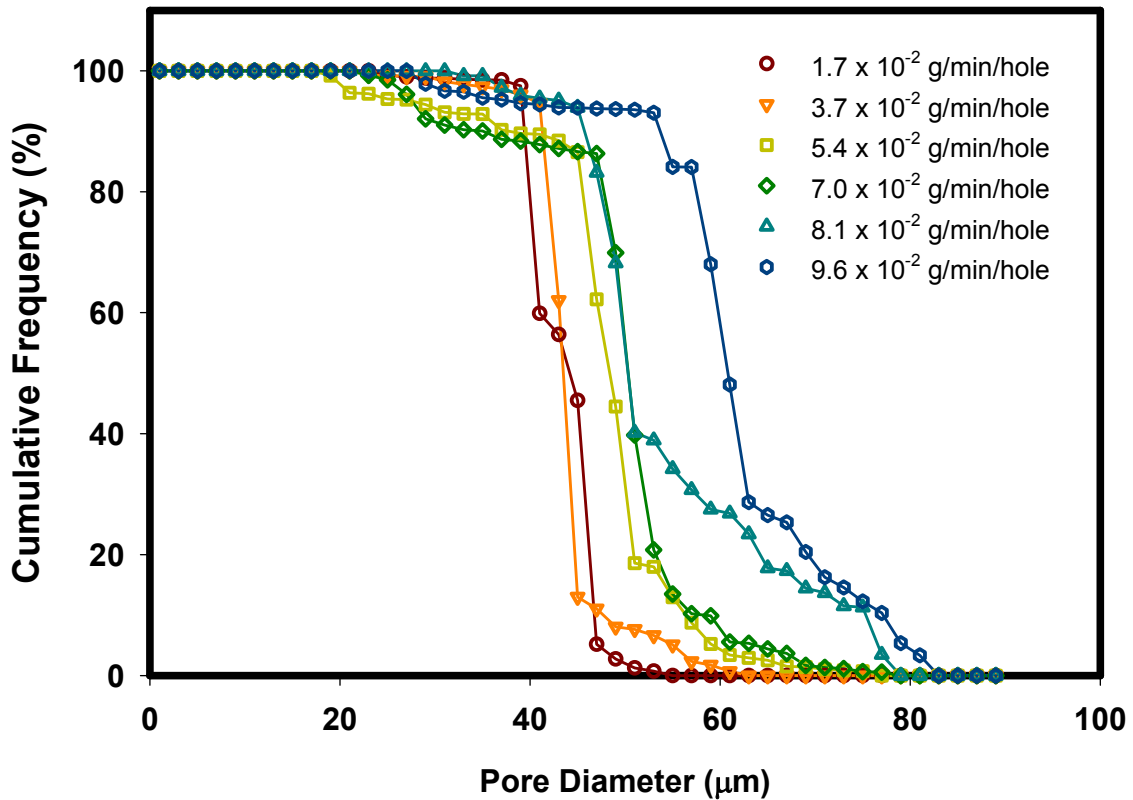


Figure 4.7: Cumulative Frequency for MB PP fabrics for variation in the Polymer Throughput (Take Up Speed: 6.09 m/min, Die to Collector Distance: 15.24 cm, Attenuating Air Pressure: 1.4 bar, Approach Angle 90 degree).

Also, the work conducted to study the effects of standard deviation of the ODF and the fiber diameter of the webs by Kim *et al* [48] on the pore size indicate, that an increase in the fiber diameter increases the anisotropy parameter in the simulated webs. The results obtained from real meltblown webs in the current study show an influence of the polymer throughput on the ODF of the fibers in the web, although the anisotropy parameter is not affected by the polymer throughput.

4.2 INFLUENCE ATTENUATING AIR PRESSURE

Figure 4.8 shows the effect of attenuating air pressure on the fiber diameter distribution. As expected and reported in literature, the fiber diameter decreases as we increase the attenuating air pressure [15]. The range of fiber diameters also decreases with increase in the air pressure [9]. With a change in attenuating air pressure from 1.05 bar (15 PSI) to 2.80 bar (40 PSI) the percentage of fiber that were below 5 microns in diameter increased from 65% to about 100%. This is a meaningful increase in the number of fibers that have very small diameters. An increase in the attenuating air pressure increases the drag force of the air and also the velocity of the fiber as it is being formed. Similar effects have been found at small variations in the attenuating air pressure. Bresee et al [38] have varied the air pressure from 0.21 bar to 0.28 bar (3 PSI to 4 PSI) on meltblown webs made on a 30-hole die. Their results show that the mean fiber diameter changes from 13 μm to 9.5 μm when close to the die and the corresponding change of 6 μm to 4 μm when the collecting distance is 30 cm. A Chi-square analysis of the diameter frequency distribution data from current research further indicates that the distributions are not the same. ($\chi^2 = 64.37$, with a probability <0.001 at $df = 6 \times 5 = 30$, 7 fiber diameter categories, 6 air pressures).

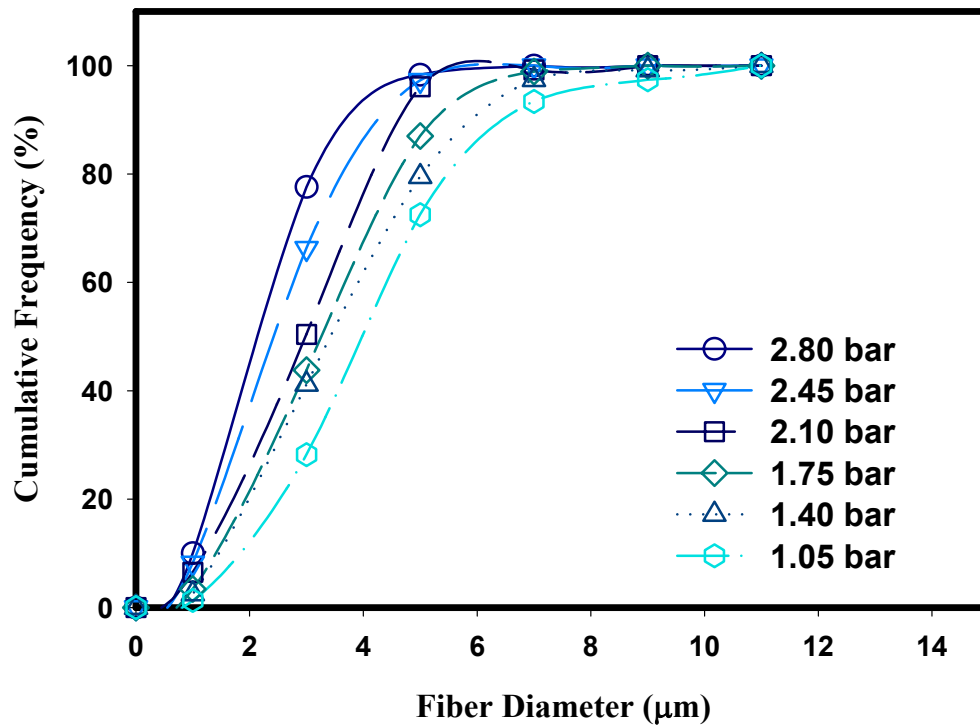


Figure 4.8: Effect of Attenuating Air Pressure on the Fiber Diameter Distribution of the COPE MB Webs (Take up speed 8.23 m/min, Throughput: 3.7×10^{-2} g/min/hole, DCD 15.24 cm)

The SEM pictures of the webs produced at 0.7 bar and 2.8 bar are given in Figure 4.9 and Figure 4.10 respectively. An increase in the attenuating air pressure results in an increase in the velocity of the forming air and hence an increase in the drag force exerted on the fiber, which causes the formation of finer fibers. Finer fibers result in a higher surface area and increased cover in the web, leading to a decrease in the size of the pores formed in the web. Figure 4.11 shows the cumulative frequency of pore size distribution for the webs formed at various attenuating air pressures.

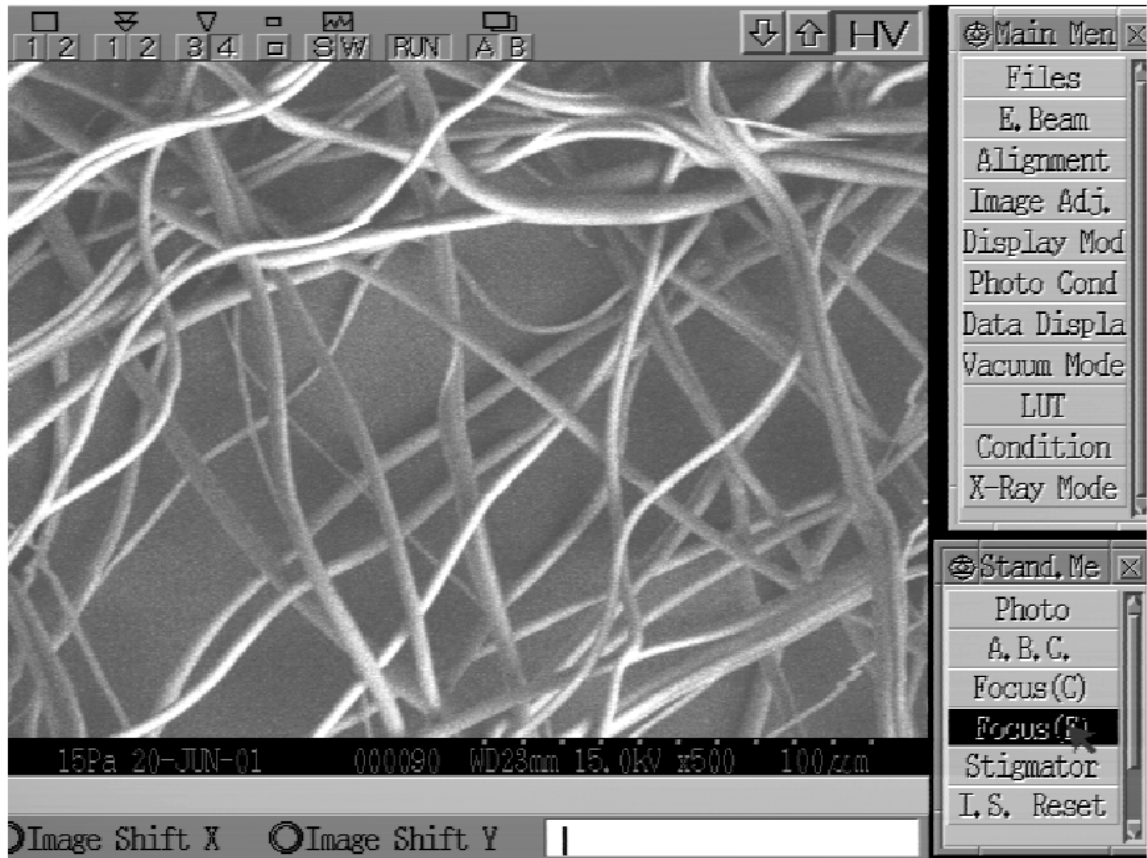


Figure 4.9: Scanning Electron Micrograph of the COPE webs produced at 0.7 bar attenuating air pressure (Take up speed 8.23 m/min, Throughput: 3.7×10^{-2} g/min/hole, DCD 15.24 cm)

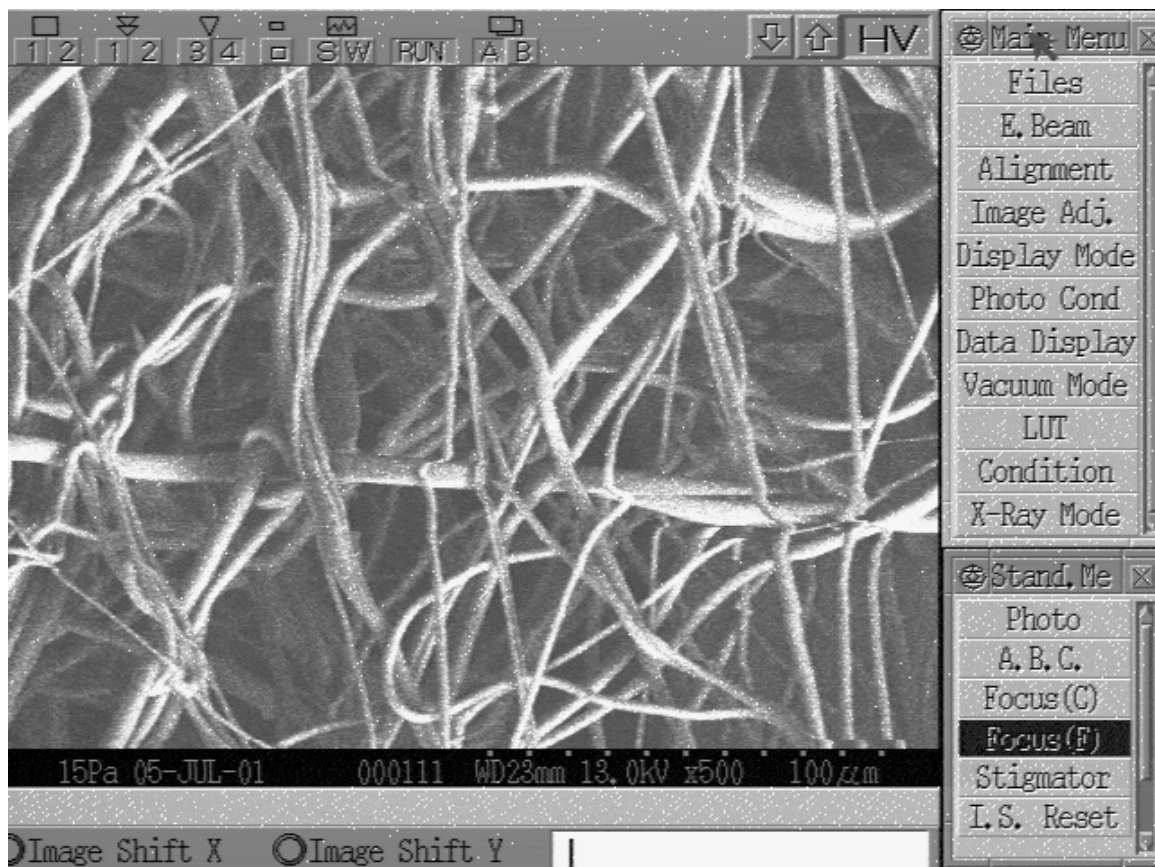


Figure 4.10: Scanning Electron Micrograph of the MB COPE webs produced at 2.8 bar attenuating air pressure (Take up speed 8.23 m/min, Throughput: 3.7×10^{-2} g/min/hole, DCD 15.24 cm)

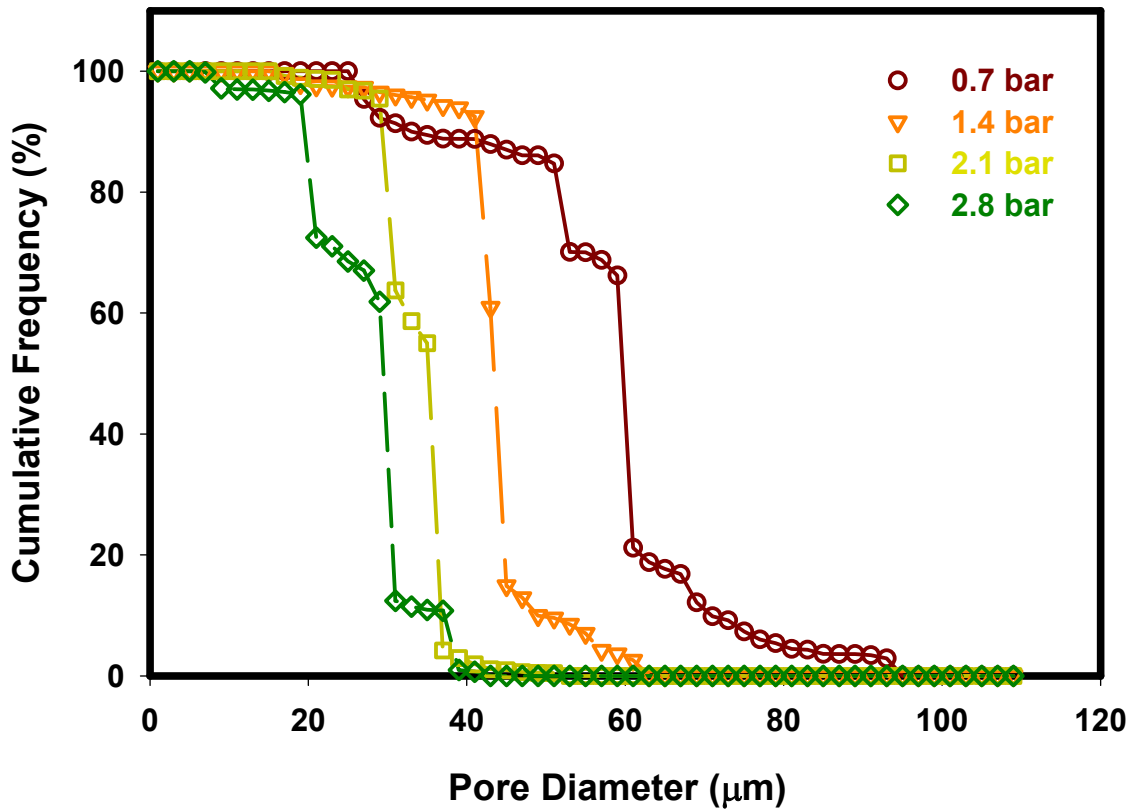


Figure 4.11: Cumulative Frequency (%) for MB PP webs for variation in attenuating air pressure (Die to Collector Distance: 15.24 cm, Take Up Speed: 6.09 m/min, Throughput: 3.7×10^{-2} g/min/hole)

The cumulative frequency indicates the percentage volume of air that flows through the sample as it is subjected to increasing air pressures. The amount of air flowing through the pore is directly related to its diameter and hence indicates the size of the particle that can pass through the sample at a given percentage. The cumulative frequency shows that a higher number of finer fibers will lead to better control on the filtration efficiency of the webs [81, 87, 88]. The average pore size for the webs at various attenuating air pressures are shown in Figure 4.12. Similar to the range of the pores seen in the cumulative frequency distribution, the average pore size of the webs decreases with increasing attenuating air pressures.

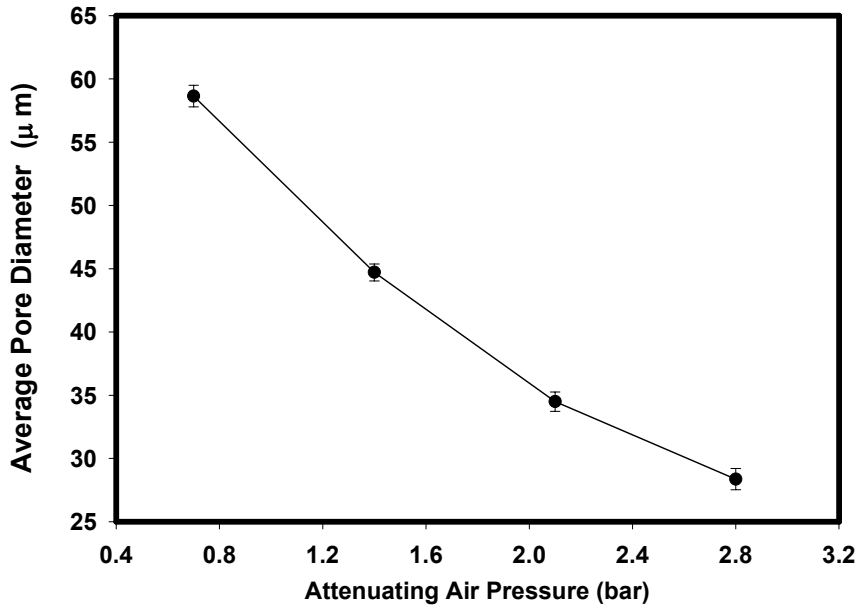


Figure 4.12: Average pore size for MB PP Webs for variation in the attenuating air pressure (Die to Collector Distance: 15 cm. Take up Speed: 6.09 m/min, Throughput: 3.7×10^{-2} g/min/hole, Basis Weight 13 g/m², with Standard Error of 5 Sample Averages).

The behavior seen in the figures can be explained by the results of the fiber diameter shown in Table 4.2. An increase in the attenuating air pressure results in an increase in the velocity of the forming air and hence an increase in the drag force exerted on the fibers, which causes the formation of finer fibers. Finer fibers result in a higher surface area and increased covering power of the structure leading to a decrease in the size of the pores formed in the web. Statistical analysis using Chi-square tests show that the cumulative distributions are significantly different from each other ($\chi^2 = 843.48$, $df = 44 \times 3 = 132$, 4 air pressures, 45 pore diameters, probability < 0.0001 , Table Value 156.57).

Table 4.2: Average Fiber Diameter at Various Attenuating Air Pressures for MB PP Webs

Air Pressure (bar)	Fiber Diameter (μm)	
	Mean	Standard Error
1.05	6.61	0.549
1.40	6.14	0.555
1.75	5.68	0.535
2.10	5.22	0.530
2.45	4.76	0.507
2.80	4.30	0.484
Mean and Standard Error of the mean of the 5 Samples		

4.3 INFLUENCE OF WEB TAKE UP SPEED

Figure 4.13 and Figure 4.14 are the ODF and anisotropy parameter of the meltblown copolyester webs at different take-up speeds of the collector with the other parameters of processing kept constant. Visually, the ODF of the webs is different for different take-up speeds. They indicate that the orientation of the fibers towards the machine direction increase with an increase in the collector take-up speed. The increase in the collector speed increases the velocity of the drum that induces a drag force on the fibers in the web to align along the direction of application of the force or the machine direction.

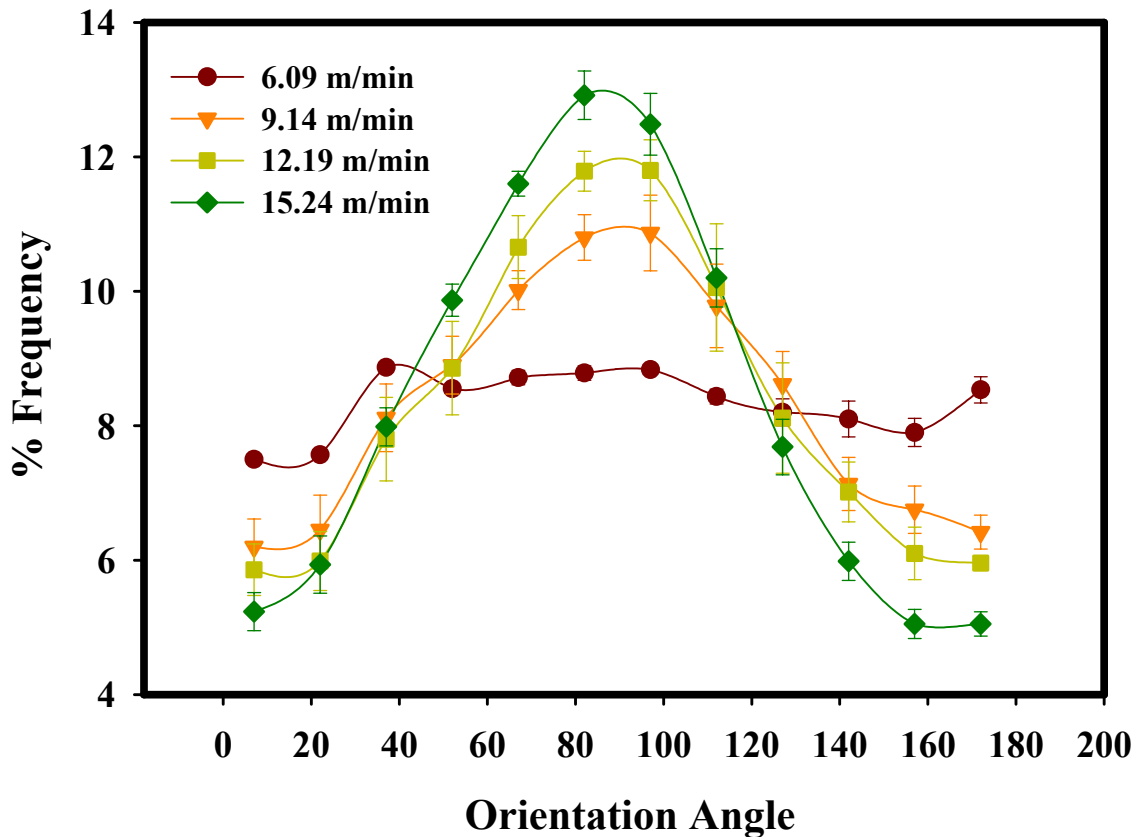


Figure 4.13: ODF for MB COPE webs at different Collector Take-up Speeds (Polymer Throughput 3.7×10^{-2} g/min/hole, Attenuating air pressure: 1.05 bar, DCD 25.4 cm, with Standard Error for 5 Samples)

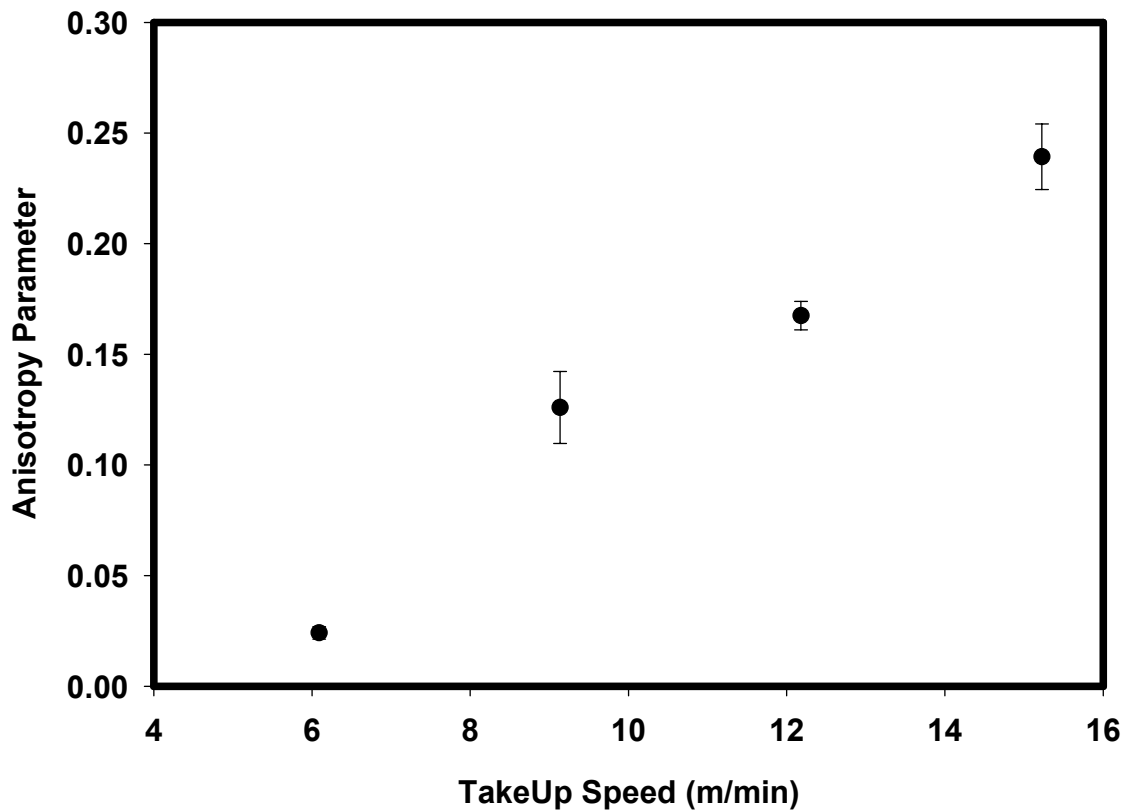


Figure 4.14: Anisotropy parameter for MB COPE webs at different Collector Take-up Speeds (Polymer Throughput 3.7×10^{-2} g/min/hole, Attenuating air pressure: 1.05 bar, DCD 25.4 cm)

Statistical analysis of the distribution of the ODF and the anisotropy parameter using analysis of variance are given in Table A-3 and Table A-4. The analysis clearly shows that the distribution of the frequency are different at each take-up speed, and the anisotropy thus exhibited by the web due to the structural arrangement of the fibers in the web is also influenced by the collector surface speed (take-up speed). Although the sum of the frequencies at each take-up speed totaled to 100, there is meaningful influence of the take-up speed on the frequency distribution of the fibers at various orientation angles. The model and each of the parameter effect (except the random sample within the treatment effect) in the model are statistically significant. Thus, the hypothesis that there is no effect on difference between the orientation distributions of fibers in the web due to the take-up speed is rejected. This is further reinforced by the F-value of anisotropy

60.54361 ($P < 0.0001$). This indicates that the anisotropy parameters are significantly affected by the take-up speed of the collecting surface.

Figure 4.15 is the cumulative distribution of fiber diameters as a function of the take up speed of the collecting surface. As the collecting speed increases the fiber diameters also decrease, the percentage of fibers with finer diameters increases with increase in the speed of the collecting surface. Increase in the surface speed of the collecting surface increases the drag force applied on the fibers as they are being collected on the surface of the collector drum. This increase in the drag attenuates the fibers and orients the fiber in the direction of the collecting surface. The scanning electron micrograph of the webs produced at 6.09 m/min and 14.33 m/min are shown in Figure 4.16 and Figure 4.17 respectively. These images show that fibers at higher take-up speeds have finer fibers while those at the lower take-up speeds have thicker fibers. The χ^2 value for these distributions is 414.68 as compared to a critical value of 26.51, indicating that the distributions are significantly different from each other. The investigation by Bresee *et al* [38] on the effect of the take-up speed on the fiber diameter only reports the mean values obtained at two different speeds (producing 1.0 and 0.36 oz/yd²).

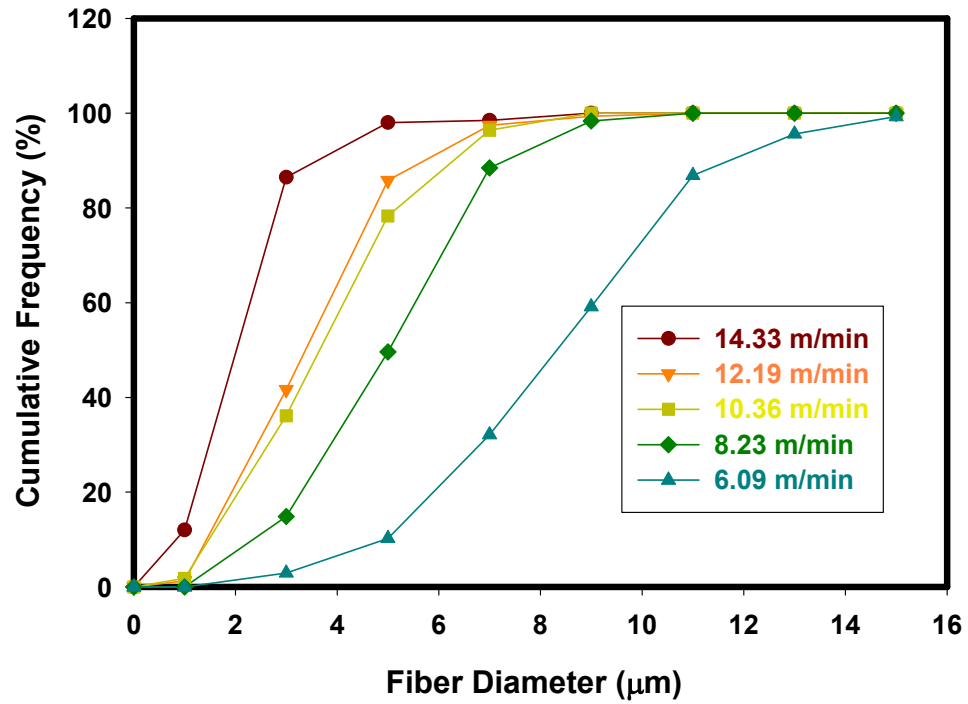


Figure 4.15: Cumulative distribution of Fiber diameter distribution for MB COPE webs as a function of the Take-up speed (Attenuating air pressure 1.05 bar, Polymer throughput 3.7×10^{-2} g/min/hole, DCD 15.24 cm).

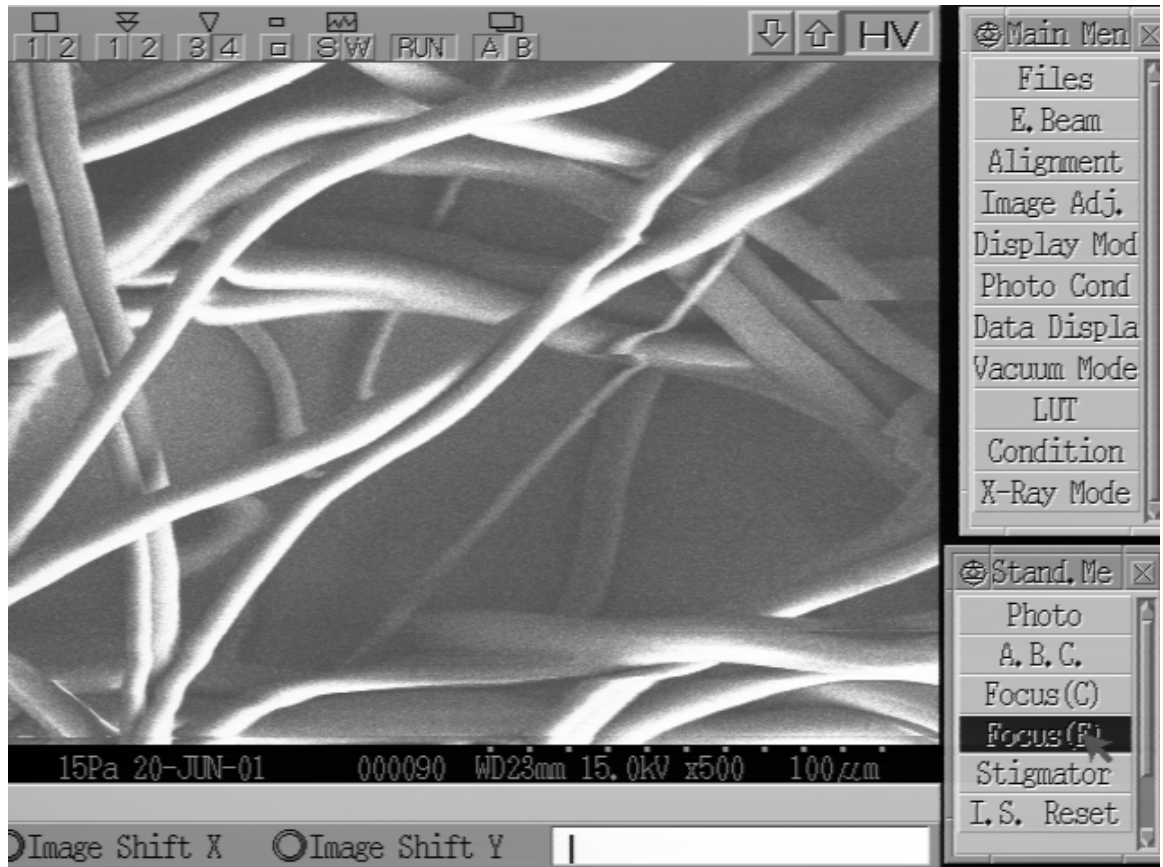


Figure 4.16: Scanning Electron micrograph of the MB COPE web at 6.09 m/min take-up speed (Attenuating air pressure 1.05 bar, Polymer throughput 3.7×10^{-2} g/min/hole, DCD 15.24 cm)

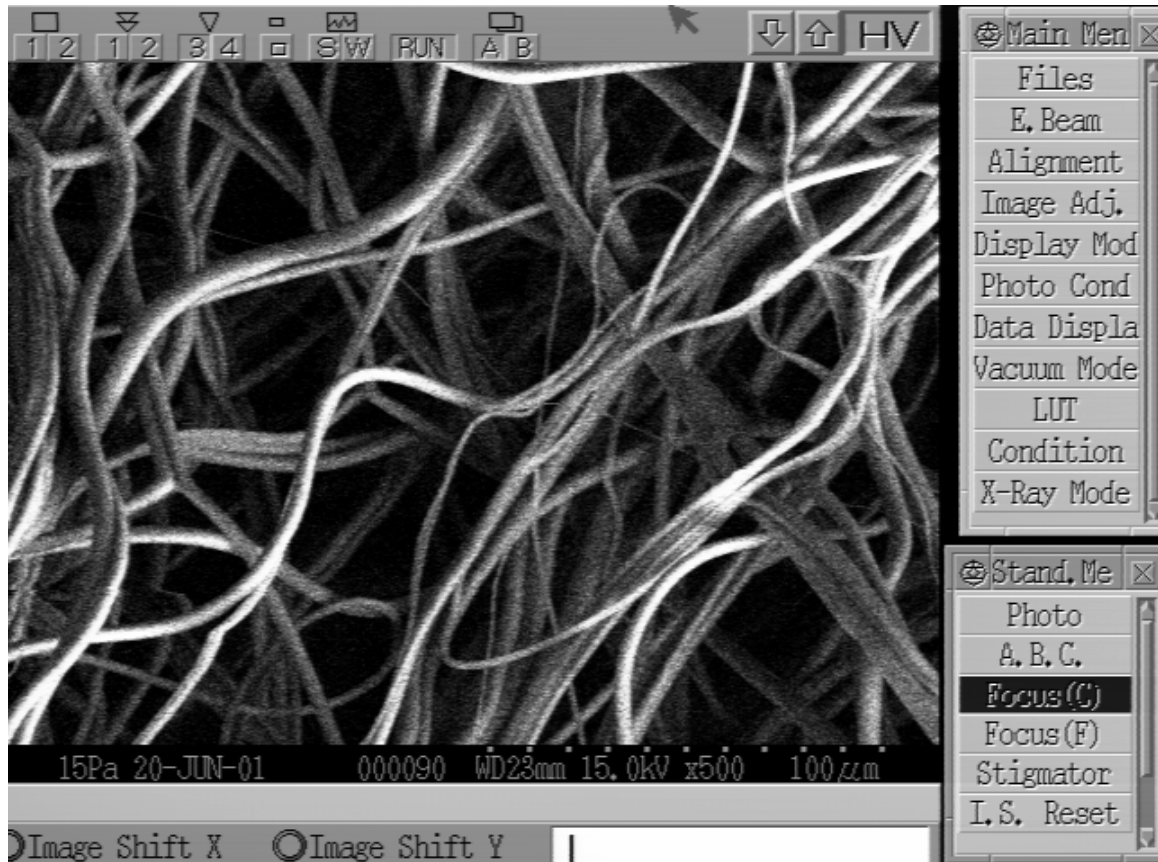


Figure 4.17: Scanning Electron micrograph of the MB COPE web at 14.33 m/min take-up speed (Attenuating air pressure 1.05 bar, Polymer throughput 3.7×10^{-2} g/min/hole, DCD 15.24 cm)

Figure 4.18 and Figure 4.19 show the behavior of the average pore size and the cumulative frequency as influenced by the process take-up speed. It can be seen from these figures that the average pore size reduces with increase in take-up speed. This is contrary to the intuitive expectation since the basis weight reduces with take-up speed (Figure 4.18). The basis weight, however, is not the only structure parameter that is influenced by the take-up speed. The pore size is influenced by the two structural parameters, fiber diameter and fiber orientation. The results of the fiber diameter and orientation, for the MB webs produced using PP resin, are depicted in Table 4.3. These results, along with the data depicted in Figures 4.15, 4.16 and 4.17, indicate that the fiber diameter increases and fiber orientation in MD decreases with reduction in take-up speed. On the other hand pore size increases with an increase in fiber diameter and reduction in fiber orientation along MD. Our results of the pore size trend with take-up speed suggest that the effect of the fiber orientation and fiber diameter is more dominant than the effect

of basis weight. As more fibers are oriented in a particular direction, as against a random orientation, the pore size will decrease. To support this, SEM images were taken for the fabrics produced at the extreme take-up speeds. Figure 4.16 and Figure 4.17 show the structures of the fabrics processed at 6.09 m/min and 14.33 m/min take-up speed. It is obvious from the images that the pore size of the fabric produced at low speed is larger than the pore size of the fabric produced at high speed. Further, the χ^2 value (923.64 with a P-value <0.001, as against a tabulated value of 69.13) for the analysis shows that the cumulative distribution of the pore diameters is significantly affected by the web take-up speed.

Table 4.3: Average Diameter of Fibers and Anisotropy Parameter of PP MB webs at various Take-up speeds

Take-up Speed (m/min)	Fiber Diameter (μm)		Anisotropy Parameter	
	Average	Standard Error	Average	Standard Error
6.09	6.14	0.458	0.142	0.0028
9.14	5.30	0.441	0.156	0.0163
12.19	4.49	0.435	0.165	0.0064
15.24	3.01	0.365	0.212	0.0148
Mean and Standard Error of the mean of the 5 Samples				

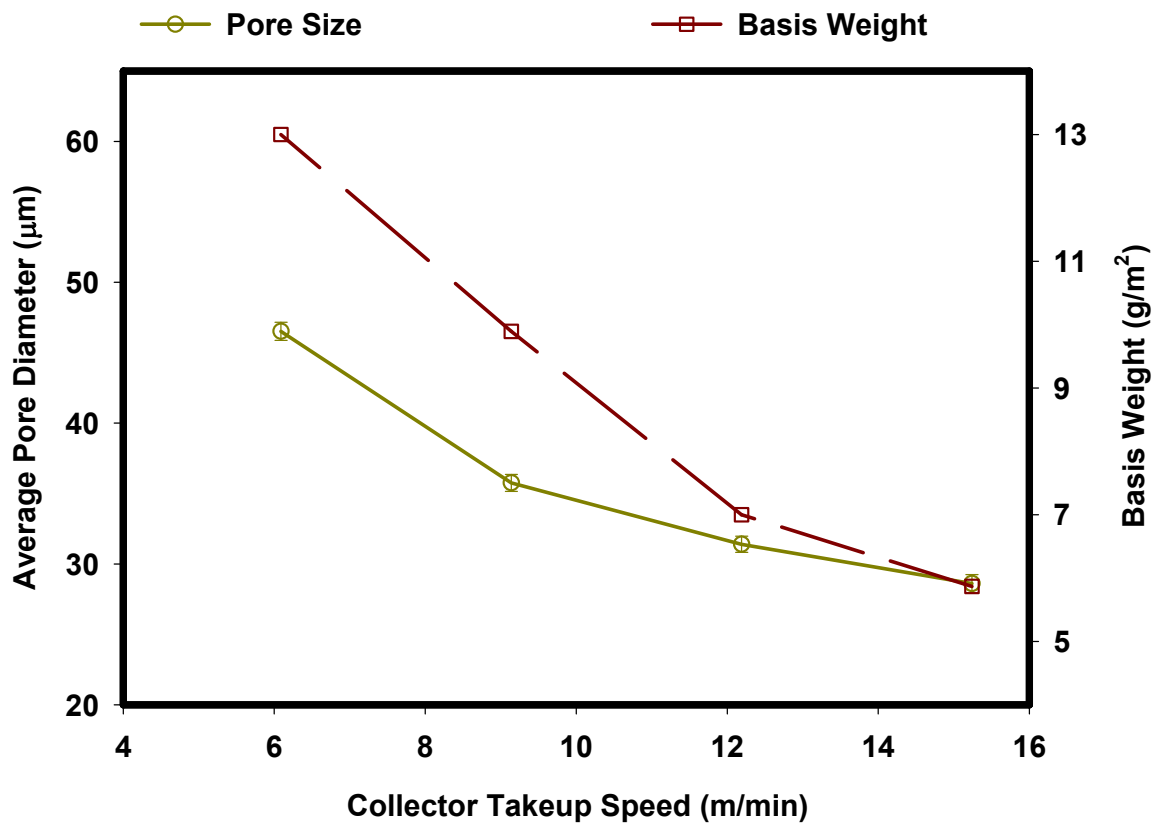


Figure 4.18: Average Pore Size and Basis Weight for MB PP webs for variation in the collecting drum Take-up Speed (Die to Collector Distance: 15.24 cm, Attenuating Air Pressure: 1.4 bar, Throughput: 3.7×10^{-2} g/min/hole, with Standard Error for 5 Samples).

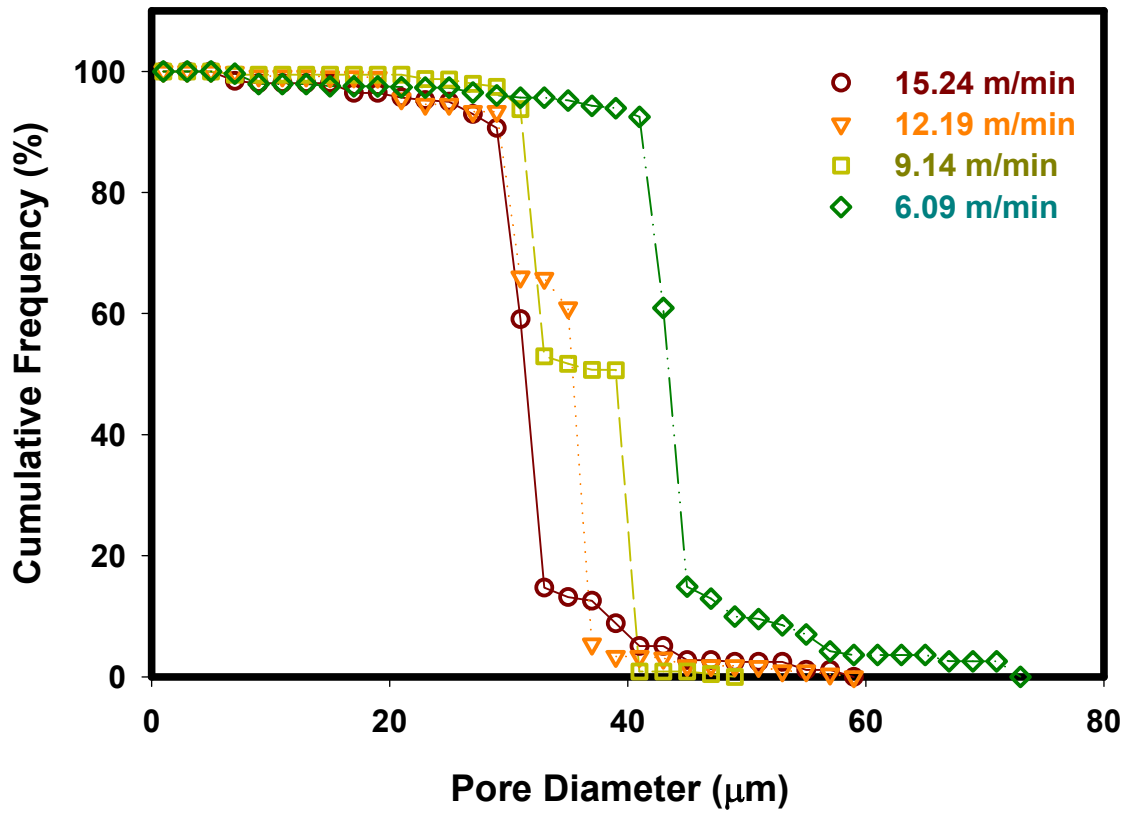


Figure 4.19: Cumulative Flow Frequency for MB PP Webs for variation in the Web Take up Speed (Throughput : 3.7×10^{-2} g/min/hole, Die to Collector Distance : 15.24 cm, Attenuating Air Pressure: 1.4 bar).

4.4 INFLUENCE OF DIE TO COLLECTOR DISTANCE

Figure 4.20 and Figure 4.21 show the influence of DCD on the ODF and the anisotropy parameter for webs formed with the other processing parameters that were kept constant. Within the current range of experiments the anisotropy parameter exhibits a linear relationship with DCD. As the collecting distance decreases from 35 cm to 5 cm, the fibers are more oriented in the machine direction. When the distance between the collector and the die increases the attenuating air loses its force to align the fibers in the direction of its flow and hence has smaller influence on the orientation of the fibers in the web [98]. The fibers have greater freedom of movement and orient themselves randomly. At short distances the attenuating air has a higher velocity and orients the fiber in the direction of the flow of the air [99]. The statistical analysis of ODF and anisotropy parameter shows that DCD has a significant influence on the orientation of the fibers in the web (TableA-5 and TableA-6).

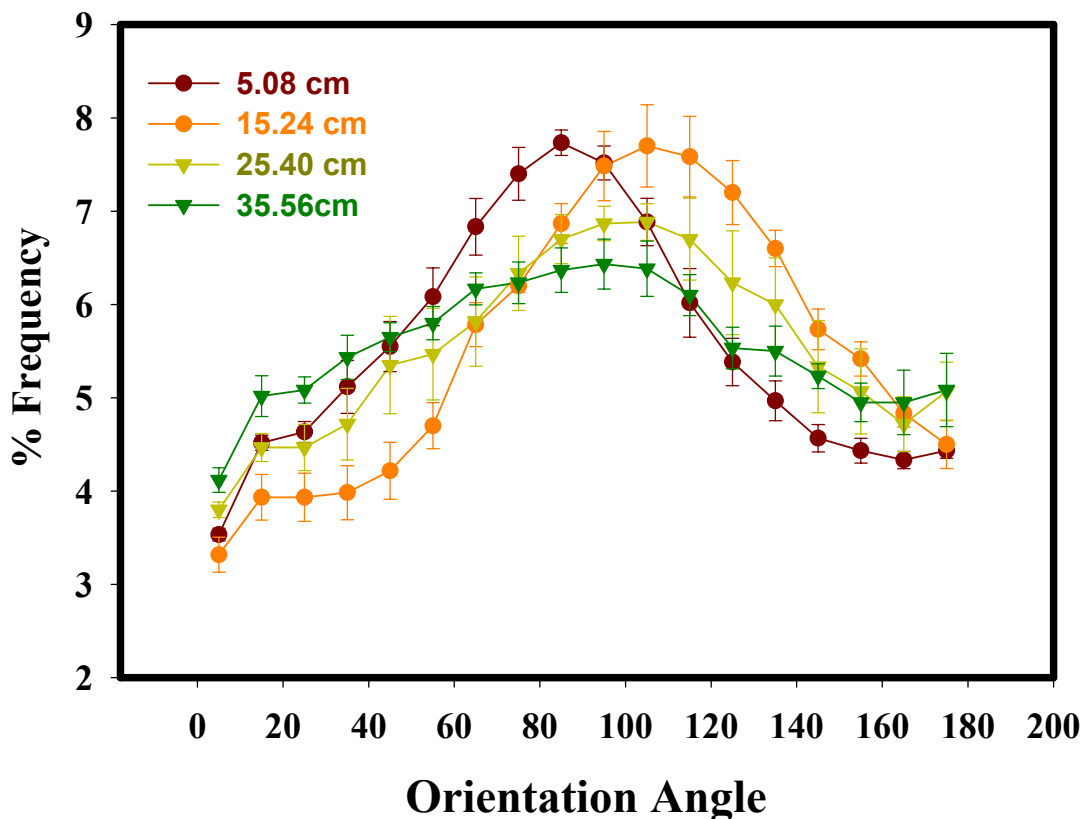


Figure 4.20: Influence of DCD on ODF of COPE MB Webs (Attenuating air pressure 1.05 bar, take-up speed 8.23 m/min, Throughput 3.7×10^{-2} g/min/hole)

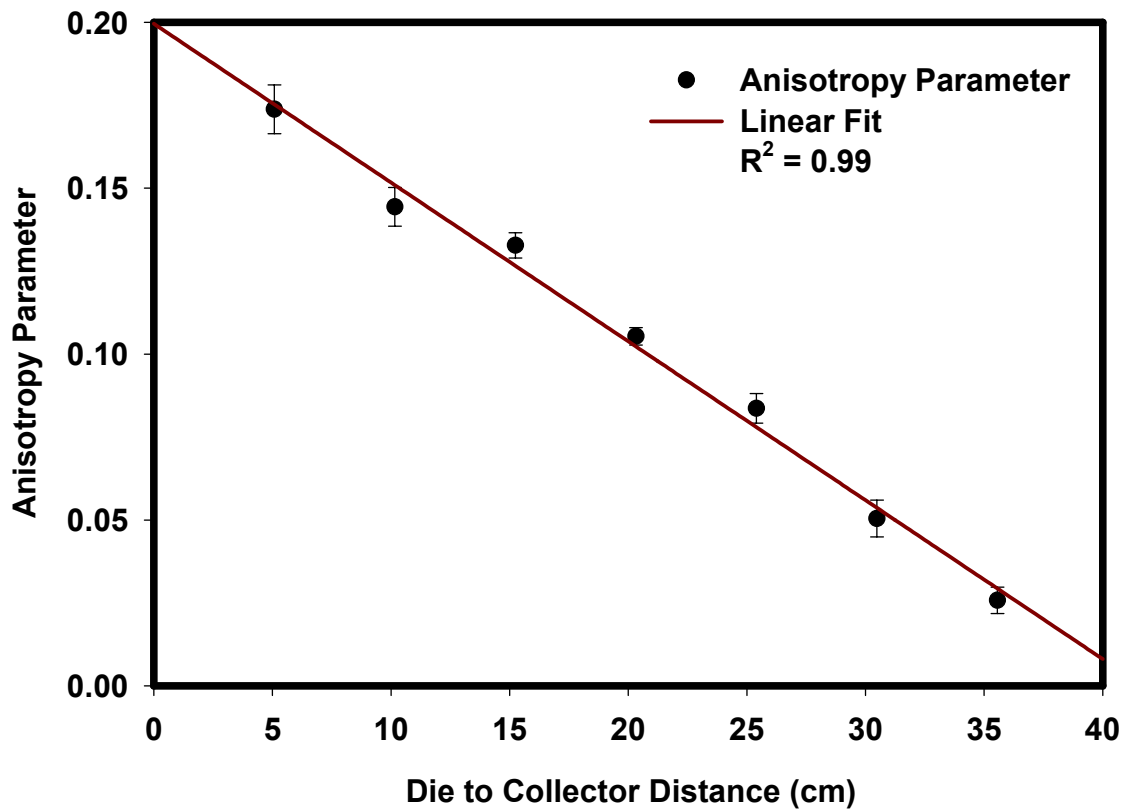


Figure 4.21: Anisotropy Parameter for COPE MB Webs at a various DCD (Attenuating air pressure 1.05 bar, take-up speed 8.23 m/min, Throughput 3.7×10^{-2} g/min/hole, with Standard Error of 5 Samples)

Figure 4.22 gives the diameter distribution of the fibers in the web formed at different DCD. The average diameter of the fiber decreases as the DCD increases, implying that the fibers are not fully attenuated even at large distances. A chi-square estimate ($\chi^2 - 126.71$ with a P-value < 0.001 at an α of 0.05 and $df = 18$, 7 diameter groups and 4 distances) of the curves indicates that the distribution of these fiber diameters is not the same. Experimental results from research conducted by Bresee *et al* [38], show that although the major attenuation is completed within 5.08 cm from the die, the fiber undergoes attenuation even at distances of 35 cm and beyond. The drag forces and the elongational forces acting on the fibers near the die and the collector surface influence the attenuation of the fibers in the web. Since the attenuating air in the region close to the die loses its temperature rapidly, the fibers would be crystallized close to the die. The assumption that the fibers would have completely crystallized and will not attenuate

beyond a few centimeters from the die is discounted based on the current research and also corroborated by research conducted by Bresee *et al* [38].

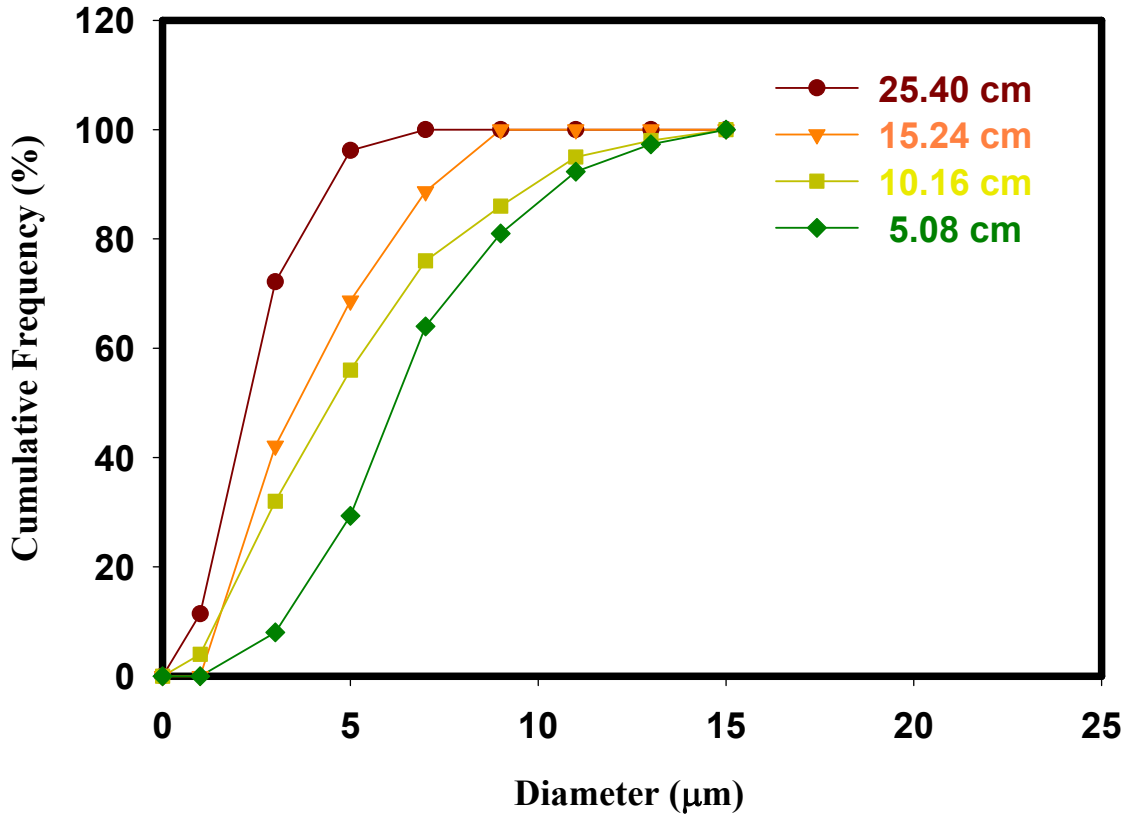


Figure 4.22: Fiber Diameter Distribution for COPE MB Webs at a various DCD (Attenuating air pressure 1.05 bar, take-up speed 8.23 m/min, Throughput 3.7×10^{-2} g/min/hole)

Figure 4.23 shows the cumulative frequency distribution of the pore diameter of PP meltblown fibers formed due to varying die to collector distances. The average diameter of the pore initially decreases with increase in the distance. The average diameter of the pore on a web collected at a distance of 15.24 cm from the die is $46.74 \mu\text{m}$ (Figure 4.24). Further increase in the die to collector distance, beyond the 15.24 cm, increases average pore size.

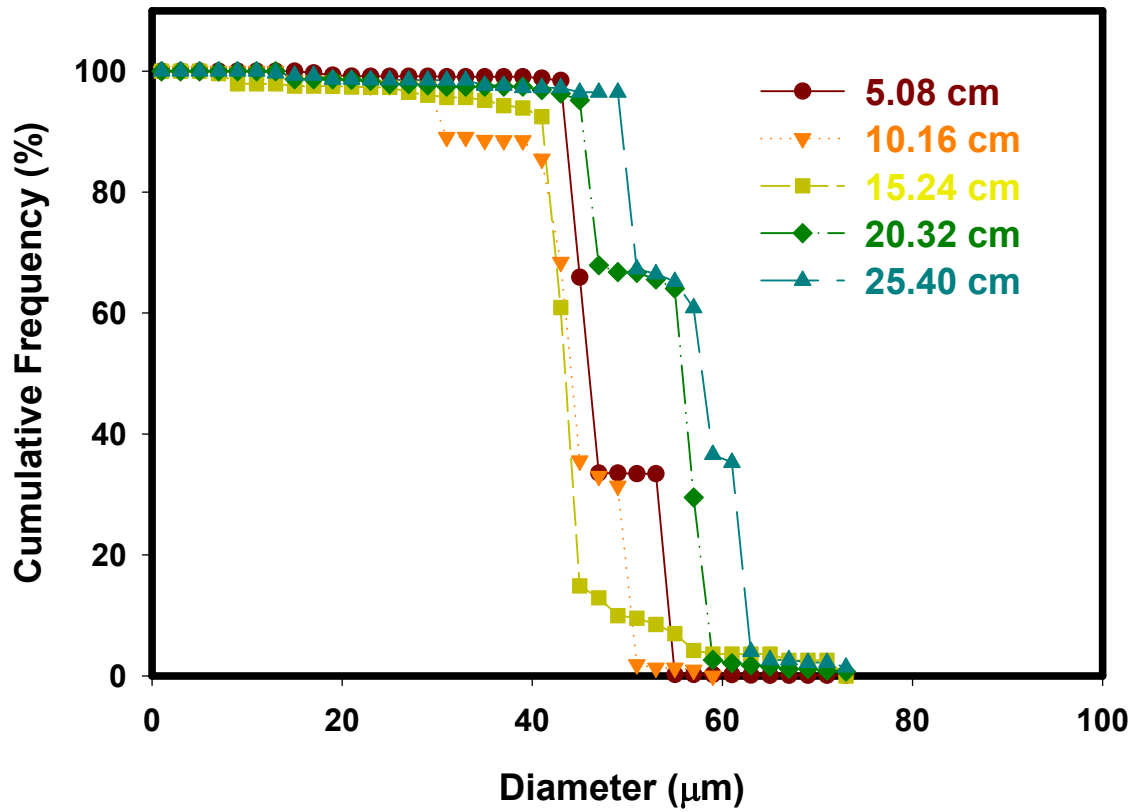


Figure 4.23: Pore Size Distribution for MB PP Fabrics at different Die to Collector Distances (Throughput: 3.7×10^{-2} g/min/hole, Attenuating Air Pressure: 1.4 bar, Take-up Speed: 6.09 m/min)

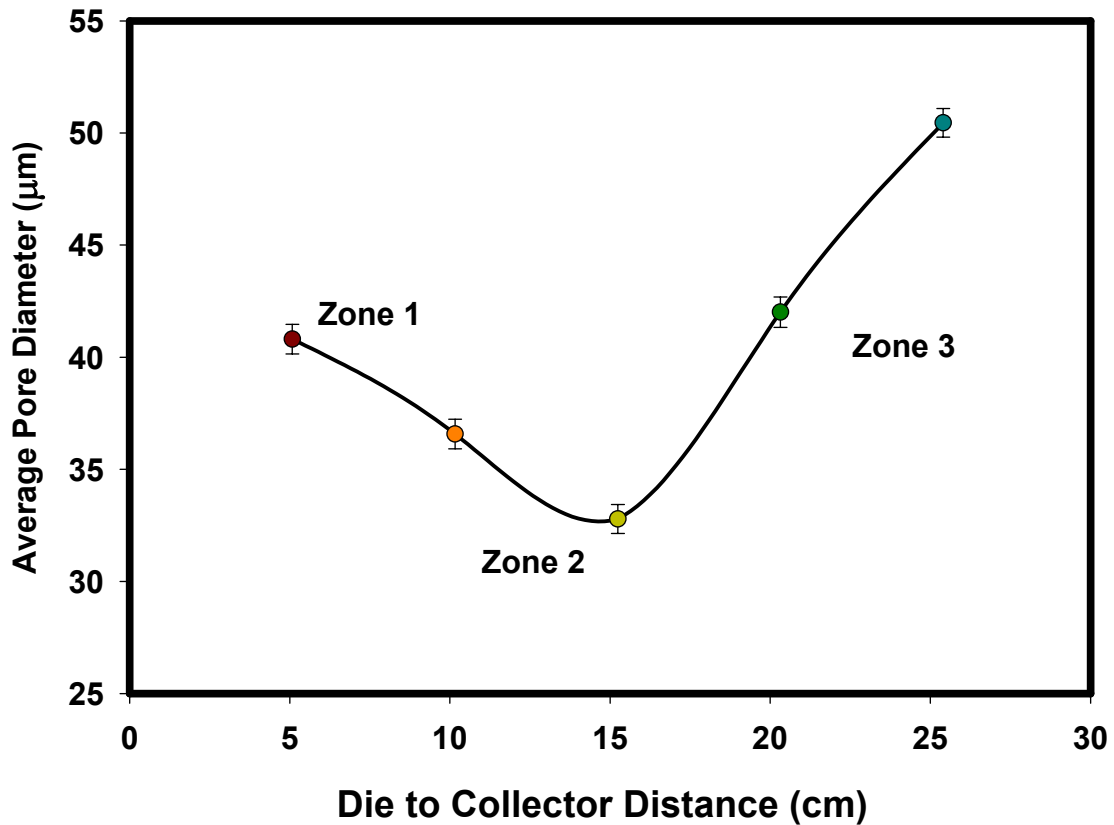


Figure 4.24: Average Pore Diameter Distribution for MB PP Webs with Varying Collecting Distances (Throughput: 3.7×10^{-2} g/min/hole, Attenuating Air Pressure: 1.4 bar, Take-up Speed: 6.09 m/min, Standard Error of 5 Samples)

It is important to investigate the initial decrease in the pore diameter. As discussed by Shambaugh and others [76, 99], the space between the die and the collector of a meltblown system can be divided into three zones, namely Zone A, Zone B and Zone C. Zone A is close to the die and the fibers are oriented in the direction parallel to the machine direction and fiber motion is in the same direction. The temperature and the velocity of the attenuating air in this zone is decaying, but is higher than temperature required to attenuate the polymer and hence the attenuation of the fiber is not complete [100, 101, 102]. The web formed when the collector is placed in this region will not have fully attenuated fibers. This will lead to shots and fibers with larger diameter and hence the pore diameter will be larger [103, 104, 125]. The average diameter of the fiber decreases when the DCD changes from lower values to 15.24 cm (Table 4.4). These

results of fiber diameter as impacted by the DCD are in agreement with previous postulation above [102, 103, 103].

Table 4.4: Diameter of Fibers and Anisotropy Parameter of MB PP webs at various DCD

DCD (cm)	Fiber Diameter (μm)		Anisotropy Parameter	
	Average	Standard Error	Average	Standard Error
5.08	9.16	0.449299	0.171	0.007336
10.16	7.97	0.407556	0.149	0.005849
15.24	6.14	0.43865	0.142	0.003798
20.32	6.09	0.478138	0.106	0.00262
25.40	6.03	0.477992	0.074	0.004454
Average and Standard Error of the mean of the 5 Samples				

Beyond the critical distance, the fibers are fully formed and any change that is seen in the pore size is due to the changes in the arrangement of fibers in the web. The behavior of the fiber orientation with DCD explains the behavior of pore size with DCD since pore size increases with decrease in fiber orientation in MD. As is seen in the study of ODF, beyond the 15.24 cm, the fibers are more randomly oriented and this leads to the formation of larger pores. The pore size decreases as fiber orientation increases in a particular direction. This is because the number of crossover points of a given fiber decreases with increase in fiber orientation, which increases the covering power of the structure. Scanning electron micrographs of the webs at 15.24 cm and 35.46 cm are shown in Figure 4.25 and Figure 4.26. Further, shorter DCD is known to produce smaller pore sizes as compared to larger DCD's [5].

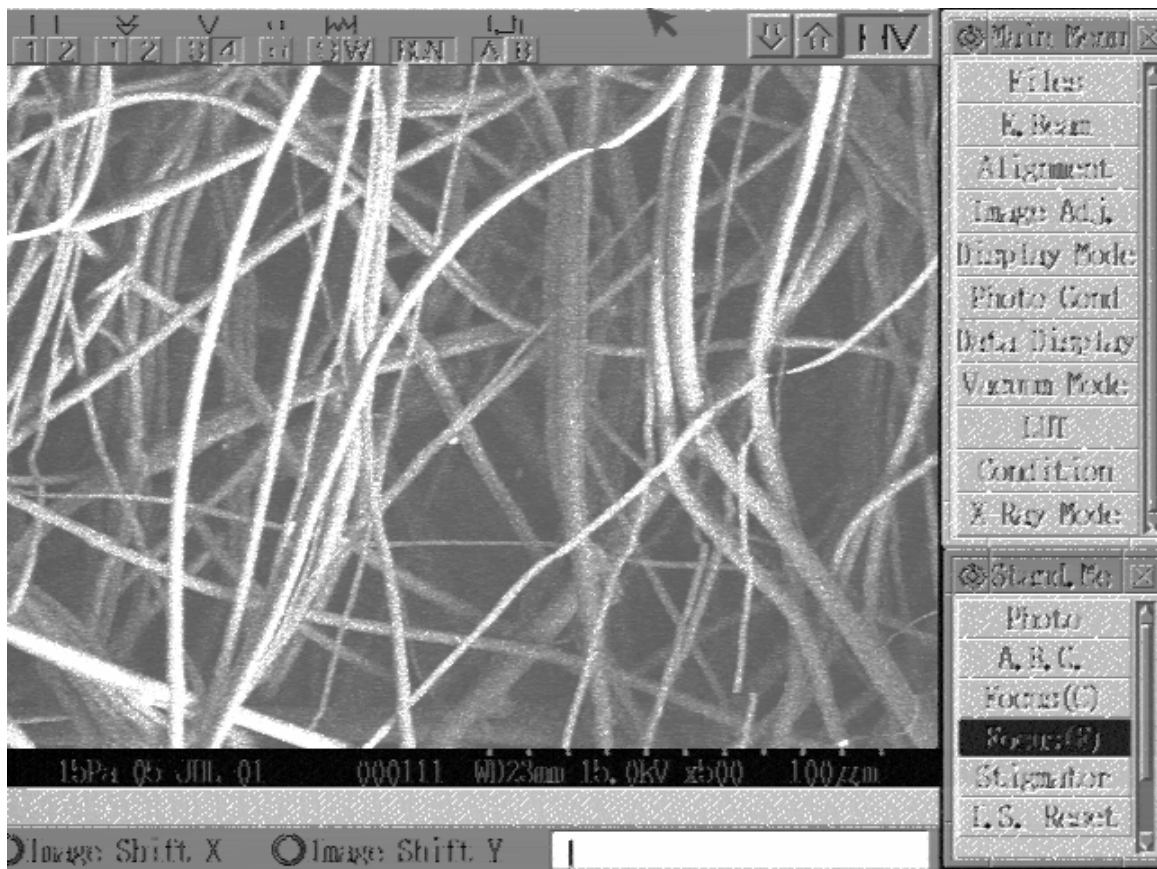


Figure 4.25: Scanning Electron Micrograph of the COPE MB web at 15.24 cm DCD (Attenuating air pressure: 1.05 bar, Throughput: 3.7×10^{-2} g/min/hole, Take-up Speed 8.23 m/min)

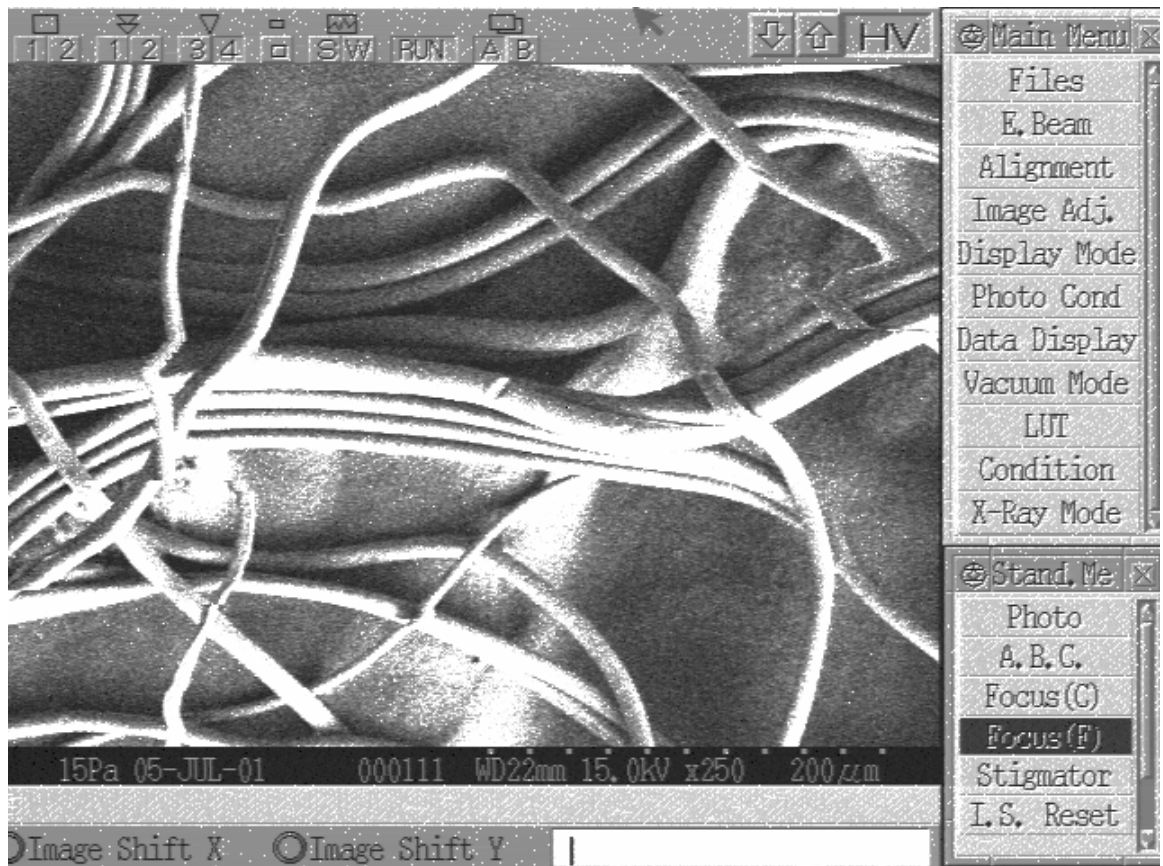


Figure 4.26: Scanning Electron Micrograph of the COPE MB web at 35.46 cm DCD (Attenuating air pressure: 1.05 bar, Throughput: 3.7×10^{-2} g/min/hole, Take-up Speed 8.23 m/min)

4.5 INFLUENCE OF FIBER STREAM APPROACH ANGLE

4.5.1.1 Influence of Fiber Stream Approach Angle on ODF

As explained earlier, fiber stream approach angle is the angle between the plane containing the fiber stream and the tangent at the point of impact on the collecting surface. At 90 degree approach angle, the fiber stream is normal to the collecting surface, while at 0 degree approach angle the fiber will blow past the collecting surfaces as the fiber stream will be parallel to the tangent at the collecting surface.

Figure 4.27 shows the ODF of the webs at different approach angles. The statistical analysis for the ODF is given in Table A-7. The relative number of fibers oriented in the machine direction of the web increases with decrease in the approach angle. As the approach angle increases, the fibers are more randomly arranged in the web. At lower approach angles, a section of the fibers will have an additional length in the path traveled by the fibers before being laid on the collector surface. This will force those fibers to be more tangential to the collecting surface and lay the fiber in the direction of the velocity vector at the point of impingement on the collecting surface. At a curvature of 4.71 m^{-1} , the minimum approach angle that was feasible was 37.91 degrees. The ODF and anisotropy parameter for the webs at different approach angles follows the same trend as exhibited by structures formed on a drum as investigated by Farer [9]. Further analysis of the ODF data using analysis of variance indicate that the approach angle is a significant process parameter influencing the ODF of the fibers in the web (Table A-8).

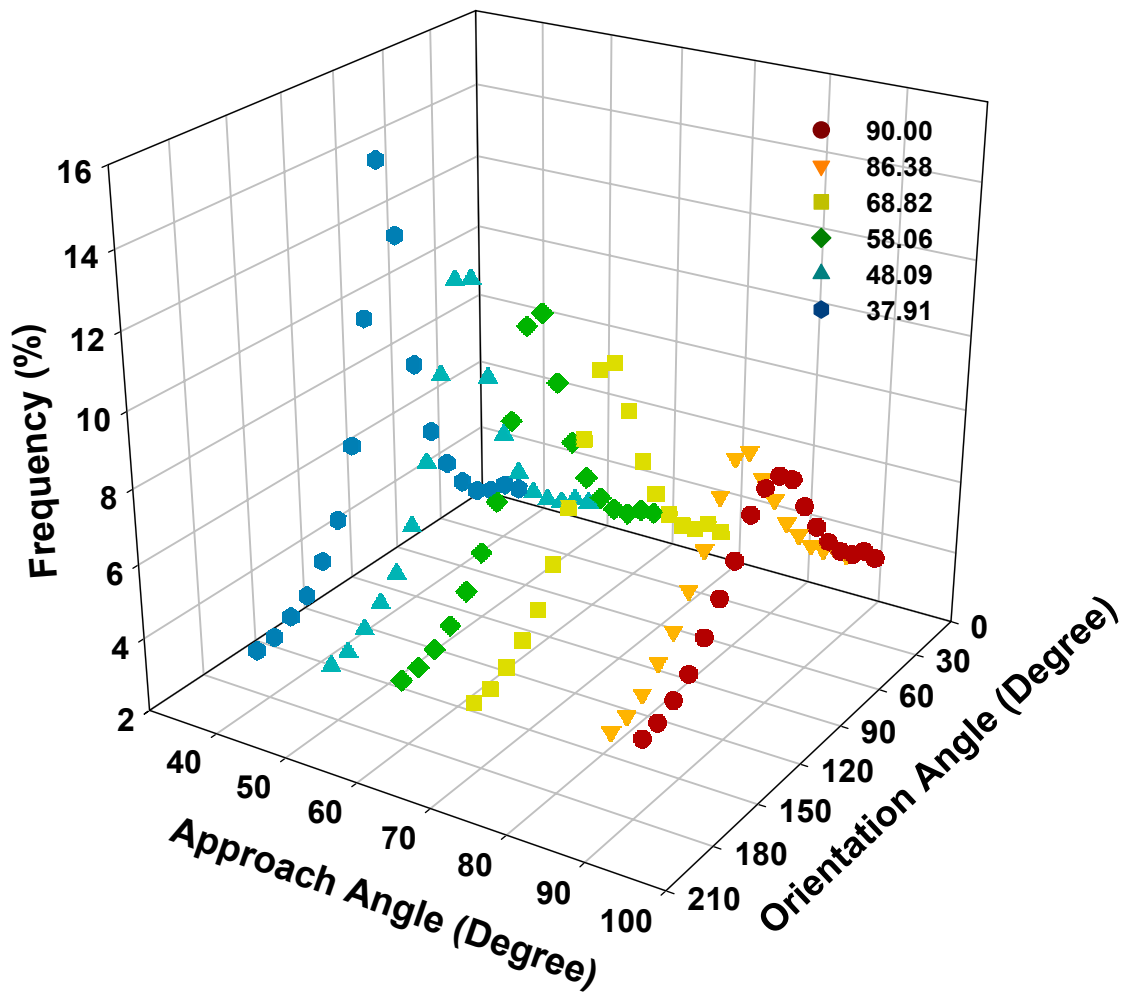


Figure 4.27: ODF for PP MB 3D webs formed at different Approach Angles (Throughput: 3.7×10^{-2} g/min/hole, Attenuating Air Pressure:1.4 bar, Take-up Speed: 6.09 m/min, Curvature 4.71 m^{-1})

Figure 4.28 shows the comparative data for anisotropy data for webs formed at different approach angle in this study as against the data evaluated from the ODF data obtained by Farer. They reveal that the trends exhibited by both sets of web are the same while that in the case of the webs at higher curvature exhibit a higher anisotropy as compared to data of 2D structure. Within the curvatures investigated, the data reveals a decrease in the anisotropy when the webs are formed at 90 degrees as compared to lower approach angles. TableA-8 gives the statistical analysis of the data for a hypothesis that the anisotropy parameter for all the webs produced at different approach angles is the same.

Since, the F value of 84.06 ($P < 0.001$) is greater than the critical value of 2.62 ($\alpha = 0.05$), it is clear that the null hypothesis is to be rejected.

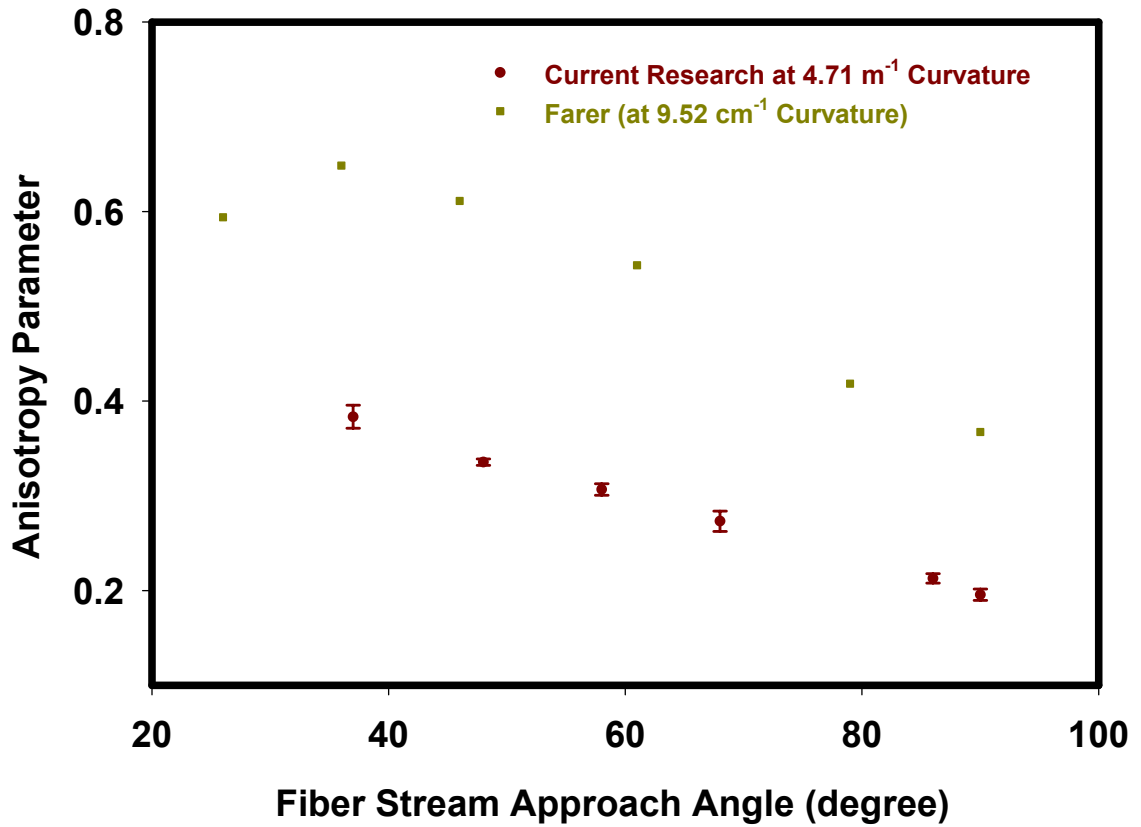


Figure 4.28: Comparative Anisotropy parameter for PP MB webs (Throughput: 3.7×10^{-2} g/min/hole, Attenuating Air Pressure: 1.4 bar, Take-up Speed: 6.09 m/min, Curvature 4.71 m^{-1} , Standard Error of 5 Samples)

4.5.1.2 Influence of Approach Angle on the Fiber Diameter Distribution and Pore Size Distribution.

Figure 4.29 gives the fiber diameter distribution of the webs at various approach angles. At lower approach angles the fiber diameters are smaller as more and more fibers are laid parallel to the machine direction. The fibers at lower approach angles will have to travel the additional distance to reach the surface of the collector. Also the fibers are laid parallel to the machine direction as the approach angle decreases. The fibers are subjected to a larger drag force that is applied on them causing the attenuation of the fibers [38]. Figure 4.30 shows the variation in the average pore size in the webs formed at different approach angles on the webs collected at curvature of 4.71 m^{-1} . The pore size increases by approximately 25 % when the approach angle changes from 37 to 90 degrees. At low approach angles, the fibers are more oriented in the machine direction, decreasing the pore size. Figure 4.31 gives the distribution of the pore sizes at different approach angles. As the approach angle increases the distribution is shifts towards larger pore sizes.

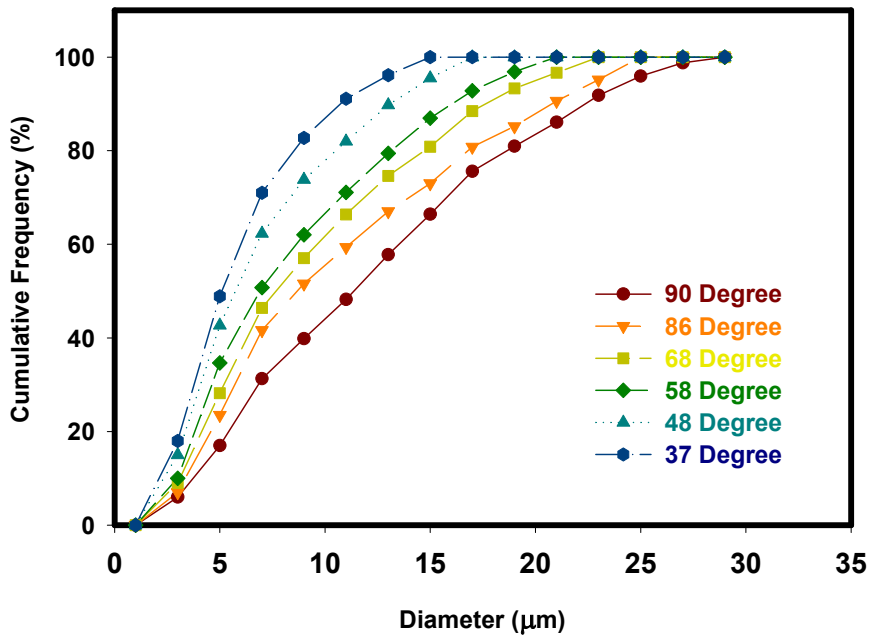


Figure 4.29: Fiber Diameter Distribution of the MB PP web 3D webs formed at varying approach angles (Throughput: $3.7 \times 10^{-2} \text{ g/min/hole}$, Attenuating Air Pressure: 1.4 bar, Take-up Speed: 6.09 m/min, Curvature 4.71 m^{-1})

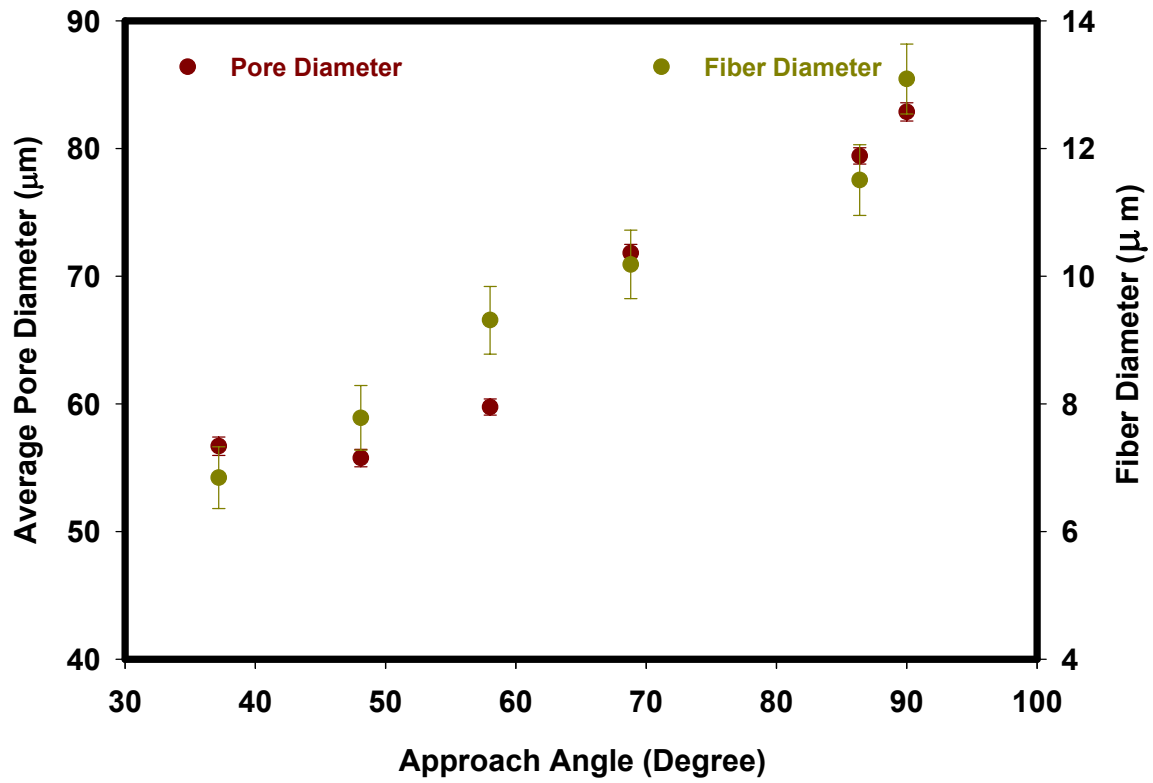


Figure 4.30: Average pore diameter and fiber diameter of PP 3D MB webs formed at varying approach angles (Throughput: 3.7×10^{-2} g/min/hole, Attenuating Air Pressure: 1.4 bar, Take-up Speed: 6.09 m/min, Curvature 4.71 m^{-1} , Standard Error 5 Samples)

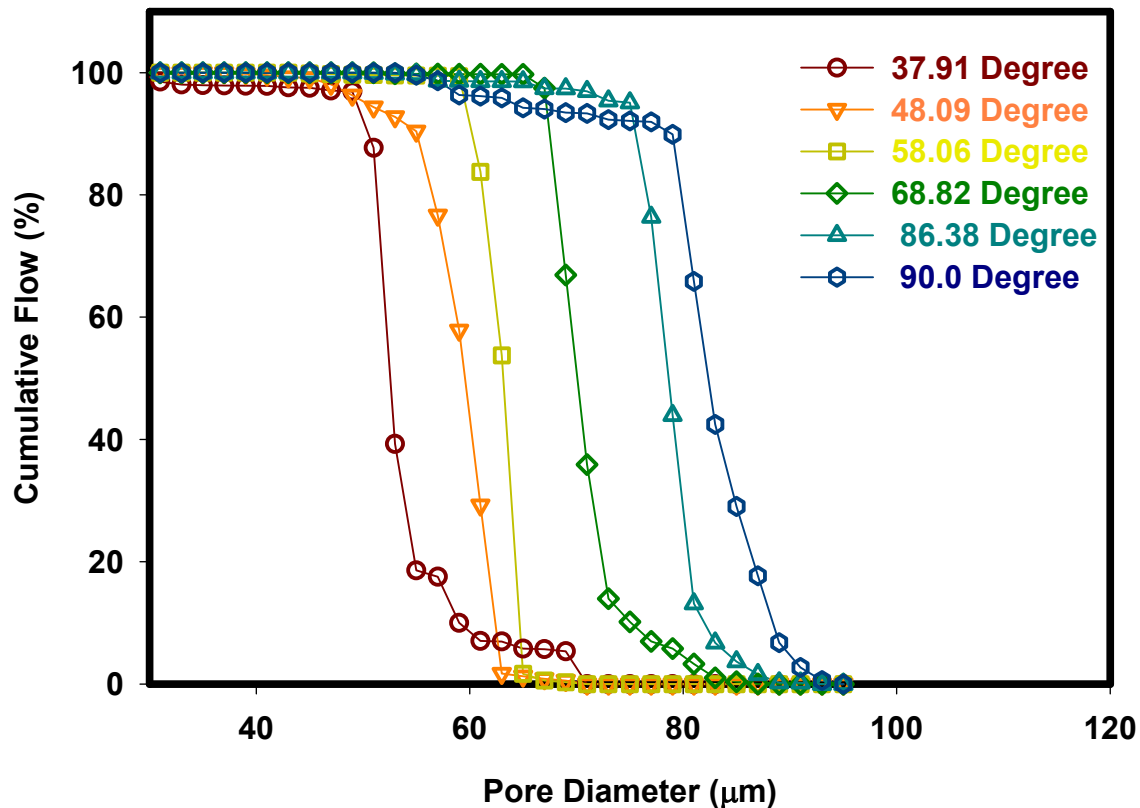


Figure 4.31: Cumulative Frequency of PP 3D MB webs formed at varying approach angles (Throughput: 3.7×10^{-2} g/min/hole, Attenuating Air Pressure: 1.4 bar, Take-up Speed: 6.09 m/min, Curvature 4.71 m^{-1})

The range of pore size diameters in the web changes for different approach angles. The range decreases as the approach angle decreases to around 60 degrees and then the statistical range (the difference between the maximum and minimum value) again increases. The effect is seen in the data obtained on the tests conducted on initial PP samples to understand the distribution of pore size on the planar webs (Figure 4.32). The data shows that the pore diameter decreases with decrease in the fiber diameter. Simulation studies by Kim *et al* [48], show similar results between the pore size and the fiber diameter. The pore size, further relationships discussed in section 5, is influenced by the two structural parameters viz, the fiber diameter and the fiber orientation distribution. The chi-square data for the pore size and fiber diameter are given in Table 4.5.

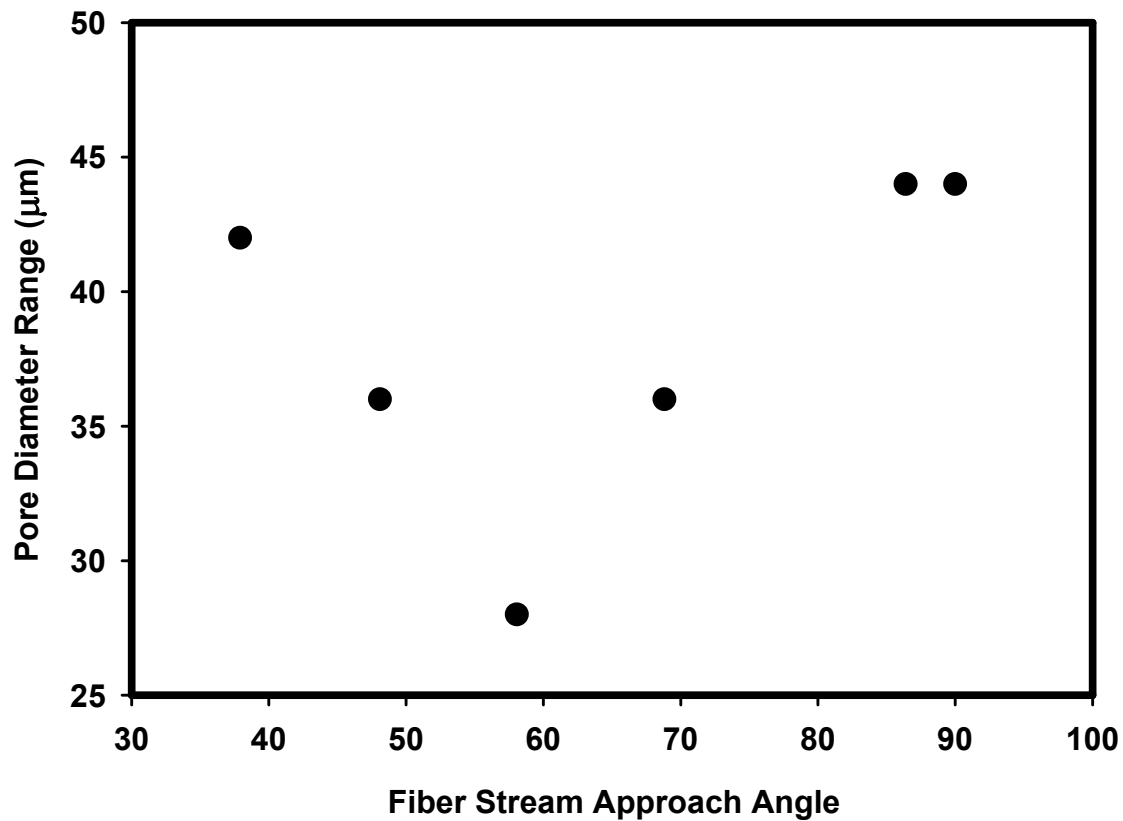


Figure 4.32: Range of pore size distribution of PP 3D MB webs formed at different approach angles (Throughput: 3.7×10^{-2} g/min/hole, Attenuating Air Pressure: 1.4 bar, Take-up Speed: 6.09 m/min; Curvature 9.52 m^{-1})

SEM images of the webs produced at the two extreme conditions of the approach angle investigated are shown in Figure 4.33 and Figure 4.34. It is clear from these images that the pore size of the web produced at higher approach angles has a larger pore size compared to the webs produced at lower approach angles.

Table 4.5: Chi-Square Statistic for Fiber Diameter and Pore Diameter of 3D webs formed at Different Approach Angle

	Chi-Square	df	Probability
Fiber Diameter	111.704315	13 X 5 = 65	0.0003
Pore Size	1643.24145	32 X 5 = 160	<0.0001

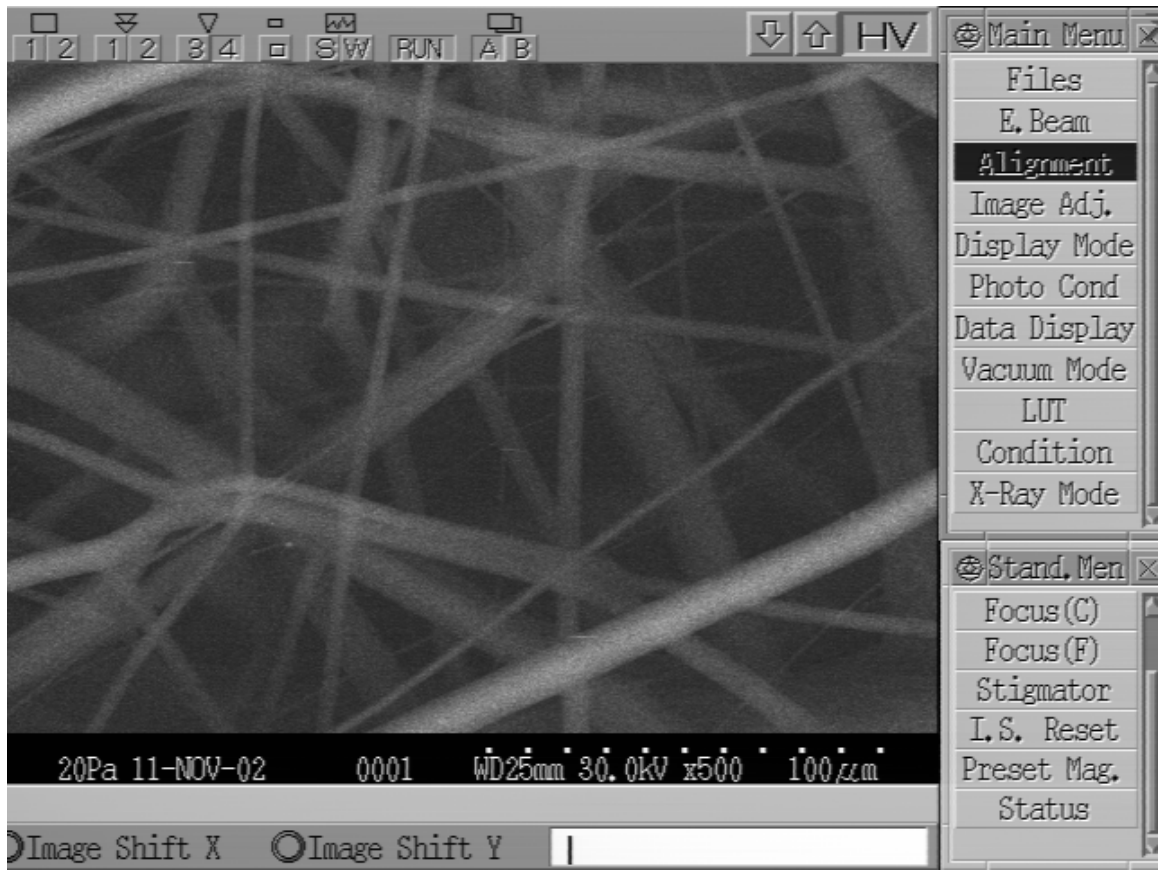


Figure 4.33: SEM Image of the MB PP web at 90 degree Approach Angle (Throughput: 3.7×10^{-2} g/min/hole, Attenuating Air Pressure:1.4 bar, Take-up Speed: 6.09 m/min; Curvature 9.52 m^{-1})

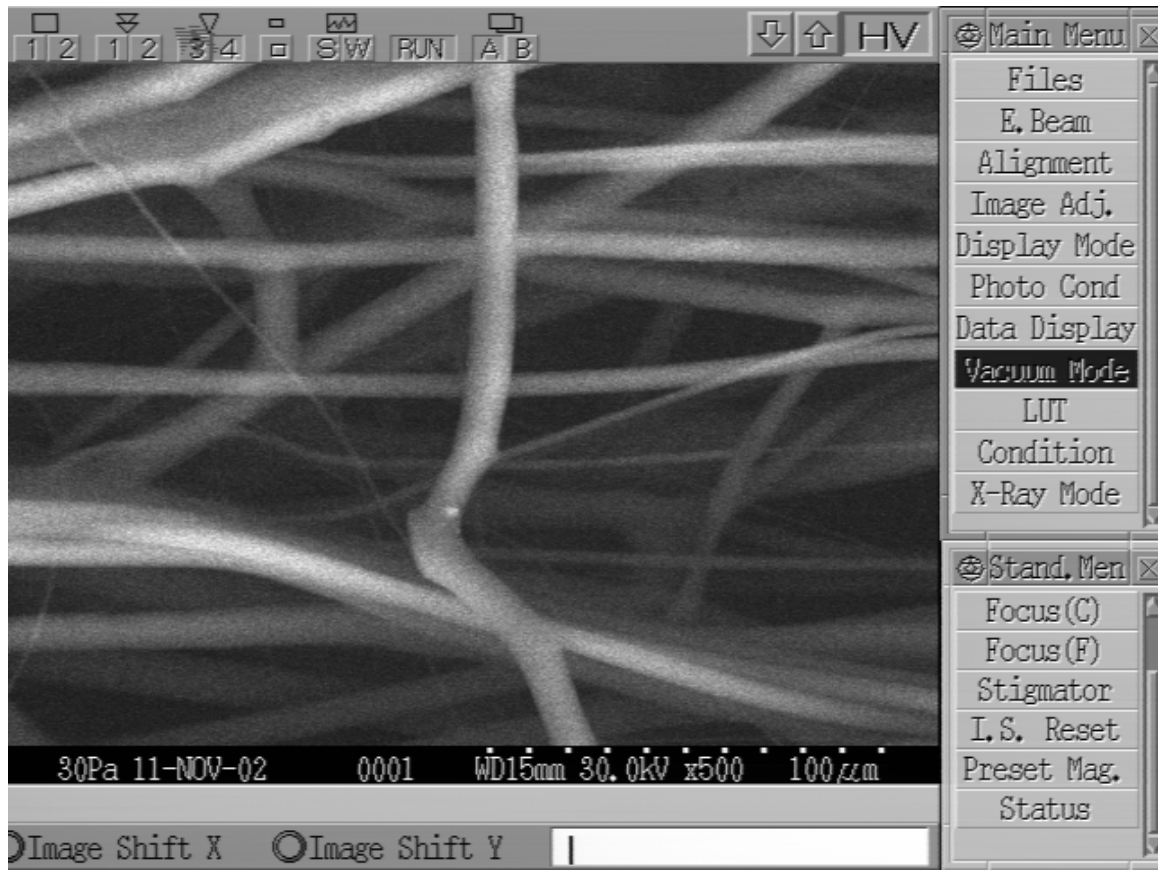


Figure 4.34: SEM Image of the MB PP web at 37 degree Approach Angle (Throughput: 3.7×10^{-2} g/min/hole, Attenuating Air Pressure:1.4 bar, Take-up Speed: 6.09 m/min; Curvature 9.52 m^{-1})

4.6 INFLUENCE OF CURVATURE OF COLLECTING SURFACE

4.6.1 Influence of Curvature of Collecting Surface on ODF

The ODF and the anisotropy parameter of the webs formed at different curvatures on the mold are given in Figure 4.35 and Figure 4.36 respectively. As the curvature of the collecting surface decreases, the velocity of the collecting surface increases. This, in an ideal condition would lead to the preferential orientation of the fibers in the direction of the tangential direction of the rotating surface. To overcome the issue of change in surface speed along the curvature of the collecting surface, the RFACS was programmed such that the relative surface speed of the mold would be close to constant.

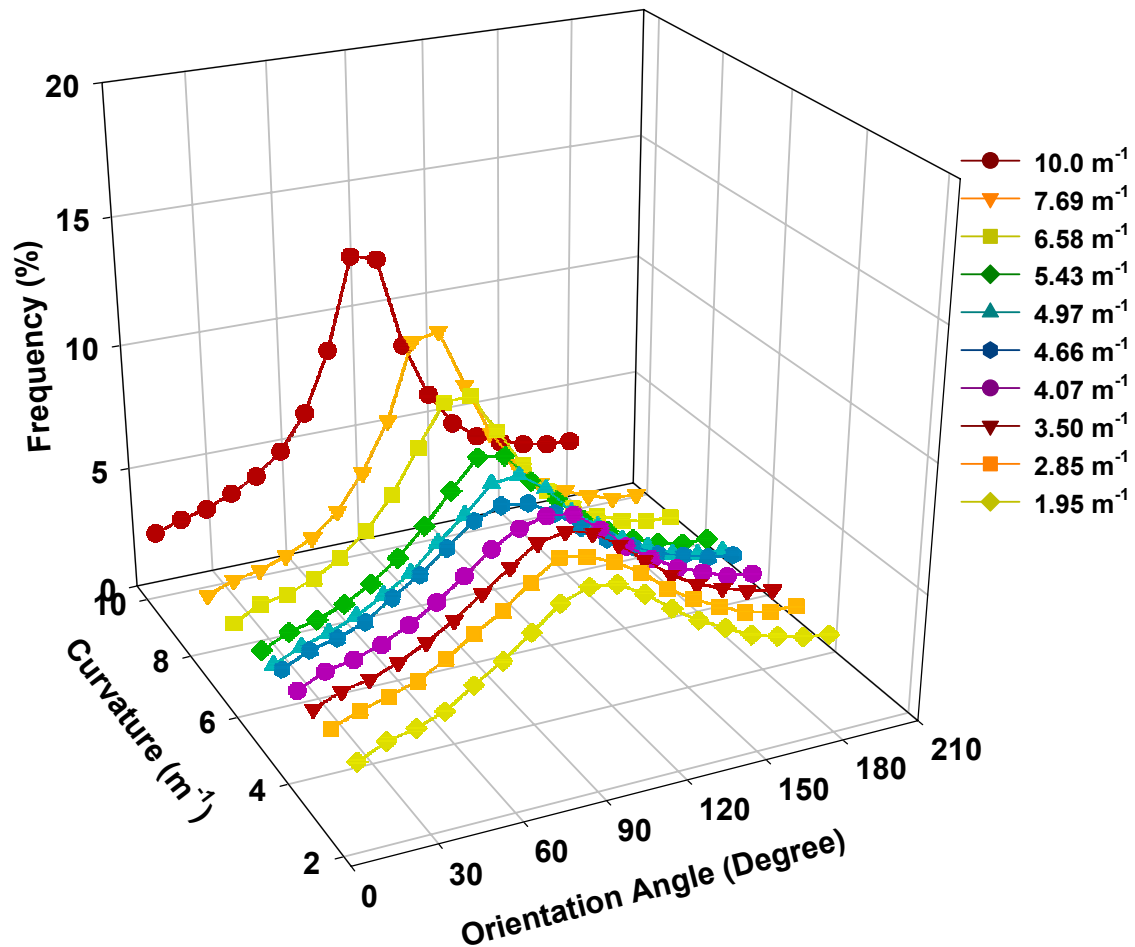


Figure 4.35: ODF for webs at PP MB webs collected at different curvatures (Throughput: 3.7×10^{-2} g/min/hole, Attenuating Air Pressure: 1.4 bar, Take-up Speed: 6.09 m/min; Approach Angle: 90 degree)

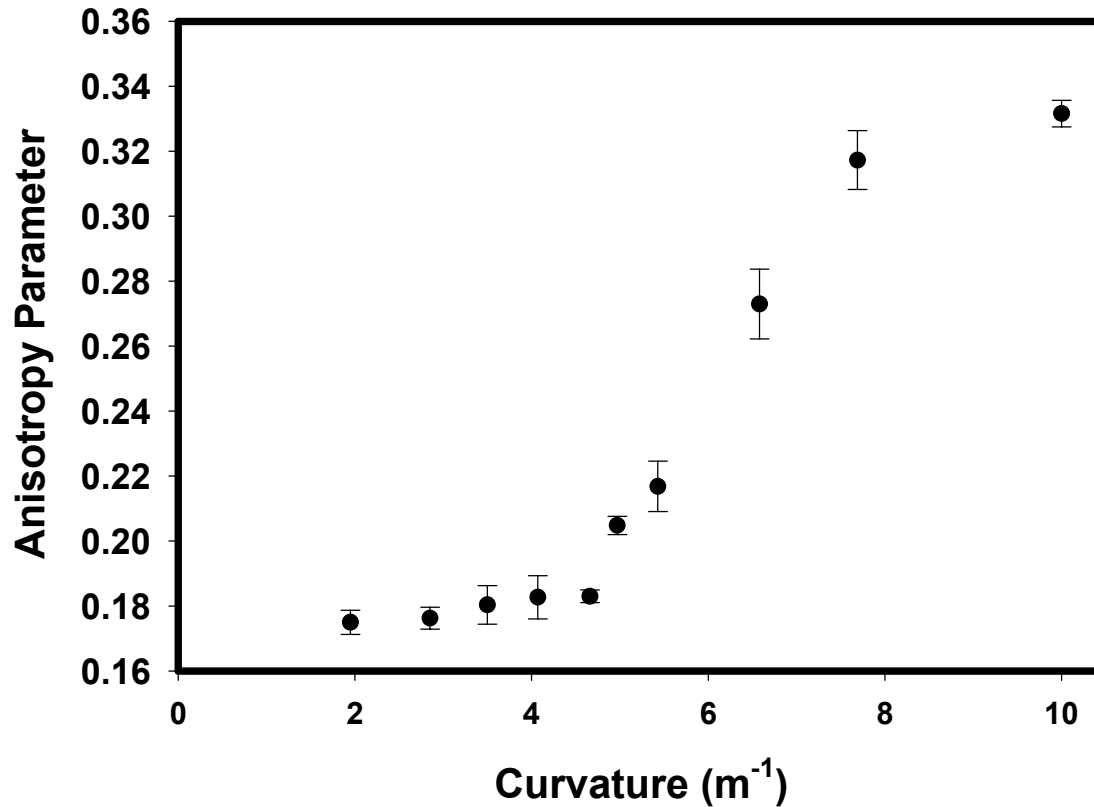


Figure 4.36: Anisotropy parameter for PP MB webs collected at different curvatures along the mold (Throughput: 3.7×10^{-2} g/min/hole, Attenuating Air Pressure: 1.4 bar, Take-up Speed: 6.09 m/min; Approach Angle: 90 degree, with Standard Error of 5 Samples).

At constant surface speed the basis weight of the web does not vary significantly, as is evident in Figure 4.37. Hence, the variation in the fiber arrangement is significantly due to the curvature of the collecting surface. As the curvature increases some of the fibers will travel a longer distance to reach the collecting surface (Figure 4.38). The fibers at high curvatures travel along the longer path parallel to the tangent of the curve, and will be forced to orient themselves in the direction of the velocity vector at the point on the curve. This leads to more fibers orienting in the direction of rotation of the curve leading to greater anisotropy in the web as the curvature increases. The curvature of the collecting surface for the web, has a significant influence on the log(frequency) distribution of the fibers in the web (Table A-9). The F-value obtained from the model

indicates that the $\log(\text{frequency})$ is also influenced by the orientation angle under consideration i.e. there is an interaction between the orientation angle and curvature on the frequency of the fibers in that particular orientation.

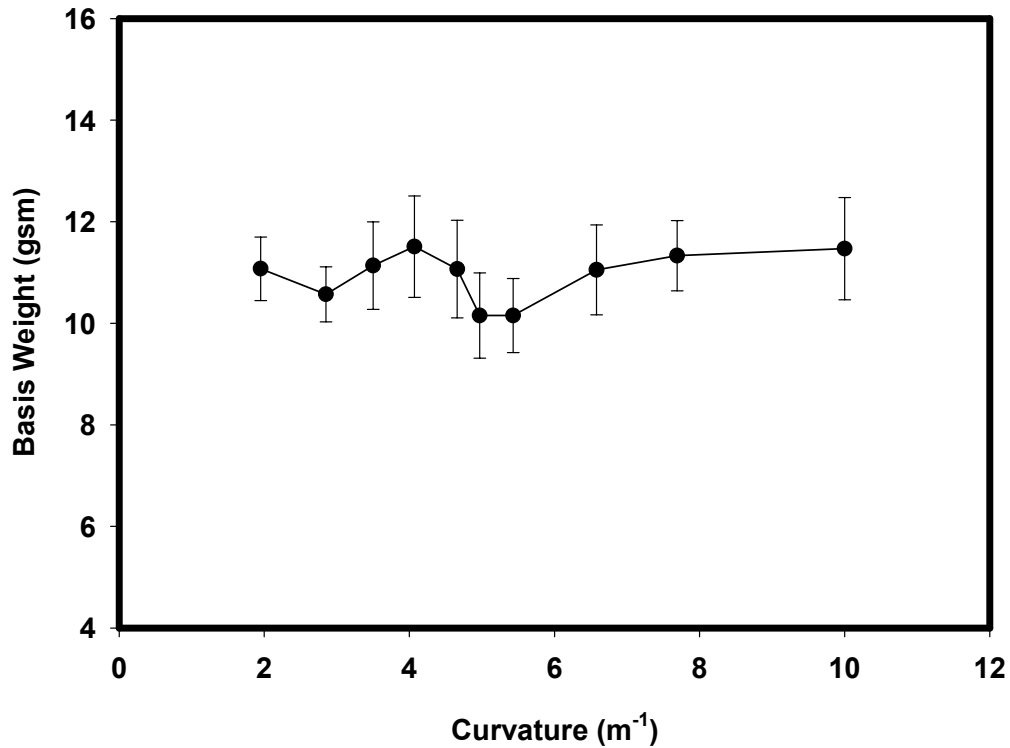


Figure 4.37: Basis weight for PP MB webs collected at different curvatures of the collecting surface (Throughput: 3.7×10^{-2} g/min/hole, Attenuating Air Pressure: 1.4 bar, Take-up Speed: 6.09 m/min; Approach Angle: 90 degree, with Standard Error of 5 Samples)

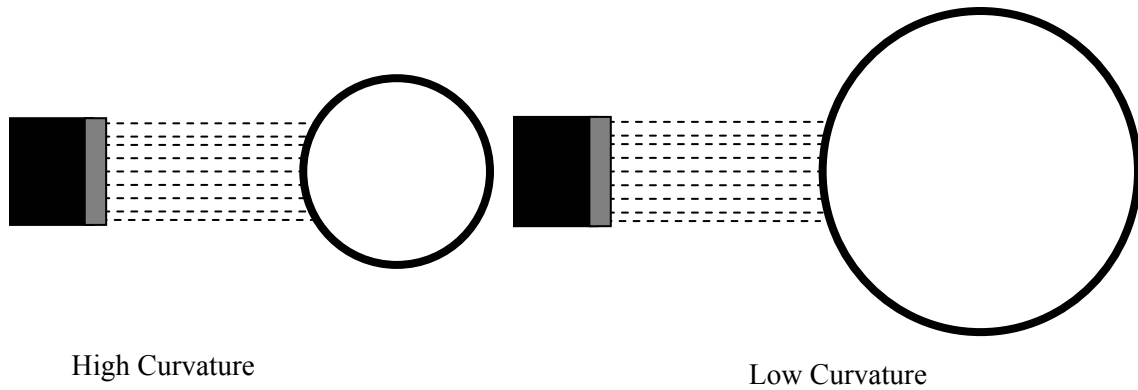


Figure 4.38: Curvature effects on the die to collecting distance of the fibers at different points on the die (Plan of the Die and Curved Surface)

4.6.1.2 Influence of Curvature of the Surface on Fiber Diameter and Pore Size Distribution

The average pore size of the web is given in Figure 4.39. As the curvature of the collecting surface increases, the average pore size of the web decreases. As discussed in the previous section, an increase in the curvature increases the orientation of the fibers in the machine direction (along the velocity vector) of the collecting surface. As more fibers are parallelized, the distance between the fibers will decrease. This reduces the effective pore diameter. The cumulative frequency (Figure 4.40 and Figure 4.41) of the distribution of pore sizes has a wider range at low curvatures, (more random fiber arrangement) while at high curvatures the distribution range is narrower. SEM images of the webs produced at 1.95 m^{-1} and 10 m^{-1} curvature are shown in Figure 4.42 and Figure 4.43. It is obvious from the images that webs produced at higher curvatures have smaller pore size. The Chi-square test conducted on the pore diameter and fiber diameter is summarized in Table 4.6. The analyses imply that the pore diameter distributions and fiber diameter distributions for the various webs tested are significantly different from each other, and that the fiber diameter and pore diameter are significantly affected by the curvature of the collecting surface.

Table 4.6: Chi-Square and its Probability for the fiber and pore diameter of webs formed at different curvatures

	Chi-Square	df	Probability
Fiber Diameter	621.9392664	9*22=198	<0.0001
Pore Size	4104.41	9*41=369	0

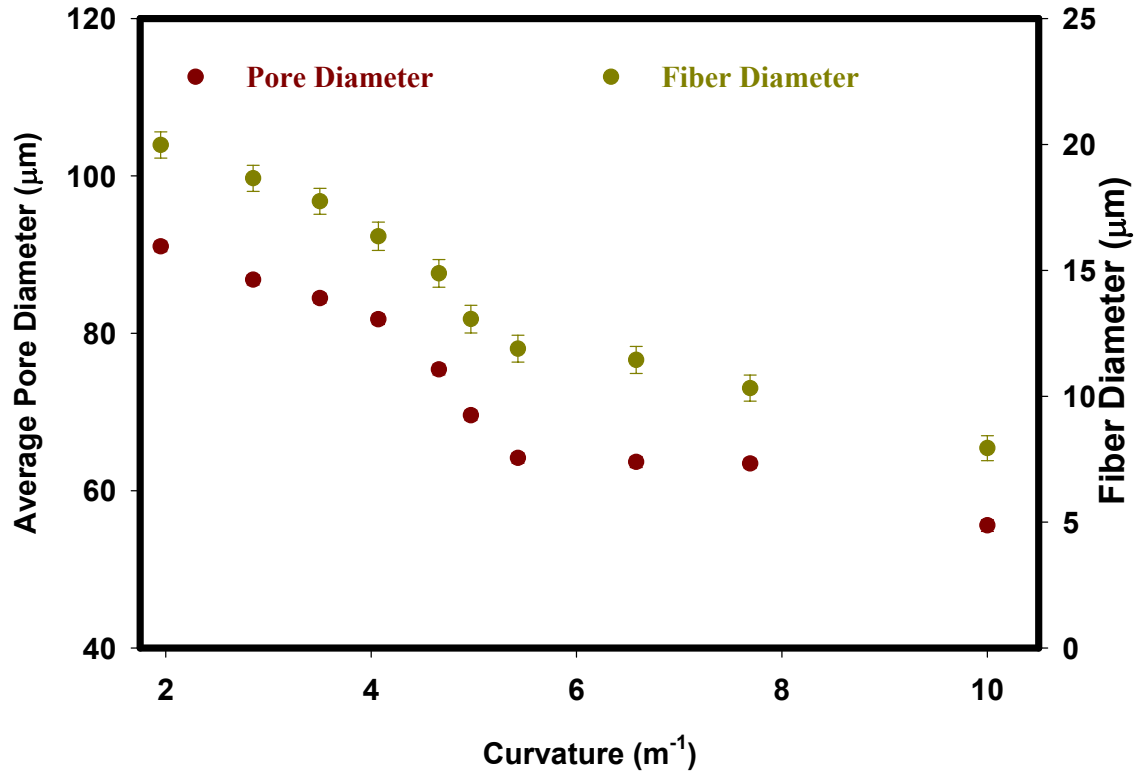


Figure 4.39: Average pore diameter and fiber diameter of PP 3D MB webs obtained at different curvatures (Throughput: 3.7×10^{-2} g/min/hole, Attenuating Air Pressure: 1.4 bar, Take-up Speed: 6.09 m/min; Approach Angle: 90 degree, with Standard Error of 5 Samples)

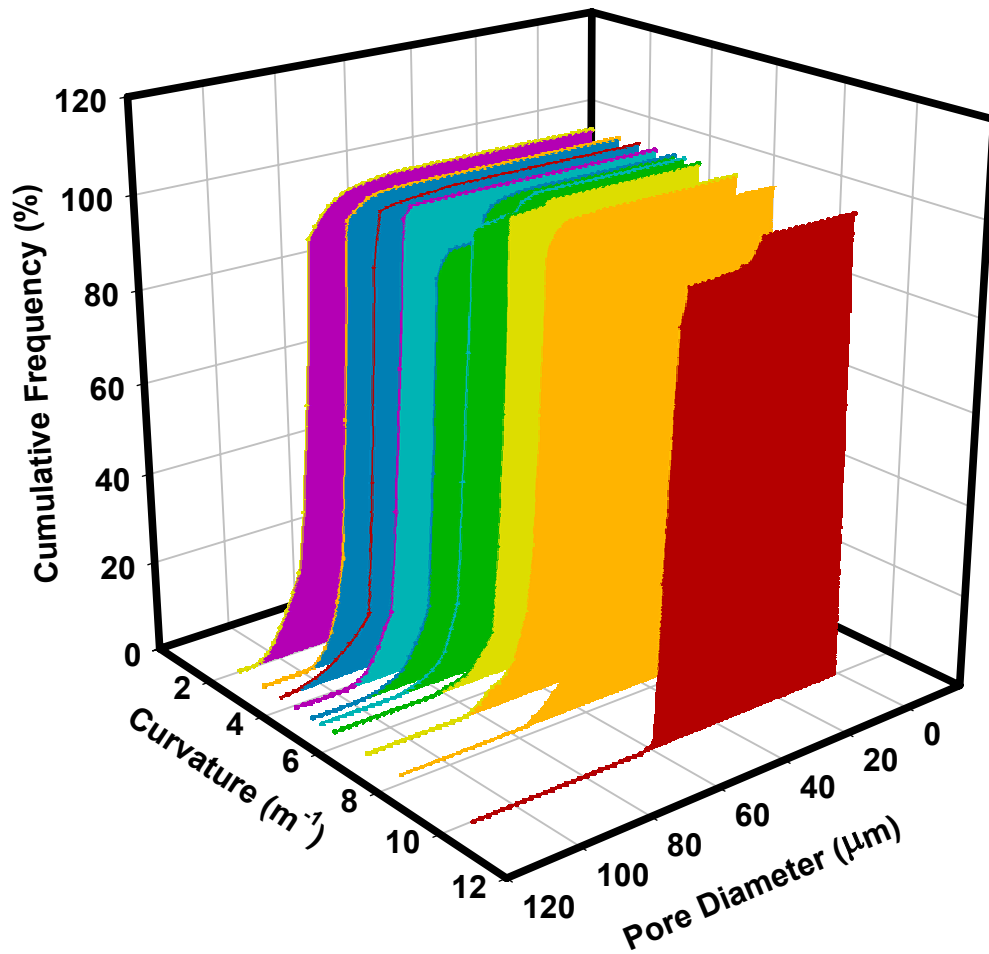


Figure 4.40: Cumulative Frequency of PP 3D MB webs formed at different curvatures (Throughput: 3.7×10^{-2} g/min/hole, Attenuating Air Pressure: 1.4 bar, Take-up Speed: 6.09 m/min; Approach Angle: 90 degree)

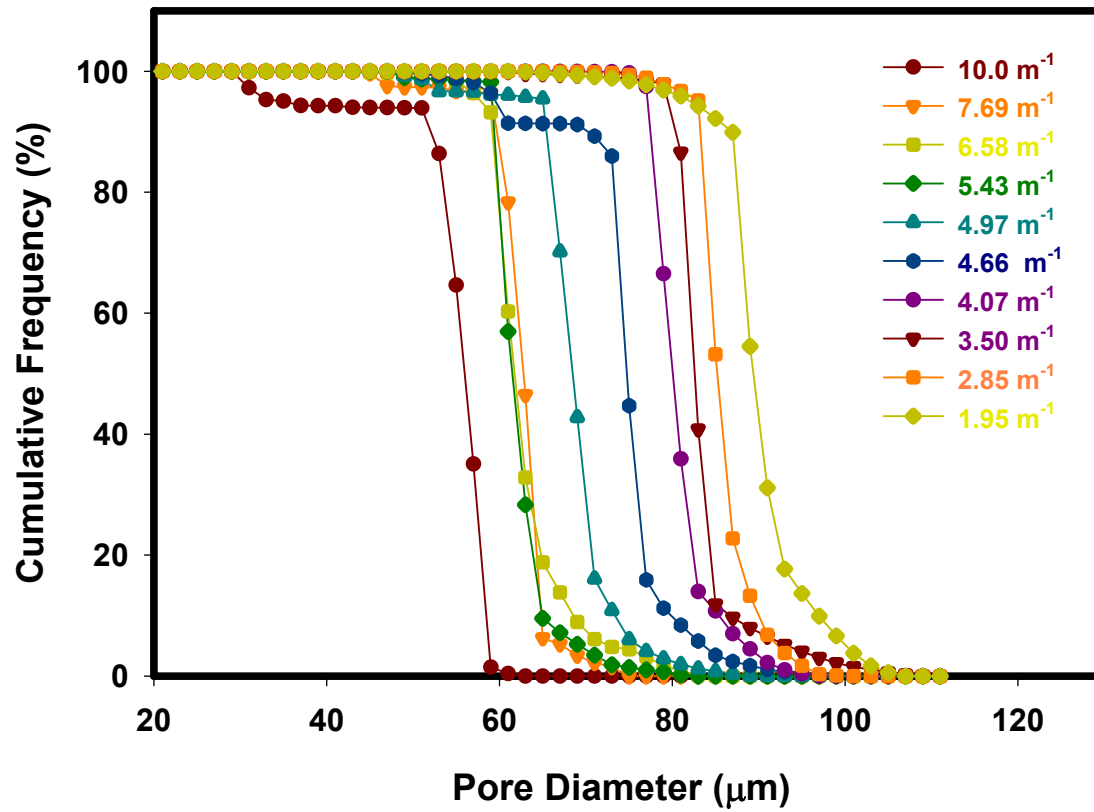


Figure 4.41: Cumulative Frequency of PP 3D MB webs formed at different curvatures (Throughput: 3.7×10^{-2} g/min/hole, Attenuating Air Pressure: 1.4 bar, Take-up Speed: 6.09 m/min; Approach Angle: 90 degree)

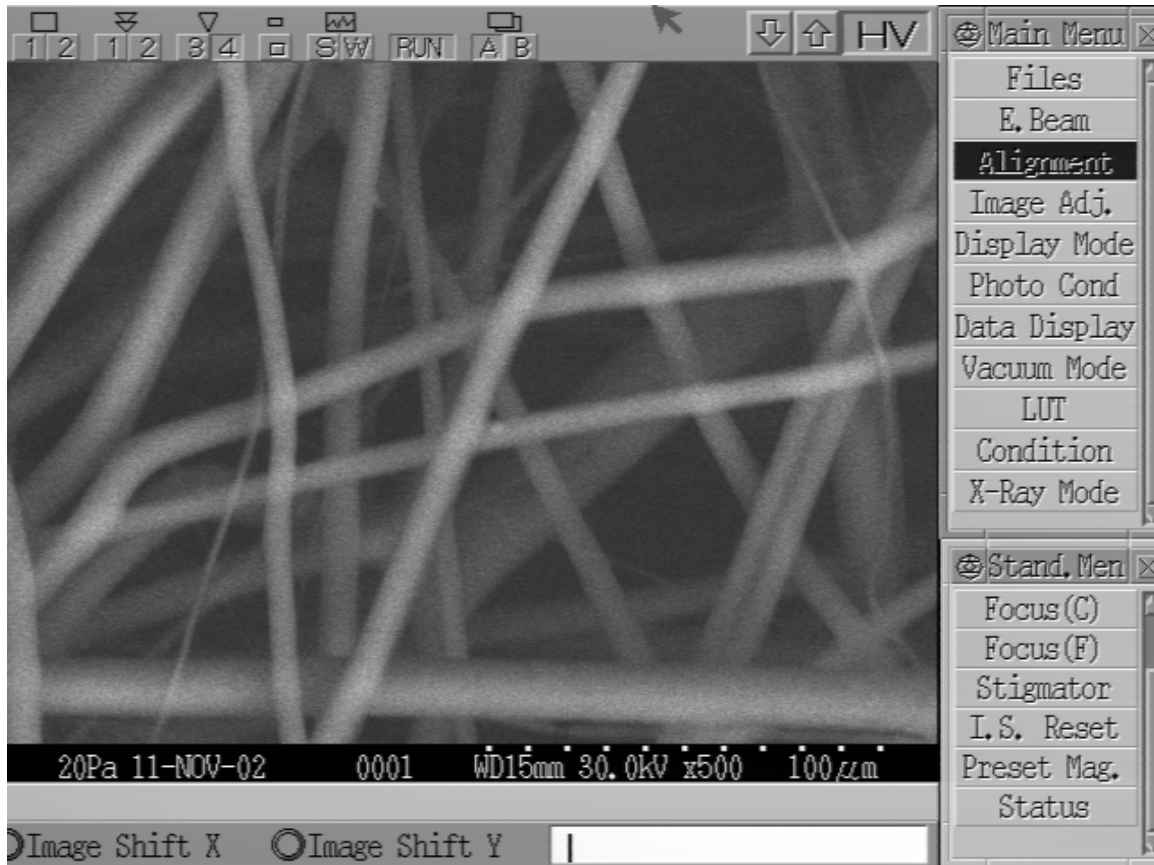


Figure 4.42: SEM Image of MB PP web at 1.95 m^{-1} Curvature (Throughput: 3.7×10^{-2} g/min/hole, Attenuating Air Pressure: 1.4 bar, Take-up Speed: 6.09 m/min; Approach Angle: 90 degree)

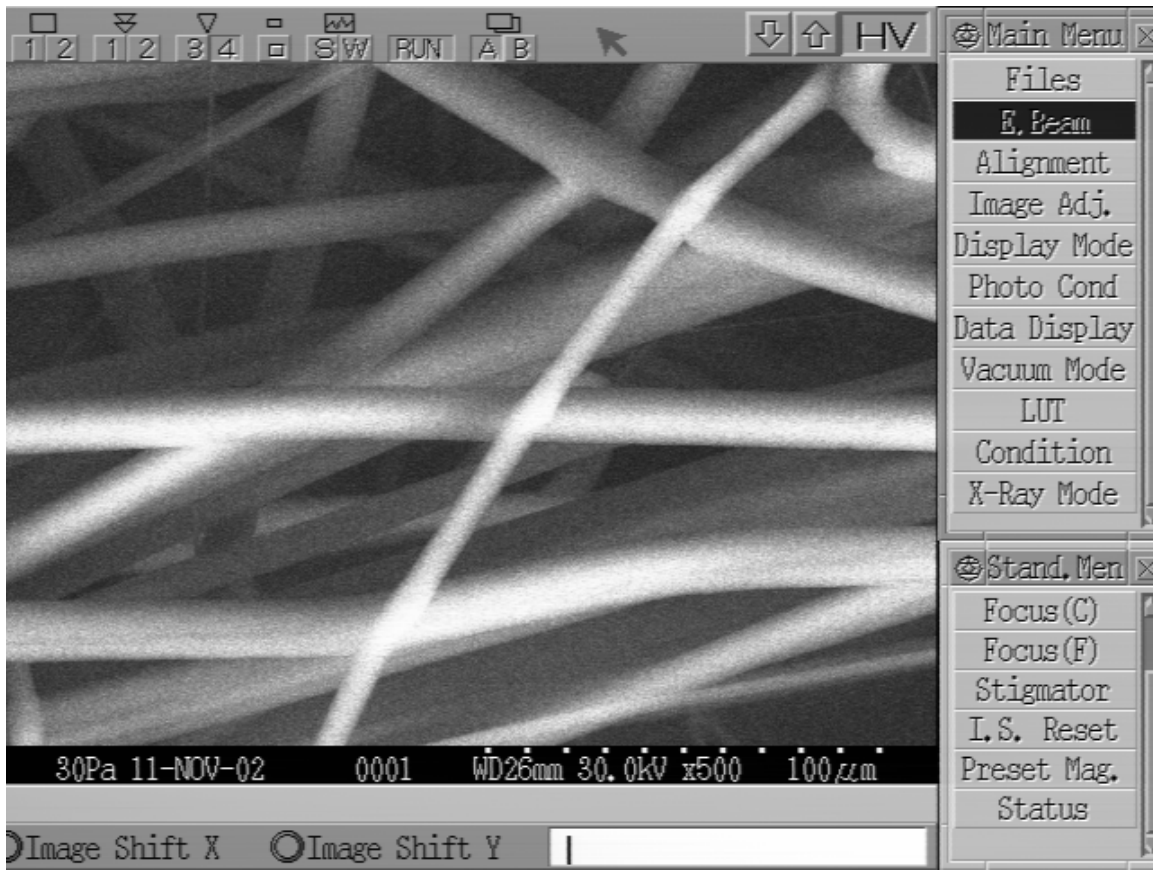


Figure 4.43: SEM Image of MB PP web at 10 m^{-1} Curvature (Throughput: 3.7×10^{-2} g/min/hole, Attenuating Air Pressure:1.4 bar, Take-up Speed: 6.09 m/min;Approach Angle: 90 degree)

5 INTERACTION BETWEEN STRUCTURAL PARAMETERS

It is known that for a given fabric density and structure, smaller pores can be formed utilizing smaller diameter fibers [48]. However the structure of the web (fiber orientation distribution) can also affect the web pore size distribution and at the same time influence the properties of the web. The fiber-to fiber contacts and pore distribution affect the fluid transportation within the web and its mechanical properties, surface appearance and hand [92]. Various researchers have simulated the structure of the webs and measure the effects of the structure on the properties of the web. Published literature in the area of modeling of porous media involves the use of one-dimensional structure representation or a random aggregation process involving extended geometric objects [106].

The simpler models consider that the elements are regularly arranged in the structure. Bear[82], for granular materials, Kyan *et al* [107] for fibrous material have used this approach. This approach does not take into account the random distribution of the elements. Probabilistic models were considered for porous media. Piekaar *et al* [47] used it for fibrous materials, Abdel-Ghani *et al* [46] for nonwoven coalesces, Lombard *et al* [49] for geotextiles. As mentioned in Equation 1, in the earlier discussion, Abdel-Ghani *et al* [60] analyzed the structure of the nonwoven needled fabrics considering the fabric as a composition of multiple layers of randomly distributed fibers. Using Monte-Carlo procedures, the fiber network has been simulated and the average pore area has been found to be proportional to the square of the diameter of the fiber. The use of analytical models for pore size distribution in multi-planar stochastic porous media has been proposed by Dodson *et al*[108]. Recently, Kim *et al* [48], discovered a relationship that exists between the fiber crimp and the orientation of the web.

5.1 GEOMETRICAL PARAMETERS OF A SIMULATED PORE

Roundness of a shape is also known as circularity. This is a measure that compares the shape of an object to that of a circle. For a circle of radius, r , we know that its perimeter P and area A are given by:

$$A = \pi r^2$$

$$P = 2\pi r$$

The ratio of the square of its perimeter to the area, of a circle, is always a constant (4π) and hence, roundness, R , can be defined as

$$R = \frac{P^2}{4\pi A}$$

R has a maximum value of 1 and decreases as the region deviates from a perfect circle.

The bounding rectangle is the smallest rectangle that encloses the pore with the same orientation as the pore. Its width will be larger than the diameter of a circular pore fitted into the pore (Figure 5.1).

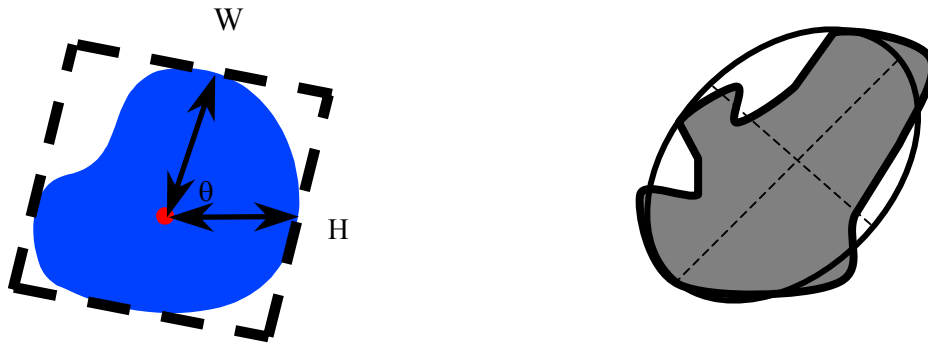


Figure 5.1: An irregular pore with a bounding rectangle and best-fit ellipse

The ellipticity of the pore gives the measure of shape anisotropy. Also the radius of the best-fit circle in the pore can be obtained from the semi-minor axis of the ellipses. The semi-major and semi-minor axes (A_s) are the lengths of a best-fit ellipse to the pore. Pourdeyhimi *et al* [84] have discussed the procedural details of determining these values. The hydrodynamic radius (R_h) of the pore has been defined as the ratio of twice the pore

area (total area) to that of the pore perimeter. The hydrodynamic radius can also be obtained from the geometric roundness of the pore and the area of the pore as given in the equation below.

$$R_h = \sqrt{\frac{AR}{\pi}}$$

Another radius, the equivalent radius (R_e), is also widely used and is defined as diameter of a circle whose area or perimeter is same as the pore [109, 110]. For a perfectly circular pore, the hydrodynamic radius and the equivalent radius would be equal to each other. For pores which are polygonal in shape, the hydrodynamic radius would be smaller than the equivalent radius. Opening radius (R_o)(Figure 5.2) of the pore is the radius of the maximum circle that can fit the pore and determines the largest particle that can pass through the pore. For nonwoven webs that are single layered, the opening radius will be different from that of the hydrodynamic radius. While considering a multiple layered structure of the web, the opening radius would be equivalent to the hydrodynamic radius.

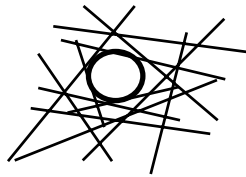


Figure 5.2: Fibrous Structure with a Pore.

The practical model developed by Lombard *et al*[49] for the prediction of the opening radius distribution is a Poisson distribution and is given in the Equation below

$$f(R_o) = R_o L^2 C (R_o L + 1)^{C-1} \exp(-R_o L C)$$

where L is the length of the fibers per unit area and C is a factor associated with the thickness of the fabric. These are estimated from the thickness (T) of the web, the fiber diameter d_f , the fiber density ρ_f and the basis weight of the fabric w_g [49].

$$L = \frac{8b_s}{\pi T_g d_f \rho_f}, \text{ and}$$

$$C = \frac{T_g}{d_f}$$

In making this prediction, assumptions have been made that the web can be divided into elementary planes having the same thickness equal to four times the radius of the fiber and the density of the fiber is the same. The web structure cannot be divided into layers of equal thickness and their orientation of the fibers in these layers is not the same.

Various authors have examined the structure to determine the interaction of the pore area distribution with the density of the web and fiber diameter. Kim *et al* [48], have investigated the pore area with the orientation distribution, density and the fiber diameter in the structure. As it is well known that smaller fiber diameters produce smaller pore areas, the current work will be restricted to the investigation of the pore radius (R_h) ($\Leftrightarrow w, A_s$) with the anisotropy in web (\Leftrightarrow standard deviation in orientation distribution) and the density of the web structure.

Meltblown structures are multi-planar fibrous webs with little or no orientation through the thickness of the web. For a comparison of pore size obtained from simulated models to the pore size obtained using real webs, the presence of the third dimension, although very small, has to be recognized. Simulation techniques measure the pore size distribution in the web by calculating the pixels of the number of pixels in the pore [89]. These measurements are for the total area of the pore, while the experimental methodology available measures circle particles (either using granulometry or capillary techniques). Hence an ideal situation to make the comparison would be between the

radius of the circle largest that would fit the pore in a multi-layered simulated structure to a similar radius of the real web. Since the hydrodynamic radius of the pore, in a single layered web, takes into account the lack of roundness of the pore, R_h will be utilized to investigate the effect of the fiber orientation distributions and fiber diameter on average pore radius.

The average pore size variation due to the variation process parameters, along with the corresponding variations in the fiber diameter and the anisotropy measurements have been reported and discussed in the previous Chapter. Simulated two-dimensional nonwoven webs were formed using techniques discussed by Pourdeyhimi *et al* [62, 89, 48] for the purpose of developing a comparison between the simulated structures with the structures of the real webs. The geometrical descriptors of the pore, viz., the roundness (R) of the pore, pore area (A), the pore perimeter (P), minor axis of the best fitting ellipse and the width of the bounding rectangle are utilized to describe the pore. The standard deviation of the orientation distribution in the simulated web is used as a measure of its anisotropy parameter. As the standard deviation in the orientation distribution of the fibers increases the structures are more random in nature and hence their anisotropy parameter will be closer to 0 (Figure 5.3). Similar structures of varying area coverage (density of fibers) were produced for the purpose of the analyses of the ODF, pore radius and the interaction between them in the simulated images.

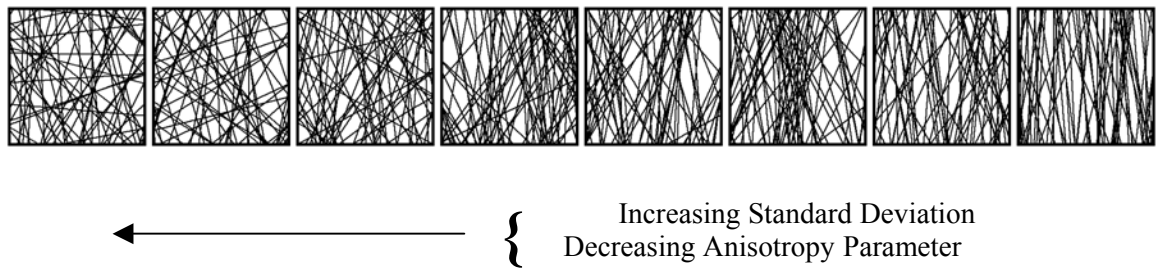


Figure 5.3: Simulated Structures with varying ODF [48]

A series of web structures with varying orientation distribution functions, and density of the web with zero crimp in the fibers of 2 pixel diameter were simulated using techniques described elsewhere [89]. The various geometrical shape descriptors of these structures

were determined using the techniques described by Kim *et al* [48]. The details of the images are given in Table 5.1 and typical images are given in Figure 5.3.

Table 5.1: Simulation Conditions for the Webs

Area (%)	ODF Standard Deviation
15	10, 15, 20, 25, 30, 40, 45
35	10, 15, 20, 25, 30, 40, 45
40	10, 15, 20, 25, 30, 40, 45
45	10, 15, 20, 25, 30, 40, 45
50	10, 15, 20, 25, 30, 40, 45

The results for the pore roundness (R), and pore radius (R_h) are given in the Figure 5.4 to Figure 5.8. All of the data obtained indicate that the pore radius decreases with increase in anisotropy parameter, the pore radius decreases with decrease in roundness. Similar effects are also observed with the width of the bounding rectangle and the minor axis of the best fitting ellipse. The interaction of the fiber diameter on the pore diameter is well known [48]. Based on the results from these simulation studies, a statistical model to fit the fiber diameter, pore diameter and web anisotropy, using the data generated from the analysis of real webs, is made in the next section.

Fiber Diameter = 2 Pixel, Crimp = Zero

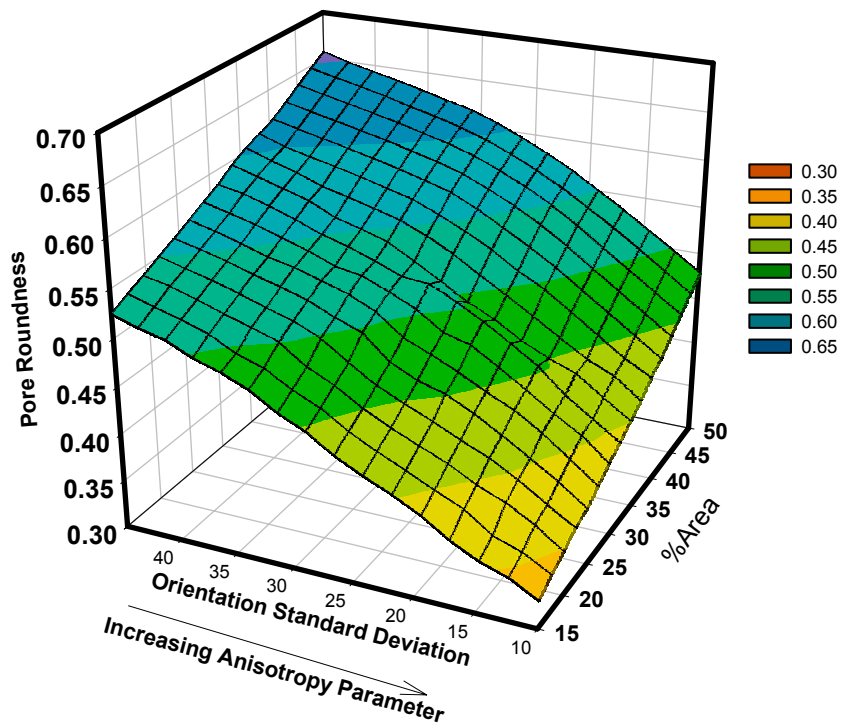


Figure 5.4: Variation in the Pore Roundness as a function of Std Deviation of Orientation and Area Density

Area = 45 %
Fiber Diameter = 2 pixel
Crimp = Zero

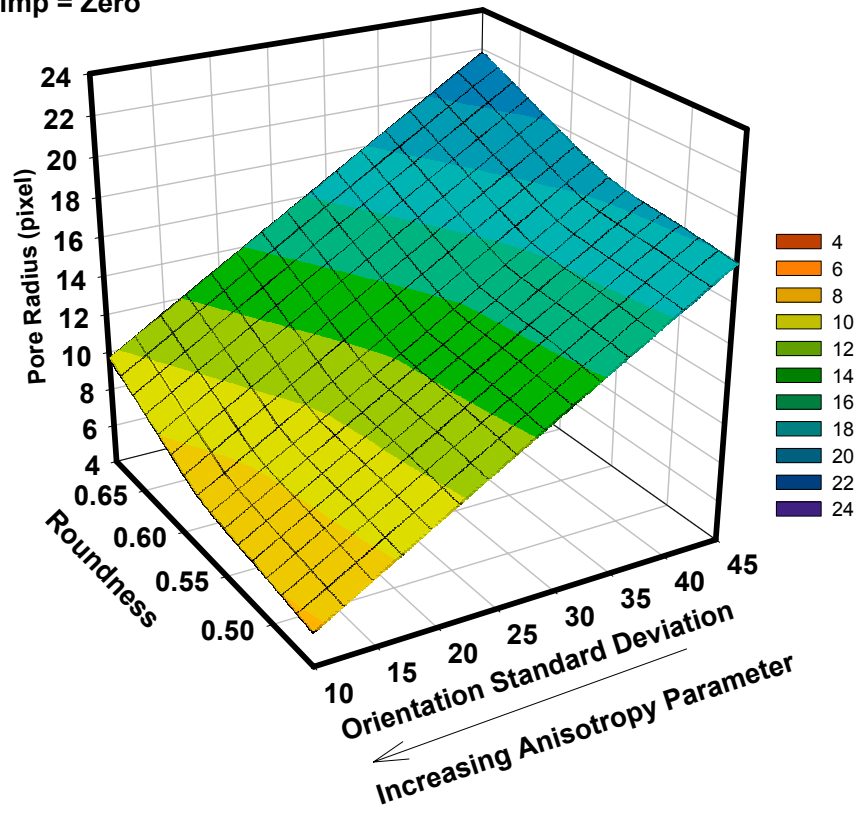


Figure 5.5: Pore radius variation as a function of Std Deviation of Orientation and Roundness of the pore.

Fiber Diameter = 2 pixel
Crimp = Zero

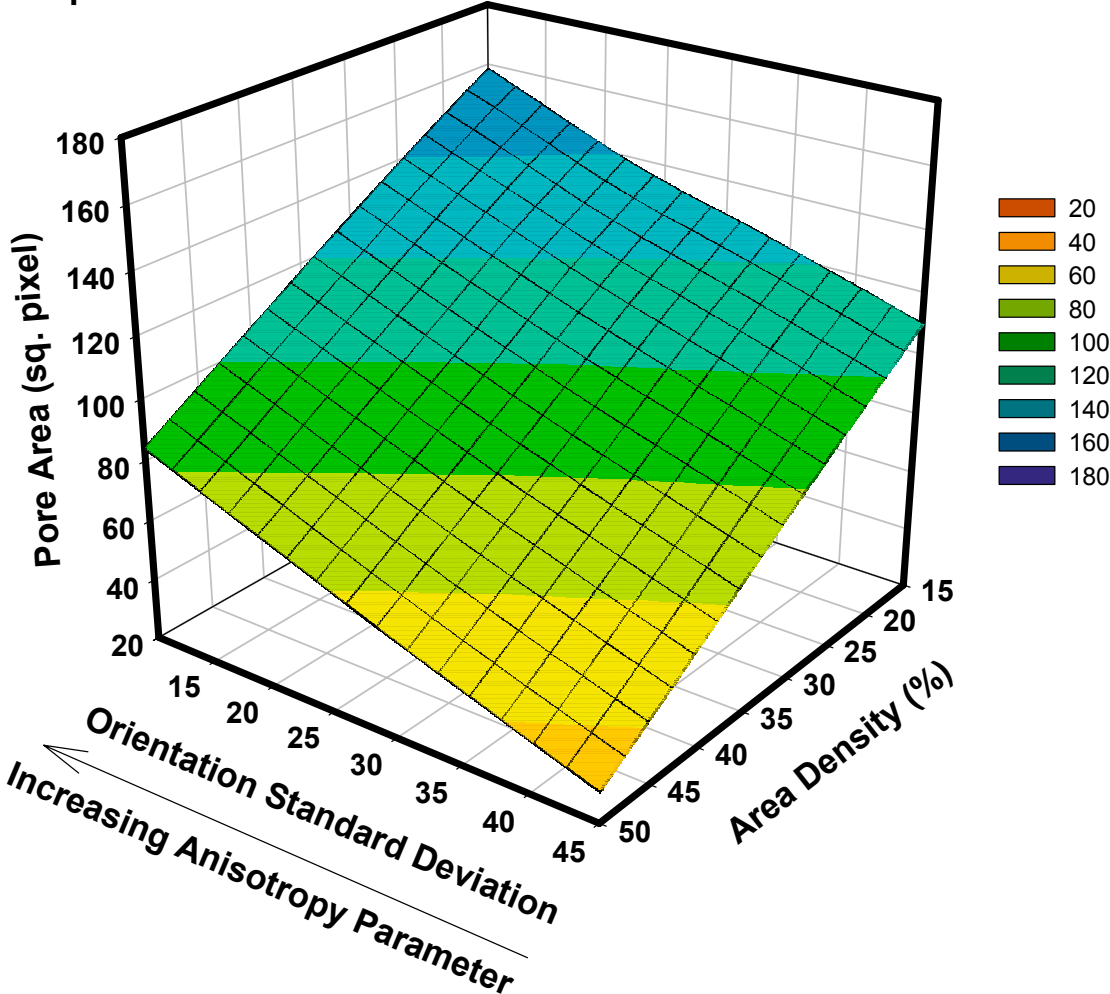


Figure 5.6: Pore Area as a variation of the density of the web and the Std Deviation of Orientation

Fiber Diameter = 2 Pixel
Crimp = Zero

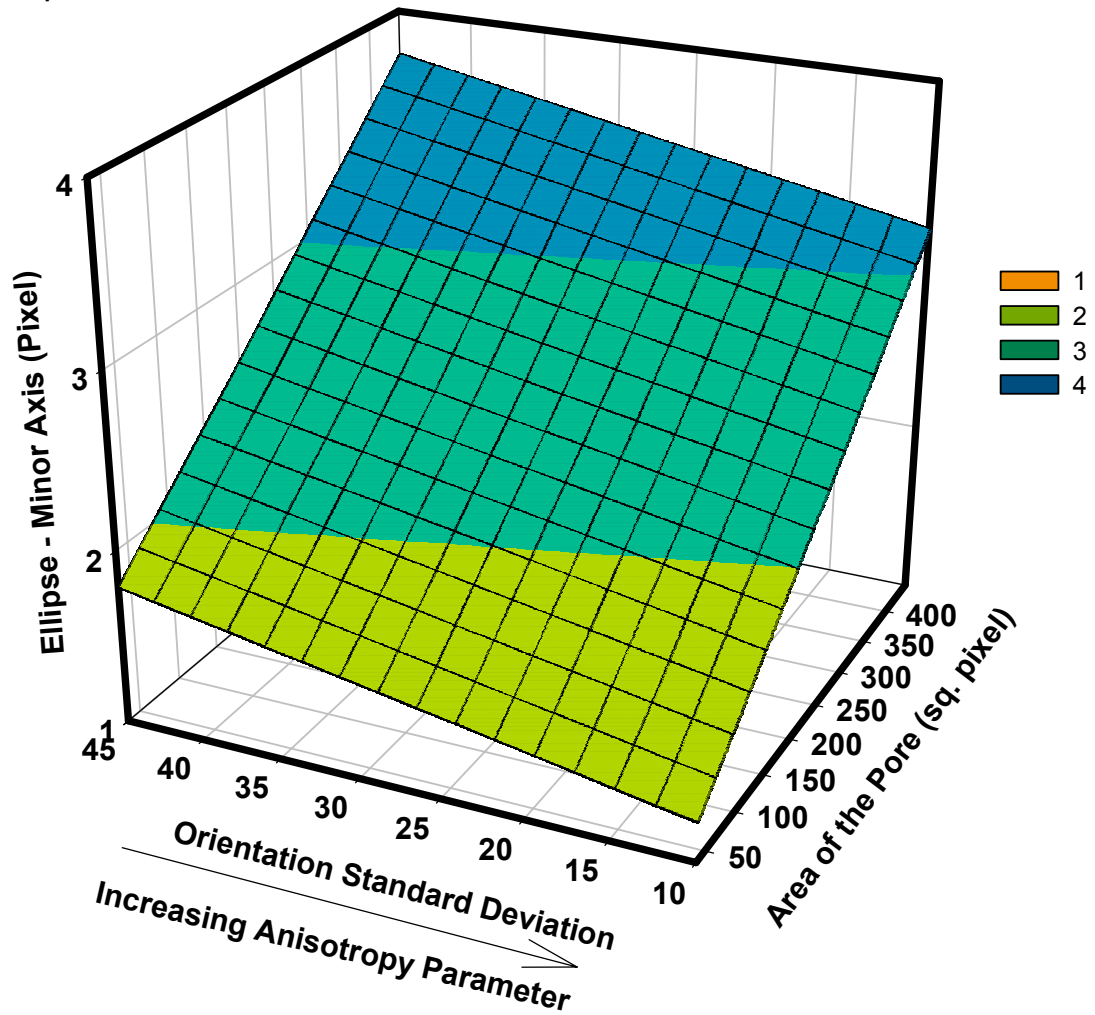


Figure 5.7: Variation of Minor axis of the Best-fit Ellipse with the Standard Deviation of Orientation and Area of the Pore.

Fiber Diameter = 2 Pixel
Crimp = Zero

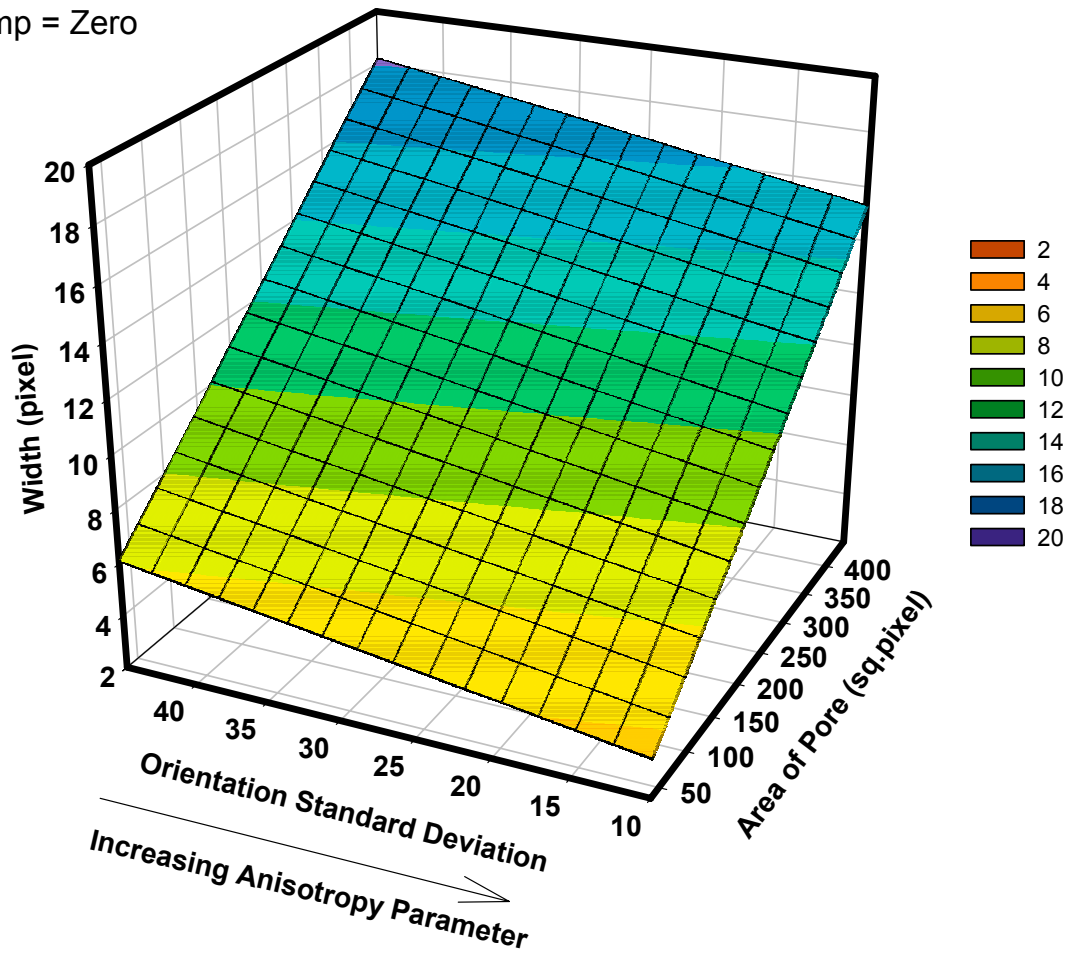


Figure 5.8: Variation of the Width of the Best-fit Rectangle with Standard Deviation of Orientation and Area of Pore

5.2 STATISTICAL MODELING OF FIBER DIAMETER, PORE DIAMETER AND ANISOTROPY PARAMETER INTERACTIONS

For the purpose of modeling the structural interaction between three parameters, the anisotropy parameter and average fiber diameter are the independent variables while the average pore radius of the web is the dependent variable. These data were collected on the webs analyzed earlier and can be categorized into two broad groups. The first is the result from the analysis of planar webs obtained by varying the process parameters, viz. polymer throughput, DCD, take-up speed and attenuating air pressure. The second set of data is obtained from varying the two new parameters i.e. the approach angle and the curvature of the collecting surface. An initial model developed to examine the relation between the structural variables for the planar web is extended to the 3D webs. The actual and expected values for the 3D webs based on the model developed for the planar webs are also reported.

Based on the trends seen on a scatter plot (Figure 5.9) of the three parameters for the planar webs and the 3D webs, and also from the simulated structure results, a simple statistical full model that has a direct relationship between the fiber diameter (f_d), an inverse relationship with the anisotropy parameter (f_p) and pore diameter (p_d) was developed.

$$p_d = \beta_0 + \beta_1 * f_d + \beta_2 * f_p^{-1} + \beta_3 * f_d * f_p^{-1}$$

where

β_0 is the intercept,

β_1, β_2 are the linear coefficients, and;

β_3 is the coefficient for the interaction.

The data for the developing the correlation between the pore size, fiber diameter, and anisotropy parameter of the web was obtained from the investigation of the variation in the process parameters on the structural parameters of the web.

Table 5.2 gives the estimated coefficients of the parameters in this model. The F-value for the model is less than 0.0001 hence the model is significant. Each estimate for the parameters are also significant. The value for an average pore at known fiber diameter and a web of known anisotropy parameter in the web can be determined with the following equation.

$$\hat{p}_d = 18.95 + 2.514 * f_d + 0.70 / f_p - 0.06 * f_d / f_p$$

Table 5.2: ANOVA and Regression of Structural Parameter Estimate for the Planar Web

Procedure: Regression; Dependent Variable: Pore Diameter Analysis of Variance					
Source	Degree of Freedom	Sum of Square	Mean Square	F-Value	Pr>F
Model	3	1590.172	530.0572	156.57	<0.001
Error	41	138.805	3.3854		
Total	44	1728.977			
Root MSE	Dependent Mean	Coeff. Of Var	R Sqaure	Adj. RSquare	
1.839	37.706	4.8798	0.99	0.97	
Parameter Estimates					
Variable	Degree of Freedom	Parameter Estimate	Standard Error	t-Value	Pr > t
Intercept (β_0)	1	18.9468	1.4078	13.46	<0.0001
Diameter (β_1)	1	2.5146	0.2025	12.42	<0.0001
Anisotropy ⁻¹ (β_2)	1	0.6999	0.1605	4.36	<0.0001
Dia * Ani ⁻¹ (β_3)	1	-0.0607	0.0177	-3.43	<0.0014

The relationship between the predicted pore diameter and the observed pore diameter for planar webs is given in Figure 5.10.

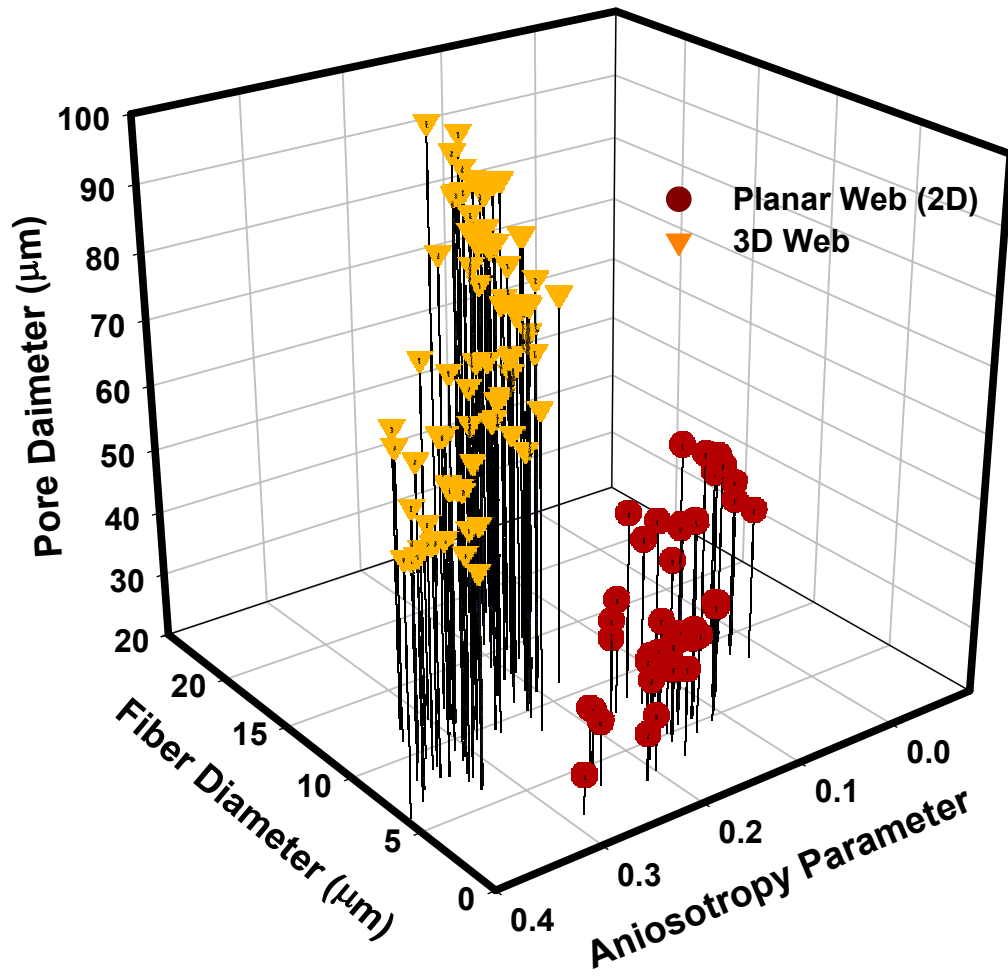


Figure 5.9: Scatter plot of the Pore Diameter, Anisotropy Parameter and Fiber Diameter for the webs.

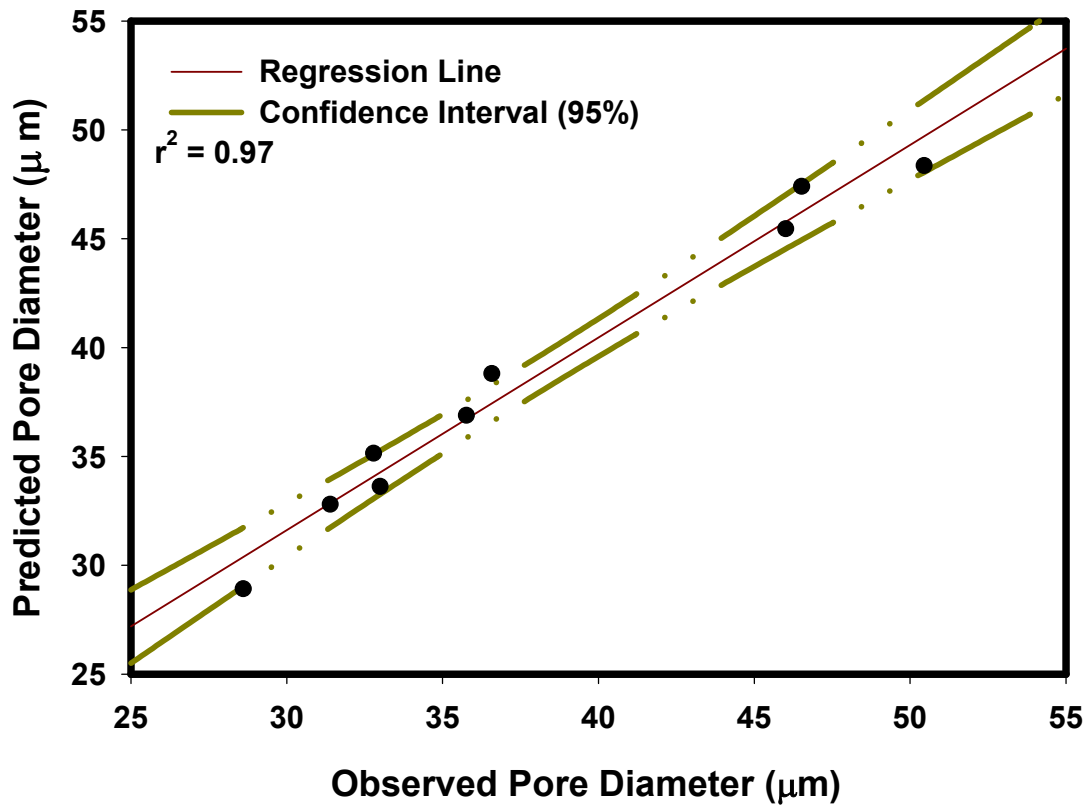


Figure 5.10: Plot showing the relationship between the predicted Pore diameter and observed pore diameter for the planar webs

The Table 5.3 gives the parameters for a similar model that was developed for the 3D web structures and the relationship equation is given below.

$$\hat{p}_d = 24.29 + 2.591 * f_d + 5.893 / f_p - 0.196 * f_d / f_p$$

Table 5.3: ANOVA and Regression of Structural Parameter Estimate for the 3D Web

Procedure: Regression; Dependent Variable: Pore Diameter Analysis of Variance					
Source	Degree of Freedom	Sum of Square	Mean Square	F-Value	Pr>F
Model	3	9480.449	3160.950	148.77	<0.001
Error	76	1614.412	21.242		
Total	79	11095			
Root MSE	Dependent Mean	Coeff. Of Var	R Square	Adj. R Square	
4.6089	71.3289	6.4615	0.9545	0.9487	
Parameter Estimates					
Variable	Degree of Freedom	Parameter Estimate	Standard Error	t-Value	Pr > t
Intercept (β_0)	1	24.2873	6.4137	3.79	<0.0003
Diameter (β_1)	1	2.5914	0.6307	4.11	<0.0001
Anisotropy ⁻¹ (β_2)	1	5.8932	1.5613	3.77	<0.0003
Dia * Ani ⁻¹ (β_3)	1	-0.1968	0.1086	-1.81	<0.0074

The two sets of equations for the pore size of the web show that the pore diameter is affected not only by the fiber diameter but also by the fiber orientation in the web. The predicted and observed values for the pore diameters in the 3D are given in Figure 5.11. The scatter plot of all the data is shown in Figure 5.12. This relationship further shows that the diameter of the pore is also affected by the curvature of the collecting surface and the fiber stream approach angle.

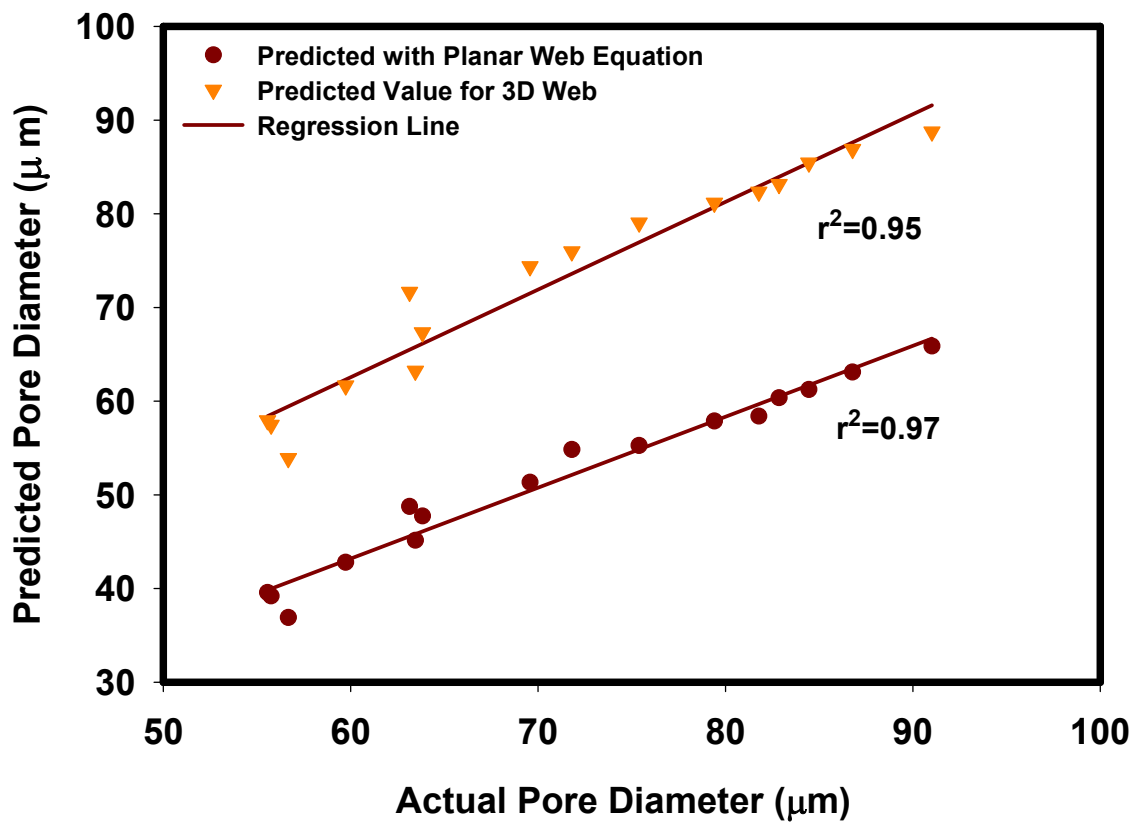


Figure 5.11: Plot showing the relationship between the predicted Pore diameter and observed pore diameter for the 3D webs

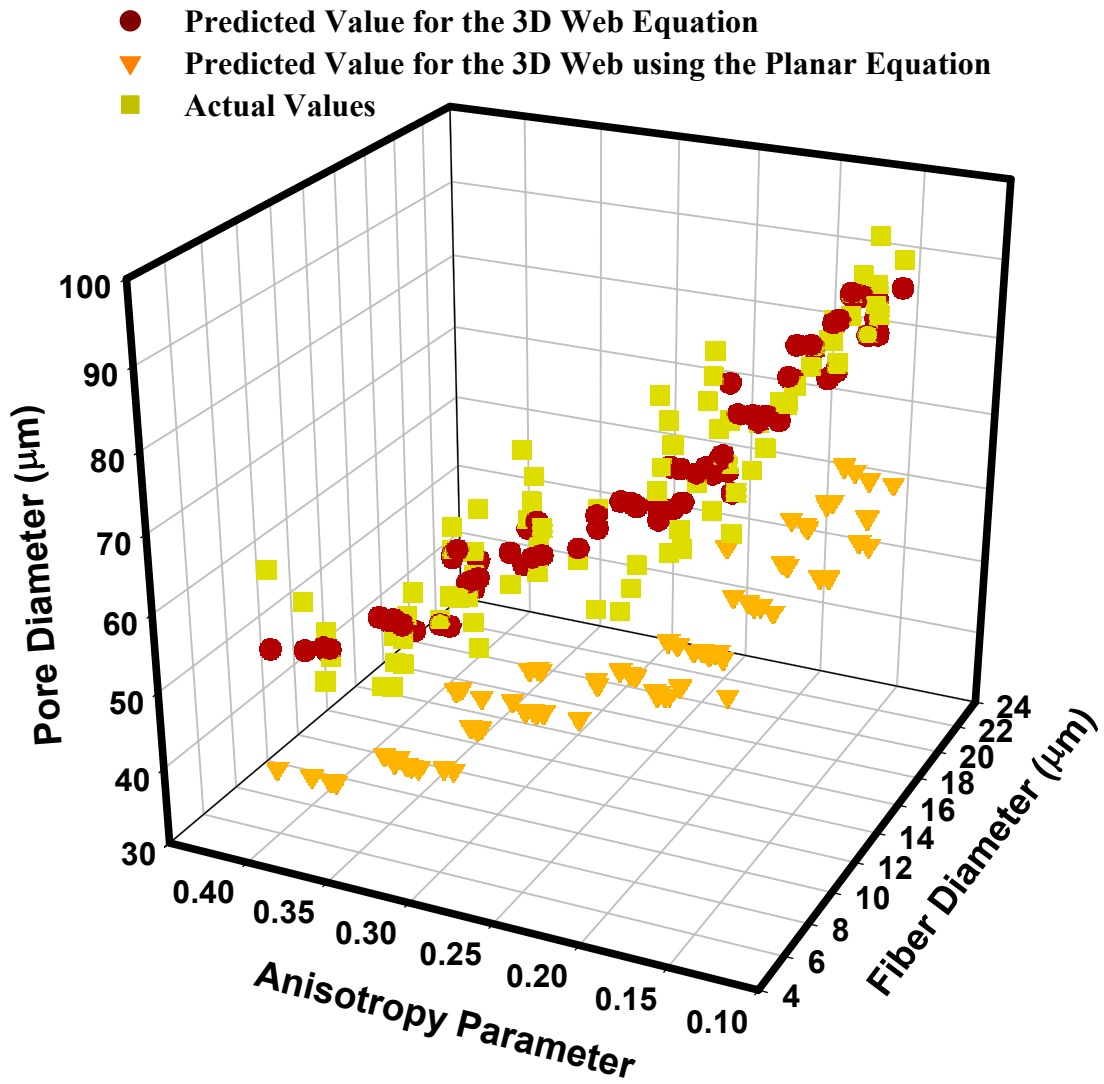


Figure 5.12: Scatter Plot of the observed and predicted pore diameters for the 3D webs

6 CONCLUSIONS

It has been shown that 3D web structures have been formed using the robotic and meltblown technology integrated system. A mold with continuously varying curvatures that can be used to remove the complete 3D web structure has been integrated with the system. Control over the application of the fibers on the mold has been achieved as described in the experimental section. The process for the formation of the webs using two different polymeric resins has been described (PP and COPE). The 3D web structures formed were at different fiber stream approach angles and curvatures of the collecting surface. The effects of the process variables on the structural parameters of the web have been investigated and their results can be summarized as follows:

Polymer Throughput:

- Does meaningfully influence the orientation distribution of the fibers in the web, but does not influence the anisotropy in the fiber distribution
- As the throughput increases the average fiber diameter increases and the distribution of the fiber diameter increases
- As the throughput increases the average pore size in the web also increases

Attenuating Air Pressure:

- An increase in the attenuating fluid pressure leads to the formation of finer fibers and narrower distribution of the fiber diameter
- It also leads to the formation of pores which are smaller in the web

Take-up Speed (Collector Surface Speed):

- As the take-up speed increases, the fibers are more oriented in the machine direction leading to the formation of web structures that are highly anisotropic in the distribution of the fibers
- The average fiber diameter in the web that are formed is found to decrease as the take-up speed increases
- The pore diameter in the web is also found to decrease as the take-up speed increases

Die to Collector Distance (DCD):

- An increase in the DCD causes randomization of the fibers in the web structure. The anisotropy in the fiber distribution decreases with increase in the DCD
- The diameter of the fibers that are formed in the web is found to decrease as the DCD increases
- The average pore diameter in the web is initially found to decrease (until 15 cm) and then the diameter of the pore is found to increase. This phenomenon

is attributed to the interaction between the ODF and the fiber diameter on the pore diameter. Upto a DCD of 15 cm, the fiber diameter plays a crucial role while beyond that distance the structural rearrangement of the fibers in the web forces the formation of larger pores.

Fiber Stream Approach Angle:

- As the approach angle increases (i. e. as the fiber stream becomes more normal to the collecting surface), the fibers are more randomly oriented. When the approach angle is decreased, the fibers travel a longer distance and also the tangential drag force acting on the fibers at the point of contact with the collecting surface increases, resulting in the fiber being aligned in the machine direction of the collector surface.
- An increase in the approach angle leads to the formation of thin fibers as the fibers are pulled into the web structure with a higher drag force at the point of contact.
- The highly oriented fibers at low approach angles and the finer fibers present in the webs formed at low approach angles lead to the formation of the finer pores in the web.

Curvature of the Collecting Surface:

- An increase in the curvature of the collecting surface affects the fiber alignment in the web significantly. An increase in the curvature causes the fibers in the web to be more oriented in the machine direction due to increase in the force acting on the fibers at the point of contact.
- Further, an increase in the curvature leads to the formation of finer fibers (viz. fibers with smaller diameters). Again the increase in the drag force on the fibers causes the attenuation of the fibers. A larger percentage of the fibers in the web have smaller diameters as the curvature of the collecting surface increases.
- As the curvature increases, the formation of finer pores in the web is the combined effect of finer fibers that highly oriented in the machine direction. The distribution of the pores in the web also decreases with the increase in the curvature of the collecting surface.

From these results we can conclude that the process parameters independently affect the ODF (anisotropy) and the fiber diameter in the web. But the pore diameter is dependent on the ODF and the fiber diameter, and hence is not an independent variable with respect to the process parameters.

The pore diameter for the simulated web structures is found to have an inverse relationship with the anisotropy parameter. Scatter plot of the three parameters show that the pore diameter is directly proportional to the fiber diameter. A Statistical model to study the interaction between the three structural parameters has been developed. The

two models developed for the 2D and 3D structures is used to predict the pore diameter for the 3D web structure. The pore diameter of the real web is found to behave as the hydrodynamic pore diameter of the simulated webs.

7 RECOMMENDATIONS

The robotic and meltblown integrated system can be exploited to form complex web structures that could find use in a variety of applications.

The RFAC system has to be developed to interface it with an external computer so as to modify and control the system independent of the “teach pendent”. This is essential to improve the safety around the system and also for improving the efficiency of the system.

For the formation of 3D structures it is essential that the product formed can be removed from the collecting surface. In this regard,

- A completely collapsible mannequin (which can be reassembled at a fast rate) has to be developed
- Different low melt polymeric resins have to be explored so that the web structure formed can retain its shape after it is subjected to other physical forces

The webs that are formed do not have an inherent strength, as they are not physically bonded. A suitable bonding technique to the system is required to impart the necessary strength to the web structure.

The structure of the web that is formed needs further investigation in the following areas:

- The length distribution as a function of the various process parameters has to be investigated
- The physical and mechanical properties of the webs formed, as a function of the newly exploited process variables (fiber stream approach angle and curvature of the collecting surface), has to be explored.
- Develop a theoretical model to predict the pore diameter and its distribution based on the fiber diameter distribution and the ODF of the web.
- Investigate the effects of processing parameters on the morphology of the fibers that are formed and model the morphology of the fibers based on the processing parameters.

8 BIBLIOGRAPHY

1. Miura, Y., and J. Hosoka, "Electrochemical Process in the Molding of Nonwoven Structures", *Textile Research Journal*, 49, 685-690 (1979).
2. Griesbach, H, L., R. D. Pike; S. W. Gwaltney; R. L. Levy; L. H. Sawyer; R. M. Shane; P. A. Sasse; "Method for making shaped nonwoven fabric", U. S. Patent 5,575894, 1996.
3. Griesbach, H, L., R. D. Pike; S. W. Gwaltney; R. L. Levy; L. H. Sawyer; R. M. Shane; P. A. Sasse; "Shaped nonwoven fabric", U. S. Patent 5643653, 1997
4. <http://www.innovent.com>
5. Johnston, M., Resin to Web Process—Meltblowns, International Nonwoven Fabrics Conference, 67–86, 1988.
6. Eian, G., Durable melt-blown fibrous sheet material, U. S. Patent 4,681,801., 1997.
7. Lee Y. C., and Wadsworth, L. C., Structure and Filtration Properties of Melt Blown Polypropylene Webs, *Polymer Engineering and Science*, 30 (22), 1413-1419, 1990.
8. Narasimhan, K. M., and Shambaugh, R. L., The Process of Melt Blowing, INDA-Tec 1987—Book of Papers, 189-205, 1987
9. Farer, R., Formation of 3D Meltblown Structures Using Robotic Control of Fiber Deposition., a Ph.D. Dissertation., North Carolina State University, 1999.
10. V. A. Wentz, Superfine Thermoplastic Fibers, *Industrial and Engineering Chemistry*, Vol. 48, (8), 1342 – 1346 , 1956.
11. R. G. Mansfield, Microdenier Nonwovens: Looking for Markets, *Textile World*, 83 – 84, 1979.
12. Jones, L. C. Wadsworth Novel Melt Blown Research Findings, *Nonwovens Industry*, 17, No. 11, 44, 47-51, Nov., 1986.
13. Okada, H., S. Asano, United States Patent 5,364,694, Polyethylene terephthalate based meltblown nonwoven fabric and process for producing the same, Kuraray Co. Ltd. Kurashiki, Japan, Nov, 15 1994.
14. Meyer et al., United States Patent 5,141,699, Tubular Chamber, Minnesota Mining and Manufacturing Company, St. Paul, Minnesota, August 25, 1992.
15. S. R. Malkan and L. C. Wadsworth. *Polymer Laid Systems. Nonwovens—Theory, Process, Performance and Testing*, TAPPI Press, Atlanta, 171–192, 1993.
16. M. Grayson. *Encyclopedia of Textiles, Fibers, and Nonwoven Fabrics*, Wiley-Interscience, New York, 265 – 278, 1984.
17. F. Rodriguez, *Principles of Polymer Systems*, 3rd Edition, Hemisphere Publishing Corporation, New York, 265 – 374, 1989.
18. McAmish, Larry H., Tralance O. Addy, George F. Lee, United States Patent 4,622,259, Nonwoven Medical Fabric, Surgikos Inc., Arlington, Tx, Nov. 11, 1986.
19. T. J. Wisneski, M. T. Morman, United States Patent 4,663,220, Polyolefin Containing Extrudable Compositions and Methods for their Formation into Elastomeric Products Including Microfibers, Kimberly-Clark Corporation, Neenah, Wis, May 5, 1987
20. Nyssen, Peter R., A. Kreimer, W. Wagner, D. Berkenhaus, United States Patent 5,260,003, Method And Device For Manufacturing Ultrafine Fibres From Thermoplastic Polymers, Dormagen, Germany, Nov. 9, 1993.

21. Eugene, Joseph, International Publication Number WO 93/07321, Stretchable Nonwoven Webs Based On Multilayer Blown Microfibers, Minnesota Mining and Manufacturing Company, St. Paul, Wis., April 15, 1993.
22. R. L. Shambaugh. A Macroscopic View of the Meltblowing Process for Producing Microfibers, Nonwoven Technology Today Miller Freeman Publication, San Francisco, CA, 41-54, 1989.
23. Dullien F. A., Porous Media – Fluid Transport and Pore Structure, 2nd Ed., Academic Press, New York, 1992.
24. Ando, K.,. Melt blown webs for Thermal Insulation. Proceedings of the International Symposium on Fiber Science and Technology, 238, 20–24, 1985.
25. S.B. Warner, C. A. Perkins and A. S. Abhiraman, “Melt Blown Polypropylene Fibers Part I: Physical Properties”, INDA Journal 2(2), 33 – 37, 1990
26. E. Vargas, Meltblown Markets, Meltblown Technology Today, Miller Freeman Publications, 13 - 23, 1990.
27. Hearle, J.W. S., and Stevenson, P.J., Nonwoven Fabric Studies, Part III: The Anisotropy of Nonwoven Fabrics, Textile Research Journal 33, 877 – 888, 1963.
28. Backer S and Petterson D R, Some Principles of Nonwoven Fabrics. Textile Research Journal, 30, 709, 1960.
29. S. R. Malkan and L.C. Wadsworth. Process-Structure-Property Relationships in Melt Blowing of Different Molecular Weight Polypropylene Resins Part I – Physical Properties. INDA Journal, 3(2), 21-34, 1991
30. G. S. Bhat, V. Narayanan, and L. C. Wadsworth. Dimensionally stable fibers and non-woven webs, United States Patent 5,753,736, The University of Tennessee Research Corporation, Knoxville, TN, May 19, 1998.
31. F. C. Haides, Polypropylene for Meltblown Applications, Meltblown Technology Today, Miller Freeman Publications, 61 – 63, 1990.
32. W. A. Haile, Polyesters for Meltblowing, Meltblown Technology Today, Miller Freeman Publications, 69 – 71, 1990
33. W. A. Haile, Private Communication.
34. Milligan, Mancil W., United States Patent 5,273,565, Meltblown Fabric, Exxon Chemical Patents Inc., Linden, N.J., Dec. 28, 1993.
35. Hodgson, W. J. Jr., European Patent Application 88300241.2, Melt blown nonwoven web from fiber comprising an elastomer, Exxon Chemical Patents Inc., Jan. 12, 1988.
36. Lau, Jark C., United States Patent 4,526,733, Meltblown Die And Method, Kimberly-Clark Corporation, Neenah, Wis., Jul. 2, 1985.
37. Lau, Jark Chong, UK Patent Application GB 2 130 260 A, Non-woven web formation, Kimberly-Clark Corporation, Neenah, Wis., Nov. 17, 1982.
38. Yin, H., Yan, Z., and Bresee, R, R., “Experimental Study of the Meltblowing Process”, International Nonwovens Journal, Spring, 130- 139, 1999
39. Bresee, R, R., “Fiber Motion Near the Collector During Melt Blowing: Part II: General Considerations”, International Nonwovens Journal, Summer, 27 -33, 2002
40. Bresee, R, R., “Fiber Motion Near the Collector During Melt Blowing: Part I: Fly Formation”, International Nonwovens Journal, Fall, 21-27, 2002
41. Wadsworth, L. C., Novel Melt Blown Research Findings, Nonwovens Industry, 17, No. 11, 44, 47-51, Nov. , 1986

42. Jones, A. M., L. C. Wadsworth, TAPPI Nonwovens Conference Proceedings 1986, Advances in Melt Blown Resins, 23-30, 1986
43. Cheng, C. Y., A polypropylene extrusion system for nonwoven processes, Tappi Journal , 77 (12), 167-173, 1994.
44. Ogata, Satoshi, European Patent Application 0 622 101 A1, Cylindrical filter and process for producing the same, Japan, April 30, 1993
45. Schwarz, E. C. A., INDA-TEC 1987. Book of Papers, New Concepts In Melt-Blown Design Applied To Microfibers, Co-Spun And Co-Extruded Products, 206-220, 1987
46. Abdel-Ghani, M. S. and G. A. Davies, “ Simulation of Non-woven Fiber mats and the Application to Coalescers”, Chemical Engineering Science , 40, 117-129 , 1985.
47. Piekaar H. W. and Clarenburg L. A., “Aerosol filters – Pore size distribution in fibrous filters”, Chemical Engineering and Science, 22, 1399 - 1407, 1967.
48. Kim, H. S. and b. Poudeyhimi., “ A note on the effect of fiber diameter, fiber crimp and fiber orientation on pore size in thin webs”, International Nonwovens Journal, Winter, 2000.
49. Lombard, G., A. Rollin., and C. Wolff., Theoretical and Experimental Opening Sizes of Heat-Bonded Geotextiles., Textile Research Journal., April 1987, 208.
50. Masounave, J., A. Rollin., and R. Denis., “Prediction of Permeability of Nonwoven Geotextiles from Morphometry Analysis”, Journal of Microscopy, 121(1), 99-110, 1981.
51. Hammersley, J.M., and D. C. Handscomb., “Monte Carlo Methods”., Wiley, New York, 1964.
52. George, F. S., “Monte Carlo: Concepts, Algorithms, and Applications”., Springer-Verlag, 1996.
53. Larson, J, H, “Introduction to Probability Theory and Statistical Inference”, Wiley, New York, 1982.
54. Brunnschweiler, D., Haigh – Chadwick: Microweb Card Monitor, Textile World., 135, 47-48, 1986.
55. Lennox-Kerr., Laser Card Monitor., Melliand Textilberichte 72, 253 1991
56. Brunnschweiler, D., Johnson, P. G., and Henderson, N. R., Textile Structure Measurement, U. S. Patent 4,733,080, 1988.
57. Gupta, B. S., and Pichardo, C., Characterization of the Areal Density and Uniformity in Nonwovens Using Capacitive Methods Part I: General Approach and Preliminary results., Tappi Nonwovens Conference, 303 – 307, 1990.
58. Purdy A., Developments in Nonwoven Fabrics, Textile Progress., 17-19. 1983
59. Testing Nonwovens: Equipment and Procedures, Seminar: June 11-12, Philadelphia College of Textiles & Science, Philadelphia, PA., 1985
60. Huang, X., and Breese, R. R., Characterizing Nonwoven Web Structure Using Image Analysis Techniques, Part II: Fiber Orientation Analysis, INDA Journal of Nonwovens Research. 5 (2), 14 – 21, 1993.
61. Hearle, J. W. S., and Sultan, M. A. I., A Study of Needled Fabrics, Part IV, J. Textile Institute., 59, 161, 1968.
62. Hearle, J. W. S, and Stevenson, P. J. Nonwoven Fabric Studies, Part III: The Anisotropy of Nonwoven Fabrics, Textile Research Journal , 66(11), 713-722 1996.
63. Pourdeyhimi, B., Ramanathan, R., Measuring Fiber Orientation in Nonwovens, Part I; Simulation, Textile Research Journal, 66 (11), 713-722 1996.

64. Cox, H. L., The Elasticity and Strength of Paper and Other Fibrous Materials, *British Journal of Applied Physics*, 3, 72-79, 1952.
65. Mohammed, A., Shambaugh, R. L., Three-Dimensional Flow Field of a Rectangular Array of Practical Air Jets, *Industrial and Engineering Chemistry Research.*, 32, 976-980, 1993.
66. Komori, T., and Makashima, K., Estimation of Fiber Orientation and Length in Fiber Assemblies., *Textile Research Journal*, 49 (6), 309 – 314, 1978.
67. Class Notes TT305 Spring 2001 North Carolina State University.
68. Pourdeyhimi, B and Kim, H. S., Angular Nonwoven Properties., *Textile Asia*, 3, 33-36, 2000
69. Kim, H. S., Pourdeyhimi, B., Abhiraman, A., Desai, P., Effect of Bonding Temperature on Load-Deformation Structural Changes in Point Bonded Nonwoven Fabrics., *Textile Research Journal*, 72 (7), 645-653, 2002.
70. Crosby C M., Eusufari, A. R. K., and Mark, R. E., A Digitizing System for Quantitative Measurement of Structural Parameters in Paper, *Tappi Journal* 64 (3), 103 – 106, 1981.
71. Cowan, W. F. and Cowdrey, E. J. K., Evaluation of Paper Strength Components by Short-Span Tensile Analysis, *Tappi Journal*, 62(2), 90-93, 1979
72. Tsai, P., and Bresee, R., Fiber Orientation Distribution in Thin Nonwoven Webs from Electrical Measurements, *INDA Journal of Research*, 3, 30-35, 1991
73. Watson, R. L., Method and Apparatus for Optically Monitoring Fiber Orientation in Nonwoven Webs, U. S. Patent 4,730,931, 1986.
74. Boulay, R., Drouin, B., and Gagnon, R., Method for Measuring Fiber Orientation Anisotropy in a Fibrous Structure, U. S. Patent 4,654,529, 1986.
75. Pourdeyhimi, B, Davis, H., and Dent, R., Measuring Fiber Orientation in Nonwovens Part III: Fourier Transform, *Textile Research Journal*, 67 (2), 143 - 151, 1997
76. Yan, Y. Y., and Bresee, R. R., Flexible Multifunction Instrument for Automated Nonwoven Web Structure Analysis, *Textile Research Journal*, 69 (11), 795 – 804, 1999
77. Bansal, V., and Shambaugh, R., On-line Determination of Fiber Diameter and Temperature during Melt Blowing of Polypropylene, *Industrial and Engineering Chemistry Research*, 37 , 1799-1806, 1998.
78. Pourdeyhimi, B., Online 'Image' Product Literature, Roswell, GA, 1998.
79. Buntin, R. R., and Lokhamp, D. T., Melt Blowing – One Step Web Process for New Nonwoven Products, *TAPPI*, 56 (4), 74 – 77, 1973.
80. Milligan, M. W., and Utsman, An Investigation of the Meltblown Web Defect known as Shot, *International Nonwovens Journal*, 7(2), 65 – 68, 1995.
81. Wallen, J., Fellers. J. F., Milligan, M. W., Small Angle Light Scattering Studies of Fiber Orientation and Shot Formation in the Melt Blowing Process, *International Nonwovens Journal*, 7(3), 51 – 55, 1995.
82. Allen, T., Particle Size Measurement, 5th Ed., Chapman and Hall, New York, 1997.
83. Bear, J., Dynamics of Fluids in Porous Media, American Elsevier Publication Company, New York, 1972.
84. Perna, V., and Jena, A. K., In-plane and Through-plane Porosities in Nonwovens, Proceedings of TAPPI Nonwovens Conference, Orlando Fl, March 15 – 17, 177 – 187, 1999

85. Xu, B, Pourdeyhimi, B., and Sobus, J., Fiber Cross-Sectional Shape-Analysis Using Image-Processing Techniques, *Textile Research Journal*, 63 (12), 717 – 730, 1993
86. Defay, R., Prigogine, I., and Sanfield, A., Surface Thermodynamics, *Journal of Colloid Interface Science*, 58 (3), 498-510, 1977
87. Choi, K., Permeability –Pore Size Relationships of Nonwoven Filter Media, *Tappi Nonwovens Conference*, 49-50, 1995.
88. Bhatia, S. K., Smith, J. L., and Christopher, B. R., Geotextile Characterization and Pore Size Distribution: Part III. Comparison of Methods and Application to Design, *Geosynthetics International*, 3 (3), 301 – 328, 1996.
89. Bhatia, S. K., and Smith, J.L., Geotextile Characterization and Pore Size Distribution: Part I. A Review of Manufacturing Processes, *Geosynthetics International*, 3 (1), 85-105, 1996.
90. Xu, B., Measurement of Pore Characteristics in Nonwoven Fabrics using Image Analysis, *Clothing and Textile Research Journal*, 14 (1), 81 – 88, 1996
91. Dent, R., Pore Volume Distribution in Press Felts, *TexTechtil Conference*, 2001
92. <http://www.eastman.com>
93. Gong, R. H., Newton, A., Image-analysis Techniques Part II: The Measurement of Fibre Orientation in Nonwoven Webs, *Journal of the Textile Institute*, 87, Part I, No. 2, 371-388, 1996.
94. Pourdeyhimi, B., Dent, R., Jerbi, A., Tanaka, S., and Deshpande, A., Measuring Fiber Orientation in Nonwovens, Part V: Real Webs, *Textile Research Journal*, 69, 185-192, 1999.
95. Goodman, J. W., “Introduction to Fourier Optics,” McGraw-Hill, San Francisco, 1968.
96. Veerabhadran, K., “Studies on the Uniformity of Fiberweb basis Weight and Structure”, Doctoral Dissertation, North Carolina State University, 1994.
97. Veerabadran, K., Davis, H. A., Batra, S. K., and Bullerwell, A. C., Devices for On-Line Assessment of Nonwovens’ Basis Weights and Structures, *Textile Research Journal*, 66, 257, 1996.
98. Ott, R. L.; “An Introduction to Statistical Methods and Data Analysis”, 4Th edition.
99. Chhabra, R. S., and Shambaugh, R. L., Experimental Measurements of Fiber Threadline Vibrations in the Melt-Blowing Process, *Industrial and Engineering Chemistry Research*, 35, 4366-4374, 1996.
100. Wu, T. T., Shambaugh, R. L., Characterization of the Melt Blowing Process with Laser Doppler Velocimetry, *Industrial and Engineering Chemistry Research*, 31, 379-389, 1992.
101. Majumdar, B., and Shambaugh, R. L., Velocity and Temperature Fields of Annular Jets, *Industrial and Engineering Chemistry Research*, 30, 1300 – 1301, 1991
102. Uyttendale, M. A. J., and Shambaugh, R. L., The Flow Field of Annular jets at Moderate Reynolds Numbers, *Industrial and Engineering Chemistry Research*, 28, 1735 – 1740, 1989
103. Uyttendale, M. A. J., and Shambaugh, R. L., Melt Blowing: General Equation Development and Experimental Verification, *AIChE Journal*, 36 (2), 175 – 186, 1990.
104. Tsai, P. P., Effect of Melt Blown Web Defects on Filtration Efficiency, *Proceedings of TAPPI Nonwovens Conference, Orlando Fl, March 15 – 17, 137 – 146, 1999*

105. Turbak, A. F., *Nonwovens: Theory, Process, Performance, and Testing*, Tappi Press, Atlanta, GA., 1993.
106. Wadsworth, L. C., and Fagan, J., Melt blown processing and Characterization of Fluoropolymer Resins, *INDA Journal of Nonwovens Research*, 4 (4), 27 – 31.
107. Scharcanski, J., and C. T. J. Dodson, Textural Analysis for Estimating Spatial Variability and Anisotropy in Planar Stochastic Structures., *Optical Engineering Journal*, 35 (8), 2302-2309, 1996.
108. Kyan, C.P., D.T. Wasan and R.C. Kintner., “Flow of Single Phase Fluid through Fibrous Beds,” *Industrial Engineering and Chemistry Fundamentals*, 9, 596-603, 1970.
109. Dodson., C. T. J. and Sampson W. W., Modeling a Class of Stochastic Porous Media, *Applied Mathematics Letters*, 10 (2), 87-89, 1997.
110. Gong, R. H. and A. Newton, “ Image Analysis Techniques Part I: The measurement of Pore-Size Distribution”, *Journal of the Textile Institute*, 83, 253-268, 1992.
111. Huang , X. C. and R. R. Bresee,, “Characterizing Nonwoven Web Structures Uisng Image Analysis Technqiues, Part I: Pore Analysis in Thin Webs, *INDA Journal of Nonwovens Research*, 5, 13-20, 1993.

APPENDIX

Table A-1: ANOVA for ODF of fibers in MB COPE Webs at Various Polymer Throughputs

SAS PROCEDURE: PROC glm					
Dependent Variable: log(Frequency)					
Source	Degrees of freedom	Type III squares	Mean square	F-value	Pr > f
Polymer Throughput	3	0.0038	0.0013	0.68	0.5770
Sample(Throughput)	16	0.0310	0.0019		
Orientation Angle	17	5.1728	0.3043	41.53	<0.0001
Throughput*Orientation Angle	51	0.5266	0.0103	1.41	0.0448
Error	272	1.9930	0.0073		

Table A-2: ANOVA for Anisotropy of the MB COPE Web at Various Polymer Throughputs

Source of Variation	SS	Df	Ms	F	P-value	F crit
Between groups	0.0008	4	0.0002	0.2669	0.8958	2.8661
Within groups	0.0158	20	0.0008			
Total	0.0166	24				

Table A-3: ANOVA for ODF of the MB COPE Web at Various Take-up Speeds

SAS PROCEDURE: PROC glm					
Dependent variable: log(Frequency)					
Source	Degrees of freedom	Type III sum of squares	Mean Square	F-value	Pr > F
Take-up Speed	3	0.1024	0.0341	42.63	<0.0001
Sample(TakeupSpeed)	16	0.0120	0.0008		
Orientation angle	11	10.0636	0.9149	171.15	<0.0001
TakeupSpeed*Orientation angle	33	2.9765	0.0902	16.87	<.0001
Error	176	0.9407	0.0053		

Table A-4: ANOVA for Anisotropy of the MB COPE Web at Various Take-up Speeds

ANOVA						
Source of Variation	SS	df	MS	F	P-value	F crit
Between Groups	0.1212	3	0.0404	60.5436	0	3.2389
Within Groups	0.0107	16	0.0007			
Total	0.1319	19				

TableA-5: ANOVA for ODF of the MB COPE Web at Various DCD

SAS PROCEDURE: PROC glm					
Dependent variable: log(Frequency)					
Source	Degrees of freedom	Type III sum of squares	Mean Square	F-value	Pr > F
DCD	3	0.0306	0.0102	4.72	0.0152
Sample(DCD)	16	0.0345	0.0022		
Orientation angle	17	10.3214	0.6071	62.08	<.0001
DCD*Orientation angle	51	2.9107	0.0571	5.84	<.0001
Error	272	2.6602	0.0098		

Table A-6: ANOVA for Anisotropy of the MB COPE Web at Various DCD

ANOVA						
Source of Variation	SS	df	MS	F	P-value	F crit
Between Groups	0.0835	6	0.0139	14.7206	0	2.4452
Within Groups	0.0264	28	0.0009			
Total	0.1100	34				

TableA-7: ANOVA for ODF of the MB COPE Web at Various Fiber Stream Approach Angles

SAS PROCEDURE: PROC glm					
Dependent variable: log(Frequency)					
Source	Degrees of freedom	Type III sum of squares	Mean Square	F-value	Pr > F
Approach Angle	5	0.8047	0.1609	27.27	<0.0001
Sample(Approach Angle)	24	0.1419	0.0059		
Orientation angle	17	82.2516	4.8383	1777.95	<0.001
ApproachAngle*Orientation angle	85	4.4949	0.0529	19.43	<0.0001
Error	408	1.1103	0.0027		

Table A-8: ANOVA for Anisotropy of MB PP webs at Various Approach Angles

ANOVA						
Source of Variation	SS	df	MS	F	P-value	F crit
Between Groups	0.1303	5	0.0261	84.0600	0	2.6207
Within Groups	0.0074	24	0.0003			
Total	0.1377	29				

TableA-9: ANOVA for ODF of the MB COPE Web at Various Curvatures of Collecting Surface

SAS PROCEDURE: PROC glm					
Dependent variable: log(Frequency)					
Source	Degrees of freedom	Type III sum of squares	Mean Square	F-value	Pr > F
Curvature	9	6.9960	0.7773	485.81	0
Sample(Curvature)	40	0.0640	0.0016		
Orientation angle	11	0.8021	0.0729	1.00	0.0307
Curvature*Orientation angle	99	38.4957	0.3888	5.32	<0.0001
Error	740	54.1180	0.0731		

Table A-10: ANOVA for Anisotropy of MB PP webs at Various Curvatures of Collecting Surface

ANOVA						
Source of Variation	SS	df	MS	F	P-value	F crit
Between Groups	0.1654	9	0.0184	94.2143	0	2.1240
Within Groups	0.0078	40	0.0002			
Total	0.1732	49				

MATHEMATICA CODE FOR EQUATION SOLVER

```
d=ReadList["c:\.....",Number,RecordLists->True];
Print[%]
For [i=1, i<n,i++,
e1=d[[i]][[1]]*xc[i]+d[[i]][[2]]*yc[i]+d[[i]][[3]]*zc[i]-d[[i]][[4]];
e2=d[[i+1]][[1]]*xc[i]+d[[i+1]][[2]]*yc[i]+d[[i+1]][[3]]*zc[i]-d[[i+1]][[4]];
e3=d[[i+2]][[1]]*xc[i]+d[[i+2]][[2]]*yc[i]+d[[i+2]][[3]]*zc[i]-d[[i+2]][[4]];
s[i]=NSolve[{e1==0,e2==0,e3==0},{xc[i],yc[i],zc[i]}];
Print[s[i]]]
```

ABBROBOT CODE FOR GENERATING WEBS OF DIFFERENT CURVATURES AT SAME SURFACE SPEED

%%%

VERSION:1

LANGUAGE:ENGLISH

%%%

MODULE VelocityConstant

VAR robtarget l0:=[[[-582.12,-5428.53,-4831.67],[0.70455,-0.011227,0.709336,0.018083],[0,-1,0,0],[0.116504,9E+09,9E+09,9E+09,9E+09,9E+09]]];

VAR robtarget l45:=[[[-5.76,-5623.12,-4810.15],[0.699711,-0.053376,0.709988,0.058934],[0,-1,0,0],[45.0621,9E+09,9E+09,9E+09,9E+09,9E+09]]];

VAR robtarget l90:=[[[-637.74,-5428.74,-4827.83],[0.704559,-0.011246,0.709326,0.01808],[0,-1,0,0],[90.0358,9E+09,9E+09,9E+09,9E+09,9E+09]]];

VAR robtarget l135:=[[[-1633.63,-5019.28,-4729.92],[0.699136,0.048725,0.711535,-0.050528],[0,0,-1,0],[134.986,9E+09,9E+09,9E+09,9E+09,9E+09]]];

VAR robtarget l180:=[[[-574.61,-5428.84,-4824.02],[0.704558,-0.011257,0.709327,0.018083],[0,-1,0,0],[179.944,9E+09,9E+09,9E+09,9E+09,9E+09]]];

VAR robtarget l225:=[[45.28,-5633.6,-4804.87],[0.699283,-0.056366,0.709896,0.062247],[0,-1,0,0],[224.964,9E+09,9E+09,9E+09,9E+09,9E+09]]];

VAR robtarget l270:=[[[-637.38,-5428.92,-4820.29],[0.704558,-0.011273,0.709326,0.018096],[0,-1,0,0],[270.081,9E+09,9E+09,9E+09,9E+09,9E+09]]];

VAR robtarget l315:=[[[-1703.01,-4943.78,-4759.21],[0.699388,0.056247,0.710504,-0.053638],[0,0,-1,0],[315.047,9E+09,9E+09,9E+09,9E+09,9E+09]]];

CONST speeddata v512_74:=[512.74,500,5000,1000];

CONST speeddata v838_16:=[838.16,500,5000,1000];

CONST speeddata v883_22:=[883.22,500,5000,1000];

CONST speeddata v506_29:=[506.29,500,5000,1000];

CONST speeddata v552_60:=[552.6,500,5000,1000];

CONST speeddata v908_88:=[908.88,500,5000,1000];

CONST speeddata v947_73:=[947.73,500,5000,1000];

CONST speeddata v471_86:=[471.86,500,5000,1000];

PROC turn_up()

FOR i FROM 1 TO 40 DO

MoveL l0,v947_73,z5,MB_DIE_R_CORNER;

l0:=Offs(l0,0,0,15);

IndDMove IC7MID1,1,45,35;

MoveL l45,v471_86,z5,MB_DIE_R_CORNER;

l45:=Offs(l45,0,0,15);

```

IndDMove IC7MID1,1,45,35;
MoveL I90,v512_74,z5,MB_DIE_R_CORNER;
I90:=Offs(I90,0,0,15);
IndDMove IC7MID1,1,45,35;
MoveL I135,v838_16,z5,MB_DIE_R_CORNER;
I135:=Offs(I135,0,0,15);
IndDMove IC7MID1,1,45,35;
MoveL I180,v883_22,z5,MB_DIE_R_CORNER;
I180:=Offs(I180,0,0,15);
IndDMove IC7MID1,1,45,35;
MoveL I225,v506_29,z5,MB_DIE_R_CORNER;
I225:=Offs(I225,0,0,15);
IndDMove IC7MID1,1,45,35;
MoveL I270,v552_60,z5,MB_DIE_R_CORNER;
I270:=Offs(I270,0,0,15);
IndDMove IC7MID1,1,45,35;
MoveL I315,v908_88,z5,MB_DIE_R_CORNER;
I315:=Offs(I315,0,0,15);
IndDMove IC7MID1,1,45,35;
ENDFOR
ENDPROC

```

```

PROC turn_down()
FOR i FROM 1 TO 40 DO
MoveL I0,v471_86,z5,MB_DIE_R_CORNER;
I0:=Offs(I0,0,0,-15);
IndDMove IC7MID1,1,-45,35;
MoveL I1315,v947_73,z5,MB_DIE_R_CORNER;
I1315:=Offs(I1315,0,0,-15);
IndDMove IC7MID1,1,-45,35;
MoveL I1270,v908_88,z5,MB_DIE_R_CORNER;
I1270:=Offs(I1270,0,0,-15);
IndDMove IC7MID1,1,-45,35;
MoveL I1225,v552_60,z5,MB_DIE_R_CORNER;
I1225:=Offs(I1225,0,0,-15);
IndDMove IC7MID1,1,-45,35;
MoveL I1180,v506_29,z5,MB_DIE_R_CORNER;
I1180:=Offs(I1180,0,0,-15);
IndDMove IC7MID1,1,-45,35;
MoveL I1135,v883_22,z5,MB_DIE_R_CORNER;
I1135:=Offs(I1135,0,0,-15);
IndDMove IC7MID1,1,-45,35;
MoveL I190,v838_16,z5,MB_DIE_R_CORNER;
I190:=Offs(I190,0,0,-15);
IndDMove IC7MID1,1,-45,35;
MoveL I145,v512_74,z5,MB_DIE_R_CORNER;

```

```
l45:=Offs(l45,0,0,-15);  
IndDMove IC7M1D1,1,-45,35;  
ENDFOR  
ENDPROC
```

```
PROC main()  
turn_up;  
l0:=Offs(l0,0,0,15);  
turn_down;  
l0:=Offs(l0,0,0,-15);  
ENDPROC  
ENDMODULE
```